



UNIVERSITY OF
CAMBRIDGE

Nonlinear Acoustics in a General Waveguide



James Peter McTavish

Department of Applied Mathematics and Theoretical Physics
University of Cambridge

This dissertation is submitted for the degree of
Doctor of Philosophy

Downing College

September 2018

Nonlinear Acoustics in a General Waveguide

James Peter McTavish

Until this present work, the acoustics of waveguides has been divided into two broadly distinct fields—linear acoustics in ducts of complex geometry such as those with curvature or varying width, and nonlinear acoustics restricted to simple geometry ducts without curvature or flare. This PhD unites these distinct branches to give a complete mathematical description of weakly nonlinear wave propagation in a general shaped duct in both two and three dimensions. Such ducts have important applications—the clearest example is that of brass instruments, where it has been demonstrated that nonlinear wave steepening gives rise to the characteristic “brassy” sounds of, for example, the trombone. As the ducts of these instruments have a very complicated geometry involving curvature, torsion and varying width, the goal of the PhD is to address what effect, if any, such changes in duct geometry have on the acoustic properties of such instruments. Other potential applications include the study of acoustics in curved aircraft engine intakes and even the nonlinear sound propagation through the trunk of an elephant.

The first results chapter is focused on the exposition of the method used for the remainder of the paper, with the introduction of a new “nonlinear admittance term” as well as the associated algebra for it. An elegant notation for the nonlinear algebra is also developed, greatly simplifying the equations. The method is applied to one and two dimensional ducts and some analytical results are derived relating the work to previously published results. Numerical results are also presented and compared to other sources. The concept of nonlinear reflectance is also introduced—illustrating the effect of wave amplitude on the amount of energy reflected in a duct. The next results chapter builds on this work extending it to three dimensions. Numerical results are presented for three characteristic ducts—a curved duct, a horn and a helical duct, being one of the first works to study acoustics in helical pipes for both linear and nonlinear sound propagation. The final results chapter, utilising all of the previous work, addresses the problem of an open ended duct of finite length with nonlinear effects included. Results are compared with the linear results from the Wiener-Hopf method and new results are presented illustrating the effect of geometry and nonlinearity on the resonances of finite length waveguides culminating in the study of the resonances of a trombone.

To Mum and Dad.

Declaration

I hereby declare that except where specific reference is made to the work of others, the contents of this dissertation are original and have not been submitted in whole or in part for consideration for any other degree or qualification in this, or any other university. This dissertation is my own work and contains nothing which is the outcome of work done in collaboration with others, except as specified in the text and Acknowledgements. The work of chapter 2 has been submitted for publication (McTavish and Brambley, 2018).

James Peter McTavish
September 2018

Acknowledgements

First of all I would like to thank my parents for all the love and support you have given me during this PhD and in all my endeavours—it means everything to me. I would like to thank my girlfriend, Mariann, for all of her help and support, particularly in these last few difficult months—I’m not sure if you helped the progress of this PhD, but your distraction was certainly welcome and you have no doubt made these last couple of years some of my happiest. I would like to thank all of the friends I have met along the way: Jordan, Talbot, Josh, Lewis, Dave, Niall, Jenny—you *definitely* didn’t help with the progress of my PhD, but thanks for all of the (very) silly times and the memories (or lack thereof...)—it’s been fun. I would like to thank my supervisor, Dr. Ed Brambley, for giving me this opportunity. I would like to thank Downing college for their financial support in attending conferences and assistance in my fourth year. In particular, I would also like to thank the college MCR over the years for making this experience so special. Finally, I would like to thank Professor Ray Goldstein and, in particular, Dr Adriana Pesci—the help and guidance you have given me from all the way back when I was thinking of applying to Cambridge, through my undergraduate years to part III and throughout my PhD has been so important to me—I would not be in the position I am now if it weren’t for you—thank you.

Table of contents

List of figures	xv
List of tables	xxi
Nomenclature	xxiii
1 Introduction	1
2 2D Ducts	9
2.1 Introduction	9
2.2 Governing Equations	9
2.2.1 Duct Geometry	13
2.3 Boundary Conditions for an Infinite Uniform Duct Outlet	20
2.3.1 Stability of fixed points of the admittance	22
2.4 Special Cases	23
2.4.1 1D Duct and the Equivalence to the Fubini and Sawtooth Solutions	23
2.4.2 Uniform Straight Ducts	25
2.4.3 Linear Acoustics in a Non Uniform Straight Duct	28
2.4.4 Linear Acoustics in a Curved Duct	29
2.5 Numerical Method	30
2.5.1 Numerical Viscosity	32
2.5.2 Ducts of Increasing Width	33
2.6 Results	34
2.6.1 1D Duct	34
2.6.2 2D Straight Duct	36
2.6.3 Variable Width Straight Duct	36
2.6.4 Uniform Curved Ducts	38
2.6.5 Nonuniform Curved Ducts	38
2.7 Comparisons Between Ducts	42

2.8	Nonlinear Reflection	44
2.9	Conclusion	49
3	3D Ducts	53
3.1	Introduction	53
3.2	Governing Equations	53
3.3	Boundary Condition for an Infinite Uniform Duct Outlet	65
3.3.1	Torsion Free Outlets	65
3.3.2	Boundary Conditions for an Infinite Helical Duct	66
3.4	Numerical Method	73
3.5	Results	74
3.5.1	Uniform Curved Ducts	74
3.5.2	Variable Width Straight Ducts	75
3.5.3	Linear Acoustics in Helical Ducts	78
3.5.4	Nonlinear Acoustics in Helical Ducts	80
3.6	Conclusion	82
4	Open Ducts	87
4.1	Introduction	87
4.2	Governing Equations	88
4.2.1	Baffled Ducts	88
4.2.2	Dipole Sources	91
4.2.3	Unbaffled Ducts	92
4.3	Numerical Method	96
4.4	Comparison with the Wiener-Hopf Solution	98
4.5	Results	103
4.5.1	Resonances in finite length duct	104
4.5.2	Cylindrical Ducts	107
4.5.3	The Effect of the Bell	126
4.5.4	Conical Ducts	136
4.5.5	Curved Ducts	147
4.5.6	Helical Ducts	157
4.6	Acoustics in a Trombone	163
4.7	Conclusion	172
5	Conclusion	177
5.1	Further Work	181

Table of contents	xiii
References	185
Appendix A Modes of Zero Frequency	189
Appendix B Analytic Expressions for the Ψ Matrices	191
B.1 2D	191
B.2 3D	192
B.3 Open Ducts	194
Appendix C Inverting F	195
Appendix D A Simplifying Substitution	197
D.1 2D	197
D.2 3D	198
Appendix E Nonlinear Inverse Method	201

List of figures

1.1	The original illustration from Stokes (1848) showing waveform steepening	3
1.2	A shock wave radiating from the bell of a trumpet. Taken from Pandya et al. (2003)	4
2.1	Illustration of the geometry of the duct	12
2.2	Convergence of the method fixing the number of temporal or spatial modes	31
2.3	Comparison of modal amplitudes along the waveguide between our method and the analytic Blackstock solution	35
2.4	Pressure scan at 1 times the shock formation distance of the shock produced by a planar wave at 84° . Compare with figure 3 from Fernando et al. (2011).	36
2.5	Plots of the pressure distributions inside the exponential horn. Plots are normalised to the source amplitude.	39
2.6	Normalised RMS of the pressure along the centreline of the duct. The horn exit is at $s = 4.5$	40
2.7	Plots of a uniform curved duct for various Mach numbers. Plots are normalised to the source amplitude. Source at bottom left.	41
2.8	Plots of the elephant's trunk for various Mach numbers. Plots are normalised to the source amplitude. Source at bottom left.	43
2.9	Comparing the modal amplitudes throughout the curved uniform duct along different paths to the straight uniform duct. $M = 2/(L\beta k)$.	45
2.10	Comparing the modal amplitudes of the straight horn and straight uniform duct. $M = 2/(L\beta k)$.	46
2.11	Comparing the modal amplitudes throughout the curved uniform duct to the curved horn along different paths. $M = 2/(L\beta k)$.	47
2.12	Comparing the power outputs of the different ducts.	48

2.13 Modulus of the reflection coefficient at various amplitudes for the uniform curved duct described in section 2.6.4. The ‘o’ are the experimental results of Cabelli (1980)	50
2.14 Modulus of the reflection coefficient at various amplitudes for the elephant’s trunk described in section 2.6.5	50
2.15 Modulus of the reflection coefficient at various amplitudes for the horn described in section 2.6.3	51
3.1 Geometry of the 3D duct	54
3.2 Spectrum of L for an infinite helical duct with $\kappa = 2/3$, $h = 1$ and $k = 0.95k_c$ as the torsion τ is varied	69
3.3 Spectrum of L for an infinite helical duct with $\kappa = 2/3$, $h = 1$ and $k = 2 \times 0.95k_c$ as the torsion τ is varied	70
3.4 Spectrum of L for an infinite helical duct with $\kappa = 2/3$, $h = 1$ and $k = 3 \times 0.95k_c$ as the torsion τ is varied	70
3.5 Spectrum of L for an infinite toroidal duct with $h = 1$ and $k = 0.95k_c$ as the curvature κ is varied	71
3.6 Spectrum of L for an infinite toroidal duct with $h = 1$ and $k = 2 \times 0.95k_c$ as the curvature κ is varied	71
3.7 Spectrum of L for an infinite toroidal duct with $h = 1$ and $k = 3 \times 0.95k_c$ as the curvature κ is varied	72
3.8 Plots of the pressure in a 90° bend with $h\kappa = 2/5$ and wavenumber $kh = 2.4$ at various Mach numbers. Plots are normalized to the source amplitude. Source at top left.	76
3.9 Plots of the same duct as figure 3.8 at various Mach numbers. Plots are radial cross sections taken through the points of maximal and minimal amplitude either side of the shock	77
3.10 Plots of the pressure cross section through the 3D exponential horn at various Mach numbers. Plots normalized to Mach number.	79
3.11 Plots of normalized RMS along the horn centreline. Duct exit is at $s = 4.5$	80
3.12 Plots of the pressure distributions on the surface of the infinite helical duct. Linear acoustics. The source is at the bottom of the plots. Pressure normalized to source amplitude.	81
3.13 $\tau h = 0.14$. Plots of the pressure distributions on the surface of a helical duct terminated by an infinite torsionless duct. The source is at the bottom of the plots. Pressure normalized to source Mach number.	83

3.14	$\tau h = 0.20$. Plots of the pressure distributions on the surface of a helical duct terminated by an infinite torsionless duct. The source is at the bottom of the plots. Pressure normalized to source Mach number.	84
3.15	$\tau h = 1.00$. Plots of the pressure distributions on the surface of a helical duct terminated by an infinite torsionless duct. The source is at the bottom of the plots. Pressure normalized to source Mach number.	85
4.1	Geometry of the baffled duct	88
4.2	Geometry of the dipole source	91
4.4	Geometry of the open duct	94
4.5	Branch cuts of γ	101
4.6	Comparison of the reflection coefficient produced by our numerical method to the analytic solution of Levine and Schwinger (1948)	103
4.7	Comparison of the end reflection produced by our numerical method to the analytic solution of Levine and Schwinger (1948)	104
4.8	Comparison of the pressure distributions by our numerical method to the analytic solution of Levine and Schwinger (1948)	105
4.9	Impedance plots for a cylindrical duct at different aspect ratios	109
4.10	Pitches produced by an open duct $L = 8h$	110
4.11	The harmonic series	110
4.12	Pressure profiles of the open duct $L = 8h$ at various resonant frequencies.	111
4.13	Pitches produced by a closed duct $L = 8h$	113
4.14	Pressure profiles of the closed duct $L = 8h$ at various resonant frequencies.	114
4.15	Pitches produced by a closed duct $L = 16h$	116
4.16	Pressure profiles of the open duct $L = 16h$ at various resonant frequencies.	117
4.17	Pressure profiles of the closed duct $L = 16h$ at various resonant frequencies.	118
4.18	Comparing impedance in the linear and nonlinear regime for a cylindrical duct with $L = 8h$	121
4.19	Normalized harmonic amplitudes through the duct along the centreline at the 5th resonance for the open duct	122
4.20	Normalized harmonic amplitudes through the duct along the centreline at the 5th resonance for the closed duct	123
4.21	Pressure profiles of the open duct $L = 8h$ at various resonant frequencies in the nonlinear regime $M = 0.1$	124
4.22	Pressure profiles of the closed duct $L = 8h$ at various resonant frequencies in the nonlinear regime $M = 0.1$	125

4.23 Impedance plots for the horn compared to the equivalent length straight walled duct	128
4.24 Pitches produced by the horn closed at one end	129
4.25 Pitches produced by the horn open at both ends	129
4.26 Pressure profiles of the closed horn at various resonant frequencies.	131
4.27 Detail of radiation in region 2 from figure 4.26.	132
4.28 Comparing impedance in the linear and nonlinear regime for the horn .	133
4.29 Pressure profiles of the horn at various resonant frequencies in the nonlinear regime $M = 0.05$	134
4.30 Detail of the exit pressure in region 2 for the horn in the nonlinear regime $M = 0.05$	135
4.31 Impedance of the horn given by (4.65)	137
4.32 Pressure profiles of the horn given by (4.65).	138
4.33 Impedance plots for the conical duct compared to the equivalent length straight walled duct	139
4.34 Pitches produced by the conical duct closed at one end	139
4.35 Pitches produced by the conical duct open at both ends	141
4.36 Pressure profiles of the closed conical duct at various resonant frequencies.	142
4.37 Detail of radiation in region 2 from figure 4.36.	143
4.38 Pressure profiles of the open conical duct at various resonant frequencies.	144
4.39 Detail of radiation in region 2 from figure 4.38.	145
4.40 Comparing impedance in the linear and nonlinear regime for the conical duct	146
4.41 Pressure profiles of the closed conical duct at various resonant frequencies in the nonlinear regime $M = 0.10$	148
4.42 Detail of the exit pressure in region 2 for the closed conical duct in the nonlinear regime $M = 0.10$	149
4.43 Impedance plots for the curved duct compared to the equivalent length straight duct	150
4.44 Pressure profiles of the closed curved duct at various resonant frequencies. Source at bottom.	153
4.45 12th resonance of the closed curved duct, illustrating the change in direction of radiation caused by curvature in the duct	154
4.46 The resonance 5' of the closed curved duct, illustrating higher modal resonances induced	154

4.47 Comparing impedance in the linear and nonlinear regime for the curved duct	155
4.48 Pressure profiles of the closed curved duct at various resonant frequencies in the nonlinear regime $M = 0.10$	156
4.49 Impedance plots for the helical duct compared to the equivalent length, equivalent curvature torsion free curved duct	158
4.50 Plot of the duct at resonance with the path $\mathbf{x}(s) = \mathbf{q}(s) - h\hat{\mathbf{n}}(s)$ highlighted	160
4.51 Pressure profiles of the closed helical duct at various resonant frequencies. Source to the left.	161
4.52 13th resonance from different perspectives showing angled radiation	162
4.53 Comparing impedance in the linear and nonlinear regime for the helical duct	163
4.54 5th resonance at $M = 0.1$	164
4.55 Impedance plots for the trombone	166
4.56 Comparing the impedance for two identical length trombones—with and without a mouthpiece	167
4.57 Pressure profiles of the trombone.	168
4.58 Detail of exit pressure from the trombone. Distance in metres. Bell radius $\approx 0.11\text{m}$. Radiation from the left.	169
4.59 Comparing the impedance for the trombone model at various Mach numbers	170
4.60 Pressure at different locations through the instrument	173
4.61 Pressure distributions for the trombone model in the nonlinear regime $M = 0.1$ at the 8th resonance. Normalized to Mach number.	174
E.1 Modal amplitudes of nonlinear propagation down a 1D duct to achieve a sinusoidal wave	202
E.2 Modal amplitudes through the duct from an initial condition calculated by the inverse method	204
E.3 Pressure profile of the curved duct from chapter 3 with initial condition calculated by the inverse method	205

List of tables

3.1	Ordering of the modes	73
4.1	Resonant frequencies of a cylindrical open duct $L = 8h$ and the corresponding musical intervals	110
4.2	The harmonic series and the corresponding musical intervals	110
4.3	Resonant frequencies of a cylindrical closed duct $L = 8h$ and the corresponding musical intervals	113
4.4	Resonant frequencies of a cylindrical open duct $L = 16h$ and the corresponding musical intervals	115
4.5	Resonant frequencies of a cylindrical closed duct $L = 16h$ and the corresponding musical intervals	115
4.6	Resonant frequencies of the open cylindrical duct $L = 8h$ when $M = 0.20$ and the corresponding change in pitch compared with the linear regime	121
4.7	Resonant frequencies of the closed cylindrical duct $L = 8h$ when $M = 0.20$ and the corresponding change in pitch compared with the linear regime	126
4.8	Resonant frequencies of the horn closed at one end	129
4.9	Resonant frequencies of the horn open at both ends	129
4.10	Resonant frequencies of the horn when $M = 0.05$ and the corresponding change in pitch compared with the linear regime	136
4.11	Resonant frequencies of the conical duct closed at one end	140
4.12	Resonant frequencies of the conical duct open at both ends	140
4.13	Resonant frequencies of the closed conical duct when $M = 0.10$ and the corresponding change in pitch compared with the linear regime	141
4.14	Resonant frequencies of the curved duct closed at one end and the comparison to the equivalent length straight duct	151
4.15	Resonant frequencies of the curved duct open at both ends and the comparison to the equivalent length straight duct	151

4.16	Resonant frequencies of the closed curved duct when $M = 0.20$ and the corresponding change in pitch compared with the linear regime	155
4.17	Resonant frequencies of the helical duct closed at one end and the comparison to the equivalent length, equivalent curvature torsion free duct	159
4.18	Resonant frequencies of the helical duct open at both ends and the comparison to the equivalent length, equivalent curvature torsion free duct	159
4.19	Resonant frequencies of the closed helical duct when $M = 0.20$ and the corresponding change in pitch compared with the linear regime	160
4.20	Description of the trombone model	165
4.21	Resonant frequencies of the trombone model, taking $A_4 = 440\text{Hz}$	166
4.22	Resonant frequencies of the trombone model at $M = 0.05$ and the corresponding change in pitch compared with the linear regime	171

Nomenclature

Roman Symbols

A, B	coefficients in expansion of equation of state
$\mathcal{A}, \mathcal{B}, \mathcal{C}, \mathcal{D}, \mathcal{E}$	nonlinear coupling tensors
Br	brassiness parameter
$\hat{\mathbf{b}}$	binormal vector
c_0	ambient speed of sound
C_p	modal normalization factor
$\mathbf{e}_s, \mathbf{e}_r, \mathbf{e}_\theta$	coordinate basis vectors
\mathbf{F}	matrix of integrals over inner/outer duct modes
h_\pm	duct wall distances (2D)
h	duct width (2D), duct radius (3D)
h_1, h_2	inner/outer duct radius (chapter 4)
h_s, h_r, h_θ	Lamé coefficients
i	imaginary unit
I_a	modified Bessel function of the first kind
	identity matrix
J_a	Bessel function of the first kind
j_{pq}	q^{th} zero of the derivative of J_p
k	wavenumber
k_p^a	longitudinal wavenumber for each mode
K_a	modified Bessel function of the second kind
L	linear operator
L	duct length
\mathcal{L}	Lagrangian density

M	Mach number
$\mathbf{M}, \mathbf{N}, \mathbf{G}, \mathbf{H}$	linear coupling matrices
$\hat{\mathbf{n}}$	normal vector
p	pressure
p_0	ambient pressure
P^a	pressure temporal Fourier mode
P_p^a	pressure duct mode (temporal upper, spatial lower)
\mathbf{p}	pressure duct mode (vector representation of above)
\mathbf{p}^\pm	forwards and backwards pressure modes
\mathbf{p}^1	pressure modes in region 1 (chapter 4)
$\mathbf{p}_h^i, \mathbf{p}_d^i, \mathbf{p}^i$	pressure modes in region i ($i = 2, 3$) for baffled, dipole and unbaffled sources respectively (chapter 4)
\mathbf{q}	duct centreline
r	radial distance
R	linear reflectance
\mathcal{R}	nonlinear reflectance
s	longitudinal arc length
S	entropy
S_0	ambient entropy
t	time
$\hat{\mathbf{t}}$	tangent vector
\mathbf{u}	velocity vector
\mathbf{U}^a	velocity temporal Fourier mode vector
U^a	longitudinal velocity Fourier mode
U_p^a	longitudinal velocity duct mode (temporal upper, spatial lower)
\mathbf{u}	longitudinal velocity duct mode (vector representation of above)
\mathbf{u}^\pm	forwards and backwards velocity modes
$\mathbf{u}_h^i, \mathbf{u}_d^i, \mathbf{u}^i$	pressure modes in region i ($i = 1, 2, 3$) for baffled, dipole and unbaffled sources respectively(chapter 4)
V^a	radial velocity Fourier mode

\mathbf{v}_i	eigenvectors of $\mathbf{M}\mathbf{N}$
\mathbf{V}	eigenvector matrix of above (2D). Maps pressure modes to radial velocity modes (3D).
W^a	azimuthal velocity Fourier mode
W	power
\mathbf{W}	maps pressure modes to azimuthal velocity modes (3D)
\mathbf{x}	position vector
\mathbf{Y}	linear admittance
\mathbf{Y}^\pm	characteristic linear admittances
$\mathbf{Y}_h^1, \mathbf{Y}_d^1, \mathbf{Y}^1$	linear admittance in region 1 for baffled, dipole and unbaffled sources respectively (chapter 4)
\mathcal{Y}	nonlinear admittance
\mathcal{Y}^\pm	characteristic nonlinear admittances
$\mathcal{Y}_h^1, \mathcal{Y}_d^1, \mathcal{Y}^1$	nonlinear admittance in region 1 for baffled, dipole and unbaffled sources respectively (chapter 4)
Z	linear impedance
\mathcal{Z}	nonlinear impedance

Greek Symbols

β	coefficient of nonlinearity $\beta = 1 + B/(2A)$
$\chi_{\alpha\beta\gamma}$	integral over radial components of duct modes
γ	ratio of specific heats
κ	curvature
λ	straight duct mode eigenvalue
Λ	diagonal matrix of eigenvalues λ_i
ω	angular frequency
Ω	counting function for the number of radial modes
ψ	duct mode basis function
$\Psi_{\alpha\beta\gamma}$	integrals over the duct modes
ϕ	$\phi = \theta - \theta_0$ (chapter 3). Velocity potential otherwise.
ρ	density
ρ_0	ambient density

σ	distance normalized to shock formation distance
θ	azimuthal angle
θ_0	$\theta'_0 = \tau$
$\Theta_{\alpha\beta\gamma}$	integral over azimuthal components of duct modes
δ_{pq}	Kronecker delta
τ	torsion

Superscripts

a, b, c, \dots	temporal indices
------------------	------------------

Subscripts

p, q, r, \dots	spatial indices (2D)
$\alpha, \beta, \gamma, \dots$	spatial indices (ordered triplet 3D)
p, s, u, \dots	azimuthal spatial indices (3D)
q, t, v, \dots	radial spatial indices (3D)
ξ, η, ζ, \dots	symmetric/antisymmetric ($=0/1$) spatial indices (3D)
$\Psi_{[p]qr}$	integral over duct modes p, q, r . Radial derivative of p^{th} mode
$\Psi_{(p)qr}$	integral over duct modes p, q, r . Azimuthal derivative of p^{th} mode
$\Psi_{\{p\}qr}$	integral over duct modes p, q, r . Longitudinal derivative of p^{th} mode

Other Symbols

∇	gradient operator
$\nabla \cdot$	divergence operator
$\nabla \times$	curl operator
∇^2	Laplacian operator
\mathcal{O}	Big O
$(\mathbf{M}\mathbf{p})_p^a$	$= \sum_{q=0}^{\infty} \mathbf{M}_{pq}^a P_q^a$
$(\mathcal{A}[\mathbf{x}, \mathbf{y}])_p^a$	$= \sum_{b=-\infty}^{\infty} \sum_{q,r=0}^{\infty} \mathcal{A}_{pqr}^{ab} X_q^{a-b} Y_r^b$
$(\mathbf{Z}\mathcal{A}[\mathbf{X}, \mathbf{Y}])_{pqr}^{ab}$	$= \sum_{s,t,u=0}^{\infty} \mathbf{Z}_{pu}^a \mathcal{A}_{ust}^{ab} \mathbf{X}_{sq}^{a-b} \mathbf{Y}_{tr}^b$

Chapter 1

Introduction

Acoustic ducts of different shapes and sizes are ubiquitous in engineering applications as well as everyday life. From the curves and flare in a trombone (Hirschberg et al., 1996; Rendón et al., 2010), the call of an elephant propagating down its trunk (Gilbert et al., 2014) to the curved air intakes on military aircraft (Brambley and Peake, 2008), many of these ducts feature both a complex geometry and sound waves of sufficient amplitude that nonlinearity should not be ignored. Until now, most work has dealt with either the geometrical problem of duct acoustics in a linear regime or nonlinear acoustics in simple geometries. In this thesis we shall address the combination of the two problems.

The study of nonlinear acoustics in waveguides has hitherto largely focussed on the study of straight, uniform ducts or simplified wave approximations (for a detailed overview see Hamilton and Blackstock, 1998, chapter 1). The history of nonlinear acoustics spans the work of many of the greatest minds in applied mathematics—many of whom got it wrong in one way or another. Newton (1687) was the first to calculate the speed of sound as $\sqrt{p_0/\rho_0}$ giving a value 16% lower than experimental values. Euler (1759) was the first, using his celebrated equations of fluid dynamics, to derive a nonlinear wave equation for finite amplitude sound waves. He did not make any progress in solving this equation, but did suggest the nonlinear terms could be responsible for the difference in theoretical and observed sound speed. Lagrange (1760) derived a second order solution to an (incorrect) nonlinear wave equation, observing that such a solution had a speed of propagation dependant on the amplitude of the signal. However, he discarded his solution as “the new formula would destroy the uniformity of the speed of sound and would make it depend in some way on the nature of the original disturbances”, ultimately concluding that the theory of linear acoustics was “the only one acceptable”. Poisson (1808) also found a solution to a (now correct)

nonlinear wave equation, however, by only considering a pulse (whose length ultimately did not change) he concluded that “sound, loud or faint, is transmitted with the same speed”. It was not until 1848 that Eli W. Blake was the first to correctly note that the speed of sound *does* depend on the amplitude of the signal—higher pressure in a signal compresses the particles locally resulting in a higher local density. As the density is increased the sound speed is increased. Challis (1848) (in an argument with Airy) showed using Poisson’s solution that for a plane wave, the wave peak will eventually coincide with the point of zero amplitude, stating “Plane waves are thus shown to be physically impossible”. From this result, Stokes (1848) was the first to give a full description of waveform steepening—the peaks in a wave have a higher local pressure (and hence local density) resulting in a greater local sound speed. As such the peaks of the wave travel faster than the troughs and the waveform begins to steepen (see figure 1.1). This is the fundamental effect of nonlinearity in acoustics—an effect that shall be demonstrated throughout this thesis. Stokes was also the first to point out the consequences of such a solution—eventually a discontinuity will be formed—that is a *shock*. Following this, in response to Challis, Airy (1849) showed that from a sinusoidal source a second harmonic arises, growing as the wave propagates. This, together with further harmonic enrichment, will be referred to many times throughout this work—the effect is able to heuristically explain much of what will be observed. Earnshaw (1860) was the first to provide a complete solution to the problem of a plane piston oscillating in arbitrary motion in a tube. Riemann (1860) generalised this result from simple waves (those propagating in one direction) to compound waves (those travelling in both directions). Rankine (1870) and Hugoniot (1887), elaborated on the theory of shock waves by (independently) forming their famous shock relations, noting that an energy equation including losses is necessary to produce a solution with shocks (for energy is dissipated at the shock). Hugoniot also calculated the distance from a sinusoidal planar pressure source vibrating at angular frequency ω with amplitude u_0 to a shock first being formed as

$$\bar{x} = \frac{c_0^2}{\beta u_0 \omega} \quad (1.1)$$

where $\beta = 1 + B/(2A)$ is the coefficient of nonlinearity defined in detail in the next chapter. In 1910, in the same journal, both Rayleigh and Taylor included viscosity into the problem—something that shall be neglected in this work. In doing so Taylor was able to determine the profile of a shock wave. In the 1930’s, explicit solutions to the plane piston problem were sought (the Earnshaw and Riemann solutions were given implicitly). The Fay (1931) solution gives the explicit Fourier amplitudes for the

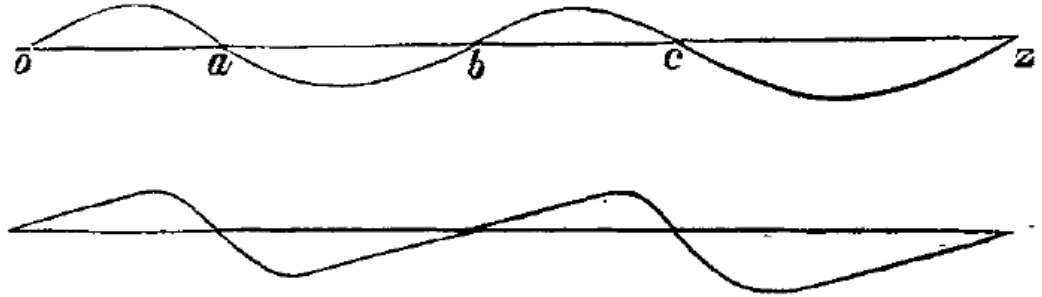


Fig. 1.1 The original illustration from Stokes (1848) showing waveform steepening

most nearly stable viscous solution. For strong waves, in the limit of shock formation distance being much greater than the dissipation lengthscale, the Fay solution tends to a sawtooth shape. This is the general shape obtained by planar waveforms in the inviscid limit and shall be used as a point of reference when numerical viscosity is discussed in the next chapter. The Fubini (1935) solution describes the explicit Fourier amplitudes for waves propagating in a lossless medium. Due to the lack of losses, this solution is only valid up to the point of shock formation. The Fay and the Fubini solution do not agree in the limit of zero viscosity—the Fubini solution being valid before shock formation and the Fay much after. A connection between the two was established by Blackstock (1966). These three solutions will be shown to be solutions of the method presented in this thesis.

Experimentally, shock formation in acoustic ducts can be observed in a wide variety of situations. A noteworthy paper by Hirschberg et al. (1996) was the first to demonstrate the formation of shock waves in the bore of a trombone when played at loud volumes. Subsequently this has also been pictured using Schlieren imaging for a trumpet by Pandya et al. (2003) (see figure 1.2). Theoretical work inspired by these experimental observations have typically used the Burgers equation as the model (see for example Gilbert et al., 2008; Thompson and Strong, 2001). The Burgers (1948) equation is a simple weakly nonlinear model (i.e. retaining only second order nonlinearities) incorporating viscous attenuation. Despite some successes with such models, a fundamental drawback of the Burgers equation is that it only applies to plane progressive waves. Few works have dealt with nonlinear propagation of sound for something other than planar waves—something clearly lacking in a model of a trombone whose duct curves through three dimensional space with variations in duct diameter. A noteworthy exception is the paper by Fernando et al. (2011), who utilise a spatial modal decomposition and a Fourier temporal decomposition. Assuming a slow variation of the modal amplitudes, they are able to describe the nonlinear propagation of progressive

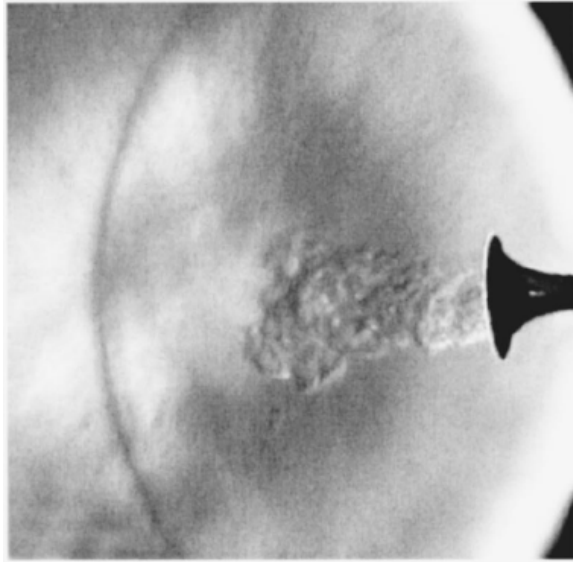


Fig. 1.2 A shock wave radiating from the bell of a trumpet. Taken from Pandya et al. (2003)

waves of various shapes or propagation angles in a rigid walled straight duct. This method provides inspiration for the present thesis. One fundamental drawback of the method, however, is that it cannot be extended to compound waves—something which is necessary once curvature is introduced into a duct (or when the duct is terminated by something other than an anechoic outlet). This brings us to the second branch of topics for this thesis—the geometrical aspects of duct acoustics.

There are a number of works dealing with curved waveguides. One of the first authors to address the problem was Lord Rayleigh in his 1878 work the *Theory of Sound*. In this he demonstrated that long wavelength waves travelling through a curved duct of small cross section behave exactly as those travelling through a straight duct. As a result, the problem received little attention until the 1970's with a resurgence of interest in the topic (see Rostafinski, 1991, for a fairly comprehensive review) . The methods presented generally fall into one of three categories: perturbation methods (e.g. Ting and Miksis, 1983), direct computation (e.g. Cabelli, 1980) and methods based on the separation of variables. Perturbation methods are of limited application, often restricting the problem to, for example, slender ducts or small curvatures. Direct numerical computation, while providing good solutions to a wide range of problems, are often computationally expensive and do not lend themselves to much physical insight into the problem. Methods based on the separation of variables serve as an intermediate between the fully analytic perturbation methods and the fully computational ones. Often a large amount of progress can be made analytically. Rostafinski (1972) used

the technique of separation of variables together with a long wavelength approximation to explicitly calculate the associated eigenvalues in the duct. Most other authors have made analytic progress with separation of variables, completing the solution with computational work to find, for example, the associated eigenvalues of the curved duct modes (for example Ko, 1979). Difficulties arise with such methods, however, when one considers curved duct segments adjoined to straight sections—for this reasons authors have often considered infinitely long bends (for example Krasnushkin, 1945). One such method which overcomes this issue is the multimodal method—first proposed by Pagneux et al. (1996) for the study of ducts of varying cross section and subsequently generalised to 2D curved ducts (Félix and Pagneux, 2001), 3D curved ducts (Félix and Pagneux, 2002) and lined ducts (Bi et al., 2006). This method decomposes the pressure and velocity into a basis of straight duct modes, relates these modes via an impedance matrix, and numerically solves the resulting equations throughout the duct, allowing for greater insight without the cost of restrictive approximations. This method shall form the basis of the present work, where we extend it to a weakly nonlinear regime. We also extend the range of possible duct shapes from rigid circular sections to a duct described by a general centreline using the coordinate system of Germano (1982)—originally used to describe the flow in helical ducts.

Similarly to curved ducts, ducts of varying width also have received much attention (see Campos, 1984, for a review). A noteworthy equation used in the study of such ducts is Webster's horn equation (Webster, 1919)—originally studied by Bernoulli, Lagrange and Euler. The equation assumes planar wave propagation the ducts of varying width. We shall see later that this is in fact a rather poor approximation—particularly for ducts of large flare, where the wave fronts take on a particularly curved profile. Despite this, the equation provides some useful insights into the effect of acoustical horns, for example, the exponential horn acting as a high pass filter. Another noteworthy duct shape is the Bessel horn (with radius inversely proportional to a power of the distance through the duct), originally solved for by Lagrange (1760), which provides a good approximation to the shape of the bells of brass instruments. For a large list of authors who have solved problems using the horn equation see Eisner (1967). Several authors have approached the problem of variable width ducts taking into account higher order modes (allowing for nonplanar propagation) with mixed results—often the resulting equations are numerically unstable (e.g. Stevenson, 1951). The method by Pagneux et al. (1996) overcomes these issues by solving for the duct impedance. This method, being a precursor to the curved duct work of Félix and Pagneux (2001), shares much in common with their method—the decomposition into straight duct modes and the

solving for the variable impedance through the duct. As such, the method of Pagneux et al. shall be another limiting case of our method.

The final topic of interest to us is radiation from open ducts. The landmark paper in this field is by Levine and Schwinger (1948) who used the Wiener-Hopf technique to calculate the radiation from an unflanged cylindrical pipe below the first cut-off frequency. Using this method they were able to analytically calculate the reflection coefficient of the planar modes and also the end correction of the duct. The end correction is the theoretical distance outside of the duct from which the planar wave appears to be reflected from, and depends on the relationship between the frequency of the signal and the width of the duct. Experimental measurements to find the value of the end correction had been performed for over a hundred years before the work of Levine and Schwinger—notably by Rayleigh (again, in his 1878 work *The Theory of Sound*) who obtained a value of $0.6h$ for the duct radius h . This was confirmed by additional experimentalists who noted the frequency dependence of the end correction. The analytical solution of Levine and Schwinger (1948) finally resolved the issue. Further generalizations, such as to higher order modes by Weinstein (1948), or to ducts with mean flow by Rienstra (1984) followed. In his classic text on the Wiener-Hopf technique, Noble (1958) presents several other related solutions including the radiation from a 2D duct. His derivation of the radiation from a cylindrical duct is somewhat simpler than that of Levine and Schwinger. An outline of this solution is presented in chapter 4 and is used as a comparison to our numerical method.

This concludes the brief outline of the relevant background material to this thesis. The thesis itself has a rather simple outline: a chapter relating to 2D ducts, one to 3D ducts and one for open (3D) ducts. Each chapter builds on the previous and so they must be read in that order.

Chapter 2 covers the basic introduction, deriving the fundamental equations from the basic mass and momentum conservations in an isotropic fluid. These equations are then applied to the specific case of a 2D duct. While much of the 2D work is less relevant to physical problems, the simpler algebra makes the steps in the derivation much clearer and allows certain analytic results to be proved (which are more difficult in 3D). The boundary conditions for an infinite duct outlet (both straight and curved) are derived. Following, we shall present the bulk of the analytic results with this method—demonstrating that the method permits solutions such as the Fubini or sawtooth in the relevant regions, and proving that the method reduces to other previously published work (mentioned above) in the linear regime under certain restrictions to the duct geometry. The numerical method is presented followed by a collection of results for

various ducts from the literature to illustrate the effect of nonlinearity on a known solution. We shall also give a brief comparison of various ducts to illustrate the effect of geometry (this will be done in greater detail with open ducts in chapter 4). Finally, we shall introduce the concept of nonlinear reflection—a concept which we shall also come back to in chapter 4.

Chapter 3 serves as a bridge from chapter 2 to chapter 4. We derive the equations in a general 3D coordinate system. Much of the same theory applies as with the 2D duct. We discuss the new boundary condition associated with helical ducts and give some analysis of the interesting new effects produced by torsion. To conclude the chapter we look at some results, again, with ducts from the literature where possible.

Chapter 4 uses the theory built up from the previous two chapters and applies it to open ducts, deriving an approximate solution for nonlinear acoustics in a finite length open duct of arbitrary shape. Numerical issues are discussed, and a comparison with the analytic Levine and Schwinger solution (also derived) is presented. Finally, to conclude the chapter a comparison between many different duct geometries is made, with a strong emphasis on the applications to musical acoustics. Here, we shall use the nonlinear reflectance from chapter 2 to analyse the resonances of various different shaped ducts (loosely related to many members of the wind instrument family) culminating in the study of a scaled model of a trombone.

To conclude the thesis we discuss possible extensions the work and various loose ends not covered here.

Chapter 2

2D Ducts

2.1 Introduction

This chapter introduces the basics of our method and applies it to two dimensional ducts. In section 2.2, we present an exposition of our method and derive its governing equations. This includes the introduction of our novel ‘nonlinear admittance’ term and the associated algebra governing it. In section 2.3 we derive the boundary conditions for an infinite uniform outlet duct, including those which may be curved, and address the stability of such solutions. Analytical work is discussed in section 2.4 looking at special limiting cases. Our numerical method is presented in section 2.5, and in section 2.6 we show our numerical results, again, comparing with those previously published to illustrate the importance of taking nonlinear effects into account. In section 2.7 we compare nonlinear propagation in ducts of identical length but differing geometry to show the effect different geometries have on the acoustic wave. In section 2.8 we introduce a new ‘nonlinear reflectance’ which takes into account the amplitude of the signal and use this to demonstrate how the reflectance of a duct changes with amplitude in previously published work.

2.2 Governing Equations

Following the work of many classic texts (see for example Hamilton and Blackstock, 1998, chapter 3) we begin with the inviscid mass and momentum conservation equations

$$\frac{\partial \rho}{\partial t} + \nabla \cdot (\rho \mathbf{u}) = 0, \quad (2.1a)$$

$$\rho \left(\frac{\partial \mathbf{u}}{\partial t} + \mathbf{u} \cdot \nabla \mathbf{u} \right) = -\nabla p, \quad (2.1b)$$

and introduce non dimensional variables of the form

$$p = \rho_0 c_0^2 \hat{p}, \quad \rho = \rho_0 \hat{\rho}, \quad \mathbf{u} = c_0 \hat{\mathbf{u}} \quad (2.2a, b, c)$$

where ρ_0 and c_0 are the reference density and speed of sound for the stationary fluid respectively. Perturbations about a state of rest are then considered

$$\hat{p} = \hat{p}_0 + \hat{p}', \quad \hat{\rho} = \hat{\rho}_0 + \hat{\rho}', \quad \hat{\mathbf{u}} = \hat{\mathbf{u}}' \quad (2.3a, b, c)$$

with $\hat{p}' \sim \hat{\rho}' \sim \hat{\mathbf{u}}' \sim M$ where $M < 1$ is the perturbation Mach number, which is assumed to be small but finite. This approximation holds true in many situations. The conversion from Mach number to RMS sound pressure level (SPL) in decibels for a sinusoidal pressure source in air at 20°C is approximately

$$\text{SPL} \sim (194 + 20 \log_{10} M) \text{ dB} \quad (2.4)$$

For pressure sources such as that of the mouthpiece of the trombone when played fortissimo, SPLs can typically be around 170 dB corresponding to a Mach number of up to around 0.1. As such, the small but finite Mach number approximation is a very realistic one.

Discarding terms of $\mathcal{O}(M^3)$ and higher in equations (2.1a) and (2.1b) gives

$$\frac{1}{c_0} \frac{\partial \hat{\rho}'}{\partial t} + \nabla \cdot \hat{\mathbf{u}}' = -\hat{\mathbf{u}}' \cdot \nabla \hat{\rho}' - \hat{\rho}' \nabla \cdot \hat{\mathbf{u}}', \quad (2.5a)$$

$$\frac{1}{c_0} \frac{\partial \hat{\mathbf{u}}'}{\partial t} + \nabla \hat{p}' = -\hat{\mathbf{u}}' \cdot \nabla \hat{\mathbf{u}}' + \hat{\rho}' \nabla \hat{p}' \quad (2.5b)$$

where the linear expression for $\frac{\partial \hat{\mathbf{u}}'}{\partial t} = -\nabla \hat{p}'$ has been used in the quadratic term on the RHS of the momentum equation. In much of what will follow we will perform similar manipulations, substituting $\mathcal{O}(M)$ expressions for acoustical quantities into $\mathcal{O}(M^2)$ terms, noting that the error in doing so is $\mathcal{O}(M^3)$ which we are neglecting.

We now consider the entropy equation

$$\frac{DS}{Dt} = 0. \quad (2.6)$$

We shall take our fluid to have initially uniform entropy S_0 . By (2.6) our fluid will retain this value at all times. As a result, we may Taylor expand the equation of state $p = p(S, \rho)$ at fixed entropy

$$\begin{aligned} p' &= A \left(\frac{\rho'}{\rho_0} \right) + \frac{B}{2!} \left(\frac{\rho'}{\rho_0} \right)^2 + \dots \\ &= c_0^2 \rho' + \frac{B}{2A} \frac{c_0^2}{\rho_0} \rho'^2 + \dots \end{aligned} \quad (2.7)$$

where

$$A = \rho_0 \left(\frac{\partial p}{\partial \rho} \right)_{S_0,0} = \rho_0 c_0^2, \quad (2.8a)$$

$$B = \rho_0^2 \left(\frac{\partial^2 p}{\partial \rho^2} \right)_{S_0,0} \quad (2.8b)$$

For a perfect gas $\frac{B}{A} = \gamma - 1$ where γ is the ratio of specific heats. In non-dimensional variables

$$\hat{p}' = \hat{\rho}' + \frac{B}{2A} \hat{\rho}'^2 \quad (2.9)$$

Inverting this equation (correct to second order) gives

$$\hat{\rho}' = \hat{p}' - \frac{B}{2A} \hat{p}'^2 \quad (2.10)$$

which can be used to eliminate density from the mass and momentum equations. This gives

$$\frac{1}{c_0} \frac{\partial \hat{p}'}{\partial t} + \nabla \cdot \hat{\mathbf{u}}' = -\hat{p} \nabla \cdot \hat{\mathbf{u}}' - \hat{\mathbf{u}}' \cdot \nabla \hat{p} + \frac{1}{c_0} \frac{B}{2A} \frac{\partial}{\partial t} (\hat{p}'^2), \quad (2.11a)$$

$$\frac{1}{c_0} \frac{\partial \hat{\mathbf{u}}'}{\partial t} + \nabla \hat{p}' = -\hat{\mathbf{u}}' \cdot \nabla \hat{\mathbf{u}}' + \hat{p}' \nabla \hat{p}'. \quad (2.11b)$$

The pressure and velocity can now be expressed as Fourier series. Upper indices shall be used to denote temporal decompositions

$$\hat{p} = \sum_{a=-\infty}^{\infty} P^a(\mathbf{x}) e^{-ia\omega t}, \quad \hat{\mathbf{u}} = \sum_{a=-\infty}^{\infty} \mathbf{U}^a(\mathbf{x}) e^{-ia\omega t} \quad (2.12a, b)$$

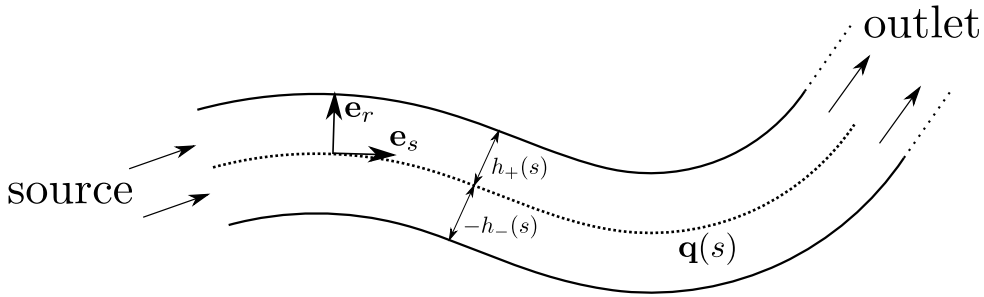


Fig. 2.1 Illustration of the geometry of the duct

where $P^{-a} = P^{a*}$ and $\mathbf{U}^{-a} = \mathbf{U}^{a*}$ (with * denoting the complex conjugate) so that both \hat{p} and $\hat{\mathbf{u}}$ are real and can be substituted into quadratic terms without worry of phase shifts. Both P^0 and U^0 are taken to be identically zero (see appendix A).

Equations (2.11a) and (2.11b) then become

$$\sum_{a=-\infty}^{\infty} \left(-iakP^a + \nabla \cdot \mathbf{U}^a \right) e^{-ia\omega t} = \sum_{b,c=-\infty}^{\infty} \left(-P^b \nabla \cdot \mathbf{U}^c - \mathbf{U}^b \cdot \nabla P^c - \frac{B}{2A} i(b+c)kP^bP^c \right) e^{-i(b+c)\omega t}, \quad (2.13a)$$

$$\sum_{a=-\infty}^{\infty} \left(-iak\mathbf{U}^a + \nabla P^a \right) e^{-ia\omega t} = \sum_{b,c=-\infty}^{\infty} \left(-\mathbf{U}^b \cdot \nabla \mathbf{U}^c + P^b \nabla P^c \right) e^{-i(b+c)\omega t}. \quad (2.13b)$$

where $k = \frac{\omega}{c_0}$ is the wavenumber. Equating terms of the Fourier series yields

$$-iakP^a + \nabla \cdot \mathbf{U}^a = \sum_{b=-\infty}^{\infty} \left(-P^{a-b} \nabla \cdot \mathbf{U}^b - \mathbf{U}^{a-b} \cdot \nabla P^b - \frac{B}{2A} iakP^bP^{a-b} \right), \quad (2.14a)$$

$$-iak\mathbf{U}^a + \nabla P^a = \sum_{b=-\infty}^{\infty} \left(-\mathbf{U}^{a-b} \cdot \nabla \mathbf{U}^b + P^{a-b} \nabla P^b \right). \quad (2.14b)$$

These are the general form of the equations we wish to solve. The ensuing steps depend on the number of dimensions of the problem—the following work is for a 2D duct although the procedure is readily generalizable to three dimensions using the appropriate coordinate system (see chapter 3).

2.2.1 Duct Geometry

Figure 2.1 illustrates the geometry of our duct. We define our duct by its centreline $\mathbf{q}(s)$ in terms of the longitudinal arc length s from the pressure source inlet. The general position vector in the duct is given by

$$\mathbf{x}(s, r) = \mathbf{q}(s) + r\hat{\mathbf{n}} \quad (2.15)$$

where $h_-(s) \leq r \leq h_+(s)$ (with $h_-(s) < 0$) defines the transverse position inside the duct of width $h = (h_+ - h_-)$ and $\hat{\mathbf{n}} = \hat{\mathbf{n}}(s)$ is the normal to the duct defined by the Frenet-Serret formulas:

$$\frac{d\mathbf{q}}{ds} = \hat{\mathbf{t}}, \quad \frac{d\hat{\mathbf{t}}}{ds} = \kappa(s)\hat{\mathbf{n}}, \quad \frac{d\hat{\mathbf{n}}}{ds} = -\kappa(s)\hat{\mathbf{t}}. \quad (2.16a, b, c)$$

with $\kappa(s)$ being the local curvature of the centreline and $\hat{\mathbf{t}} = \hat{\mathbf{t}}(s)$ the tangent vector to the centreline. The basis vectors and their corresponding Lamé coefficients are

$$\mathbf{e}_s = \hat{\mathbf{t}}, \quad h_s = 1 - \kappa r, \quad (2.17a)$$

$$\mathbf{e}_r = \hat{\mathbf{n}}, \quad h_r = 1. \quad (2.17b)$$

Using these, equations (2.14a) and (2.14b) can now be expanded in their coordinate specific forms resulting in three coupled equations for the Fourier modes of pressure P^a , longitudinal velocity U^a and transverse velocity V^a

$$-\text{i}akP^a + \frac{1}{1 - \kappa r} \frac{\partial U^a}{\partial s} + \frac{\partial V^a}{\partial r} - \frac{\kappa V^a}{1 - \kappa r} = \sum_{b=-\infty}^{\infty} \left(-\text{i}bkP^{a-b}P^b - \text{i}bkU^{a-b}U^b - \text{i}bkV^{a-b}V^b - \frac{B}{2A}\text{i}akP^bP^{a-b} \right), \quad (2.18a)$$

$$-\text{i}akU^a + \frac{1}{1 - \kappa r} \frac{\partial P^a}{\partial s} = \sum_{b=-\infty}^{\infty} \left(-\frac{U^{a-b}}{1 - \kappa r} \frac{\partial U^b}{\partial s} - V^{a-b} \frac{\partial U^b}{\partial r} + \frac{\kappa}{1 - \kappa r} U^{a-b}V^b + \text{i}bkP^{a-b}U^b \right), \quad (2.18b)$$

$$-\text{i}akV^a + \frac{\partial P^a}{\partial r} = \sum_{b=-\infty}^{\infty} \left(-\frac{U^{a-b}}{1 - \kappa r} \frac{\partial V^b}{\partial s} - V^{a-b} \frac{\partial V^b}{\partial r} - \frac{\kappa}{1 - \kappa r} U^{a-b}U^b + \text{i}bkP^{a-b}V^b \right). \quad (2.18c)$$

From here, the temporal Fourier modes are expanded about a basis of spatial straight duct modes

$$P^a = \sum_{p=0}^{\infty} P_p^a(s) \psi_p(s, r), \quad U^a = \sum_{p=0}^{\infty} U_p^a(s) \psi_p(s, r), \quad V^a = \sum_{p=0}^{\infty} V_p^a(s) \psi_p(s, r) \quad (2.19a, b, c)$$

where the ψ_p satisfy

boundary condition

$$\frac{d^2 \psi_p}{dr^2} + \lambda_p^2 \psi_p = 0, \quad \int_{-h}^h \psi_p \psi_q dr = \delta_{pq}, \quad \left. \frac{\partial \psi_p}{\partial r} \right|_{r=h\pm} = 0 \quad (2.20a, b, c)$$

and are given by

$$\psi_p = C_p \cos \left(p\pi \frac{(r - h_-)}{(h_+ - h_-)} \right), \quad C_p = \sqrt{\frac{2 - \delta_{p0}}{h_+ - h_-}}, \quad \lambda_p = \frac{p\pi}{h_+ - h_-} \quad (2.21a, b, c)$$

Here, we have expanded both the longitudinal *and* the transverse velocity components in terms of the duct basis, contrary to Félix and Pagneux (2001) who eliminated V^a from the analogous linear equations at this point. It turns out that higher radial derivatives that would arise from eliminating V^a from the above equations make it hard to apply the correct boundary conditions for the duct wall in the quadratic terms on the RHS when the resulting equations are projected onto the modal basis¹. Projecting the equations onto the modal basis first, *then* eliminating the modal amplitudes of the transverse velocity V_p^a also requires less algebra than eliminating the V^a from the above equations and then projecting onto the modal basis. The two methods do, however, produce identical results (see section 2.4.4).

As an aside, one may question the validity of expanding the temporal modes as a series of spatial duct modes, each with zero derivative on the boundary (especially if the duct in question has curved walls). This issue is dealt with in more detail in Pagneux et al. (1996), however we will briefly mention that this causes no difficulty, since an infinite series of terms with zero derivative at the boundary may *not* necessarily have a zero derivative. Rather, care must be taken to apply the correct boundary conditions *before* we expand in terms of the ψ_p .

We now wish to project the above equations onto the basis of modes. We first multiply the equations by a factor $(1 - \kappa r)$, then by a general duct mode ψ_p and integrate across the duct width, ensuring to apply the no penetration boundary condition at the

¹The higher derivatives would require us to expand the acoustical quantities into their infinite series *before* the equations are projected. In doing so we lose important terms relating to the derivatives on the boundary which may not necessarily be zero.

duct wall. This is given by

$$\mathbf{U}^a|_{r=h_\pm} \cdot \mathbf{n}^\pm = 0, \quad \mathbf{n}^\pm(s) = h'_\pm \mathbf{e}_s - (1 - \kappa h_\pm) \mathbf{e}_r \quad (2.22a, b)$$

Where \mathbf{n}^\pm are the normals to the duct wall. This corresponds to

$$h'_\pm U^a = (1 - \kappa h_\pm) V^a, \quad \text{at} \quad r = h_\pm \quad (2.23)$$

which can be used to eliminate V^a at the boundaries. For example (summation convention assumed),

$$\int_{h_-}^{h_+} \frac{\partial V^a}{\partial r} \psi_p dr = \left[\frac{h'}{1 - \kappa h} \psi_p \psi_q \right]_{h_-}^{h_+} U_q^a - \int_{h_-}^{h_+} \frac{\partial \psi_p}{\partial r} \psi_q dr V_q^a \quad (2.24)$$

Similarly,

$$\int_{h_-}^{h_+} \frac{\partial U^a}{\partial s} \psi_p dr = \frac{\partial U_p^a}{\partial s} - [h' \psi_p \psi_q]_{h_-}^{h_+} U_q^a - \int_{h_-}^{h_+} \frac{\partial \psi_p}{\partial s} \psi_q dr U_q^a. \quad (2.25)$$

Other terms of note include

$$\begin{aligned} \int_{h_-}^{h_+} U^{a-b} \frac{\partial U^b}{\partial s} \psi_p dr &= \frac{1}{2} \frac{d}{ds} \left(\int_{h_-}^{h_+} \psi_p \psi_q \psi_r dr \right) U_q^{a-b} U_r^b - \frac{1}{2} [h' \psi_p \psi_q \psi_r]_{h_-}^{h_+} U_q^{a-b} U_r^b \\ &+ \frac{1}{2} \int_{h_-}^{h_+} \psi_p \psi_q \psi_r dr \left(U_r^b \frac{d}{ds} U_q^{a-b} + U_q^{a-b} \frac{d}{ds} U_r^b \right) - \frac{1}{2} \int_{h_-}^{h_+} \frac{\partial \psi_p}{\partial s} \psi_q \psi_r dr U_q^{a-b} U_r^b, \end{aligned} \quad (2.26)$$

where the sum over b has been reordered, and

$$\begin{aligned} \int_{h_-}^{h_+} (1 - \kappa r) V^{a-b} \frac{\partial U^b}{\partial r} \psi_p dr &= [h' U^{a-b} U^b \psi_p]_{h_-}^{h_+} - \int_{h_-}^{h_+} (1 - \kappa r) V^{a-b} U^b \frac{\partial \psi_p}{\partial r} dr \\ &+ \kappa \int_{h_-}^{h_+} V^{a-b} U^b \psi_p dr - \int_{h_-}^{h_+} (1 - \kappa r) \frac{\partial V^{a-b}}{\partial r} U^b \psi_p dr \\ &= [h' U^{a-b} U^b \psi_p]_{h_-}^{h_+} - \int_{h_-}^{h_+} (1 - \kappa r) V^{a-b} U^b \frac{\partial \psi_p}{\partial r} dr \\ &- \int_{h_-}^{h_+} i(a - b) k (1 - \kappa r) P^{a-b} U^b \psi_p dr + \int_{h_-}^{h_+} \frac{\partial U^{a-b}}{\partial s} U^b \psi_p dr \end{aligned} \quad (2.27)$$

where the linear part of (2.18b) has been used to substitute for $\partial V^{a-b}/\partial r$. Equations (2.18a) and (2.18b) become

$$\begin{aligned} \frac{d}{ds} U_p^a - iak\Psi_{pq}[1 - \kappa r]P_q^a - \Psi_{\{p\}q}U_q^a - \Psi_{[p]q}[1 - \kappa r]V_q^a \\ = -(ibk + iak\frac{B}{2A})\Psi_{pqr}[1 - \kappa r]P_q^{a-b}P_r^b \\ - ibk\Psi_{pqr}[1 - \kappa r]U_q^{a-b}U_r^b - ibk\Psi_{pqr}[1 - \kappa r]V_q^{a-b}V_r^b, \end{aligned} \quad (2.28a)$$

$$\begin{aligned} \frac{d}{ds} P_p^a - iak\Psi_{pq}[1 - \kappa r]U_q^a - ([h'\psi_p\psi_q]_{h_-}^{h_+} + \Psi_{\{p\}q})P_q^a \\ = \left(\Psi_{\{p\}qr} - \frac{d}{ds}(\Psi_{pqr})\right)U_q^{a-b}U_r^b + iak\Psi_{pqr}[1 - \kappa r]P_q^{a-b}U_r^b \\ + (\kappa\Psi_{pqr} + \Psi_{[p]qr}[1 - \kappa r])U_q^{a-b}V_r^b \\ - \Psi_{pqr}\left(\frac{d}{ds}U_q^{a-b}U_r^b + U_q^{a-b}\frac{d}{ds}U_r^b\right). \end{aligned} \quad (2.28b)$$

Here, we have used Ψ as a shorthand to denote integrals over the modes. Square brackets around the index represent radial derivatives on that mode, curly brackets represent longitudinal derivatives. The square brackets after the Ψ are the integral kernel (assumed to be 1 if no brackets are present). So for example

$$\begin{aligned} \Psi_{[p]q} &= \int_{h_-}^{h_+} \frac{\partial\psi_p}{\partial r}\psi_q dr = (\Psi_{p[q]})^T \\ \Psi_{\{p\}qr}[1 - \kappa r] &= \int_{h_-}^{h_+} \frac{\partial\psi_p}{\partial s}\psi_q\psi_r(1 - \kappa r) dr \end{aligned}$$

We now turn our attention to (2.18c). Using the linear relationship between V and P and the symmetry of mixed partials, we can find the linear expression for $\frac{\partial V}{\partial s}$

$$\frac{\partial V^a}{\partial s} = \frac{1}{iak} \frac{\partial^2 P^a}{\partial s \partial r} = (1 - \kappa r) \frac{\partial U^a}{\partial r} - \kappa U^a. \quad (2.29)$$

We also require the linear expression for V_p^a in terms of P_p^a , also from the left hand side of (2.18c),

$$V_p^a = \frac{1}{iak} [\psi_p\psi_q]_{h_-}^{h_+} P_q^a - \frac{1}{iak} \Psi_{[p]q} P_q^a = \frac{1}{iak} \Psi_{p[q]} P_q^a. \quad (2.30)$$

Using these, we can eliminate V^a from the RHS of the projection of (2.18c).

$$\begin{aligned}
& -\text{i}ak\Psi_{pq}[1-\kappa r]V_q^a + \left([\psi_p\psi_q(1-\kappa r)]_{h_-}^{h_+} - \Psi_{[p]qr}[1-\kappa r] + \kappa\delta_{pq}\right)P_q^a \\
& = \frac{1}{2} \left(-[\psi_p\psi_q\psi_r(1-\kappa r)]_{h_-}^{h_+} + \Psi_{[p]qr}[1-\kappa r] - \kappa\Psi_{pqr} - \left[\frac{h'^2}{1-\kappa h}\psi_p\psi_q\psi_r\right]_{h_-}^{h_+} \right) U_q^{a-b}U_r^b \\
& - \frac{1}{2k^2(a-b)b} \left((\Psi_{[p]qr}[1-\kappa r] - \kappa\Psi_{pqr}) \left([\psi_q\psi_s]_{h_-}^{h_+} - \Psi_{[q]s}\right) \left([\psi_r\psi_t]_{h_-}^{h_+} - \Psi_{[r]t}\right) P_s^{a-b}P_t^b \right. \\
& \left. + \Psi_{pqr}[1-\kappa r] \left([\psi_r\psi_t]_{h_-}^{h_+} - \Psi_{[r]t}\right) P_q^{a-b}P_t^b \right) \quad (2.31)
\end{aligned}$$

Using (2.30) and (2.31) we can eliminate V from (2.28a) and (2.28b) to get

$$\mathbf{u}' + \mathsf{M}\mathbf{p} + \mathsf{G}\mathbf{u} = \mathcal{A}[\mathbf{u}, \mathbf{u}] + \mathcal{B}[\mathbf{p}, \mathbf{p}], \quad (2.32a)$$

$$\mathbf{p}' - \mathsf{N}\mathbf{u} - \mathsf{H}\mathbf{p} = \mathcal{C}[\mathbf{u}, \mathbf{p}] + \mathcal{D}[\mathbf{u}, \mathbf{u}] \quad (2.32b)$$

where we have switched to vector notation for ease of algebraic manipulations. Matrix multiplication is defined over spatial modes in the following manner

$$(\mathsf{M}\mathbf{p})_p^a = \sum_{q=0}^{\infty} \mathsf{M}_{pq}^a P_q^a \quad (2.33)$$

Calligraphic letter shall denote rank 5 tensors, with square brackets denoting the following action

$$(\mathcal{A}[\mathbf{x}, \mathbf{y}])_p^a = \sum_{b=-\infty}^{\infty} \sum_{q,r=0}^{\infty} \mathcal{A}_{pqr}^{ab} X_q^{a-b} Y_r^b \quad (2.34)$$

The matrices and tensors are given by

$$\mathsf{M}_{pq}^a = -\text{i}ak\Psi_{pq}[1-\kappa r] - \frac{1}{\text{i}ak}\Psi_{[p]s}[1-\kappa r]\Psi_{s[q]}, \quad (2.35a)$$

$$\mathsf{N}_{pq}^a = \text{i}ak\Psi_{pq}[1-\kappa r], \quad (2.35b)$$

$$\mathsf{G}_{pq}^a = -\Psi_{\{p\}q}, \quad (2.35c)$$

$$\mathsf{H}_{pq}^a = -\Psi_{p\{q\}}, \quad (2.35d)$$

$$\mathcal{A}_{pqr}^{ab} = -i b k \Psi_{pqr} [1 - \kappa r] \quad (2.35e)$$

$$\begin{aligned} & -\frac{1}{2} \Psi_{[p]s} [1 - \kappa r] (\mathbf{N}^{-1})_{st}^a \left(-[\psi_t \psi_q \psi_r (1 - \kappa r)]_{h_-}^{h_+} + \Psi_{[t]qr} [1 - \kappa r] \right. \\ & \left. - \kappa \Psi_{tqr} - \left[\frac{h'^2}{1 - \kappa h} \psi_t \psi_q \psi_r \right]_{h_-}^{h_+} \right), \end{aligned}$$

$$\begin{aligned} \mathcal{B}_{pqr}^{ab} = & -(ibk + iak \frac{B}{2A}) \Psi_{pqr} [1 - \kappa r] - \frac{1}{i(a-b)k} \Psi_{pst} [1 - \kappa r] \Psi_{s[q]} \Psi_{t[r]} \quad (2.35f) \\ & - \Psi_{[p]s} [1 - \kappa r] (\mathbf{N}^{-1})_{st}^a \left(\frac{-1}{2k^2(a-b)b} \left(\Psi_{[t]uv} [1 - \kappa r] - \kappa \Psi_{tuv} \right) \Psi_{u[q]} \Psi_{v[r]} \right. \\ & \left. + \Psi_{tqu} [1 - \kappa r] \Psi_{u[r]} \right), \end{aligned}$$

$$\mathcal{C}_{pqr}^{ab} = iak \Psi_{pqr} [1 - \kappa r] + \frac{1}{ibk} \left(\kappa \Psi_{pqs} + \Psi_{[p]qs} [1 - \kappa r] \right) \Psi_{s[r]} + 2 \Psi_{pqs} \mathbf{M}_{sr}^b, \quad (2.35g)$$

$$\mathcal{D}_{pqr}^{ab} = \Psi_{\{p\}qr} - \frac{d}{ds}(\Psi_{pqr}) + 2 \Psi_{pqs} \mathbf{G}_{sr}^b. \quad (2.35h)$$

The Ψ can also be calculated analytically (see appendix B). Here, $\mathbf{M}, \mathbf{N}, \mathcal{A}, \mathcal{B}$ and \mathcal{C} encode the curvature of the duct, while \mathbf{G}, \mathbf{H} and \mathcal{D} arise from variation in the duct width, vanishing when it is uniform.

Due to the presence of evanescent modes these equations are numerically unstable and cannot be integrated directly (Pagneux et al., 1996). Following the work of Félix and Pagneux (2001), we define a relation between the pressure and velocity in terms of the admittance. When solving for pressure it is easier to work with the admittance rather than the impedance to avoid inverting large matrices in the work that will follow. The following relationship is defined

$$\mathbf{u} = \mathbf{Y}\mathbf{p} + \mathcal{Y}[\mathbf{p}, \mathbf{p}] \quad (2.36)$$

where $\mathbf{Y} = \mathbf{Y}(s)$ is the linear part of the admittance ($\mathbf{Y} = \mathbf{Z}^{-1}$ where \mathbf{Z} is the impedance matrix of Félix and Pagneux, 2001) and $\mathcal{Y} = \mathcal{Y}(s)$ is the second order nonlinear correction to the admittance, henceforth referred to as the ‘nonlinear admittance’ term. We differentiate (2.36)

$$\mathbf{u}' = \mathbf{Y}'\mathbf{p} + \mathbf{Y}\mathbf{p}' + \mathcal{Y}'[\mathbf{p}, \mathbf{p}] + \mathcal{Y}[\mathbf{p}', \mathbf{p}] + \mathcal{Y}[\mathbf{p}, \mathbf{p}'], \quad (2.37)$$

substitute in (2.32a) and (2.32b),

$$\begin{aligned} -\mathbf{M}\mathbf{p} - \mathbf{G}\mathbf{u} + \mathcal{A}[\mathbf{u}, \mathbf{u}] + \mathcal{B}[\mathbf{p}, \mathbf{p}] &= \mathbf{Y}'\mathbf{p} + \mathbf{Y} \left(\mathbf{N}\mathbf{u} + \mathbf{H}\mathbf{p} + \mathcal{C}[\mathbf{u}, \mathbf{p}] + \mathcal{D}[\mathbf{u}, \mathbf{u}] \right) \\ &\quad + \mathcal{Y}'[\mathbf{p}, \mathbf{p}] + \mathcal{Y}[\mathbf{N}\mathbf{u} + \mathbf{H}\mathbf{p}, \mathbf{p}] \\ &\quad + \mathcal{Y}[\mathbf{p}, \mathbf{N}\mathbf{u} + \mathbf{H}\mathbf{p}] \end{aligned} \quad (2.38)$$

and use (2.36) to express \mathbf{u} in terms of \mathbf{p}

$$\begin{aligned} -\mathbf{M}\mathbf{p} - \mathbf{G}\mathbf{Y}\mathbf{p} - \mathbf{G}\mathcal{Y}[\mathbf{p}, \mathbf{p}] + \mathcal{A}[\mathbf{Y}\mathbf{p}, \mathbf{Y}\mathbf{p}] + \mathcal{B}[\mathbf{p}, \mathbf{p}] &= \mathbf{Y}'\mathbf{p} + \mathbf{Y} \left(\mathbf{N}\mathbf{Y}\mathbf{p} + \mathbf{N}\mathcal{Y}[\mathbf{p}, \mathbf{p}] \right. \\ &\quad \left. + \mathbf{H}\mathbf{p} + \mathcal{C}[\mathbf{Y}\mathbf{p}, \mathbf{p}] + \mathcal{D}[\mathbf{Y}\mathbf{p}, \mathbf{Y}\mathbf{p}] \right) \\ &\quad + \mathcal{Y}'[\mathbf{p}, \mathbf{p}] + \mathcal{Y}[\mathbf{N}\mathbf{Y}\mathbf{p} + \mathbf{H}\mathbf{p}, \mathbf{p}] \\ &\quad + \mathcal{Y}[\mathbf{p}, \mathbf{N}\mathbf{Y}\mathbf{p} + \mathbf{H}\mathbf{p}] \end{aligned} \quad (2.39)$$

This equation has two distinct orders of magnitude: terms linear in \mathbf{p} , and terms quadratic in \mathbf{p} . We can equate linear terms and the quadratic terms separately to get two distinct equations

$$\mathbf{Y}'\mathbf{p} + \mathbf{Y}\mathbf{N}\mathbf{Y}\mathbf{p} + \mathbf{M}\mathbf{p} + \mathbf{Y}\mathbf{H}\mathbf{p} + \mathbf{G}\mathbf{Y}\mathbf{p} = 0, \quad (2.40a)$$

$$\begin{aligned} \mathcal{Y}'[\mathbf{p}, \mathbf{p}] + \mathcal{Y}[\mathbf{N}\mathbf{Y}\mathbf{p}, \mathbf{p}] + \mathcal{Y}[\mathbf{p}, \mathbf{N}\mathbf{Y}\mathbf{p}] + \mathbf{Y}\mathbf{N}\mathcal{Y}[\mathbf{p}, \mathbf{p}] \\ + \mathbf{Y}\mathcal{C}[\mathbf{Y}\mathbf{p}, \mathbf{p}] - \mathcal{A}[\mathbf{Y}\mathbf{p}, \mathbf{Y}\mathbf{p}] - \mathcal{B}[\mathbf{p}, \mathbf{p}] \\ + \mathcal{Y}[\mathbf{H}\mathbf{p}, \mathbf{p}] + \mathcal{Y}[\mathbf{p}, \mathbf{H}\mathbf{p}] + \mathbf{G}\mathcal{Y}[\mathbf{p}, \mathbf{p}] + \mathbf{Y}\mathcal{D}[\mathbf{Y}\mathbf{p}, \mathbf{Y}\mathbf{p}] = 0 \end{aligned} \quad (2.40b)$$

As both of these equations hold true for a general \mathbf{p} we can eliminate it to obtain an equation for the linear part of the admittance and an equation for the nonlinear part of the admittance

$$\mathbf{Y}' + \mathbf{Y}\mathbf{N}\mathbf{Y} + \mathbf{M} + \mathbf{Y}\mathbf{H} + \mathbf{G}\mathbf{Y} = 0 \quad (2.41)$$

$$\begin{aligned} \mathcal{Y}'[\mathbf{I}, \mathbf{I}] + \mathcal{Y}[\mathbf{N}\mathbf{Y}, \mathbf{I}] + \mathcal{Y}[\mathbf{I}, \mathbf{N}\mathbf{Y}] + \mathbf{Y}\mathbf{N}\mathcal{Y}[\mathbf{I}, \mathbf{I}] + \mathbf{Y}\mathcal{C}[\mathbf{Y}, \mathbf{I}] - \mathcal{A}[\mathbf{Y}, \mathbf{Y}] - \mathcal{B}[\mathbf{I}, \mathbf{I}] \\ + \mathcal{Y}[\mathbf{H}, \mathbf{I}] + \mathcal{Y}[\mathbf{I}, \mathbf{H}] + \mathbf{G}\mathcal{Y}[\mathbf{I}, \mathbf{I}] + \mathbf{Y}\mathcal{D}[\mathbf{Y}, \mathbf{Y}] = 0 \end{aligned} \quad (2.42)$$

where $\mathbf{I}_{pq}^a = \delta_{pq} \forall a$ is the identity tensor. Here, the square bracket notation acting on matrices denotes

$$(\mathbf{Z}\mathcal{A}[\mathbf{X}, \mathbf{Y}])_{pqr}^{ab} = \sum_{s,t,u=0}^{\infty} \mathbf{Z}_{pu}^a \mathcal{A}_{ust}^{ab} \mathbf{X}_{sq}^{a-b} \mathbf{Y}_{tr}^b \quad (2.43)$$

These equations are solved from the outlet of the duct—where an appropriate radiation condition boundary condition is imposed²—to the inlet. Once both parts of the admittance are found throughout the duct, they can be used to express the velocity modes in terms of pressure modes in (2.32b). The result is a numerically stable³ first order equation for the pressure which can be solved from the inlet to the outlet using suitable initial conditions at the inlet to describe the waveform (both temporally and spatially) there,

$$\mathbf{p}' = \mathbf{N}\mathbf{Y}\mathbf{p} + \mathbf{N}\mathcal{Y}[\mathbf{p}, \mathbf{p}] + \mathcal{C}[\mathbf{Y}\mathbf{p}, \mathbf{p}] + \mathbf{H}\mathbf{p} + \mathcal{D}[\mathbf{Y}\mathbf{p}, \mathbf{Y}\mathbf{p}] \quad (2.44)$$

Due to the varying admittance this equation takes into account a superposition of forwards and backwards travelling modes as determined by the radiation condition at the outlet, as well as their nonlinear interaction. As such, this method is suitable for ducts where reflected waves are important, such as those that are curved or have an open/closed exit. For details of how to decompose this wave into its forward and backward propagating modes see section 2.8.

2.3 Boundary Conditions for an Infinite Uniform Duct Outlet

The simplest boundary condition to consider for the admittance is that of an outlet consisting of an infinitely long uniform duct of constant curvature for which we have only outgoing propagating waves and decaying evanescent waves. In such a duct no point can be distinguished from another longitudinally, therefore we must have the admittance being a fixed point of the admittance equations. To find the fixed points, we begin by combining (2.32a) and (2.32b) (ignoring the quadratic terms for the moment), to form a second order ODE for the pressure modes

$$\mathbf{p}'' + \mathbf{N}\mathbf{M}\mathbf{p} = 0 \quad (2.45)$$

Here we are considering a uniform duct of constant curvature, so \mathbf{G} , \mathbf{H} and the derivatives of \mathbf{M} and \mathbf{N} vanish. As previously noted, this equation is numerically unstable. We can however make progress analytically. The solution in terms of forward and backwards

²For example the radiation condition corresponding to the infinite uniform outlet covered in this chapter or the open duct outlet covered in chapter 4.

³As we have suppressed the exponentially growing evanescent solutions.

modes is given by

$$\mathbf{p} = \mathbf{p}^+ + \mathbf{p}^- = \sum_{i=1}^{\infty} \left(c_i^+ \mathbf{v}_i e^{i\lambda_i s} + c_i^- \mathbf{v}_i e^{-i\lambda_i s} \right) \quad (2.46)$$

where the \mathbf{v}_i are the eigenvectors of \mathbf{NM} with eigenvalues λ_i^2 , with arbitrary c_i^+ and c_i^- . Here, we have split the solution into forward and backward waves. The roots of the λ_i are chosen as follows

$$\lambda_i = \begin{cases} (\lambda_i^2)^{1/2} & \lambda_i^2 > 0 \\ i(-\lambda_i^2)^{1/2} & \lambda_i^2 < 0. \end{cases} \quad (2.47)$$

to ensure either propagating or decaying evanescent modes in the positive direction. Based on extensive numerical evaluations, we observe that all of the eigenvectors of \mathbf{NM} are real (even though \mathbf{NM} is not necessarily symmetric for $\kappa \neq 0$). We now introduce the characteristic forward and backwards admittance, linearly relating the forwards and backwards modes

$$\mathbf{u}^\pm = \mathbf{Y}^\pm \mathbf{p}^\pm \quad (2.48)$$

Using this, together with the linear equation relating pressure and velocity $(\mathbf{p}^\pm)' = \mathbf{N}\mathbf{u}^\pm$, we obtain an expression for \mathbf{Y}^\pm

$$\mathbf{Y}^\pm = \pm \mathbf{N}^{-1} \mathbf{V} \Lambda \mathbf{V}^{-1} = \pm i \mathbf{N}^{-1} \sqrt{\mathbf{NM}} \quad (2.49)$$

where $\mathbf{V} = (\mathbf{v}_1, \mathbf{v}_2, \mathbf{v}_3, \dots)$ and $\Lambda = \begin{pmatrix} i\lambda_1 & 0 & \dots \\ 0 & i\lambda_2 & \dots \\ \vdots & \vdots & \ddots \end{pmatrix}$. These can be shown to be

fixed points of the linear admittance equation by direct substitution into (2.41) (again, ignoring \mathbf{G} and \mathbf{H} as the duct is assumed uniform)

$$\mathbf{Y}^{\pm'} = \mathbf{N}^{-1} \sqrt{\mathbf{NM}} \mathbf{N} \mathbf{N}^{-1} \sqrt{\mathbf{NM}} - \mathbf{M} = 0 \quad (2.50)$$

Therefore, $\mathbf{Y} = \mathbf{Y}^+$ is the boundary condition to (2.41), applied at the exit, implying only outgoing propagating waves and decaying evanescent waves in the outlet.

Using these characteristic linear admittances, we now wish to find the fixed points of the nonlinear admittance in equation (2.42). In order to do so we first introduce a matrix \mathbf{W} with columns given by the eigenvectors of $\mathbf{Y}^\pm \mathbf{N}$ with corresponding eigenvalue matrix $\pm \Lambda$. Fixed points of the nonlinear admittance equation satisfy

$$\mathcal{Y}^\pm[\mathbf{NY}^\pm, \mathbf{I}] + \mathcal{Y}^\pm[\mathbf{I}, \mathbf{NY}^\pm] + \mathbf{Y}^\pm \mathbf{N} \mathcal{Y}^\pm[\mathbf{I}, \mathbf{I}] + \mathbf{Y}^\pm \mathcal{C}[\mathbf{Y}^\pm, \mathbf{I}] - \mathcal{A}[\mathbf{Y}^\pm, \mathbf{Y}^\pm] - \mathcal{B}[\mathbf{I}, \mathbf{I}] = 0 \quad (2.51)$$

We apply W^{-1} on the left of this equation and V to the right on both terms in the square brackets

$$\begin{aligned} W^{-1}\mathcal{Y}^\pm[\pm V\Lambda, V] + W^{-1}\mathcal{Y}^\pm[V, \pm V\Lambda] + W^{-1}Y^\pm N\mathcal{Y}^\pm[V, V] + \\ W^{-1}Y^\pm C[Y^\pm V, V] - W^{-1}A[Y^\pm V, Y^\pm V] - W^{-1}B[V, V] = 0 \end{aligned} \quad (2.52)$$

where we recall that V , W and Λ each have an upper index and the matrix square bracket algebra is defined by (2.43). Next, we transform \mathcal{Y}^\pm in the following manner

$$\mathcal{Y}^\pm[\mathbf{x}, \mathbf{y}] = W\tilde{\mathcal{Y}}^\pm[V^{-1}\mathbf{x}, V^{-1}\mathbf{y}] \quad (2.53)$$

to obtain

$$\begin{aligned} \tilde{\mathcal{Y}}^\pm[\pm \Lambda, I] + \tilde{\mathcal{Y}}^\pm[I, \pm \Lambda] \pm \Lambda\tilde{\mathcal{Y}}^\pm[I, I] \\ + W^{-1}Y^\pm C[Y^\pm V, V] - W^{-1}A[Y^\pm V, Y^\pm V] - W^{-1}B[V, V] = 0 \end{aligned} \quad (2.54)$$

As we are acting $\tilde{\mathcal{Y}}$ on purely diagonal matrices, its components can easily be read off

$$(\tilde{\mathcal{Y}}^\pm)_{pqr}^{ab} = \frac{(W^{-1}A[Y^\pm V, Y^\pm V] + W^{-1}B[V, V] - W^{-1}Y^\pm C[Y^\pm V, V])_{pqr}^{ab}}{\pm i\lambda_p^a \pm i\lambda_q^{a-b} \pm i\lambda_r^b} \quad (2.55)$$

The reverse transformation is then applied to obtain the characteristic nonlinear part of the admittance. It can easily be seen that $\mathcal{Y}^+ = -\mathcal{Y}^-$.

Similarly, $\mathcal{Y} = \mathcal{Y}^+$ can be used as a boundary condition to (2.42), again applied at the duct exit. The solutions $Y = Y^+$ and $\mathcal{Y} = \mathcal{Y}^+$ correspond to the radiation condition

$$\mathbf{u} = Y^+ \mathbf{p} + \mathcal{Y}^+[\mathbf{p}, \mathbf{p}] \quad (2.56)$$

relating pressure and velocity modes at the exit, implying only outgoing waves and decaying evanescent waves in the uniform duct outlet of constant curvature. As the equation governing \mathcal{Y} is linear, the \mathcal{Y}^+ is unique (up to the equivalence class under summation—see section 2.4.2) for a given choice of Y^+ .

2.3.1 Stability of fixed points of the admittance

One may question the stability of these fixed points by considering a small perturbation. For the linear part of the admittance take a small matrix perturbation ε

$$Y^\pm = \pm N^{-1}V\Lambda V^{-1} + N^{-1}V\varepsilon V^{-1} \quad (2.57)$$

In equation (2.41) this becomes

$$\varepsilon' = \mp \varepsilon \Lambda \mp \Lambda \varepsilon + \mathcal{O}(\varepsilon^2) \quad (2.58)$$

Hence, \mathbf{Y}^+ is (at least Lyapunov) stable to small perturbations provided all the components of Λ have $\text{Re } \Lambda \leq 0$ (remembering that we are solving in the negative s direction, so a positive exponential solution corresponds to a decaying perturbation) which is the case given our choice of decaying evanescent solutions. In a physical situation, we would in fact expect all of the components of Λ to have at least a small negative real part (due to losses in the system), in which case this would be an asymptotically stable fixed point. On the other hand, due to the opposite signs our \mathbf{Y}^- can be seen to be unstable⁴. This justifies the use of \mathbf{Y}^+ as a boundary condition for our linear admittance.

Similarly for the nonlinear part of the admittance consider a corresponding tensor perturbation ε

$$\mathcal{Y} = \mathcal{Y}^+ + W\varepsilon[V^{-1}, V^{-1}] \quad (2.59)$$

In equation (2.42), we get

$$\varepsilon'[I, I] = -\varepsilon[\Lambda, I] - \varepsilon[I, \Lambda] - \Lambda\varepsilon[I, I] \quad (2.60)$$

So similarly, we have (at least Lyapunov) stability provided all the components of Λ have $\text{Re } \Lambda \leq 0$, again justifying the use of \mathcal{Y}^+ as a boundary condition for the nonlinear admittance.

2.4 Special Cases

2.4.1 1D Duct and the Equivalence to the Fubini and Sawtooth Solutions

The case of nonlinear sound propagation in 1D has been much studied. The Fubini solution (Fubini, 1935), which is valid up to the point of shock formation, gives the harmonic amplitudes of pressure for a sinusoidal pressure source propagating in 1D.

⁴it is possible to form a stable \mathbf{Y}^- corresponding to backwards propagating waves with forward decaying evanescent modes, however these would be unphysical. Such a solution can, however, be used to find inverses (see appendix E)

The modal amplitudes, B_a are given by

$$B_a = \frac{2}{a\sigma} J_a(a\sigma) \quad (2.61)$$

where

$$\sigma = \frac{s}{\beta M k} \quad (2.62)$$

is the distance normalized to the shock formation distance ($\beta = 1 + \frac{B}{2A}$) and the J_a are the (ordinary) Bessel functions of the first kind. In our duct modes, this corresponds to a solution

$$P_0^a = iM\sqrt{h_+ - h_-} \frac{1}{a\sigma} J_a(a\sigma) e^{iaks} \quad (2.63)$$

例1

Where the factor of i in the front ensures the solution satisfies $P^{-a} = (P^a)^*$.

In 1D, (2.44) can be heavily simplified. Both the linear and nonlinear parts of the admittance are given by their characteristic forms for a straight duct

$$\mathbf{Y}^a = 1, \quad \mathcal{Y}^{ab} = -\frac{\beta}{2\sqrt{h_+ - h_-}} \quad (2.64)$$

Thus, (2.44) reduces to

$$\frac{d}{ds} P^a = iakP^a - \sum_{b=-\infty}^{\infty} \left(\frac{iak\beta}{2\sqrt{h_+ - h_-}} P^{a-b} P^b + \frac{i(a-2b)k}{\sqrt{h_+ - h_-}} P^{a-b} P^b \right) \quad (2.65)$$

The third term on the RHS of this equation—corresponding to $\mathcal{C}[\mathbf{Y}\mathbf{p}, \mathbf{p}]$ in (2.44)—may be written

$$\frac{ik}{\sqrt{h_+ - h_-}} ((a-b) - b) P^{a-b} P^b \quad (2.66)$$

and hence vanishes on summation. This happens because the term \mathcal{C} corresponds to the Lagrangian density of energy, which vanishes for plane waves (Hamilton and Blackstock, 1990). We are therefore left with

$$\frac{d}{ds} P^a = iakP^a - \frac{iak\beta}{2\sqrt{h_+ - h_-}} P^{a-b} P^b \quad (2.67)$$

Upon substituting (2.63) into (2.67) we are left with

$$\frac{1}{\sigma} J'_a(a\sigma) - \frac{1}{a\sigma^2} J_a(a\sigma) = \sum_{b=-\infty}^{\infty} \frac{a}{2(a-b)b} J_{a-b}((a-b)\sigma) J_b(b\sigma) \quad (2.68)$$

Based upon numerical evaluations, this appears to be a Bessel identity valid for $\sigma < 1$. Under this assumption the Fubini solution is a solution to our equations up to the shock formation.

For $\sigma > 3$ the waveform assumes a sawtooth shape (Blackstock, 1966). The solution in this region (corresponding to the Fay (1931) solution in the lossless limit) is given by

$$P^a = \frac{iM\sqrt{h_+ - h_-}}{(1 + \sigma)a} e^{iaks} \quad \text{例2} \quad (2.69)$$

In (2.67) we get,

$$-\frac{1}{a} \frac{i\beta k M^2 \sqrt{h_+ - h_-}}{(1 + \sigma)^2} e^{iaks} = \sum_{b=-\infty}^{\infty} \frac{a}{2(a - b)b} \frac{i\beta k M^2 \sqrt{h_+ - h_-}}{(1 + \sigma)^2} e^{iaks} \quad (2.70)$$

The RHS factor can be split into partial fractions

$$\begin{aligned} \sum_{b=-\infty}^{\infty} \frac{a}{2(a - b)b} &= \frac{1}{2} \sum_{b=-\infty}^{\infty} \left(\frac{1}{a - b} + \frac{1}{b} \right) \\ &= \frac{1}{2} \sum_{b=1}^{a-1} \left(\frac{1}{a - b} + \frac{1}{b} \right) + \frac{1}{2} \sum_{b=1}^{\infty} \left(\frac{1}{a + b} - \frac{1}{b} \right) + \frac{1}{2} \sum_{b=a+1}^{\infty} \left(-\frac{1}{b - a} + \frac{1}{b} \right) \\ &= \frac{1}{2} \sum_{b=1}^{a-1} \left(\frac{1}{a - b} + \frac{1}{b} \right) + \sum_{b=1}^{\infty} \left(\frac{1}{a + b} - \frac{1}{b} \right) \\ &= \frac{1}{2} \sum_{b=1}^{a-1} \left(\frac{1}{a - b} - \frac{1}{b} \right) - \frac{1}{a} \\ &= -\frac{1}{a} \end{aligned} \quad (2.71)$$

Thus, the sawtooth wave is a solution to the equation.

2.4.2 Uniform Straight Ducts

Now we consider a 2D duct with no curvature or varying width. This was dealt with by Fernando et al. (2011). We will now partly demonstrate the equivalence of our method and theirs. We first simplify some of the Ψ matrix products in our definitions of the matrices and tensors.

2.19a

$$\Psi_{[p]s} \Psi_{s[q]} = \sum_{\substack{s=0 \\ s \neq p, q}}^{\infty} C_p C_q \frac{2 - \delta_{s0}}{h_+ - h_-} p^2 q^2 \frac{\left((-1)^{p+q} - (-1)^{p+s} - (-1)^{q+s} + 1 \right)}{(p^2 - s^2)(q^2 - s^2)} \quad (2.72)$$

For $p = q$ this becomes

$$\Psi_{[p]s}\Psi_{s[p]} = \sum_{\substack{s=0 \\ s \neq p}} \frac{2 - \delta_{s0}}{(h_+ - h_-)^2} (1 - (-1)^{p+s}) \left(\frac{p^2}{(s-p)^2} + \frac{p^2}{(p+s)^2} - \frac{p}{s-p} + \frac{p}{s+p} \right) \quad (2.73)$$

and the terms with numerator linear in p cancel upon summation. The terms with numerator quadratic in p correspond to the sum $\sum_{s=\text{odd}} \frac{8p^2}{s^2} = p^2\pi^2$ after rearrangement. For $p \neq q$

$$\begin{aligned} \Psi_{[p]s}\Psi_{s[q]} &= \sum_{\substack{s=0 \\ s \neq p,q}}^{\infty} C_p C_q \frac{2 - \delta_{s0}}{h_+ - h_-} \left(\frac{p^2 q}{2(p-q)(p+q)(q+s)} - \frac{p^2 q}{2(p-q)(p+q)(s-q)} \right. \\ &\quad \left. + \frac{pq^2}{2(p-q)(p+q)(s-p)} - \frac{pq^2}{2(p-q)(p+q)(p+s)} \right) \\ &\quad \left((-1)^{p+q} - (-1)^{p+s} - (-1)^{q+s} + 1 \right) \end{aligned} \quad (2.74)$$

and it can be seen that the pairs of partial fractions cancel out upon summation. Hence we are left with

$$\Psi_{[p]s}\Psi_{s[q]} = \delta_{pq} \frac{p^2\pi^2}{(h_+ - h_-)^2} = \delta_{pq} \lambda_p^2 \quad (2.75)$$

Therefore, in a straight duct we have

$$\mathbf{N}_{pq}^a = iak\delta_{pq}, \quad (2.76a)$$

$$\mathbf{M}_{pq}^a = \frac{1}{iak} (k_p^a)^2 \delta_{pq} \quad (2.76b)$$

where k_p^a is the longitudinal wavenumber for each mode (defined later by equation (2.79)). The matrix multiplications defining the tensors can also be simplified, which is made easier by the index notation used here. For example, $\Psi_{[p]s}\Psi_{sqt}\Psi_{t[r]} = \Psi_{[p]qt}\Psi_{t[r]} = \Psi_{[p]q[r]}$. We also have $\Psi_{[p]s}\Psi_{[s]qr} = -\lambda_p^2\Psi_{pqr}$ and $\Psi_{[p]q[r]} + \Psi_{[p]q[r]} = \lambda_p^2\Psi_{p[q][r]}$. The tensors simplify to

$$\begin{aligned} \mathcal{A}_{pqr}^{ab} &= -ibk\Psi_{pqr} + \frac{1}{2iak} \lambda_p^2 \Psi_{pqr} \\ &\sim \frac{1}{2iak} (a^2 k^2 + \lambda_p^2) \Psi_{pqr}, \end{aligned} \quad (2.77a)$$

$$\begin{aligned}
\mathcal{B}_{pqr}^{ab} = & -(\mathrm{i}bk + \mathrm{i}ak\frac{B}{2A})\Psi_{pqr} - \frac{1}{\mathrm{i}(a-b)k}\Psi_{p[q][r]} \\
& - \frac{1}{2k^2(a-b)b}\frac{\lambda_p^2}{\mathrm{i}ak}\Psi_{p[q][r]} - \frac{1}{\mathrm{i}ak}\Psi_{[p]q[r]} \\
\sim & -\mathrm{i}ak\frac{B}{2A}\Psi_{pqr} - \frac{\mathrm{i}ak}{2}\Psi_{pqr} - \frac{a^2k^2}{2\mathrm{i}ab(b-a)k^3}\Psi_{p[q][r]} \\
& - \frac{\lambda_p^2}{2\mathrm{i}ab(a-b)k^3}\Psi_{p[q][r]} - \frac{\lambda_p^2}{2\mathrm{i}ak}\Psi_{p[q][r]},
\end{aligned} \tag{2.77b}$$

$$\mathcal{C}_{pqr}^{ab} = \mathrm{i}ak\Psi_{pqr} + \frac{1}{\mathrm{i}bk}\Psi_{[p]q[r]} + \frac{2(k_r^b)^2}{\mathrm{i}bk}\Psi_{pqr} \tag{2.77c}$$

where the ' \sim ' denotes an equivalence relation between two tensors that, while not equal, are equivalent under summation. Because of this property it can be seen that the expressions for the tensors relating second order quantities are not unique, but do form an equivalence class under summation. Here we have expressed \mathcal{A} and \mathcal{B} in a form symmetric on interchange of $b \leftrightarrow (a-b)$ with $q \leftrightarrow r$. Having this property is sufficient to uniquely define the second order quantities.

The equation used by Fernando et al. (2011) is for the velocity potential $\hat{\mathbf{u}} = \nabla\hat{\phi}$. The velocity potential is expanded about the basis of modes, with the modal amplitudes A_p^a given by

$$\phi_p^a = A_p^a(s)e^{ik_p^a s} \tag{2.78}$$

where $A_p^a(s)$ is assumed to be $\mathcal{O}(M)$ with $\mathcal{O}(M^2)$ derivatives. The factor

$$k_p^a = \begin{cases} (a^2k^2 - \lambda_p^2)^{1/2} & ak > \lambda_p, \quad a > 0 \\ -(a^2k^2 - \lambda_p^2)^{1/2} & ak > \lambda_p, \quad a < 0 \\ \mathrm{i}(\lambda_p^2 - a^2k^2)^{1/2} & ak < \lambda_p \end{cases} \tag{2.79}$$

corresponds to the longitudinal wavenumber for each mode.

Note that while it may be more natural to work with the velocity potential⁵, there is the implicit assumption of zero vorticity when using this variable—something which cannot be assumed a priori for a curved duct.

In terms of the velocity potential, the pressure is given by

$$\hat{p} = -\frac{1}{c_0}\frac{\partial\hat{\phi}}{\partial t} - \frac{1}{2}\left((\nabla\hat{\phi})^2 - \frac{1}{c_0^2}\left(\frac{\partial\hat{\phi}}{\partial t}\right)^2\right) \tag{2.80}$$

⁵For example a second order wave equation, the Kuznetzov equation (Kuznetsov, 1971), can be formed from just this variable

corresponding to modal amplitudes given by

$$P_p^a = iakA_p^a e^{ik_p^a s} + \frac{1}{2} \left(k_q^{a-b} k_r^b \Psi_{pqr} - \Psi_{p[q][r]} - (a-b)bk^2 \Psi_{pqr} \right) A_q^{a-b} A_r^b e^{i(k_q^{a-b} + k_r^b)s} \quad (2.81)$$

In order to completely prove the equivalence of our method with that of Fernando et al. (2011), one would need to derive (2.81) from a nonlinear impedance relationship analogous to (2.36). Because of the large class of equivalent tensors relating second order quantities this has proved difficult so far.

The expression for the velocity modes is

$$U_p^a = ((A_p^a)' + ik_p^a A_p^a) e^{ik_p^a s} \quad (2.82)$$

We substitute these expressions into (2.32a) (with the above straight duct simplifications), and, after cancellation and neglecting the second derivative of A (for the second derivative is $\mathcal{O}(M^3)$) we obtain

$$2k_p^a (A_p^a)' e^{ik_p^a s} = ak \left(k_q^{a-b} k_r^b \Psi_{pqr} - \Psi_{p[q][r]} + k^2(a-b)b \frac{B}{2A} \Psi_{pqr} \right) A_q^{a-b} A_r^b e^{i(k_q^{a-b} + k_r^b)s} \quad (2.83)$$

This is the equation presented by Fernando et al. (2011) (in dimensionless variables with normalized modes). Solving this equation has some disadvantages over our method. Firstly, this method can only be used for forward propagating waves. With a suitable choice of admittance, one can solve for the nonlinear interaction of both forward and backward propagating waves together in our method. Secondly, for numerical stability, one must discard evanescent modes from the calculation because of the problems associated with defining an amplitude for an exponentially small mode. In our method this is not necessary—indeed, as shown by Félix and Pagneux (2001), the evanescent modes are important when one considers a duct with curvature.

As stated previously, this is not a complete proof of equivalence—one can instead refer to section 2.6.2 for a numerical verification.

2.4.3 Linear Acoustics in a Non Uniform Straight Duct

If we ignore the quadratic terms and terms corresponding to curvature, our equations reduce to

$$U_p^{a'} + \frac{1}{iak} (k_p^a)^2 P_p^a - \Psi_{\{p\}q} U_q^a = 0 \quad (2.84a)$$

$$P_p^{a'} - iak U_p^a + \Psi_{p\{q\}} U_q^a = 0 \quad (2.84b)$$

These are the analogous 2D matricial horn equations derived by Pagneux et al. (1996). As with their work we can consider taking only the planar modes in which case the equations become

$$U_0^{a'} - \text{i}akP_0^a + \frac{(h'_+ - h'_-)}{2(h_+ - h_-)}U_0^a = 0 \quad (2.85\text{a})$$

$$P_0^{a'} - \text{i}akU_0^a - \frac{(h'_+ - h'_-)}{2(h_+ - h_-)}P_0^a = 0 \quad (2.85\text{b})$$

Using $P^a = \frac{1}{\sqrt{h_+ - h_-}}P_0^a$ we find that

$$\frac{1}{h_+ - h_-} \left((h_+ - h_-)(P^a)' \right)' + a^2k^2P^a = 0 \quad (2.86)$$

which is Webster's horn equation in two dimensions (Webster, 1919), valid under the assumption of slowly varying duct width.

2.4.4 Linear Acoustics in a Curved Duct

In this section, we demonstrate the equivalence of our method with the multimodal method of Félix and Pagneux (2001) in the limit of infinitesimal Mach number. Ignoring quadratic terms yields

$$U_p^{a'} - \left(\text{i}ak\Psi_{pq}[1 - \kappa r] + \frac{1}{\text{i}ak}\Psi_{[p]s}[1 - \kappa r]\Psi_{s[q]} \right) P_q^a - \Psi_{\{p\}q}U_q^a = 0 \quad (2.87\text{a})$$

$$P_p^{a'} - \text{i}ak\Psi_{pq}[1 - \kappa r]U_q^a + \Psi_{\{p\}q}P_q^a = 0 \quad (2.87\text{b})$$

We have already shown in section 2.4.2 that $\Psi_{[p]s}\Psi_{s[q]} = \lambda_p^2\delta_{pq}$. It can also be shown that $\Psi_{[p]s}[r]\Psi_{s[q]} = \lambda_p^2\Psi_{pq}[r] - \Psi_{[p]q}$. Equation (2.87a) thus becomes

$$U_p^{a'} + \frac{1}{\text{i}ak} \left((a^2k^2 - \lambda_p^2)\Psi_{pq}[1 - \kappa r] - \kappa\Psi_{[p]q} \right) P_q^a - \Psi_{\{p\}q}U_q^a = 0 \quad (2.88)$$

We now transform into polar coordinates to describe the rigid bend, with \tilde{r} the distance from the polar origin and $\tilde{\theta}$ the angle. Following the notation of Félix and Pagneux (2001) we let R_1 be the distance from the polar origin to the inside of the bend, with widths given by $h_+ = -h_- = h/2$. We therefore have the following transformation between our coordinate system and theirs

$$\frac{1}{\kappa} = - (R_1 + h/2) \quad (2.89\text{a})$$

$$\tilde{\theta} = -s\kappa \quad (2.89b)$$

$$\tilde{r} = r + h/2 + R_1 \quad (2.89c)$$

The factor $(1 - \kappa r) \mapsto -\kappa \tilde{r}$ and $\frac{d}{ds} \mapsto -\kappa \frac{d}{d\tilde{\theta}}$. The equations therefore become

$$\frac{d}{d\tilde{\theta}} U_p^a = -\frac{1}{iak} \left((a^2 k^2 - \lambda_p^2) \Psi_{pq}[\tilde{r}] + \Psi_{[p]q} \right) P_q^a + \Psi_{\{p\}q} U_q^a \quad (2.90a)$$

$$\frac{d}{d\tilde{\theta}} P_p^a = iak \Psi_{pq}[\tilde{r}] U_q^a - \Psi_{\{p\}q} P_q^a \quad (2.90b)$$

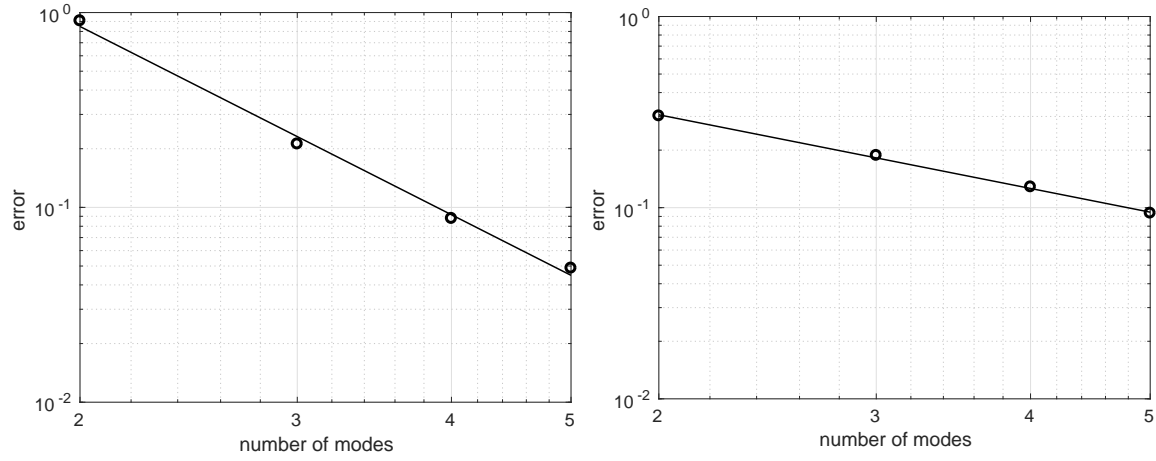
These are the equations presented by Félix and Pagneux (2001) (noting sign differences due to the opposite sign of the temporal exponential factor). We are therefore justified in expanding the transverse velocity V^a into modal components and eliminating it at the end of the derivation, as doing so produces the equivalent results to eliminating V^a before we expand about our modal basis.

2.5 Numerical Method

To implement our method we truncate the summations at a_{\max} temporal harmonics and p_{\max} spatial modes. We shall not go into great detail on the convergence of this method with respect to the number of modes taken (the convergence depends strongly on the problem being studied), but one can expect a Fourier series type convergence temporally. Spatially, the number of modes required varies greatly on the shape of the duct—uniform ducts typically require fewer modes than variable width ones to correctly apply the boundary conditions. For an example of convergence, we consider the uniform curved duct described later in section 2.6.4 with sinusoidal planar source and $M = 0.10$. We define the error to be

$$\text{error} = \frac{\int_0^{2\pi/\omega} \int_0^{s_{\max}} \int_{h_-}^{h_+} |p - p_{\text{ref}}| dr ds dt}{\int_0^{2\pi/\omega} \int_0^{s_{\max}} \int_{h_-}^{h_+} |p_{\text{ref}}| dr ds dt} \quad (2.91)$$

We take our reference pressure p_{ref} to be the solution produced by 10 spatial and 10 temporal modes. Figure 2.2 shows the error resulting from varying the number of spatial modes with fixed number of temporal modes and vice versa. Varying the number of spatial modes we obtain convergence $\sim 1/N^{3.21}$. This is almost identical to the value obtained by Félix and Pagneux (2001). Varying the number of temporal modes we obtain convergence $\sim 1/N^{1.28}$. This number is dependant on the Mach number with smaller Mach numbers resulting in a greater convergence. For high Mach



(a) 10 temporal modes, varying the number of spatial modes (b) 10 spatial modes, varying the number of temporal modes

Fig. 2.2 Convergence of the method fixing the number of temporal or spatial modes

numbers the solution is described by a sawtooth wave throughout most of the duct (see section 2.4.1) for which the convergence of the Fourier series is $\sim 1/N$. This gives the lower bound on the convergence.

While convergence of the pressure solution can take quite a few modes (and consequently a large amount of computational time), good approximations can be made with very few modes—indeed many of the duct properties discussed later (such as power output and reflectance) can be calculated with good accuracy with as few as 5 spatial / 5 temporal modes.

For the remainder of the chapter we shall be dealing with ducts with an infinite uniform outlet. As such, we set $\mathbf{Y} = \mathbf{Y}^+$ for the initial condition of (2.41) and solve backwards through the duct to calculate $\mathbf{Y} = \mathbf{Y}(s)$ at every point in the duct. Next, we solve (2.42) with initial condition $\mathcal{Y} = \mathcal{Y}^+$. Again, we solve backwards through the duct using the previously found values of \mathbf{Y} in our evaluations of (2.42). Finally we solve (2.44) *forwards* through the duct using both the previously found \mathbf{Y} and \mathcal{Y} in the evaluations of the equation. For the initial condition of the pressure we will generally be using a sinusoidal plane piston source so that

$$P_p^a(0) = \frac{1}{2} \sqrt{h_+(0) - h_-(0)} M \delta_{p0} \delta^{|a|1} \quad (2.92)$$

Many other pressure sources can be modelled, with initial conditions chosen by decomposing the desired initial waveform into the modal / Fourier basis. Once both \mathbf{Y} and

\mathcal{Y} are found throughout the duct for a particular wavenumber k , different pressure waveforms and amplitudes can be solved for without re-evaluation of (2.41) and (2.42).

To solve (2.41) and (2.42) we use a fixed step RK4 algorithm. For most cases this is adequate. Due to the temporally decoupled nature of these equations a high degree of parallelisation is possible. Indeed, when taking a_{\max} temporal modes there are $3a_{\max}(a_{\max} - 1)/2$ independent equations for \mathcal{Y} (for each $a \in [1, a_{\max}]$ we have $b \in [a - a_{\max}, a_{\max}]$ minus the cases when $b = 0$ or $a = b$) which can be solved in parallel. An issue, however, with this method is the large size of \mathcal{Y} which scales like $\mathcal{O}(a_{\max}^2 p_{\max}^3)$ with number of spatial modes p_{\max} . As a result, computational memory can be an issue. To overcome this, we opt to use a first order exponential integrator method for the pressure as this requires the calculation and evaluation of \mathcal{Y} at fewer points.

If we consider the equation for the pressure as the sum of a linear operator \mathbf{L} acting on \mathbf{p} and a nonlinear part \mathcal{N}

$$\mathbf{p}' = \mathbf{L}\mathbf{p} + \mathcal{N} \quad (2.93)$$

the exact solution is given by

$$\mathbf{p}(s) = \exp\left(\int_0^s \mathbf{L}(t) dt\right)\mathbf{p}(0) + \int_0^s \exp\left(\int_t^s \mathbf{L}(u) du\right)\mathcal{N}(t)dt \quad (2.94)$$

We now consider a small step δs and make the approximation that both \mathbf{L} and \mathcal{N} are constant over this interval (in many cases this is valid—for infinite uniform ducts of constant curvature \mathbf{L} is a fixed point and so this method provides the correct solution to the linear problem), we obtain our stepping algorithm

$$\mathbf{p}(s + \delta s) = \exp\left(\delta s \mathbf{L}(s)\right)\mathbf{p}(s) - \mathbf{L}^{-1}\left(\mathbf{I} - \exp\left(\delta s \mathbf{L}(s)\right)\right)\mathcal{N}(s) \quad (2.95)$$

Matrix exponentiation was performed using a Fortran 90 routine written by John Burkardt based on the scaling and squaring algorithm used in MATLAB (see Moler and Van Loan, 2003). Other matrix operations were performed using LAPACK routines (Anderson et al., 1999). Running the code on an 8 core 3.40GHz i7 processor with 15GB of RAM can take the order of tens of minutes when running 5 spatial / 5 temporal modes, up to the order of several hours when running 10+ spatial / 10+ temporal modes.

2.5.1 Numerical Viscosity

To overcome the errors (and numerical instabilities that can arise thereof) associated with truncation of the infinite series we add a numerical viscosity. If one considers (2.70) (where we demonstrated the sawtooth wave as a solution to our equations), we can calculate the exact error associated with a finite truncation

$$\text{error} = \frac{i\beta k M^2 \sqrt{h_+ - h_-}}{(1 + \sigma)^2} e^{iaks} \left(\sum_{b=a-a_{\max}}^{a_{\max}} \frac{a}{2(a-b)b(1+\sigma)^2} - \sum_{b=-\infty}^{\infty} \frac{a}{2(a-b)b(1+\sigma)^2} \right) \quad (2.96)$$

which, after some algebra can be found to be

$$\text{error} = \frac{i\beta k M^2 \sqrt{h_+ - h_-}}{(1 + \sigma)^2} e^{iaks} \sum_{b=0}^a \frac{1}{a_{\max} - b} \quad (2.97)$$

The summation can be approximated to $-\log(1 - \frac{a}{a_{\max}})$ using Euler's asymptotic expansion of the harmonic numbers. The factor multiplying this is proportional to the pressure. This gives us a numerical viscosity term which can be deducted from the RHS of our pressure equation

$$-\frac{\beta M k a}{1 + \sigma} \log\left(1 - \frac{a}{a_{\max}}\right) P^a \quad (2.98)$$

For $a \ll a_{\max}$ the logarithm can be Taylor expanded. For small distances we obtain the mode number squared numerical viscosity used by other authors (e.g. Fernando et al., 2011)

$$\frac{\beta M k a^2}{a_{\max}} P^a \quad (2.99)$$

however the logarithmic error is more accurate and provides better numerical results, and shall be used for the remainder of the thesis. We incorporate the viscosity by modification of L :

$$L^a \mapsto L^a + \frac{\beta M k a}{1 + \sigma} \log\left(1 - \frac{a}{a_{\max}}\right) I^a \quad (2.100)$$

As the sawtooth shape is the limiting form of all weakly nonlinear wave propagation (and the most harmonically rich) this provides a very good least upper bound for viscosity, preventing a “pooling” of energy at truncation and ensuring that the simulations remain stable.

2.5.2 Ducts of Increasing Width

As observed by Pagneux et al. (1996), ducts increasing in width—particularly those with a large degree of flare—exhibit a strong degree of coupling between spatial modes. This coupling can prove problematic numerically, especially when a large number of spatial modes are retained. To ensure good accuracy in \mathbf{Y} and especially in \mathcal{Y} , one must take smaller step sizes in the integration scheme as one increases p_{\max} . This further compounds the issue of computational complexity with increasing p_{\max} already noted.

A workaround to this issue is to truncate the number of spatial modes in proportion to the change in duct width. We retain the number of modes p_{ret} given by

$$p_{\text{ret}} = \left\lceil p_{\max} \frac{h_+(s) - h_-(s)}{h_{\max}} \right\rceil \quad (2.101)$$

So, in an increasing width duct, as we solve backwards for \mathbf{Y} and \mathcal{Y} we truncate more modes as we approach the inlet. Then, solving forwards for the pressure, we start with a reduced number of modes and include more as we approach the exit. In practice, where solutions remain stable, with a sufficient maximum number of modes, this truncation makes little difference to the output—the transverse resolution is still preserved. This issue does not arise in ducts of decreasing width as modes undergo cut-off rather than cut-on, however an unrelated mathematical difficulty does appear and is discussed in section 2.6.5.

2.6 Results

We now validate our method against previously published work and examine the effect of adding non-linearity into problems where only linear acoustics was considered.

2.6.1 1D Duct

In section 2.4.1 we show analytically that our method permits both the Fubini (pre shock) and sawtooth ($\sigma > 3$) waves as solutions. We now compare our numerical solution to the Blackstock solution—an asymptotic matching between the Fubini and sawtooth solutions (Blackstock, 1966). This has modal amplitudes given by

$$B_n = \underbrace{\frac{2}{n\pi} P_{\text{sh}}}_{\text{Sawtooth}} + \underbrace{\frac{2}{n\pi\sigma} \int_{\Phi_{\text{sh}}}^{\pi} \cos n(\Phi - \sigma \sin \Phi) d\Phi}_{\text{Fubini}} \quad (2.102)$$

for P_{sh} and Φ_{sh} satisfying

$$P_{\text{sh}} = \sin(\sigma P_{\text{sh}}), \quad \Phi_{\text{sh}} = \sigma \sin \Phi_{\text{sh}} \quad (2.103)$$

Figure 2.3 shows the modal amplitudes plotted against distance through the duct normalised in terms of the shock formation distance, comparing our method with the Blackstock solution. Truncation was taken at 100 modes. Excellent agreement can be seen up to the 80th mode and as far as 10 times the shock formation distance. Even for modes above this the agreement is still very good—there is a slight underestimation at the point of shock formation with modal peaks occurring slightly further down the duct, however beyond that the error never exceeds 5% even for the 100th mode.

2.6.2 2D Straight Duct

The case of nonplanar wave propagation in a 2D waveguide was dealt with by Fernando et al. (2011). In section 2.4.2 we gave a partial proof of the equivalence of our method with theirs. Here, we consider a numerical example from that paper to demonstrate the equivalence of our methods. Figure 2.4 shows the result of sending a finite amplitude plane wave down a rigid 2D waveguide at an angle of 84°. The frequency corresponds to $kh = 3.16$. The pressure scan is taken at the shock formation distance over one time period. Truncation was taken at 20 spatial / 20 temporal modes. If one compares with figure 3 from said paper, one can see good agreement between the two, both giving rise to oblique shocks.

In dealing with the nonlinear admittance numerically (something which isn't strictly necessary for a infinite uniform straight duct) we are forced to take fewer modes due to memory limitations. One could overcome this by substituting the analytical expression for \mathcal{Y} into the pressure equation and simplifying. Such an equation would be more advantageous (for a uniform straight duct) than both methods discussed here—it would require less memory so a better resolution could be obtained, and it would also permit evanescent modes to be solved for. However, since it would not generalize to curved ducts, we do not pursue this further here.

2.6.3 Variable Width Straight Duct

We now turn our attention to straight ducts with varying width, in particular the exponential horn. The exponential horn with duct walls given by $h(s) = (h_+(s) - h_-(s)) = h_0 e^{ms}$ and $h_-(s) = -h_+(s)$ is an attractive problem to solve, both for its real

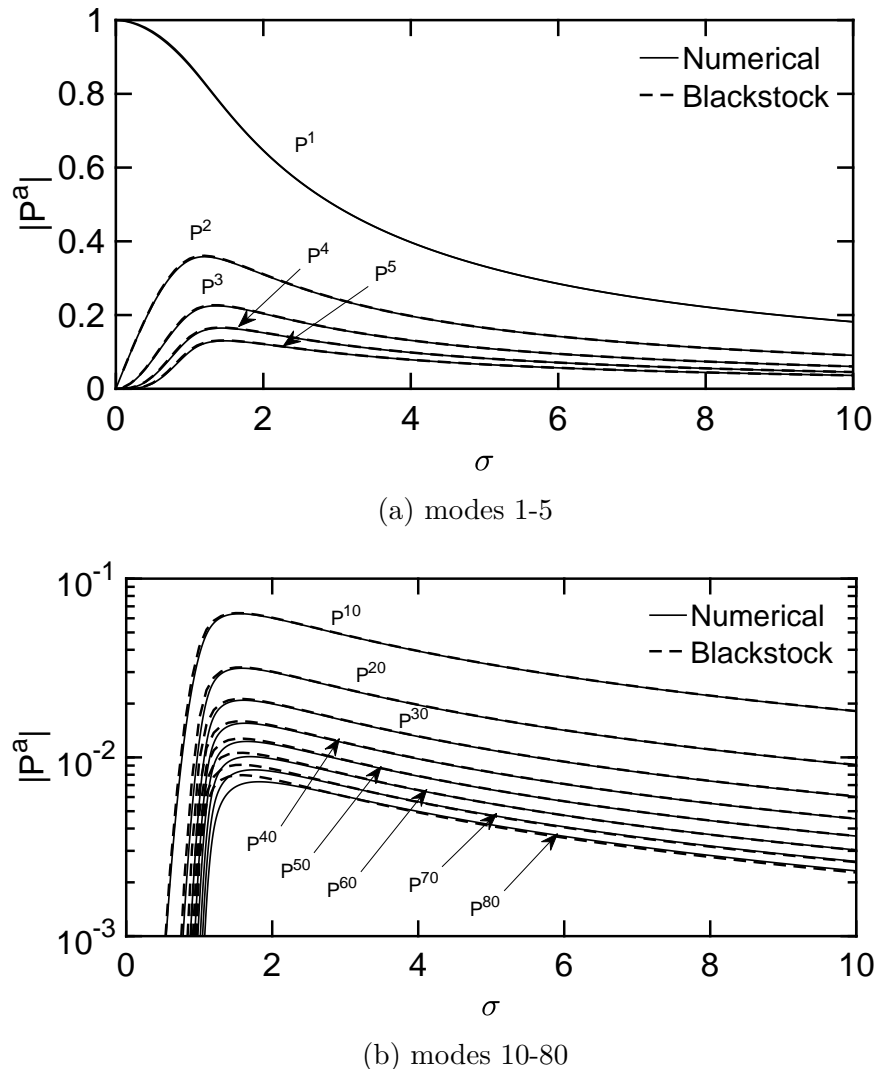


Fig. 2.3 Comparison of modal amplitudes along the waveguide between our method and the analytic Blackstock solution

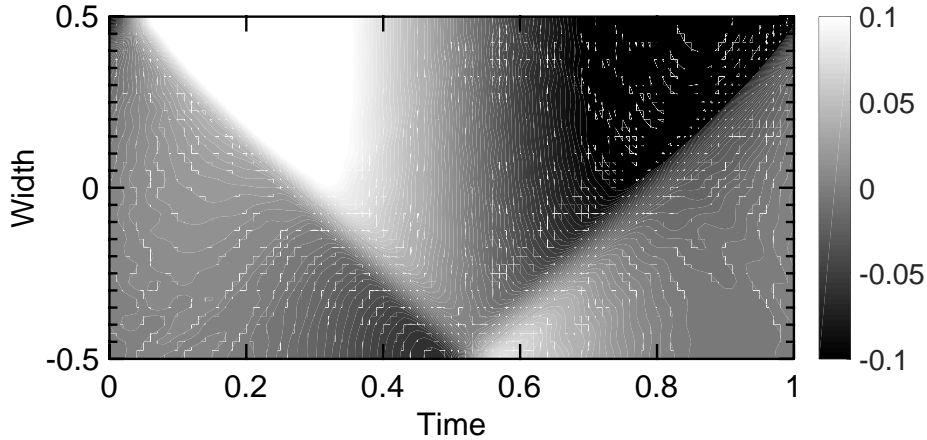


Fig. 2.4 Pressure scan at 1 times the shock formation distance of the shock produced by a planar wave at 84° . Compare with figure 3 from Fernando et al. (2011).

world applications and that it has an approximate analytical solution to the linear problem—the solution to Webster’s horn equation, given by

$$p = e^{-ms/2} (Ae^{ins} + Be^{-ins}) \quad (2.104)$$

where $n^2 = k^2 - (m/2)^2$. The factor of $1/2$ multiplying m comes from working in 2D rather than 3D when comparing with the usual solutions to the horn equation. Solutions with $k < m/2 = k_h$ are evanescent, illustrating how the horn acts as a high pass filter. One can refer to section 2.4.3 for a proof of the equivalence of our method and Webster’s horn equation in the linear limit with a plane wave approximation.

We consider an exponential horn terminated by an infinite straight duct of $h = 16h_0$ with sinusoidal pressure source with amplitude M at the throat of width $h = h_0$. The length of the horn is $4.5h_0$. This is similar to the horn studied by Pagneux et al. (1996), however they studied a 3D version. We have also increased the growth rate of the width to account for the factor of $m/2$ rather than m . The frequency is taken to be $k = 0.95k_e < k_h$, less than both the horn cutoff frequency k_h and the exit duct cutoff $k_e = \pi/(16h_0)$, so linearly we would expect solutions to largely decay, with a small amount of plane wave tunnelling.

Figure 2.5 shows plots of the pressure distributions inside the horn at two different times—when the source is at its peak in the throat and quarter of a cycle later (to illustrate how this peak exits the horn)—for various Mach numbers. Truncation was taken at 20 spatial modes / 10 temporal modes. While these Mach numbers are somewhat exaggerated, they serve to illustrate the effect of nonlinearity more clearly.

In particular, as one would expect, with a waveguide that grows in cross sectional width we require much higher Mach numbers to show a difference compared to a uniform or shrinking duct due to the spreading of energy over a larger area. Putting this aside however, there are some points to observe:

Firstly, as noted by Pagneux et al., the approximation made by Webster's Horn equation that wavefronts are flat is a very poor one—even for the linear case, but especially when nonlinear terms are taken into account, the curvature of the wavefront is very pronounced. Second, despite using straight uniform duct modes we are able to satisfy the correct boundary condition on the curved surface, due to our careful treatment of the boundary conditions when projecting the modes. Finally, a greater proportion of energy is emitted at higher Mach numbers—as was predicted, the linear solution tends to a very low amplitude plane wave resulting from a small amount of tunnelling. With a finite amplitude sound wave, some of the energy is transferred into higher temporal harmonics which are not cut off by the high pass filter—this can be seen most clearly in figure 2.5h where the pressure peak emitted is roughly half the amplitude of the source, compared to much lower fractions in the other figures.

We illustrate this further in figure 2.6 where we plot the RMS pressure normalized by the Mach number along the centreline of the duct. We also plot the linear solution and the analytic solution to Webster's horn equation as well. Clearly it shows that the RMS exit pressure as a proportion of the input pressure is higher in the nonlinear case. The analytic solution underestimates the amplitude inside the horn, but provides a reasonable estimation of the exit pressure for low and infinitesimal Mach number.

2.6.4 Uniform Curved Ducts

We now look at a uniform width duct with constant curvature. The duct we consider is that studied by Félix and Pagneux (2001) using the linear multimodal method⁶, and experimentally as well as with finite differences by Cabelli (1980). The duct consists of a single bend placed $2h$ downstream of a plane piston source of frequency $kh = 3$. The bend has a curvature $\kappa h = 8/5$ and arc length $s = 1.6375h$. The bend then joins an infinite straight outlet. Figure 2.7 shows the results. Truncation was taken at 10 spatial modes / 10 temporal modes.

It can be seen that by introducing a finite Mach number we obtain the characteristic “bunching” of high and low regions of pressure resulting from wave steepening and, eventually, at high enough Mach numbers—shock formation. It is noted that the shocks

⁶In section 2.4.4 we already demonstrated that our method reduces to the linear multimodal method in the linear limit. Here we shall give a numerical comparison.

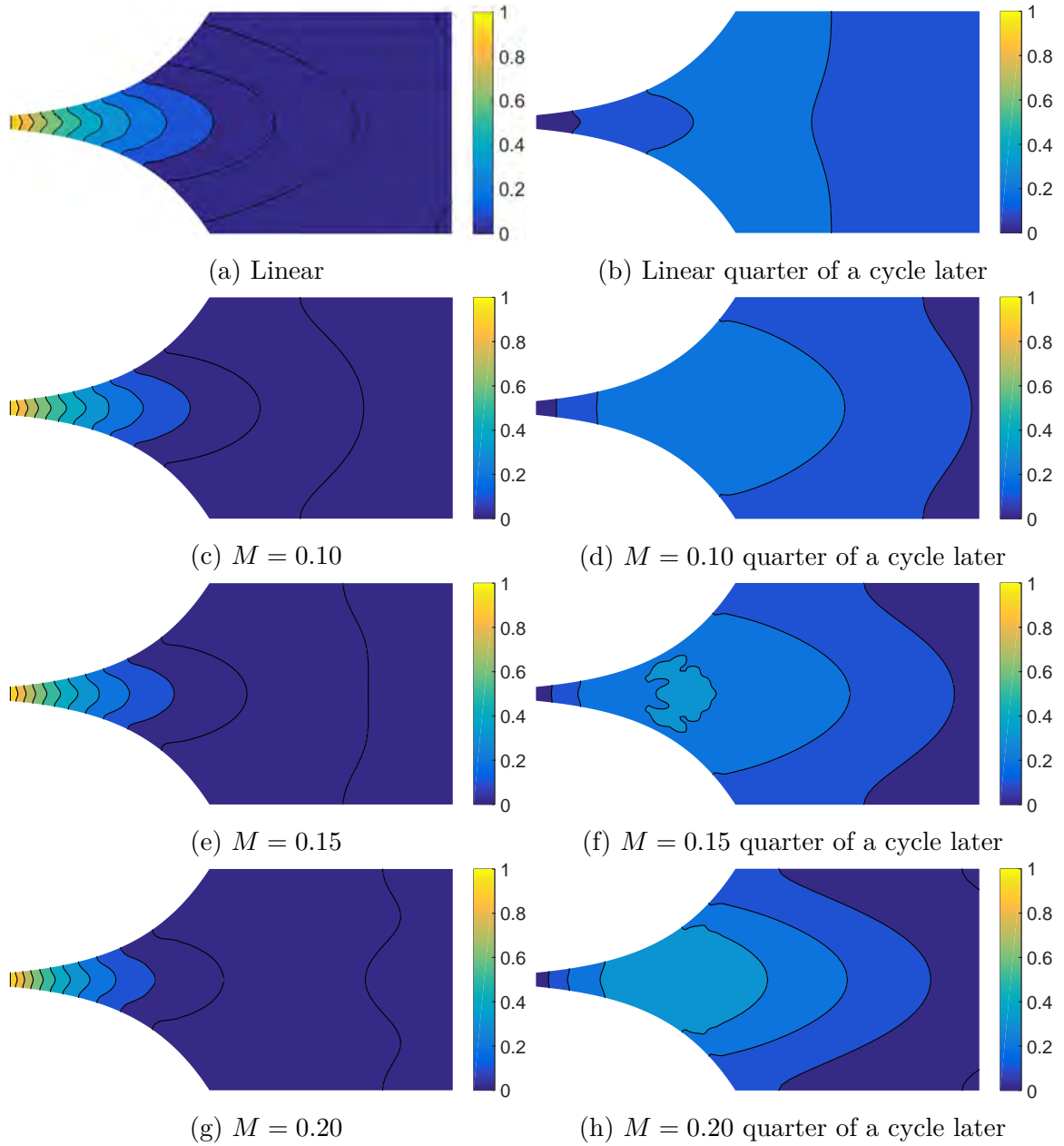


Fig. 2.5 Plots of the pressure distributions inside the exponential horn. Plots are normalised to the source amplitude.

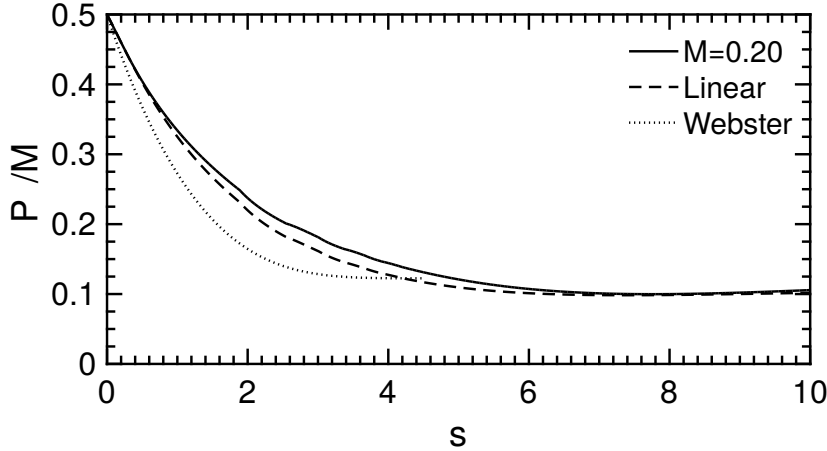


Fig. 2.6 Normalised RMS of the pressure along the centreline of the duct. The horn exit is at $s = 4.5$

form and travel on the outside of the bend. Incoming high pressure is focussed to small regions of greater amplitude than that of the incident wave which then propagate around the outside of the bend. A question which naturally arises is whether this focussing effect (and subsequent increase in local pressure) due to the bend increases, decreases or keeps the same the shock formation distance given that the outside of the bend is a longer path to take. We will begin to address this in section 2.7.

2.6.5 Nonuniform Curved Ducts

Finally we examine a duct of both varying width and with curvature. The “elephant’s trunk” is an interesting example studied by Félix and Pagneux (2001) as there have been recent work by Gilbert et al. (2014) suggesting that nonlinear acoustics may give these animals their characteristic sound. The duct is given by ratio of upstream to downstream widths $h_u/h_d = 4$ with

$$h_+(s) = (h_d - h_u) \left(\frac{s}{s_f} \right)^3 - \frac{3}{2}(h_d - h_u) \left(\frac{s}{s_f} \right)^2 + \frac{h_u}{2}, \quad \text{and,} \quad h_- = -h_+ \quad (2.105)$$

Curvature is given by $\kappa h_u = 4/5$ and the total arc length is $s_f = 3.275h_u$. We impose a plane piston source with $kh_u = 3$ at the source. Figure 2.8 shows the results. Truncation was taken at 10 spatial / 10 temporal modes.

Ducts of this kind (with decreasing width) give rise to issues not previously mentioned. If we consider a uniform straight duct, the linear admittance equation can be

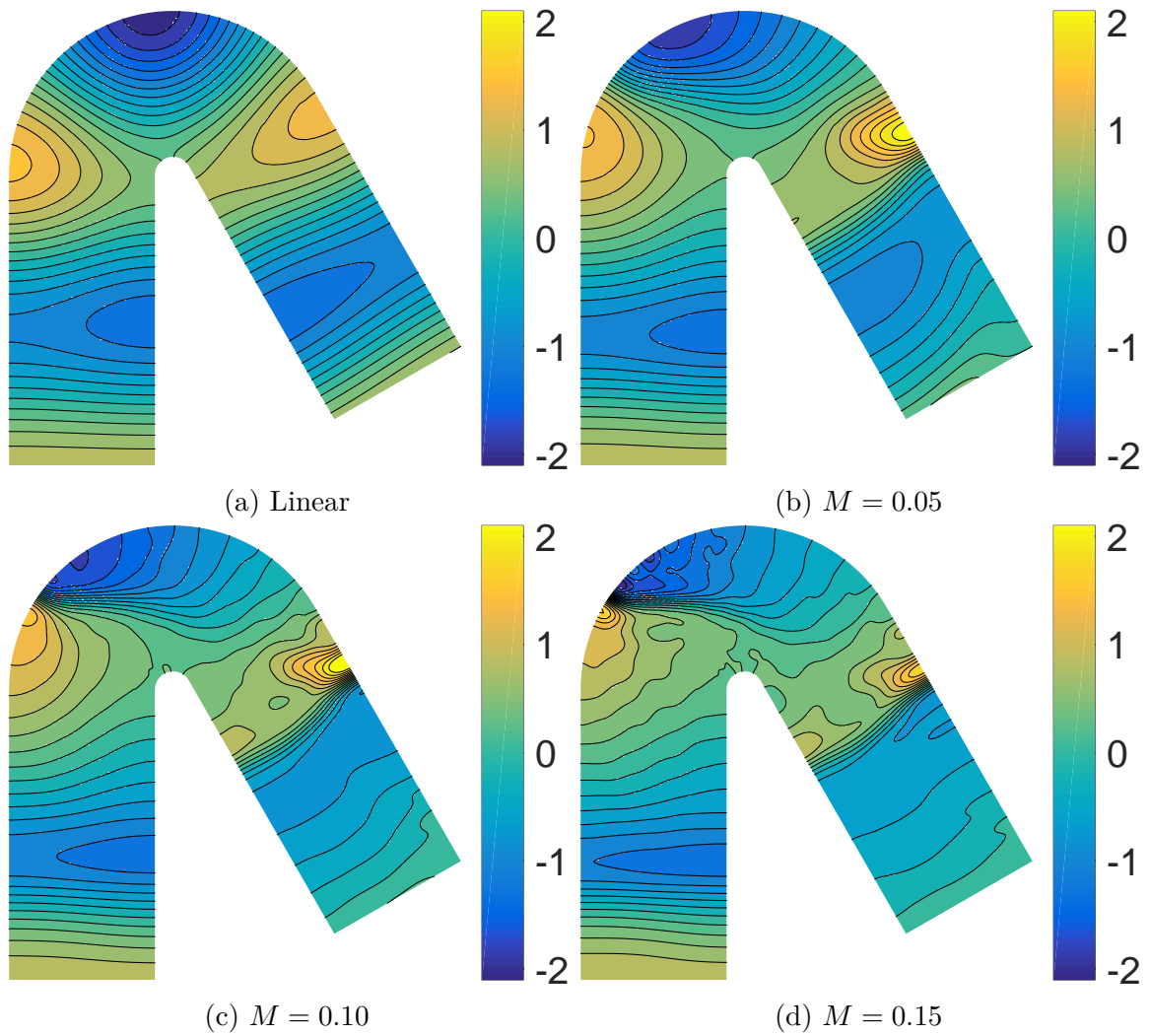


Fig. 2.7 Plots of a uniform curved duct for various Mach numbers. Plots are normalised to the source amplitude. Source at bottom left.

solved for exactly and is given by

$$\mathbf{Y}_{pq}^a = \frac{k_p^a}{ak} \tanh(\mathrm{i}k_p^a(s + c)) \delta_{pq} = \frac{\mathrm{i}k_p^a}{ak} \tan(k_p^a(s + c)) \delta_{pq} \quad (2.106)$$

for some constant c where k_p^a is defined by (2.79). Downstream, our solution is given by the fixed point

$$\mathbf{Y}_{pq}^a = (\mathbf{Y}^+)^a_{pq} \equiv \frac{k_p^a}{ak} \delta_{pq} \quad (2.107)$$

If we consider a cut-off mode downstream so that $k_p^a(s) = \mathrm{i}k^*$ for $s > s_0$ and real k^* , then, we perturb the duct width slightly upstream such that this mode is cut-on upstream ($k_p^a(s) \sim k^*$ for $s < s_0$) the admittance will have solution (for this particular p and a)

$$\mathbf{Y}_{pq}^a = \frac{\mathrm{i}k^*}{ak} \tan(k^*(s - s_0) + \pi/4) \quad \text{for } s < s_0 \quad (2.108)$$

and we get a finite distance blowup in the admittance.

Conversely, if we choose a duct of increasing width, with a mode such that $k_p^a = k^*$ for $s > s_0$ and $k_p^a \sim \mathrm{i}k^*$ for $s < s_0$, we get

$$\mathbf{Y}_{pq}^a = -\frac{k^*}{ak} \tan(\mathrm{i}k^*(s - s_0) - \pi/4) \quad \text{for } s < s_0 \quad (2.109)$$

and we do not get the blowup.

This is a mathematical difficulty previously noted by Pagneux et al. (1996) in their method. A way to overcome this is to introduce a small imaginary part to the wavenumber k (physically this could be thought of as another form of damping). This ensures we are acting our tan function on complex values and hence do not encounter singularities. The imaginary part of k can then be ignored when solving for the pressure. This procedure has little effect on the output, besides keeping the simulations stable. Comparing the linear elephant's trunk with or without the small imaginary part to k yields little difference⁷.

As one would expect with such a duct, the amplitude increases with the decreasing width causing more rapid shock formation and, as with the uniform duct, this shock propagates along the outside of the bend.

⁷In this example, the finite time blowup only occurs in the nonlinear case as only the harmonics undergo cut-off/on, not the fundamental

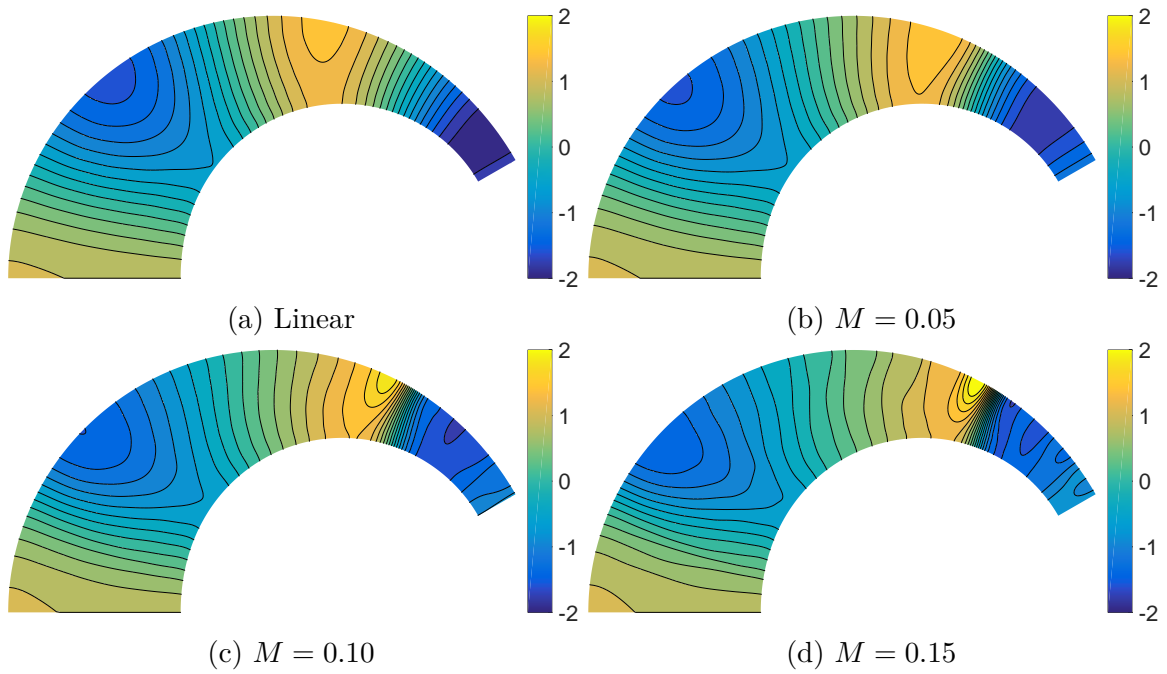


Fig. 2.8 Plots of the elephant's trunk for various Mach numbers. Plots are normalised to the source amplitude. Source at bottom left.

2.7 Comparisons Between Ducts

In the previous section we showed the effects of the introduction of nonlinearity into various different, previously studied ducts. We now consider the effect of the duct itself on the nonlinear sound propagation. To do so, we consider four different ducts all of the same length $L = 1.5\pi h$, with a sinusoidal planar pressure source at the entrance of frequency $kh = 3$ and Mach number given by $M = 2/(L\beta k)$ such that the shock formation distance (for a straight duct at least) is halfway through the duct. Each of the ducts is terminated by an infinite straight outlet. The four ducts are:

- A uniform straight duct
- A 180° circular bend
- An exponential horn with exit width $2h$
- A 180° circular horn with exit width $2h$

Thus we can purely compare the effects of curvature, varying width and the combination.

Figures 2.9, 2.10 and 2.11 compare the modal amplitudes throughout the ducts. As previously observed, the curved duct shows a strong harmonic enrichment on the

outside of the duct bend at the cost of enrichment towards the centre and inside. Therefore it would seem that the “observability” of the bend in a duct system—i.e. whether one could detect if there is a bend upstream—is dependant on whether the ensuing duct can support propagation of higher spatial modes. For low frequencies or narrow ducts it would seem likely that this extra harmonic enrichment would be lost due to reflection, but for high frequencies one could expect highly enriched localised sound to propagate downstream of a bend.

For the horn we compare the pressure normalized to the square root of the duct width to account for the spreading of the waveform. The harmonic enrichment is indeed less than a straight duct, with more energy remaining in the fundamental. However, as noted before, there is the potential for more energy to escape through these nonlinear effects.

These two effects can be seen to combine when comparing the curved uniform duct and the curved horn. While the horn effect reduces enrichment for most points across the duct, the curvature focusses the sound at the outer edge such that it is of comparable amplitude to the uniform curve. As the exit width is larger for the horn, some of these more localised modes can propagate out.

To better examine the downstream effects of the varying duct shape we consider the power spectrum associated with each of the duct modes. We vary the input power of our plane wave source and find the output power of the duct for each of the spatial modes and temporal harmonics (see figure 2.12). For the planar modes the straight duct provides the most enrichment with the curved ducts providing significantly less. When one looks at the higher spatial modes however, one finds a similar degree of enrichment, particularly with the curved horn (which has fewer cut off modes). As an aside it is also interesting to note that modes which would traditionally be cut-off and transmit no power in a linear regime can now do so at sufficiently high Mach numbers (see P_1^1 for the uniform curved duct).

2.8 Nonlinear Reflection

As we have previously noted at several points, nonlinearity can transfer energy to higher modes and allow them to propagate in to regions where a linear wave would not. We have also observed modes which would not traditionally carry energy under a linear regime now doing so. This suggests it is important to reformulate our notions of reflection coefficients and matrices to also take into account the amplitude of the sound waves we are dealing with. We begin with the characteristic admittance relation

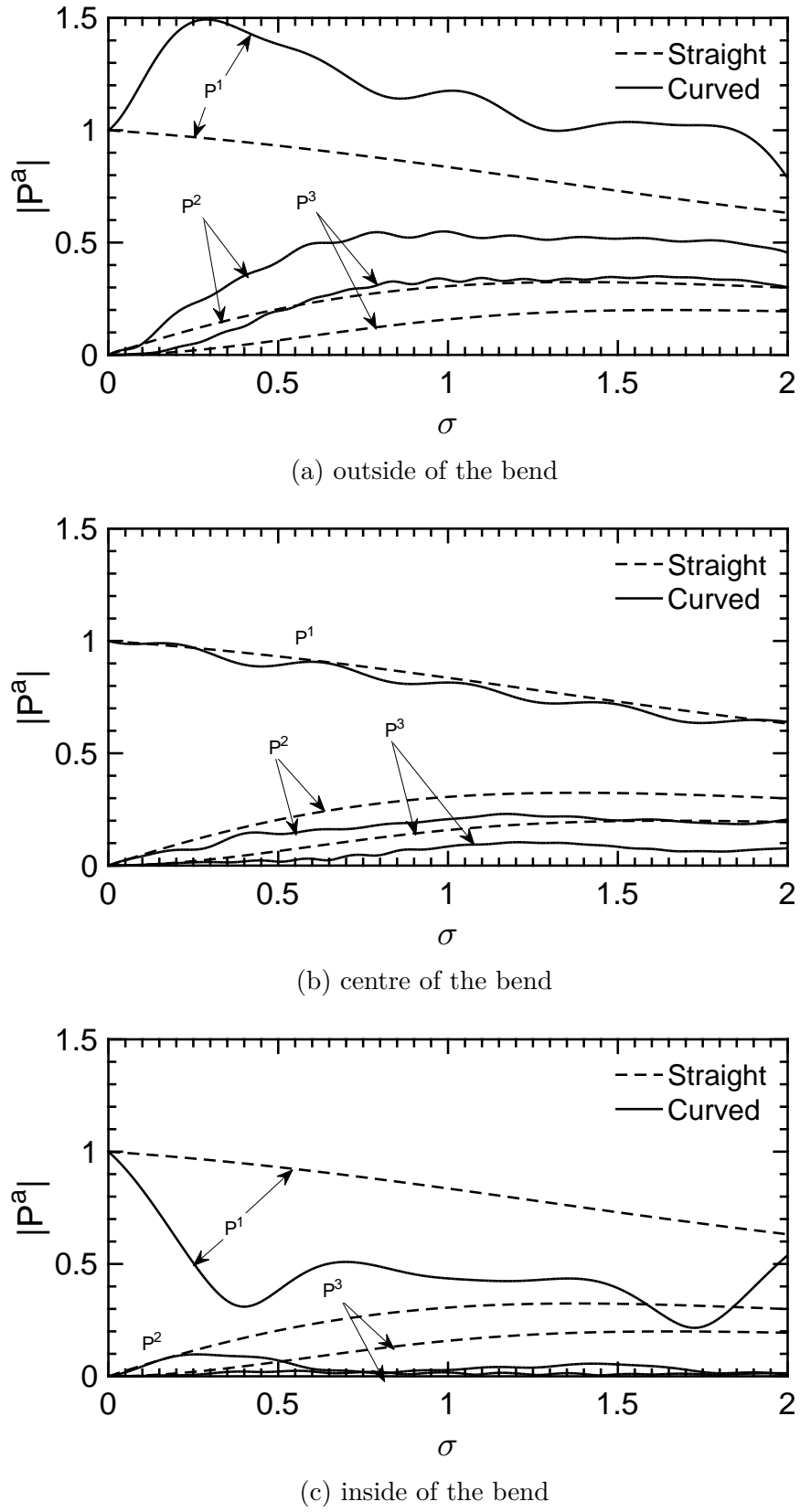


Fig. 2.9 Comparing the modal amplitudes throughout the curved uniform duct along different paths to the straight uniform duct. $M = 2/(L\beta k)$.

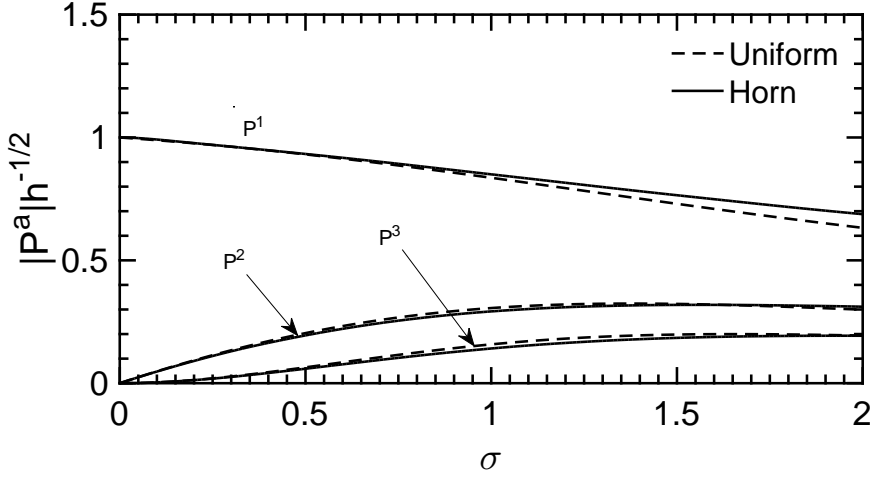


Fig. 2.10 Comparing the modal amplitudes of the straight horn and straight uniform duct. $M = 2/(L\beta k)$.

for forward and backward propagating modes

$$\mathbf{u}^\pm = \mathbf{Y}^\pm \mathbf{p}^\pm + \mathcal{Y}^\pm [\mathbf{p}^\pm, \mathbf{p}^\pm] \quad (2.110)$$

We now define a nonlinear reflection relation, relating forwards and backwards propagating pressure modes

$$\mathbf{p}^- = \mathbf{R} \mathbf{p}^+ + \mathcal{R}[\mathbf{p}^+, \mathbf{p}^+] \quad (2.111)$$

where \mathbf{R} is the common reflection matrix encountered in the linear literature and \mathcal{R} is the new nonlinear reflectance, both of which vary throughout the duct. From the standard impedance relation we have

$$\mathbf{u} = \mathbf{u}^+ + \mathbf{u}^- = \mathbf{Y} \mathbf{p} + \mathcal{Y}[\mathbf{p}, \mathbf{p}] = \mathbf{Y}(\mathbf{p}^+ + \mathbf{p}^-) + \mathcal{Y}[\mathbf{p}^+ + \mathbf{p}^-, \mathbf{p}^+ + \mathbf{p}^-] \quad (2.112)$$

The \mathbf{u}^\pm can be expressed in terms of \mathbf{p}^\pm using (2.110) and, subsequently, the \mathbf{p}^- can be expressed in terms of \mathbf{p}^+ using the reflection relation (2.111) to get

$$\begin{aligned} & \mathbf{Y}^+ \mathbf{p}^+ + \mathcal{Y}^+ [\mathbf{p}^+, \mathbf{p}^+] + \mathbf{Y}^- (\mathbf{R} \mathbf{p}^+ + \mathcal{R}[\mathbf{p}^+, \mathbf{p}^+]) + \mathcal{Y}^- [\mathbf{R} \mathbf{p}^+, \mathbf{R} \mathbf{p}^+] \\ &= \mathbf{Y} (\mathbf{p}^+ + \mathbf{R} \mathbf{p}^+ + \mathcal{R}[\mathbf{p}^+, \mathbf{p}^+]) + \mathcal{Y}[\mathbf{p}^+ + \mathbf{R} \mathbf{p}^+, \mathbf{p}^+ + \mathbf{R} \mathbf{p}^+] \end{aligned} \quad (2.113)$$

As with formulating our impedance relations, orders of magnitude can then be taken to form two distinct equations, and the \mathbf{p}^+ can be cancelled off. From this we obtain

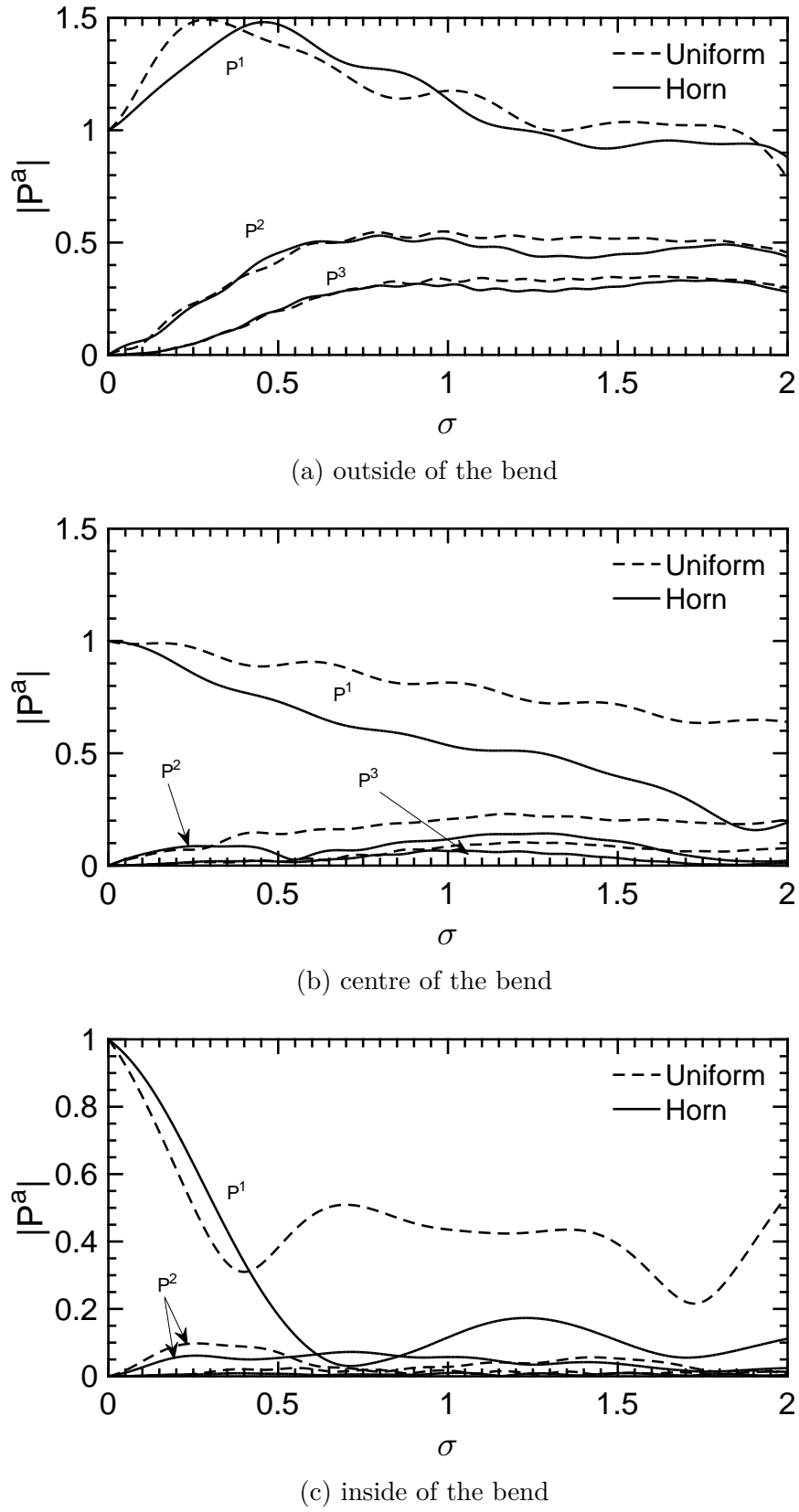
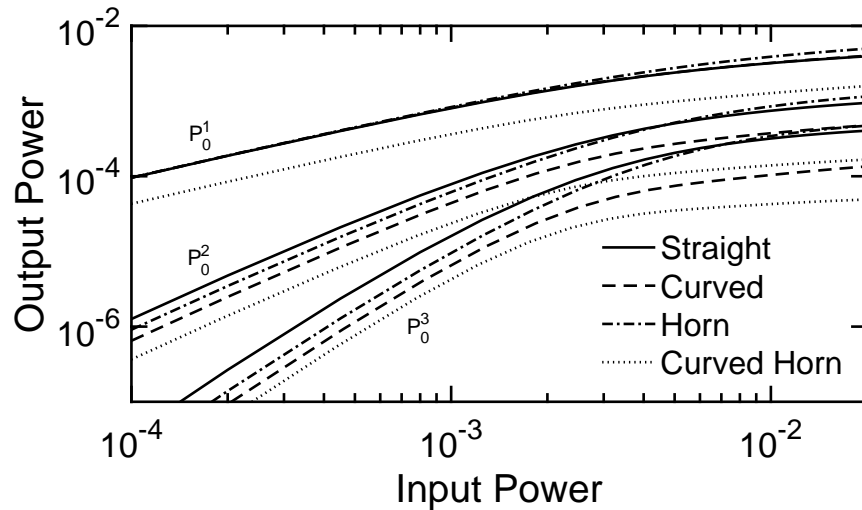
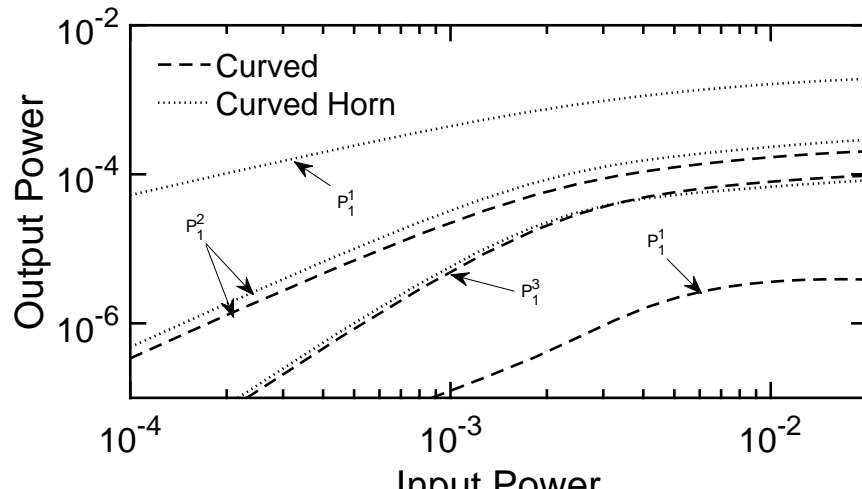


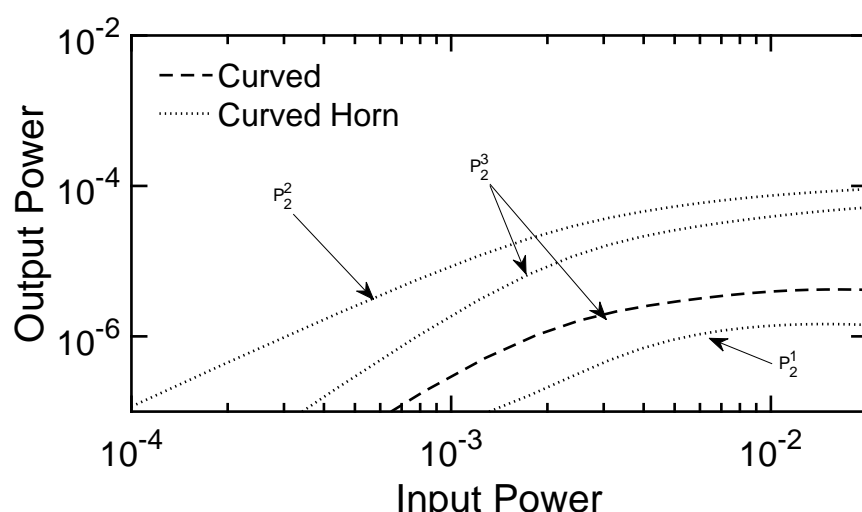
Fig. 2.11 Comparing the modal amplitudes throughout the curved uniform duct to the curved horn along different paths. $M = 2/(L\beta k)$.



(a) the planar modes



(b) mode 1



(c) mode 2

Fig. 2.12 Comparing the power outputs of the different ducts.

the usual definition of the reflection matrix

$$\mathbf{R} = (\mathbf{Y} - \mathbf{Y}^-)^{-1}(\mathbf{Y}^+ - \mathbf{Y}) \quad (2.114)$$

and the new nonlinear reflectance

$$\mathcal{R} = (\mathbf{Y} - \mathbf{Y}^-)^{-1}(\mathcal{Y}^+ + \mathcal{Y}^-[\mathbf{R}, \mathbf{R}] - \mathcal{Y}[\mathbf{I} + \mathbf{R}, \mathbf{I} + \mathbf{R}]) \quad (2.115)$$

We can use these to obtain the reflective properties of a duct. If we have an incident wave \mathbf{p}^+ , we can calculate the power associated with such a wave

$$W^+ = \text{Re}(\mathbf{p}^+ \cdot \overline{\mathbf{u}^+}) = \text{Re}(\mathbf{p}^+ \overline{\mathbf{Y}^+ \mathbf{p}^+} + \mathbf{p}^+ \overline{\mathcal{Y}^+}[\overline{\mathbf{p}^+}, \overline{\mathbf{p}^+}]) \quad (2.116)$$

The total pressure is given by

$$\mathbf{p} = (\mathbf{I} + \mathbf{R})\mathbf{p}^+ + \mathcal{R}[\mathbf{p}^+, \mathbf{p}^+] \quad (2.117)$$

Therefore the total power is

$$W = \text{Re}(\mathbf{p} \overline{\mathbf{Y} \mathbf{p}} + \mathbf{p} \overline{\mathcal{Y}}[\overline{\mathbf{p}}, \overline{\mathbf{p}}]) \quad (2.118)$$

Unlike in the linear case the total energy flux is not a sum of W^+ and the analogous W^- as there are nonlinear interactions. Instead we take our amplitude reflection modulus to be

$$R = \sqrt{\frac{W - W^+}{W^+}} \quad (2.119)$$

Figure 2.13 shows how the amount of energy reflected in the depends both on frequency of the signal and the amplitude for the uniform curved duct studied in section 2.6.4. Low frequencies have a much lower dependence on amplitude than higher frequencies and larger amplitudes have a much more sensitive dependence on frequency, with interesting new resonances arising. Also plotted are the experimental results of Cabelli (1980). Nonlinearity may account for the discrepancy between the experimental results and the linear multimodal method, though as no amplitude was stated one cannot be certain.

Figure 2.14 is a similar plot for the elephant's trunk described in section 2.6.5. In this case the effects of nonlinearity have little effect on the reflection coefficient—presumably due to the decreasing width not only reflecting many of the fundamental duct modes, but also many of the modes of the temporal harmonics as well. Thus,

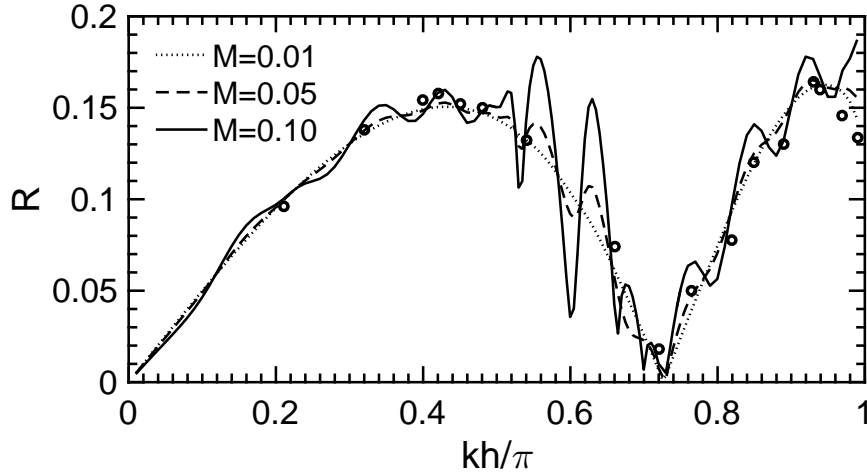


Fig. 2.13 Modulus of the reflection coefficient at various amplitudes for the uniform curved duct described in section 2.6.4. The ‘o’ are the experimental results of Cabelli (1980).

even though the sound is enriched, it is not enriched enough to propagate down the narrow exit.

Figure 2.15 illustrates the opposite effect for the horn described in section 2.6.3. Due to the increasing width, many of the modes of the harmonics produced by spectral enrichment can propagate, whereas the fundamental modes cannot. Therefore, as noted earlier, more energy can escape the horn as the enrichment increases. This is confirmed by this graph with higher Mach numbers reducing the reflection coefficient.

2.9 Conclusion

A multimodal method for the calculation of weakly nonlinear sound propagation in bends of general curvature and width has been presented. The method directly extends the work of Félix and Pagneux (2001) to a more general duct geometry and into the **weakly nonlinear regime**, while reducing to their method in the infinitesimal amplitude limit. The method reproduces the classical nonlinear acoustic phenomena such as wave steepening and shock formation, matching the analytical results for 1D.

The method was applied to ducts previously studied in the linear literature, where it was shown that wave steepening can play an important role in the shape of the waveform propagating in complex geometry. A particularly important result is that nonlinear harmonic enrichment can lead to a greater transmission of sound out of an acoustic horn.

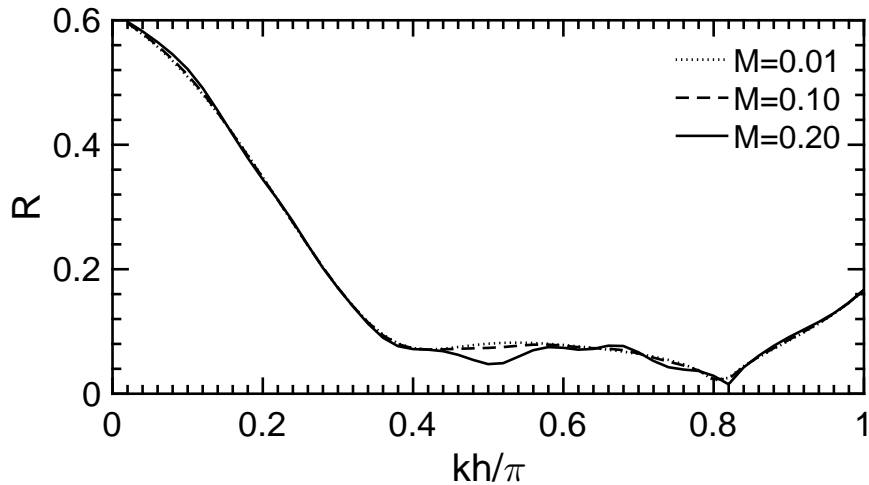


Fig. 2.14 Modulus of the reflection coefficient at various amplitudes for the elephant's trunk described in section 2.6.5

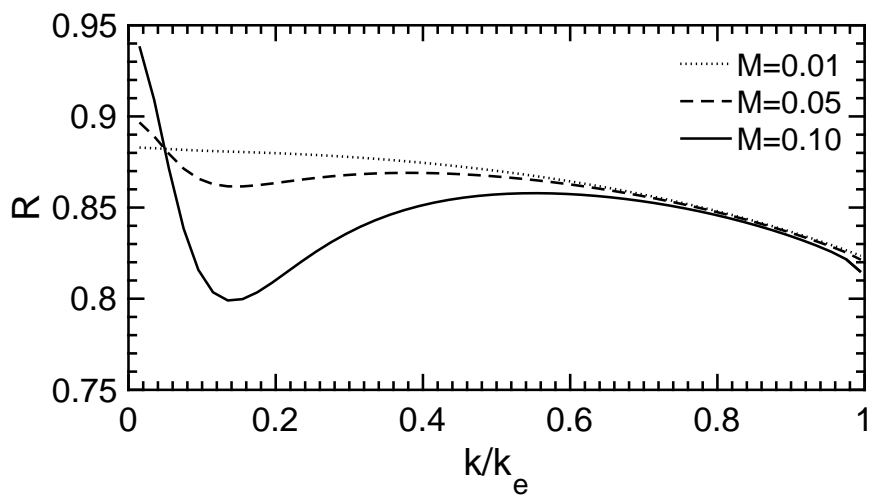


Fig. 2.15 Modulus of the reflection coefficient at various amplitudes for the horn described in section 2.6.3

Different geometries were compared to gain an insight into how the duct shape can effect the acoustic properties in the nonlinear regime. A greater degree of wave steepening was observed on the outside of a bend when compared to a straight duct due to a greater localization of energy. How this affects the sound radiated shall be touched upon in later chapters as well.

An extension to the notion of reflectance was also presented which takes into account the amplitude of the incident wave. This has important consequences for the resonances in musical instruments where, for example, one may be able to calculate the change in pitch of an instrument with the playing volume—something we shall see in chapter 4.

The next chapter extends this work into three dimensions.

Chapter 3

3D Ducts

3.1 Introduction

In this chapter we shall extend the work of the previous, deriving the equations in an analogous 3D coordinate system described by the duct centreline. Aside from the resulting definitions of the tensors, much of the resulting equations is identical in algebraic form. These are derived in section 3.2. In section 3.3 we cover the boundary conditions for the 3D duct. As the algebraic form of the governing equations is almost identical, little work needs to be done here and the same boundary conditions apply. There is the new possibility of an infinite helical duct outlet and this is derived here, with some interesting results regarding the eigenvalues of the linear operator matrix also discussed. In section 3.4 the numerical method is presented. Again, due to the algebraic similarity with the 2D duct, little extra work is required aside from a brief discussion on mode ordering and some new numerical issues that can arise. Finally in section 3.5, results are presented. Again, we compare with results from literature where possible. We also dedicate a section to linear acoustics in an infinite helical duct as, to our present knowledge, this has not been covered by other authors.

3.2 Governing Equations

For our work on the 3D duct we begin from the general form of the mass and momentum conservation derived in section 3.2, again presented here for reference

$$-iakP^a + \nabla \cdot \mathbf{U}^a = \sum_{b=-\infty}^{\infty} \left(-P^{a-b} \nabla \cdot \mathbf{U}^b - \mathbf{U}^{a-b} \cdot \nabla P^b - \frac{B}{2A} iakP^b P^{a-b} \right), \quad (3.1a)$$

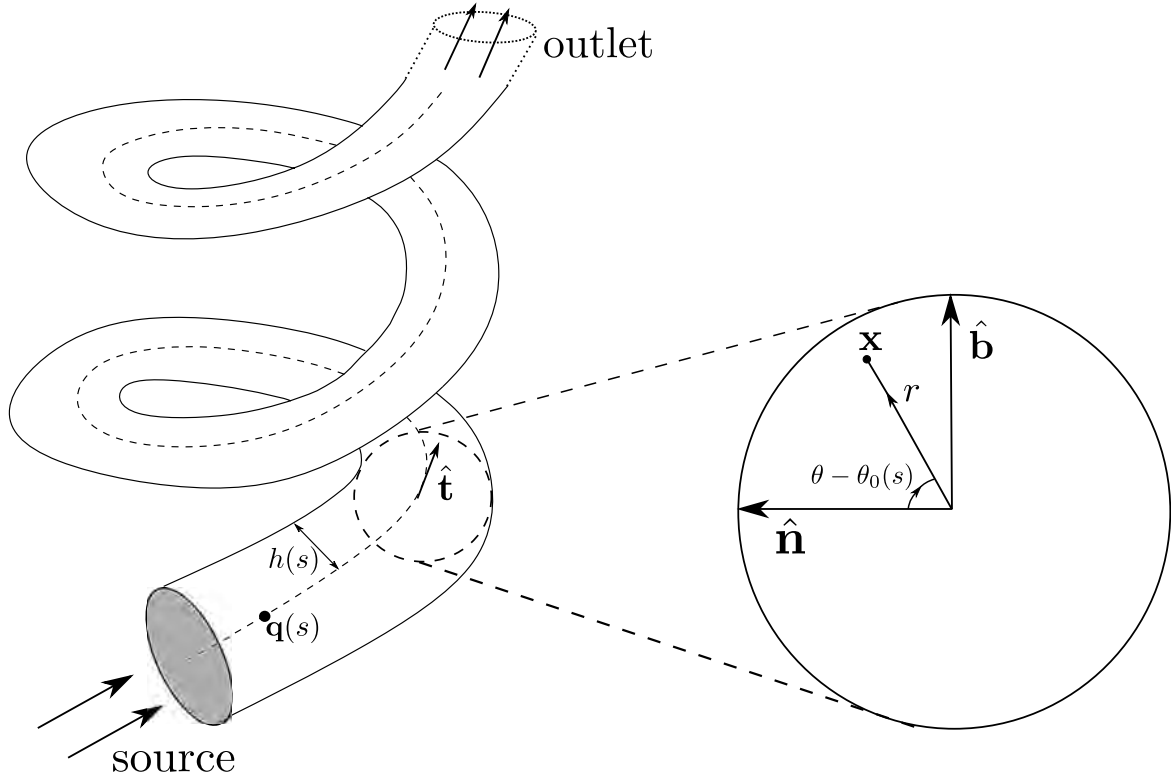


Fig. 3.1 Geometry of the 3D duct

$$-iak\mathbf{U}^a + \nabla P^a = \sum_{b=-\infty}^{\infty} \left(-\mathbf{U}^{a-b} \cdot \nabla \mathbf{U}^b + P^{a-b} \nabla P^b \right). \quad (3.1b)$$

We now proceed using a generalized 3D duct coordinate system first presented by Germano (1982) for the study of flow in helical pipes. This coordinate system allows us to describe a general 3D duct including those with curvature, torsion and axisymmetric variations in duct width. Azimuthal variations in duct width are also possible though not dealt with here.

The duct is described by its centreline $\mathbf{q}(s)$ at arclength s from the inlet of the duct and the radial distance from the centreline $h = h(s)$. The general position vector \mathbf{x} in the duct is given in terms of (s, r, θ) , with $0 \leq r \leq h(s)$ the radial distance and $0 \leq \theta \leq 2\pi$ the azimuthal angle (see figure 3.1)

$$\mathbf{x} = \mathbf{q}(s) + r \cos(\theta - \theta_0) \hat{\mathbf{n}} + r \sin(\theta - \theta_0) \hat{\mathbf{b}} \quad (3.2)$$

where $\hat{\mathbf{n}} = \hat{\mathbf{n}}(s)$ is the normal to the centreline and $\hat{\mathbf{b}} = \hat{\mathbf{b}}(s)$ is the binormal given by $\hat{\mathbf{b}} = \hat{\mathbf{t}} \times \hat{\mathbf{n}}$ for the tangent to the centreline $\hat{\mathbf{t}} = \hat{\mathbf{t}}(s)$. The vectors $\hat{\mathbf{t}}, \hat{\mathbf{n}}$ and $\hat{\mathbf{b}}$ are related

by the Frenet-Serret formulas

$$\frac{d\mathbf{q}}{ds} = \hat{\mathbf{t}}, \quad \frac{d\hat{\mathbf{t}}}{ds} = \kappa \hat{\mathbf{n}}, \quad \frac{d\hat{\mathbf{n}}}{ds} = -\kappa \hat{\mathbf{t}} + \tau \hat{\mathbf{b}}, \quad \frac{d\hat{\mathbf{b}}}{ds} = -\tau \hat{\mathbf{n}} \quad (3.3a, b, c, d)$$

where $\kappa = \kappa(s)$ is the local curvature of the duct and $\tau = \tau(s)$ is the torsion. If one considers the metric $d\mathbf{x} \cdot d\mathbf{x}$ of this coordinate system, one finds cross-term differentials. This implies the coordinate system is *not* orthogonal. To get around this, following Germano, we introduce a phase shift $\theta_0 = \theta_0(s)$ to the azimuthal angle (see equation (3.2)) such that $\theta'_0 = \tau$. With this, the cross-term differentials vanish and the metric reduces to

$$d\mathbf{x} \cdot d\mathbf{x} = (1 - \kappa r \cos \phi)^2 ds^2 + dr^2 + r^2 d\theta \quad (3.4)$$

with $\phi = \theta - \theta_0$. As a result, we have an orthogonal coordinate system and as such do not need to distinguish between covariant and contravariant bases. The Lamé coefficients can be read off from the metric, and the corresponding basis vectors can be read from the differential $d\mathbf{x}$. They are

$$h_s = 1 - \kappa r \cos \phi, \quad \mathbf{e}_s = \hat{\mathbf{t}}, \quad (3.5a)$$

$$h_r = 1, \quad \mathbf{e}_r = \cos \phi \hat{\mathbf{n}} + \sin \phi \hat{\mathbf{b}}, \quad (3.5b)$$

$$h_\theta = r, \quad \mathbf{e}_\theta = -\sin \phi \hat{\mathbf{n}} + \cos \phi \hat{\mathbf{b}}, \quad (3.5c)$$

From these the expressions for ∇ can be calculated. Letting $\mathbf{U}^a = U^a \mathbf{e}_s + V^a \mathbf{e}_r + W^a \mathbf{e}_\theta$ equations (2.14a) and (2.14b) become

$$\begin{aligned} & -iakP^a + \left\{ \frac{1}{1 - \kappa \cos \phi} \frac{\partial U^a}{\partial s} \right\} + \left\{ \frac{\partial V^a}{\partial r} + \frac{1}{r} V^a \right\} - \frac{\kappa \cos \phi}{1 - \kappa r \cos \phi} V^a + \left\{ \frac{1}{r} \frac{\partial W^a}{\partial \theta} + \frac{\kappa \sin \phi}{1 - \kappa r \cos \phi} W^a \right\} \\ &= \sum_{b=-\infty}^{\infty} \left(-ibkP^{a-b}P^b - ibkU^{a-b}U^b - ibkV^{a-b}V^b - ibkW^{a-b}W^b - \frac{B}{2A} iakP^{a-b}P^b \right), \end{aligned} \quad (3.6a)$$

$$\begin{aligned} & -iakU^a + \frac{1}{1 - \kappa r \cos \phi} \frac{\partial P^a}{\partial s} \\ &= \sum_{b=-\infty}^{\infty} \left(\frac{-U^{a-b}}{1 - \kappa r \cos \phi} \frac{\partial U^b}{\partial s} - \frac{V^{a-b}}{r} \frac{\partial U^b}{\partial r} - \frac{W^{a-b}}{r} \frac{\partial U^b}{\partial \theta} \right. \\ & \quad \left. + \frac{\kappa \cos \phi}{1 - \kappa r \cos \phi} U^{a-b}V^b - \frac{\kappa \sin \phi}{1 - \kappa r \cos \phi} U^{a-b}W^b + ibkP^{a-b}U^b \right), \end{aligned} \quad (3.6b)$$

$$\begin{aligned}
& -\mathrm{i}akV^a + \frac{\partial P^a}{\partial r} \\
= & \sum_{b=-\infty}^{\infty} \left(\frac{-U^{a-b}}{1-\kappa r \cos \phi} \frac{\partial V^b}{\partial s} - V^{a-b} \frac{\partial V^b}{\partial r} - \frac{W^{a-b}}{r} \frac{\partial V^b}{\partial \theta} \right. \\
& \left. - \frac{\kappa \cos \phi}{1-\kappa r \cos \phi} U^{a-b} U^b + \frac{W^{a-b} W^b}{r} + \mathrm{i}bk P^{a-b} V^b \right), \quad (3.6c)
\end{aligned}$$

$$\begin{aligned}
& -\mathrm{i}akW^a + \frac{1}{r} \frac{\partial P^a}{\partial \theta} \\
= & \sum_{b=-\infty}^{\infty} \left(\frac{-U^{a-b}}{1-\kappa r \cos \phi} \frac{\partial W^b}{\partial s} - V^{a-b} \frac{\partial W^b}{\partial r} - \frac{W^{a-b}}{r} \frac{\partial W^b}{\partial \theta} \right. \\
& \left. + \frac{\kappa \sin \phi}{1-\kappa r \cos \phi} U^{a-b} U^b - \frac{W^{a-b} V^b}{r} + \mathrm{i}bk P^{a-b} W^b \right). \quad (3.6d)
\end{aligned}$$

We now proceed (following the work of Félix and Pagneux, 2002) by expanding the P^a, U^a, V^a and W^a about a basis of straight cylindrical duct modes ψ_α satisfying the hard walled boundary condition. Note that this method (as with the 2D case) differs from that presented by Félix and Pagneux as we expand all the velocity modes (including the transverse modes) about the duct basis *before* eliminating them, as opposed to eliminating the V^a and W^a first and then projecting the resulting equations into the modal basis. As discussed in our previous chapter, these methods are equivalent. The advantage of projecting onto the modal basis first comes from algebraic simplicity and ease of applying the correct boundary conditions to the second order terms.

The Fourier harmonics are expanded as follows (with lower indices denoting spatial modal decompositions):

$$\begin{aligned}
P^a & = \sum_{\alpha=0}^{\infty} P_\alpha^a(s) \psi_\alpha(\textcolor{red}{s}, r, \theta), \quad U^a = \sum_{\alpha=0}^{\infty} U_\alpha^a(s) \psi_\alpha(\textcolor{red}{s}, r, \theta), \\
V^a & = \sum_{\alpha=0}^{\infty} V_\alpha^a(s) \psi_\alpha(\textcolor{red}{s}, r, \theta), \quad W^a = \sum_{\alpha=0}^{\infty} W_\alpha^a(s) \psi_\alpha(\textcolor{red}{s}, r, \theta)
\end{aligned}$$

The ψ satisfy Helmholtz's equation in cylindrical polar coordinates (with eigenvalues λ_α)

$$\frac{1}{r} \frac{\partial}{\partial r} \left(r \frac{\partial \psi_\alpha}{\partial r} \right) + \frac{1}{r^2} \frac{\partial^2 \psi_\alpha}{\partial \theta^2} + \lambda_\alpha^2 \psi_\alpha = 0 \quad \text{只是一个特例而已} \quad (3.7)$$

and can be normalized according to

$$\int_0^{2\pi} \int_0^h \psi_\alpha \psi_\beta r \, dr \, d\theta = \delta_{\alpha\beta} \quad (3.8)$$

and satisfy the no penetration condition on the duct wall

$$\left. \frac{\partial \psi_\alpha}{\partial r} \right|_{r=h} = 0, \quad \forall \theta \quad (3.9)$$

They are given by

$$\psi_\alpha = C_\alpha J_p \left(\frac{j_{pq} r}{h} \right) \cos \left(p\phi - \frac{\xi\pi}{2} \right) \quad (3.10)$$

with normalization factor given by

$$C_\alpha = \begin{cases} \frac{1}{\sqrt{\pi h^2 J_0^2(j_{0q})}} & p = 0 \\ \frac{1}{\sqrt{\frac{\pi h^2}{2} \left(1 - \frac{p^2}{j_{pq}^2} \right) J_p^2(j_{pq})}} & p > 0 \end{cases} \quad (3.11)$$

and eigenvalues

$$\lambda_\alpha = \frac{j_{pq}}{h} \quad (3.12)$$

Here, J_p denotes the ordinary Bessel function of the first kind and j_{pq} denotes the q^{th} zero of the derivative of $J_p(r)$, noting that $j_{00} = 0$ (corresponding to plane wave modes) and $j_{0q} > 0$ for $q > 0$. The index α maps to the triplet of integers (p, q, ξ) with $p \in [0, \infty)$, $q \in [0, \infty)$ and $\xi = 0, 1$. The basis functions can be well ordered by pairing modes differing only by the ξ index (aside from the $p = 0$ modes which do not come in a pair) and ordering them by the size of their eigenvalues $\lambda_\alpha < \lambda_{\alpha+2}$.

In order to project equations onto the modal basis, we multiply equations (3.6a) – (3.6d) by $r(1 - \kappa r \cos \phi)\psi_\alpha$ and integrate across the cross section of the duct. Special attention must be given to the boundary conditions on the duct wall. The no penetration boundary condition is

$$\mathbf{U}^a \cdot \mathbf{n}^+ = 0, \quad \text{at } r = h, \quad \forall \theta \quad (3.13)$$

where \mathbf{n}^+ is the normal to the duct wall and is given by

$$\underline{\mathbf{n}^+} = -h' \mathbf{e}_s + (1 - \kappa h \cos \phi) \mathbf{e}_r \quad \text{由于流道弯曲所带来的影响} \quad (3.14)$$

This gives a relationship between U^a and V^a at the boundary which can be used to eliminate V^a boundary terms

$$h' U^a = V^a (1 - \kappa h \cos \phi), \quad \text{at } r = h, \quad \forall \theta \quad (3.15)$$

When projecting the mass conservation equation (3.6a), we perform integration by parts to shift the derivatives from the acoustical quantities to the general duct mode ψ_α , using (3.15) to replace V^a with U^a in the resulting boundary terms. Only when there are no derivatives acting on the acoustical quantities do we then expand about the duct modes. So, for example, we have (summation convention assumed from now on)

$$\begin{aligned} \int_0^{2\pi} \int_0^h \frac{\partial V^a}{\partial r} \psi_\alpha r dr d\theta &= \int_0^{2\pi} [V^a \psi_\alpha r]_0^h d\theta - \int_0^{2\pi} \int_0^h V^a \psi_\alpha dr d\theta - \int_0^{2\pi} \int_0^h V^a \frac{\partial \psi_\alpha}{\partial r} r dr d\theta \\ &= \int_0^{2\pi} \left[\frac{rh'}{1 - \kappa h \cos \phi} \psi_\alpha \psi_\beta \right]_0^h d\theta U_\beta^a - \int_0^{2\pi} \int_0^h \psi_\alpha \psi_\beta dr d\theta V_\beta^a \\ &\quad - \int_0^{2\pi} \int_0^h \frac{\partial \psi_\alpha}{\partial r} r \psi_\beta dr d\theta V_\beta^a \end{aligned} \quad (3.16)$$

In doing so, we ensure our modes correctly satisfy the boundary conditions when the duct is not uniform in width (see Pagneux et al., 1996).

At this point we reintroduce a notation used in our previous chapter using Ψ matrices to denote integrals over the duct modes, with square brackets (e.g. $\Psi_{[\alpha]\beta}$) denoting radial derivatives of the particular modes, circular brackets (e.g. $\Psi_{(\alpha)\beta}$) denoting azimuthal derivatives and curly brackets (e.g. $\Psi_{\{\alpha\}\beta}$) denoting longitudinal derivatives. We also use square brackets following the Ψ matrices to denote the kernel of the integral. If none is present then the kernel shall be assumed to be unity. In this notation (3.16) becomes

$$\int_0^{2\pi} \int_0^h \frac{\partial V^a}{\partial r} \psi_\alpha r dr d\theta = \Psi_{[\alpha\beta]} \left[\frac{hh'}{1 - \kappa h \cos \phi} \right] U_\beta^a - \Psi_{\alpha\beta} V_\beta^a - \Psi_{[\alpha]\beta}[r] V_\beta^a \quad (3.17)$$

Using this notation, the mass conservation equation (3.6a) (after much cancellation) becomes

$U_{\beta} * \delta_{\alpha\beta}$

$$\begin{aligned} &\frac{d}{ds} U_\alpha^a - iak\Psi_{\alpha\beta}[r(1 - \kappa r \cos \phi)] P_\beta^a \quad \text{单个UVW都积分为0} \\ &- \Psi_{\{\alpha\}\beta}[r] U_\beta^a - \Psi_{[\alpha]\beta}[r(1 - \kappa r \cos \phi)] V_\beta^a - \Psi_{(\alpha)\beta}[1 - \kappa r \cos \phi] W_\beta^a \\ &= \Psi_{\alpha\beta\gamma}[r(1 - \kappa r \cos \phi)] \left(-ibkP_\beta^{a-b}P_\gamma^b - ibkU_\beta^{a-b}U_\gamma^b - ibkV_\beta^{a-b}V_\gamma^b - ibkW_\beta^{a-b}W_\gamma^b - iak \frac{B}{2A} P_\beta^{a-b} P_\gamma^b \right) \quad (3.18) \end{aligned}$$

The momentum conservation equations prove to be slightly more challenging to project while retaining the correct boundary terms. Considering the RHS of (3.6b)

(after multiplying through by $r(1 - \kappa r \cos \phi)\psi_\alpha$ and integrating), we have three types of terms: derivatives of acoustical quantities from the $\mathbf{U} \cdot \nabla \mathbf{U}$ term, terms arising from the derivatives of the basis vectors in the $\mathbf{U} \cdot \nabla \mathbf{U}$ term and the pressure term.

$$\begin{aligned} \text{RHS} = & \int_0^{2\pi} \int_0^h \left(-r U^{a-b} \frac{\partial U^b}{\partial s} - r(1 - \kappa r \cos \phi) V^{a-b} \frac{\partial U^b}{\partial r} - (1 - \kappa r \cos \phi) W^{a-b} \frac{\partial U^b}{\partial \theta} \right. \\ & + \kappa r \cos \phi U^{a-b} V^b - \kappa r \sin \phi U^{a-b} W^b \\ & \left. + i b k r (1 - \kappa r \cos \phi) P^{a-b} U^b \right) \psi_\alpha \, dr \, d\theta \end{aligned} \quad (3.19)$$

The second two sets of terms are trivial to evaluate. For the first set, we integrate by parts to obtain four new sets of terms: boundary terms, terms involving the derivative of ψ_α , terms with a factor $\psi_\alpha U^b$ and a term arising from the longitudinal derivative:

$$\begin{aligned} & \int_0^{2\pi} \int_0^h \left(-r U^{a-b} \frac{\partial U^b}{\partial s} - r(1 - \kappa r \cos \phi) V^{a-b} \frac{\partial U^b}{\partial r} - (1 - \kappa r \cos \phi) W^{a-b} \frac{\partial U^b}{\partial \theta} \right) \psi_\alpha \, dr \, d\theta \\ &= \int_0^{2\pi} h' h [U^{a-b} U^b \psi_\alpha]_{r=h} \, d\theta - \int_0^{2\pi} \left[h(1 - \kappa h \cos \phi) V^{a-b} U^b \psi_\alpha \right]_{r=h} \stackrel{=0}{d\theta} \\ & \quad - \int_0^h \left[(1 - \kappa r \cos \phi) W^{a-b} U^b \psi_\alpha \right]_0^{2\pi} \, dr \\ &+ \int_0^{2\pi} \int_0^h \left(\frac{\partial \psi_\alpha}{\partial s} U^{a-b} U^b + r(1 - \kappa r \cos \phi) \frac{\partial \psi_\alpha}{\partial r} V^{a-b} U^b \right. \\ & \quad \left. + (1 - \kappa r \cos \phi) \frac{\partial \psi_\alpha}{\partial \theta} W^{a-b} U^b \right) \, dr \, d\theta \\ &+ \int_0^{2\pi} \int_0^h \left(r \frac{\partial U^{a-b}}{\partial s} + \frac{\partial}{\partial r} \left(r(1 - \kappa r \cos \phi) V^{a-b} \right) \right. \\ & \quad \left. + \frac{\partial}{\partial \theta} \left((1 - \kappa r \cos \phi) W^{a-b} \right) \right) U^b \psi_\alpha \, dr \, d\theta \\ & - \frac{\partial}{\partial s} \left(\int_0^{2\pi} \int_0^h U^{a-b} U^b \psi_\alpha r \, dr \, d\theta \right) \end{aligned} \quad (3.20)$$

The boundary terms vanish—the first two cancel using (3.15), the third vanishes by periodicity. In the terms with ψ_α derivatives, we can now explicitly expand our acoustical quantities as a series of duct modes as no derivatives act on them. The third set of terms with factor $U^b \psi_\alpha$ can be simplified by replacing the terms in the bracket with $i(a - b)kr(1 - \kappa r \cos \phi)P^{a-b}$ using the LHS of (3.6a). The term arising from the

longitudinal derivative can also be expanded about the duct modes

$$\frac{\partial}{\partial s} \left(\int_0^{2\pi} \int_0^h U^{a-b} U^b \psi_\alpha r dr d\theta \right) = \frac{\partial}{\partial s} (\Psi_{\alpha\beta\gamma}[r]) U_\beta^{a-b} U_\gamma^b + \Psi_{\alpha\beta\gamma}[r] \left(\frac{dU_\beta^{a-b}}{ds} U_\gamma^b + U_\beta^{a-b} \frac{dU_\gamma^b}{ds} \right) \quad (3.21)$$

Putting this all together (3.6b) becomes

$$\begin{aligned} & \frac{d}{ds} P_\alpha^a - iak\Psi_{\alpha\beta}[r(1 - \kappa r \cos \phi)] U_\beta^a - \left(\Psi_{[\alpha\beta]}[hh'] + \Psi_{\{\alpha\}\beta}[r] \right) P_\beta^a \\ &= iak\Psi_{\alpha\beta\gamma}[r(1 - \kappa r \cos \phi)] P_\beta^{a-b} U_\gamma^b \\ &+ \Psi_{\{\alpha\}\beta\gamma}[r] U_\beta^{a-b} U_\gamma^b + \Psi_{[\alpha]\beta\gamma}[r(1 - \kappa r \cos \phi)] V_\beta^{a-b} U_\gamma^b + \Psi_{(\alpha)\beta\gamma}[1 - \kappa r \cos \phi] W_\beta^{a-b} U_\gamma^b \\ &+ \kappa\Psi_{\alpha\beta\gamma}[r \cos \phi] U_\beta^{a-b} V_\gamma^b - \kappa\Psi_{\alpha\beta\gamma}[r \sin \phi] U_\beta^{a-b} W_\gamma^b \\ &- \frac{\partial}{\partial s} (\Psi_{\alpha\beta\gamma}[r]) U_\beta^{a-b} U_\gamma^b - \Psi_{\alpha\beta\gamma}[r] \left(\frac{dU_\beta^{a-b}}{ds} U_\gamma^b + U_\beta^{a-b} \frac{dU_\gamma^b}{ds} \right) \end{aligned} \quad (3.22)$$

Identical steps can be performed on equations (3.6c) and (3.6d) to obtain

$$\begin{aligned} & - iak\Psi_{\alpha\beta}[r(1 - \kappa r \cos \phi)] V_\beta^a + \left(\Psi_{[\alpha\beta]}[h(1 - \kappa h \cos \phi)] - \Psi_{[\alpha]\beta}[r(1 - \kappa r \cos \phi)] - \Psi_{\alpha\beta}[1 - 2\kappa r \cos \phi] \right) P_\beta^a \\ &= iak\Psi_{\alpha\beta\gamma}[r(1 - \kappa r \cos \phi)] P_\beta^{a-b} V_\gamma^b \\ &+ \Psi_{\{\alpha\}\beta\gamma}[r] U_\beta^{a-b} V_\gamma^b + \Psi_{[\alpha]\beta\gamma}[r(1 - \kappa r \cos \phi)] V_\beta^{a-b} V_\gamma^b + \Psi_{(\alpha)\beta\gamma}[1 - \kappa r \cos \phi] W_\beta^{a-b} V_\gamma^b \\ &- \kappa\Psi_{\alpha\beta\gamma}[r \cos \phi] U_\beta^{a-b} U_\gamma^b + \Psi_{\alpha\beta\gamma}[1 - \kappa r \cos \phi] W_\beta^{a-b} W_\gamma^b \\ &- \frac{\partial}{\partial s} (\Psi_{\alpha\beta\gamma}[r]) U_\beta^{a-b} V_\gamma^b - \Psi_{\alpha\beta\gamma}[r] \left(\frac{dU_\beta^{a-b}}{ds} V_\gamma^b + U_\beta^{a-b} \frac{dV_\gamma^b}{ds} \right), \end{aligned} \quad (3.23a)$$

$$\begin{aligned} & - iak\Psi_{\alpha\beta}[r(1 - \kappa r \cos \phi)] W_\beta^a - \left(\Psi_{(\alpha)\beta}[1 - \kappa r \cos \phi] + \kappa\Psi_{\alpha\beta}[r \sin \phi] \right) P_\beta^a \\ &= iak\Psi_{\alpha\beta\gamma}[r(1 - \kappa r \cos \phi)] P_\beta^{a-b} W_\gamma^b \\ &+ \Psi_{\{\alpha\}\beta\gamma}[r] U_\beta^{a-b} W_\gamma^b + \Psi_{[\alpha]\beta\gamma}[r(1 - \kappa r \cos \phi)] V_\beta^{a-b} W_\gamma^b + \Psi_{(\alpha)\beta\gamma}[1 - \kappa r \cos \phi] W_\beta^{a-b} W_\gamma^b \\ &+ \kappa\Psi_{\alpha\beta\gamma}[r \sin \phi] U_\beta^{a-b} U_\gamma^b - \Psi_{\alpha\beta\gamma}[1 - \kappa r \cos \phi] W_\beta^{a-b} V_\gamma^b \\ &- \frac{\partial}{\partial s} (\Psi_{\alpha\beta\gamma}[r]) U_\beta^{a-b} W_\gamma^b - \Psi_{\alpha\beta\gamma}[r] \left(\frac{dU_\beta^{a-b}}{ds} W_\gamma^b + U_\beta^{a-b} \frac{dW_\gamma^b}{ds} \right) \end{aligned} \quad (3.23b)$$

We now wish to eliminate the transverse velocity modes from our equations. Using the linear relationships

$$iakV^a = \frac{\partial P^a}{\partial r} \quad (3.24a)$$

$$\text{i}akW^a = \frac{1}{r} \frac{\partial P^a}{\partial \theta} \quad (3.24b)$$

we can establish relationships between the transverse modes and the pressure modes (no summation over a)

$$V_\alpha^a = V_{\alpha\beta}^a P_\beta^a \quad (3.25a)$$

$$W_\alpha^a = W_{\alpha\beta}^a P_\beta^a \quad (3.25b)$$

with

$$V_{\alpha\beta}^a = \frac{1}{\text{i}ak} (\Psi_{[\alpha\beta]}[h] - \Psi_{\alpha\beta} - \Psi_{[\alpha]\beta}[r]) = \frac{1}{\text{i}ak} \Psi_{\alpha[\beta]}[r] \quad (3.26a)$$

$$W_{\alpha\beta}^a = -\frac{1}{\text{i}ak} \Psi_{(\alpha)\beta} = \frac{1}{\text{i}ak} \Psi_{\alpha(\beta)} \quad (3.26b)$$

We also require modal expressions for $\frac{d}{ds}V_\alpha^a$ and $\frac{d}{ds}W_\alpha^a$. We differentiate (3.24a) with respect to s

$$\frac{\partial V^a}{\partial s} = \frac{1}{\text{i}ak} \frac{\partial^2 P^a}{\partial s \partial r} = \frac{\partial}{\partial r} ((1 - \kappa r \cos \phi) U^a) \quad (3.27)$$

where we have used symmetry of mixed partials and the linear expression for $\frac{\partial P^a}{\partial s}$ from (3.6b). Multiplying this expression by $r\psi_\alpha$ and integrating across the cross section of the duct, we obtain

$$\begin{aligned} \frac{d}{ds}V_\alpha^a &= \Psi_{[\alpha\beta]} \left[\frac{hh'^2}{1 - \kappa h \cos \phi} \right] U_\beta^a + \Psi_{\{\alpha\}\beta}[r] V_\beta^a \\ &\quad + \left(\Psi_{[\alpha\beta]}[h(1 - \kappa h \cos \phi)] - \Psi_{\alpha\beta}[1 - \kappa r \cos \phi] - \Psi_{[\alpha]\beta}[r(1 - \kappa r \cos \phi)] \right) U_\beta^a \end{aligned} \quad (3.28)$$

Similarly for W^a , differentiating (3.24b) and substituting the linear expression for $\frac{\partial P^a}{\partial s}$ from (3.6b)

$$\frac{\partial W^a}{\partial s} = \frac{1}{\text{i}ak} \frac{1}{r} \frac{\partial^2 P^a}{\partial s \partial \theta} = \frac{1}{r} \frac{\partial}{\partial \theta} ((1 - \kappa r \cos \phi) U^a) \quad (3.29)$$

from which one obtains

$$\frac{d}{ds}W_\alpha^a = \Psi_{[\alpha\beta]}[hh'] W_\beta^a + \Psi_{\{\alpha\}\beta} W_\beta^a - \Psi_{(\alpha)\beta}[1 - \kappa r \cos \phi] U_\beta^a \quad (3.30)$$

These can be used to substitute pressure modes for transverse velocity modes in the RHS quadratic terms of (3.18), (3.22), (3.23a) and (3.23b). Equations (3.23a) and (3.23b) can then be used to eliminate the transverse modes from the linear LHS

of equations (3.18) and (3.22) to obtain two equations involving just pressure and longitudinal velocity modes

$$\mathbf{u}' + \mathsf{M}\mathbf{p} + \mathsf{G}\mathbf{u} = \mathcal{A}[\mathbf{u}, \mathbf{u}] + \mathcal{B}[\mathbf{p}, \mathbf{p}] + \mathcal{E}[\mathbf{u}, \mathbf{p}] \quad (3.31a)$$

$$\mathbf{p}' - \mathsf{N}\mathbf{u} - \mathsf{H}\mathbf{p} = \mathcal{C}[\mathbf{u}, \mathbf{p}] + \mathcal{D}[\mathbf{u}, \mathbf{u}] \quad (3.31b)$$

Here, we have switched to the vector notation used in our previous chapter with vectors \mathbf{p} and \mathbf{u} representing the P_α^a and U_α^a respectively. The matrix multiplication is defined as follows

$$(\mathsf{M}\mathbf{p})_\alpha^a = \sum_{\beta=0}^{\infty} \mathsf{M}_{\alpha\beta}^a \mathbf{p}_\beta^a \quad (3.32)$$

The calligraphic quantities are rank 5 tensors (2 upper, 3 lower) which act on the vectors in the following manner

$$(\mathcal{A}[\mathbf{x}, \mathbf{y}])_\alpha^a = \sum_{b=-\infty}^{\infty} \sum_{\beta, \gamma=0}^{\infty} A_{\alpha\beta\gamma}^{ab} X_\beta^{a-b} Y_\gamma^b \quad (3.33)$$

and on matrices as follows

$$(\mathcal{A}[\mathbf{X}, \mathbf{Y}])_{\alpha\beta\gamma}^{ab} = \sum_{\delta, \epsilon=0}^{\infty} A_{\beta\delta\epsilon}^{ab} \mathbf{X}_{\delta\beta}^{a-b} \mathbf{Y}_{\epsilon\gamma}^b \quad (3.34)$$

The matrices and tensors are given by

$$\mathsf{M}_{\alpha\beta}^a = -ik\Psi_{\alpha\beta}[r(1 - \kappa r \cos \phi)] - \Psi_{[\alpha]\delta}[r(1 - \kappa r \cos \phi)] \mathbf{V}_{\delta\beta}^a - \Psi_{(\alpha)\delta}[1 - \kappa r \cos \phi] \mathbf{W}_{\delta\beta}^a \quad (3.35a)$$

$$\mathsf{N}_{\alpha\beta}^a = ik\Psi_{\alpha\beta}[r(1 - \kappa r \cos \phi)] \quad (3.35b)$$

$$\mathsf{G}_{\alpha\beta}^a = -\Psi_{\{\alpha\}\beta}[r] \quad (3.35c)$$

$$\mathsf{H}_{\alpha\beta}^a = -\Psi_{\alpha\{\beta\}}[r] \quad (3.35d)$$

$$\begin{aligned}
\mathcal{A}_{\alpha\beta\gamma}^{ab} = & -ik\Psi_{\alpha\beta\gamma}[r(1-\kappa r \cos \phi)] \\
& - \Psi_{[\alpha]\delta}[r(1-\kappa r \cos \phi)](\mathbf{N}^{-1})_{\delta\epsilon}^a \left(-\Psi_{\epsilon\beta\mu}[r] \left(\Psi_{[\mu\gamma]} \left[\frac{hh'^2}{1-\kappa h \cos \phi} \right] \right. \right. \\
& \left. \left. + \Psi_{[\mu\gamma]}[h(1-\kappa h \cos \phi)] - \Psi_{\mu\gamma}[1-\kappa r \cos \phi] - \Psi_{[\mu]\gamma}[r(1-\kappa r \cos \phi)] \right) \right. \\
& \left. - \kappa\Psi_{\epsilon\beta\gamma}[r \cos \phi] \right) \\
& - \Psi_{(\alpha)\delta}[1-\kappa r \cos \phi](\mathbf{N}^{-1})_{\delta\epsilon}^a \left(\Psi_{\epsilon\beta\mu}[r]\Psi_{(\mu)\gamma}[1-\kappa \cos \phi] + \kappa\Psi_{\epsilon\beta\gamma}[r \sin \phi] \right) \\
\end{aligned} \tag{3.35e}$$

$$\begin{aligned}
\mathcal{B}_{\alpha\beta\gamma}^a = & -\frac{B}{2A}ik\Psi_{\alpha\beta\gamma}[r(1-\kappa r \cos \phi)] - ik\Psi_{\alpha\beta\gamma}[r(1-\kappa r \cos \phi)] \\
& - ik\Psi_{\alpha\beta\gamma}[r(1-\kappa r \cos \phi)][\mathbf{V}, \mathbf{V}] - ik\Psi_{\alpha\beta\gamma}[r(1-\kappa r \cos \phi)][\mathbf{W}, \mathbf{W}] \\
& - \Psi_{[\alpha]\delta}[r(1-\kappa r \cos \phi)](\mathbf{N}^{-1})_{\delta\epsilon}^a \left(\Psi_{\epsilon\beta\gamma}[r][\mathbf{M}, \mathbf{V}] + ik\Psi_{\epsilon\beta\gamma}[r(1-\kappa r \cos \phi)][\mathbf{l}, \mathbf{V}] \right. \\
& \left. + \Psi_{[\epsilon]\beta\gamma}[r(1-\kappa r \cos \phi)][\mathbf{V}, \mathbf{V}] + \Psi_{(\epsilon)\beta\gamma}[1-\kappa r \cos \phi][\mathbf{W}, \mathbf{V}] \right. \\
& \left. + \Psi_{\epsilon\beta\gamma}[1-\kappa r \cos \phi][\mathbf{W}, \mathbf{W}] \right) \\
& - \Psi_{(\alpha)\delta}[1-\kappa r \cos \phi](\mathbf{N}^{-1})_{\delta\epsilon}^a \left(\Psi_{\epsilon\beta\gamma}[r][\mathbf{M}, \mathbf{W}] + ik\Psi_{\epsilon\beta\gamma}[r(1-\kappa r \cos \phi)][\mathbf{l}, \mathbf{W}] \right. \\
& \left. + \Psi_{[\epsilon]\beta\gamma}[r(1-\kappa r \cos \phi)][\mathbf{V}, \mathbf{W}] + \Psi_{(\epsilon)\beta\gamma}[1-\kappa r \cos \phi][\mathbf{W}, \mathbf{W}] \right. \\
& \left. - \Psi_{\epsilon\beta\gamma}[1-\kappa r \cos \phi][\mathbf{W}, \mathbf{V}] \right) \\
\end{aligned} \tag{3.35f}$$

$$\begin{aligned}
\mathcal{C}_{\alpha\beta\gamma}^{ab} = & \Psi_{\alpha\beta\gamma}[r][\mathbf{l}, \mathbf{M}] + \Psi_{\alpha\beta\gamma}[r][\mathbf{M}, \mathbf{l}] + ik\Psi_{\alpha\beta\gamma}[r(1-\kappa r \cos \phi)] \\
& + \Psi_{[\alpha]\beta\gamma}[r(1-\kappa r \cos \phi)][\mathbf{l}, \mathbf{V}] + \Psi_{(\alpha)\beta\gamma}[1-\kappa r \cos \phi][\mathbf{l}, \mathbf{W}] \\
& + \kappa\Psi_{\alpha\beta\gamma}[r \cos \phi][\mathbf{l}, \mathbf{V}] - \kappa\Psi_{\alpha\beta\gamma}[r \sin \phi][\mathbf{l}, \mathbf{W}]
\end{aligned} \tag{3.35g}$$

$$\mathcal{D}_{\alpha\beta\gamma}^{ab} = -\frac{\partial}{\partial s} \left(\Psi_{\alpha\beta\gamma}[r] \right) + \Psi_{\alpha\delta\gamma}[r][\mathbf{G}, \mathbf{l}] + \Psi_{\alpha\beta\gamma}[r][\mathbf{l}, \mathbf{G}] + \Psi_{\{\alpha\}\beta\gamma}[r] \tag{3.35h}$$

$$\begin{aligned}
\mathcal{E}_{\alpha\beta\gamma}^{ab} = & -\Psi_{[\alpha]\delta}[r(1-\kappa r \cos \phi)](\mathbf{N}^{-1})_{\delta\epsilon}^a \left(-\frac{\partial}{\partial s} \left(\Psi_{\epsilon\beta\gamma}[r] \right) [\mathbf{l}, \mathbf{V}] + \Psi_{\epsilon\beta\gamma}[\mathbf{G}, \mathbf{V}] \right. \\
& \left. + \Psi_{\epsilon\beta\gamma}[\mathbf{l}, \mathbf{GV}] + \Psi_{\{\epsilon\}\beta\gamma}[\mathbf{l}, \mathbf{V}] \right) \\
& - \Psi_{(\alpha)\delta}[1-\kappa r \cos \phi](\mathbf{N}^{-1})_{\delta\epsilon}^a \left(-\frac{\partial}{\partial s} \left(\Psi_{\epsilon\beta\gamma}[r] \right) [\mathbf{l}, \mathbf{W}] + \Psi_{\epsilon\beta\gamma}[\mathbf{G}, \mathbf{W}] \right. \\
& \left. - \Psi_{\epsilon\beta\gamma}[\mathbf{l}, \mathbf{HW}] + \Psi_{\{\epsilon\}\beta\gamma}[\mathbf{l}, \mathbf{W}] \right)
\end{aligned} \tag{3.35i}$$

with M, N, A, B and C encoding the curvature of the duct. The terms G, H, D encode the variation in duct diameter as well as the torsion. The term E (which did not appear in the 2D case) encodes variation of diameter and the torsion together with curvature if either of the first two are present.

By separating the Ψ integrals into radial and angular parts the Ψ matrices can be further simplified (see appendix B).

Equations (3.31a) and (3.31b) are identical in form to their 2D counterparts (apart from the addition of E in (3.31a)). As such, the ensuing steps are identical to our previous work and we shall only give a brief outline here.

Due to the presence of evanescent modes, equation (3.31a) and (3.31b) cannot be integrated directly as numerical instabilities arise. To overcome this we define a nonlinear admittance relation relating the pressure and velocity modes

$$\mathbf{u} = \mathbf{Y}\mathbf{p} + \mathcal{Y}[\mathbf{p}, \mathbf{p}] \quad (3.36)$$

with $\mathbf{Y} = \mathbf{Y}(s)$ the linear admittance and $\mathcal{Y} = \mathcal{Y}(s)$ the nonlinear admittance introduced in our previous chapter. These satisfy the following equations

$$\mathbf{Y}' + \mathbf{Y}\mathbf{N}\mathbf{Y} + \mathbf{M} + \mathbf{Y}\mathbf{H} + \mathbf{G}\mathbf{Y} = 0 \quad (3.37)$$

$$\begin{aligned} \mathcal{Y}' + \mathcal{Y}[\mathbf{N}\mathbf{Y}, \mathbf{I}] + \mathcal{Y}[\mathbf{I}, \mathbf{N}\mathbf{Y}] + \mathbf{Y}\mathbf{N}\mathcal{Y} + \mathbf{Y}\mathcal{C}[\mathbf{Y}, \mathbf{I}] - \mathcal{A}[\mathbf{Y}, \mathbf{Y}] - \mathcal{B} \\ + \mathcal{Y}[\mathbf{H}, \mathbf{I}] + \mathcal{Y}[\mathbf{I}, \mathbf{H}] + \mathbf{G}\mathcal{Y} + \mathbf{Y}\mathcal{D}[\mathbf{Y}, \mathbf{Y}] - \mathcal{E}[\mathbf{Y}, \mathbf{I}] = 0 \end{aligned} \quad (3.38)$$

These equations are solved from the outlet to the inlet, applying the appropriate radiation boundary condition at the duct exit. Once \mathbf{Y} and \mathcal{Y} are found throughout the duct, equation (3.36) can then be used to replace the velocity modes with pressure modes in (3.31b) to obtain a numerically stable first order ODE for the pressure modes

$$\mathbf{p}' = \mathbf{N}\mathbf{Y}\mathbf{p} + \mathbf{N}\mathcal{Y}[\mathbf{p}, \mathbf{p}] + \mathcal{C}[\mathbf{Y}\mathbf{p}, \mathbf{p}] + \mathbf{H}\mathbf{p} + \mathcal{D}[\mathbf{Y}\mathbf{p}, \mathbf{Y}\mathbf{p}] \quad (3.39)$$

This equation can be solved from the source to the outlet. As the equation involves the local admittance at each point, the solution includes both forward and backwards propagating waves together with their nonlinear interaction.

3.3 Boundary Condition for an Infinite Uniform Duct Outlet

3.3.1 Torsion Free Outlets

As with the previous chapter, we consider the simplest boundary condition—that of an infinitely long uniform duct outlet. In this outlet we have only outgoing waves and no point inside the duct can be distinguished from another longitudinally. As such, the linear and nonlinear admittance must both be fixed points of their respective ODEs. Due to the same form of the governing equations as with the 2D case, one can refer to section 2.3 in the previous chapter for a complete derivation of the characteristic admittances \mathbf{Y}^\pm and \mathcal{Y}^\pm for an outlet of with zero torsion. These relate the forward and backward propagating modes in a uniform duct section

$$\mathbf{u}^\pm = \mathbf{Y}^\pm + \mathcal{Y}^\pm[\mathbf{p}^\pm, \mathbf{p}^\pm] \quad (3.40)$$

and are also fixed points of the governing ODEs in the corresponding duct section. The linear characteristic admittance is given by

$$\mathbf{Y}^\pm = \pm \mathbf{N}^{-1} \mathbf{V} \Lambda \mathbf{V}^{-1} = \pm i \mathbf{N}^{-1} \sqrt{\mathbf{NM}} \quad (3.41)$$

where

$$\Lambda = \begin{pmatrix} i\lambda_1 & 0 & \cdots \\ 0 & i\lambda_2 & \cdots \\ \vdots & \vdots & \ddots \end{pmatrix} \quad (3.42)$$

with λ_i^2 the eigenvalues of \mathbf{NM} with corresponding eigenvalue matrix $\mathbf{V} = (\mathbf{v}_1, \mathbf{v}_2, \mathbf{v}_3, \dots)$. The λ_i^2 are all real, and their roots are chosen as follows

$$\lambda_i = \begin{cases} (\lambda_i^2)^{1/2} & \lambda_i^2 > 0 \\ i(-\lambda_i^2)^{1/2} & \lambda_i^2 < 0 \end{cases} \quad (3.43)$$

The nonlinear characteristic admittance is given by

$$(\tilde{\mathcal{Y}}^\pm)_{pqr}^{ab} = \frac{(\mathbf{W}^{-1} \mathcal{A}[\mathbf{Y}^\pm \mathbf{V}, \mathbf{Y}^\pm \mathbf{V}] + \mathbf{W}^{-1} \mathcal{B}[\mathbf{V}, \mathbf{V}] - \mathbf{W}^{-1} \mathbf{Y}^\pm \mathcal{C}[\mathbf{Y}^\pm \mathbf{V}, \mathbf{V}])_{pqr}^{ab}}{\pm i \lambda_p^a \pm i \lambda_q^{a-b} \pm i \lambda_r^b} \quad (3.44)$$

where

$$\mathcal{Y}^\pm[\mathbf{x}, \mathbf{y}] = \mathbf{W} \tilde{\mathcal{Y}}^\pm[\mathbf{V}^{-1} \mathbf{x}, \mathbf{V}^{-1} \mathbf{y}] \quad (3.45)$$

and \mathbf{W} is the eigenvalue matrix of $\mathbf{Y}^\pm \mathbf{N}$.

As with the 2D duct, these are applied at the duct outlet and the admittance equations are solved backwards to the inlet.

3.3.2 Boundary Conditions for an Infinite Helical Duct

In the derivation of the characteristic admittances \mathbf{Y}^\pm and \mathcal{Y}^\pm for the 2D duct (and above for zero torsion), we required that the matrices (\mathbf{M} , \mathbf{N} , etc.) and tensors (\mathcal{A} , \mathcal{B} , etc.) were constant so as to have constant eigenvalues and eigenvectors—hence why we are restricted to *uniform* outlets. In three dimensions however, we can have additional matrices and tensors in the governing equations that do not vanish with uniform width yet still remain constant—those introduced by a constant torsion—namely \mathbf{G} , \mathbf{H} , \mathcal{D} and \mathcal{E} . As such it is possible to adapt our method for finding the fixed points of the admittance equations to provide the boundary conditions for an outlet of constant curvature *and* torsion—i.e. a helix.

We begin by considering the linear forms of equations (3.31a) and (3.31b)

$$\begin{pmatrix} \mathbf{u} \\ \mathbf{p} \end{pmatrix}' = \underbrace{\begin{pmatrix} -\mathbf{G} & -\mathbf{M} \\ \mathbf{N} & \mathbf{H} \end{pmatrix}}_{=\mathbf{L}} \begin{pmatrix} \mathbf{u} \\ \mathbf{p} \end{pmatrix} \quad (3.46)$$

This equation can be solved by $\mathbf{u} = \sum \mathbf{v}_i^u e^{\tilde{\lambda}_i s}$ and $\mathbf{p} = \sum \mathbf{v}_i^p e^{\tilde{\lambda}_i s}$ where the vector $\begin{pmatrix} \mathbf{v}_i^u \\ \mathbf{v}_i^p \end{pmatrix}$ is an eigenvector of the block matrix \mathbf{L} with eigenvector $\tilde{\lambda}_i$. If we consider

$$\begin{pmatrix} \mathbf{u} \\ \mathbf{p} \end{pmatrix}'' = \mathbf{L}^2 \begin{pmatrix} \mathbf{u} \\ \mathbf{p} \end{pmatrix} = \begin{pmatrix} (\mathbf{G}^2 - \mathbf{M}\mathbf{N}) & (\mathbf{G}\mathbf{M} - \mathbf{M}\mathbf{H}) \\ (\mathbf{H}\mathbf{N} - \mathbf{N}\mathbf{G}) & (\mathbf{H}^2 - \mathbf{N}\mathbf{M}) \end{pmatrix} \begin{pmatrix} \mathbf{u} \\ \mathbf{p} \end{pmatrix} \quad (3.47)$$

we see that in a torsionless duct ($\mathbf{H} = \mathbf{G} = 0$), \mathbf{L}^2 becomes a block diagonal matrix with diagonal entries $-\mathbf{M}\mathbf{N}$ and $-\mathbf{N}\mathbf{M}$. As such, the eigenvalues of \mathbf{L}^2 come in pairs and are real (remembering that the eigenvalues of $\mathbf{N}\mathbf{M}$ are real). Consequently, we can see that the eigenvalues of \mathbf{L} are either purely real or purely imaginary and come in pairs of opposite sign (assuming no eigenvalues are degenerate). Choosing those of sign corresponding to forwards propagating waves and decaying evanescent waves forms the basis of the method described in 2.3 and above in section 3.3.

When we introduce torsion, we cause bifurcations in the eigenvalues of \mathbf{L} . As the torsion increases purely real eigenvalues collide and create a pair of complex eigenvalues

conjugate to each other. Figure 3.2 illustrates this below the first mode (straight duct) cutoff frequency k_c . The first 34 eigenvalues are taken. The plot of imaginary values clearly illustrates the pair of purely imaginary eigenvalues at $\lambda \approx \pm 2$ we would expect from a straight duct, as well as the new conjugate pairs that arise as torsion is increased. Three of the bifurcations that give rise to these complex eigenvalues can be seen at $\tau \approx 0.06, 0.08, 0.32$ (with more occurring closer to $\tau = 0$) where pairs of real eigenvalues collide and give rise to complex conjugate pairs.

In figure 3.3 we examine the same problem, now with double the frequency, such that we have more modes cut-on. In this case we have a greater number of purely imaginary eigenvalues (as one would expect with a straight duct) in addition to the complex eigenvalues arising from the aforementioned bifurcations. There is also a new bifurcation seen at $\tau = 0.73$ —two purely imaginary eigenvalues collide as τ is increased, briefly producing a pair of real eigenvalues of opposite sign (too small to see in the figure), before these collide again to produce the pair of opposite sign purely imaginary values. This type of bifurcation is more clearly seen in figure 3.4—a closeup for the same duct system (now with triple the original frequency) and taking the first 72 modes. The exotic types of bifurcation that can occur at higher frequencies as torsion is increased is clearly shown.

To contrast, we can produce similar plots varying the curvature κ , this time with zero torsion. In figure 3.5, we plot the eigenvalues of a duct with $h = 1$ and $k = 0.95k_c$, with the first 34 eigenvalues taken. The behaviour is less interesting—the single pair of propagating modes remains up to $\kappa = 1/h$ (at which point the coordinate system becomes singular, corresponding to a cusp in the duct wall). In the straight duct these correspond to forward and backwards propagating plane waves. As κ is increased their phase velocity decreases. The remaining purely real eigenvalues demonstrate splitting—the degenerate eigenvalues in the straight duct corresponding to symmetric/antisymmetric modes (those with sin or cos azimuthal component) become distinct and diverge as κ is increased. This is due to the symmetry breaking of the problem.

The same splitting is observed for the imaginary eigenvalues in figure 3.6 at double the frequency. This intuitively makes sense—the propagating symmetric and antisymmetric modes will have a different phase velocity depending on whether the pressure differential lies in the plane of curvature or orthogonal to it.

Bifurcations can occur as κ is increased. Figure 3.7 is zoomed in plot at three times the frequency of above, with the first 72 eigenvalues considered. Here, we have a pair of purely imaginary eigenvalues colliding to produce a pair of purely real eigenvalues.

Again, this is not surprising—one would expect fewer modes to be able to propagate in ducts of high curvature. This is a curvature cut-off as opposed to the usual duct width cut-off and, as far as the author is aware, is a new phenomenon not previously observed in the literature.

Returning to the problem of boundary conditions for non zero torsion, the eigenvalues of L are not all purely real or purely imaginary and we have waves that decay as they propagate. To further complicate matters, some of the eigenvalues of L come in pairs with $\text{Re}\tilde{\lambda} \leq 0$ and $\text{Im}\tilde{\lambda} \leq 0$ — i.e. waves that propagate in the positive s direction but decay in the negative s direction and vice versa. We must therefore relax either the causality constraint and have waves propagating from infinity or the energy constraint and have waves growing in an unbounded manner as they propagate to infinity. We shall chose the former and relax the causality constraint, picking eigenvalues (and the corresponding eigenvectors) with real part less than (or equal to) 0 to produce a diagonal eigenvalue matrix $\tilde{\Lambda}$ and corresponding eigenvector matrix $\tilde{V} = (\mathbf{v}_1^p, \mathbf{v}_2^p, \mathbf{v}_3^p, \dots)$

Defining Y^H as the characteristic admittance in the infinite helical pipe, we can substitute \mathbf{p} for \mathbf{u} in the linear pressure mode equation

$$\mathbf{p}' = \mathbf{N}\mathbf{u} + \mathbf{H}\mathbf{u} \quad (3.48)$$

to get

$$\tilde{V}\tilde{\Lambda} = \mathbf{N}Y^H\tilde{V} + \mathbf{H}\tilde{V} \quad (3.49)$$

giving the characteristic admittance as

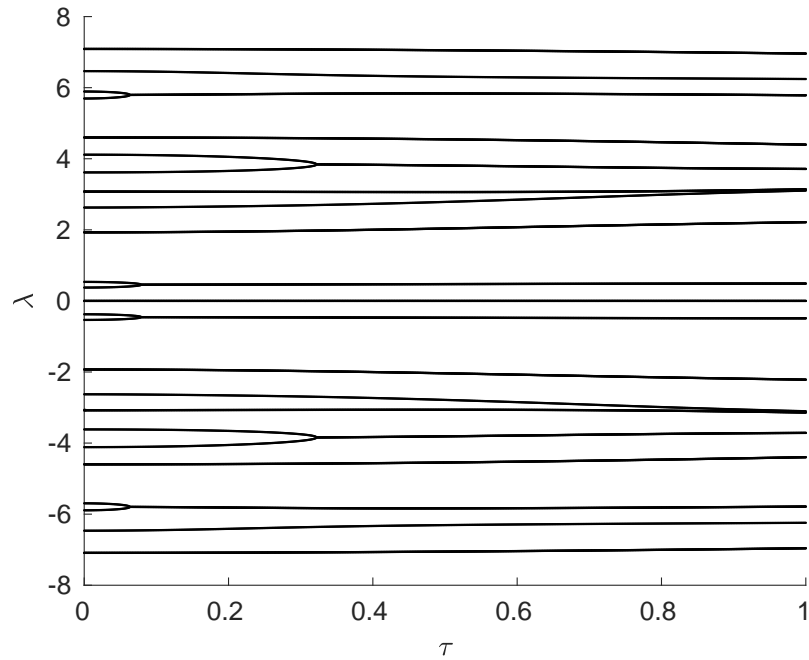
$$Y^H = \mathbf{N}^{-1} (\tilde{V}\tilde{\Lambda}\tilde{V}^{-1} - \mathbf{H}) \quad (3.50)$$

Similarly to the torsion free duct, we define the characteristic nonlinear admittance \mathcal{Y}^H to be the fixed point of its respective ODE

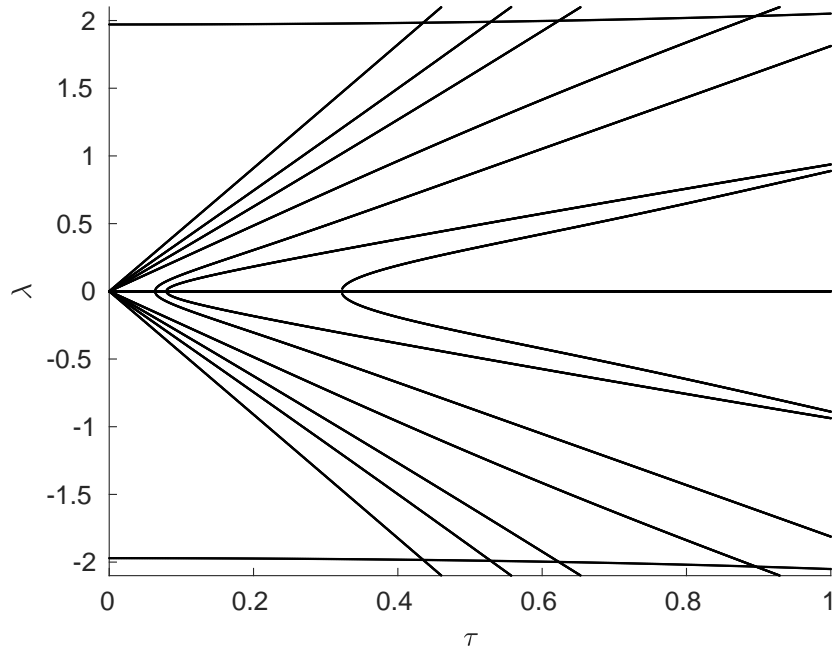
$$\begin{aligned} & \mathcal{Y}^H[\mathbf{N}Y^H, \mathbf{I}] + \mathcal{Y}^H[\mathbf{I}, \mathbf{N}Y^H] + \mathbf{Y}\mathbf{N}\mathcal{Y}^H[\mathbf{I}, \mathbf{I}] + \mathbf{Y}^H\mathcal{C}[Y^H, \mathbf{I}] - \mathcal{A}[Y^H, Y^H] - \mathcal{B}[\mathbf{I}, \mathbf{I}] \\ & + \mathcal{Y}^H[\mathbf{H}, \mathbf{I}] + \mathcal{Y}^H[\mathbf{I}, \mathbf{H}] + \mathbf{G}\mathcal{Y}^H[\mathbf{I}, \mathbf{I}] + \mathbf{Y}^H\mathcal{D}[Y^H, Y^H] - \mathcal{E}[Y^H, \mathbf{I}] = 0 \end{aligned} \quad (3.51)$$

We now define the eigenvector matrix \tilde{W} and diagonal eigenvalue matrix Δ by

$$(Y^H\mathbf{N} + \mathbf{G})\tilde{W} = \tilde{W} = \tilde{W}\Delta \quad (3.52)$$



(a) Real parts



(b) Imaginary parts

Fig. 3.2 Spectrum of L for an infinite helical duct with $\kappa = 2/3$, $h = 1$ and $k = 0.95k_c$ as the torsion τ is varied

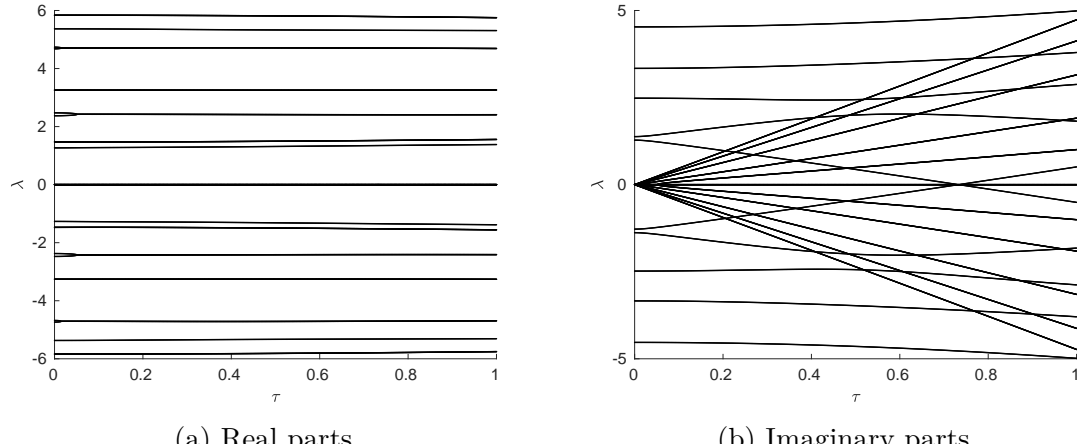


Fig. 3.3 Spectrum of L for an infinite helical duct with $\kappa = 2/3$, $h = 1$ and $k = 2 \times 0.95 k_c$ as the torsion τ is varied

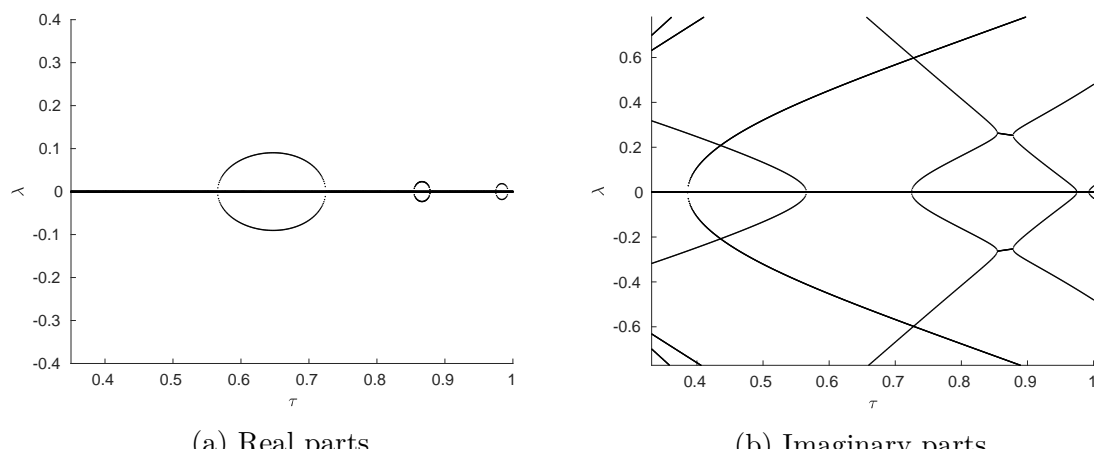


Fig. 3.4 Spectrum of L for an infinite helical duct with $\kappa = 2/3$, $h = 1$ and $k = 3 \times 0.95 k_c$ as the torsion τ is varied

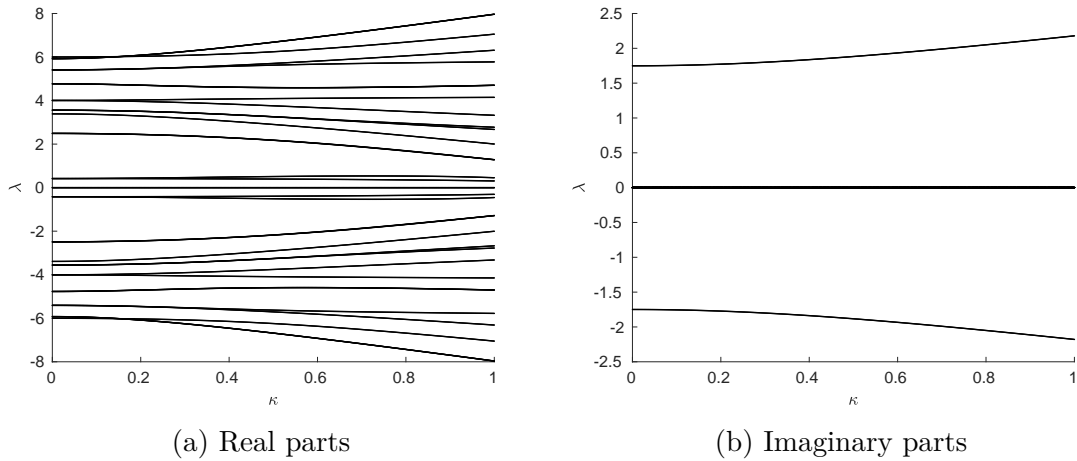


Fig. 3.5 Spectrum of L for an infinite toroidal duct with $h = 1$ and $k = 0.95k_c$ as the curvature κ is varied

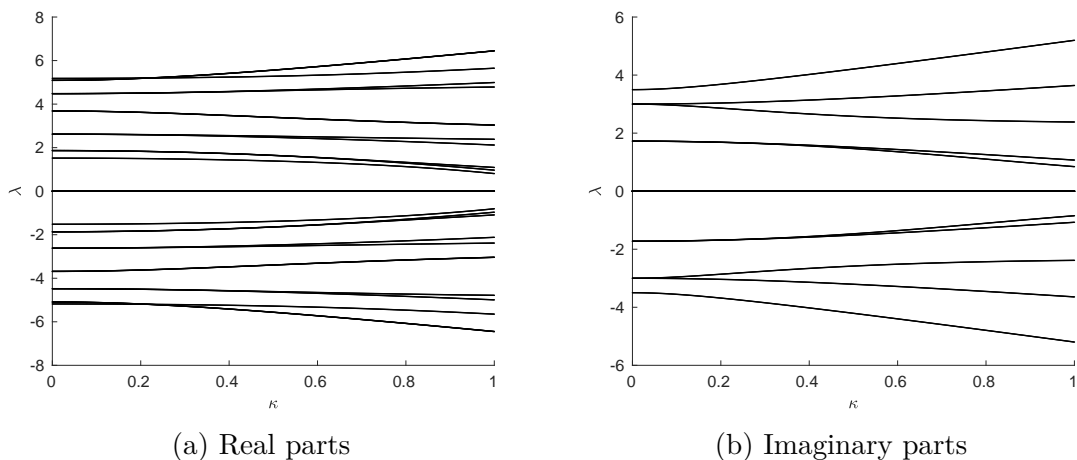


Fig. 3.6 Spectrum of L for an infinite toroidal duct with $h = 1$ and $k = 2 \times 0.95k_c$ as the curvature κ is varied

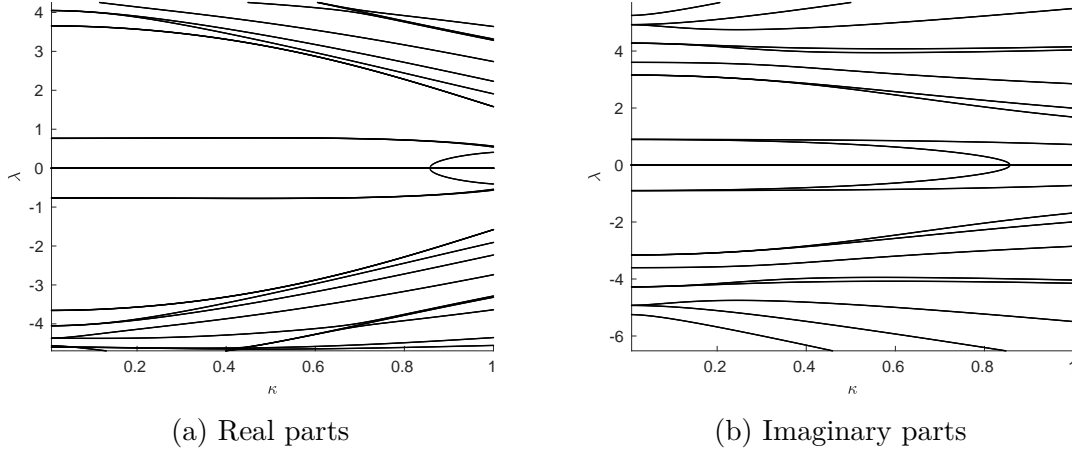


Fig. 3.7 Spectrum of L for an infinite toroidal duct with $h = 1$ and $k = 3 \times 0.95k_c$ as the curvature κ is varied

we act \tilde{W}^{-1} on the left of the above equation, and \tilde{V} on both terms in the square brackets on the right

$$\begin{aligned} & \tilde{W}^{-1}\mathcal{Y}^H[\tilde{V}\tilde{\lambda} - H\tilde{V}, \tilde{V}] + \tilde{W}^{-1}\mathcal{Y}^H[\tilde{V}, \tilde{V}\tilde{\lambda} - H\tilde{V}] + \tilde{W}^{-1}YN\mathcal{Y}^H[\tilde{V}, \tilde{V}] \\ & + \tilde{W}^{-1}YC[Y^H\tilde{V}, \tilde{V}] - \tilde{W}^{-1}A[Y^H\tilde{V}, Y^H\tilde{V}] - \tilde{W}^{-1}B[\tilde{V}, \tilde{V}] \\ & + \tilde{W}^{-1}\mathcal{Y}^H[H\tilde{V}, \tilde{V}] + \tilde{W}^{-1}\mathcal{Y}^H[\tilde{V}, H\tilde{V}] + \tilde{W}^{-1}G\mathcal{Y}^H[\tilde{V}, \tilde{V}] \\ & + \tilde{W}^{-1}Y^H\mathcal{D}[Y^H\tilde{V}, Y^H\tilde{V}] - \tilde{W}^{-1}\mathcal{E}[Y^H\tilde{V}, \tilde{V}] = 0 \end{aligned} \quad (3.53)$$

As with the torsion free duct, we transform the nonlinear admittance

$$\mathcal{Y}^H \mapsto \tilde{W}\tilde{\mathcal{Y}}^H[\tilde{V}^{-1}, \tilde{V}^{-1}] \quad (3.54)$$

to obtain

$$\begin{aligned} & \tilde{\mathcal{Y}}^H[\tilde{\Lambda}, I] + \tilde{\mathcal{Y}}^H[I, \tilde{\Lambda}] + \tilde{\Delta}\tilde{\mathcal{Y}}^H[I, I] \\ & + \tilde{W}^{-1}YC[Y^H\tilde{V}, \tilde{V}] - \tilde{W}^{-1}A[Y^H\tilde{V}, Y^H\tilde{V}] - \tilde{W}^{-1}B[\tilde{V}, \tilde{V}] \\ & + \tilde{W}^{-1}Y^H\mathcal{D}[Y^H\tilde{V}, Y^H\tilde{V}] - \tilde{W}^{-1}\mathcal{E}[Y^H\tilde{V}, \tilde{V}] = 0 \end{aligned} \quad (3.55)$$

from which we can read off the components

$$\left(\tilde{\mathcal{Y}}^H\right)^{ab}_{\alpha\beta\gamma} = \frac{\left(\tilde{W}^{-1} \begin{pmatrix} A[Y^H\tilde{V}, Y^H\tilde{V}] + B[\tilde{V}, \tilde{V}] - Y^H C[Y^H\tilde{V}, \tilde{V}] \\ - Y^H D[Y^H\tilde{V}, Y^H\tilde{V}] + E[Y^H\tilde{V}, \tilde{V}] \end{pmatrix}\right)^{ab}_{\alpha\beta\gamma}}{\lambda_\beta^{a-b} + \lambda_\gamma^b + \Delta_{\alpha\alpha}^a} \quad (3.56)$$

α	(p, q, ξ)	j_{pq}
1	(0,0,0)	0.0000...
2	(1,0,0)	1.8411...
3	(2,0,0)	3.0542...
4	(0,1,0)	3.8317...
\vdots	\vdots	\vdots
α_{\max}		
$\alpha_{\max}+1$	(0,0,1)	0.0000...
$\alpha_{\max}+2$	(1,0,1)	1.8411...
$\alpha_{\max}+3$	(2,0,1)	3.0542...
$\alpha_{\max}+4$	(3,0,1)	4.2011...
\vdots	\vdots	\vdots
$2\alpha_{\max} - \Omega(\alpha_{\max})$		

Table 3.1 Ordering of the modes

and the reverse transformation can be applied to obtain the helical characteristic nonlinear admittance.

The characteristic admittances \mathbf{Y}^H and \mathcal{Y}^H can be used applied at the exit of the duct as a boundary condition for an infinite helical outlet. In the case of zero torsion this method reduces to the method of the previous section though, in practice, for ducts of zero torsion it is simpler computationally to use the previous method.

3.4 Numerical Method

To implement the 3D duct equations requires little extra effort over the 2D problem. Indeed, much of the same code can be reused—only the definitions of the matrices and tensors given in (3.35) as well as the corresponding Ψ matrices must be changed.

One must also choose how to order the vector representations of the modes. For any given truncation α_{\max} , we take $2\alpha_{\max} - \Omega(\alpha_{\max})$ modes ordered such that for $\alpha \mapsto (p, q, \xi)$ we take α_{\max} modes with $\xi = 0$ and $\alpha_{\max} - \Omega(\alpha_{\max})$ modes with $\xi = 1$, ordering both the $\xi = 0$ and $\xi = 1$ modes by the size of j_{pq} —the q^{th} zero of the derivative of the bessel functions J_p (see table 3.1). Here, $\Omega(\alpha_{\max})$ is function counting the number of radial modes less than or equal to α_{\max} .

By ordering the modes in this manner, we clearly separate the symmetric ($\xi = 0$) and antisymmetric modes ($\xi = 1$). For ducts without torsion, the symmetric and antisymmetric modes remain uncoupled, so for sources symmetric in the plane of curvature (including those radially symmetric) our solution only requires the first α_{\max}

modes. Unfortunately, due to the specific derivation required to extend our method to the nonlinear regime, our definitions of the linear matrices and nonlinear tensors are given in terms of matrix products for which the individual matrices actually do couple symmetric/antisymmetric mode, so unlike the work of Félix and Pagneux (2002), we cannot readily ignore all of either the symmetric or antisymmetric components. For example, in the definition of \mathbf{M} we have the term $\Psi_{(\alpha)\delta} \mathbf{W}_{\delta\beta}^\alpha$. Individually both $\Psi_{(\alpha)\delta}$ and $\mathbf{W}_{\delta\alpha}$ map symmetric modes to antisymmetric ones and vice versa, but clearly the product maps (anti)symmetric modes to (anti)symmetric ones. While for this example it is easy to expand the product and choose which modes we wish to retain, in the nonlinear tensors this is not so easy. As such, for the computations we retain all of the modes.

On the other hand, if we have a duct which is radially symmetric together with a radially symmetric source, we can ignore the azimuthal modes and the problem greatly reduces in computational complexity for the same resolution.

As with section 2.5, we use a fixed step RK4 integrator for both the linear and nonlinear admittance equations applying \mathbf{Y}^+ and \mathcal{Y}^+ (or \mathbf{Y}^H and \mathcal{Y}^H for a helical outlet) at the duct exit and solving back to the inlet. We then apply a pressure condition at the inlet and solve using the exponential integrator algorithm of (2.95) applying the numerical viscosity described in section 2.5.1 (when in the nonlinear regime) and, in the case of ducts of increasing width, apply the truncations described in section 2.5.2.

3.5 Results

By taking only the planar modes in a straight duct, the 3D equations reduce to (2.67)—the same equation for the 1D duct derived from the 2D equations. As such, the code produces identical results to section 2.6.1, matching the Blackstock solution almost perfectly. As with the 2D problem we shall also consider uniform curved ducts and straight ducts of varying width, as well as the new problem of helical ducts.

3.5.1 Uniform Curved Ducts

We shall study the same uniform curved duct studied by Félix and Pagneux (2002), illustrating the effects of adding nonlinearity to their problem. The duct consists of a 90° bend with $h\kappa = 2/5$ and wavenumber $kh = 2.4$ and a plane sinusoidal pressure source. Figure 3.8 shows the results. Plots were made taking $\alpha_{\max} = 10$ and $a_{\max} = 10$.

It can be seen that, as with the 2D ducts, the alternative derivation produces nearly identical results to that of Felix and Pagneux's method in the linear case (c.f. figure 2 in their paper). As one would expect with a finite Mach number, we observe wave steepening along the outer edge of the duct—the pressure peaks catch up with the troughs—and, at higher Mach numbers, shock formation. In contrast to the similar problem discussed in section 2.6.4 for a 2D rigid bend, the pressure is much more focussed, with peak amplitude reaching up to $4\times$ the source amplitude along the outside of the duct. In 2D the peak only reached $2\times$ the source amplitude. One may suspect this is due to localization pressure not only in the plane of curvature, but also orthogonal to it—with pressure being more localized to the plane of symmetry through the bend. To examine this in more detail we examine the radial cross section through the point of maximal and minimal amplitude either side of the shock.

Figure 3.9 shows the radial cross sections through the points of greatest amplitude behind the shock and lowest amplitude ahead of the shock at $t = 0$. We can see that, as expected, the regions of extreme pressure become much more localized to the outside of the bend as the Mach number is increased. As such, similar to the 2D duct, we would also expect shock formation to occur over a shorter distance in a 3D curved duct than a straight duct or even a similar 2D curved duct. This shock is localized and whether it can propagate out is dependant on the exit conditions of the duct.

3.5.2 Variable Width Straight Ducts

As with 2D we shall study the problem of the exponential horn to comment on how the high pass filter effects are changed as Mach number is increased. The exponential horn is given by $h(s) = h_0 e^{ms}$ and the solution to Webster's horn equation for such a duct is given by

$$p = e^{-ms} (A e^{ins} + B e^{-ins}) \quad (3.57)$$

where $n^2 = k^2 - m^2$, so that we have cut-off for $k < m = k_h$, the horn horn cut-off.

The particular duct in question was studied by Pagneux et al. (1996) and is the 3D analogue to the one we previously studied in section 2.6.3. The horn is terminated by an infinite straight duct of width $h = 8h_0$, with sinusoidal pressure source of amplitude M at the throat of width h_0 . The length of the horn is $9h_0$. We shall take the frequency to be $k = 0.95k_c$, where $k_c = j_{01}/(8h_0) \approx 3.8317/(8h_0) > 0.95k_c > k_h = \log(8)/(9h_0)$, with k_c the exit cut-off. As such, waves are of sufficient frequency to propagate.

Figure 3.10 displays the results at various Mach numbers, both when pressure is maximal at the source and quarter of a cycle later to show how this peak propagates

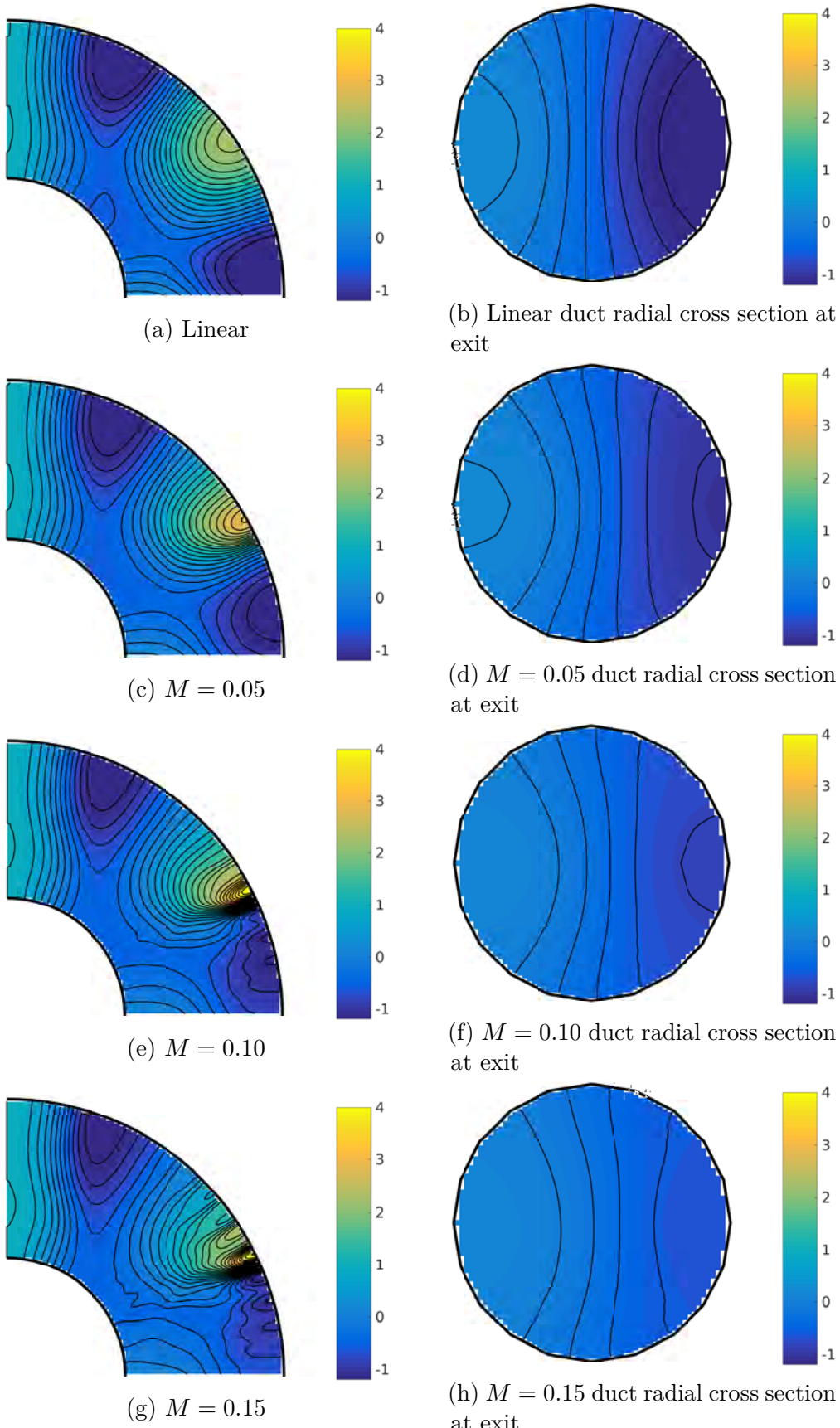


Fig. 3.8 Plots of the pressure in a 90° bend with $h\kappa = 2/5$ and wavenumber $kh = 2.4$ at various Mach numbers. Plots are normalized to the source amplitude. Source at top left.

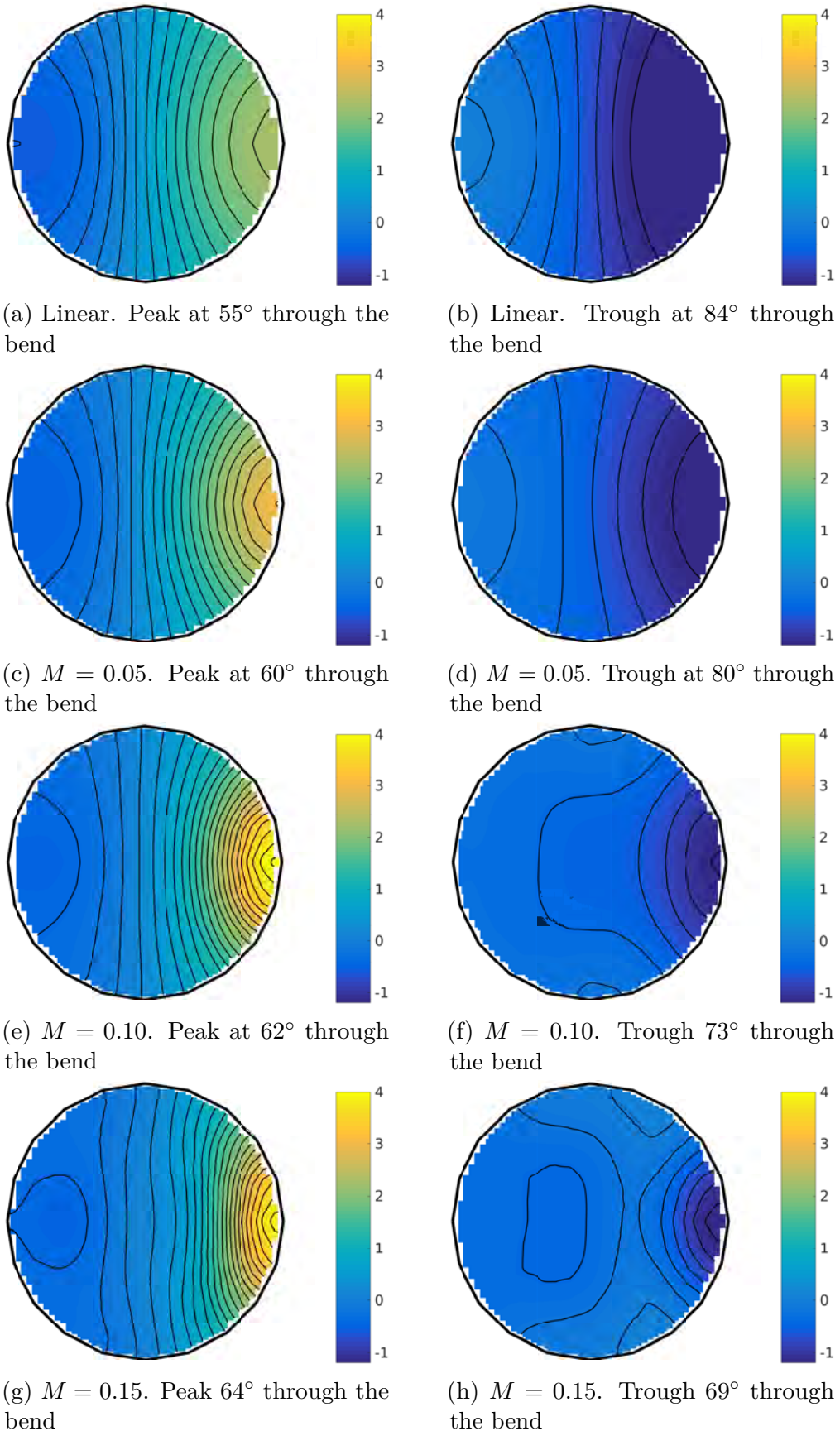


Fig. 3.9 Plots of the same duct as figure 3.8 at various Mach numbers. Plots are radial cross sections taken through the points of maximal and minimal amplitude either side of the shock

through the horn. Plots were produced taking $\alpha_{\max} = 10$ using only the radial modes, and 10 temporal modes. Similarly to the 2D duct we see a larger amount of energy is transmitted out of the horn as the Mach number is increased. As we are above the horn cut-off frequency this is no longer an example of increased tunnelling (as it was in our 2D example). But, as with the 2D example, the transfer of energy to higher frequency harmonics allows for a greater ease of propagation and less reflection.

We can examine the RMS pressure along the centreline at various Mach numbers. The results are shown by figure 3.11. We also compare with the solution of Webster's horn equation. We see that close to the source, Webster's solution, the linear solution and $M = 0.20$ are all in very close agreement. Towards the exit of the horn, where the curvature of the wavefront becomes more important, Webster's solution greatly underestimates the RMS—this is not surprising as the approximation of taking the wave to be planar is poor towards the exit. The linear and nonlinear solutions still stay comparatively close, with the finite amplitude wave having a slightly higher RMS to the exit. Outside the duct the finite amplitude wave has higher RMS compared to the linear solution (increasing monotonically with the Mach number). We should expect this increase in transmission of energy with amplitude to be important in the resonances of brass instruments and shall be discussed in the next chapter.

3.5.3 Linear Acoustics in Helical Ducts

We shall conclude our analysis of 3D ducts by examining ducts whose centreline has uniform curvature and torsion—i.e. helical ducts. To our present knowledge no work has hitherto been done on linear acoustics in a helical duct so we shall address this separately first.

In Cartesian coordinates the helical duct can be described by the centreline

$$\mathbf{q}(s) = \begin{pmatrix} a \cos \tilde{s} \\ a \sin \tilde{s} \\ b \tilde{s} \end{pmatrix} \quad (3.58)$$

where

$$a = \frac{\kappa}{\kappa^2 + \tau^2}, \quad b = \frac{\tau}{\kappa^2 + \tau^2}, \quad \tilde{s} = \sqrt{\kappa^2 + \tau^2} s \quad (3.59)$$

Using the theory of section 3.3.2 we can study the acoustics in an infinitely long helix. We shall choose the duct studied in that section with $\kappa h = 2/3$ and $k = 0.95 k_c = 0.95 j_{10}/h \approx 0.95 \times 1.8412/h$ with a planar sinusoidal pressure source, varying the torsion. Figure 3.12 shows the results, plotting the pressure on the surface of the duct

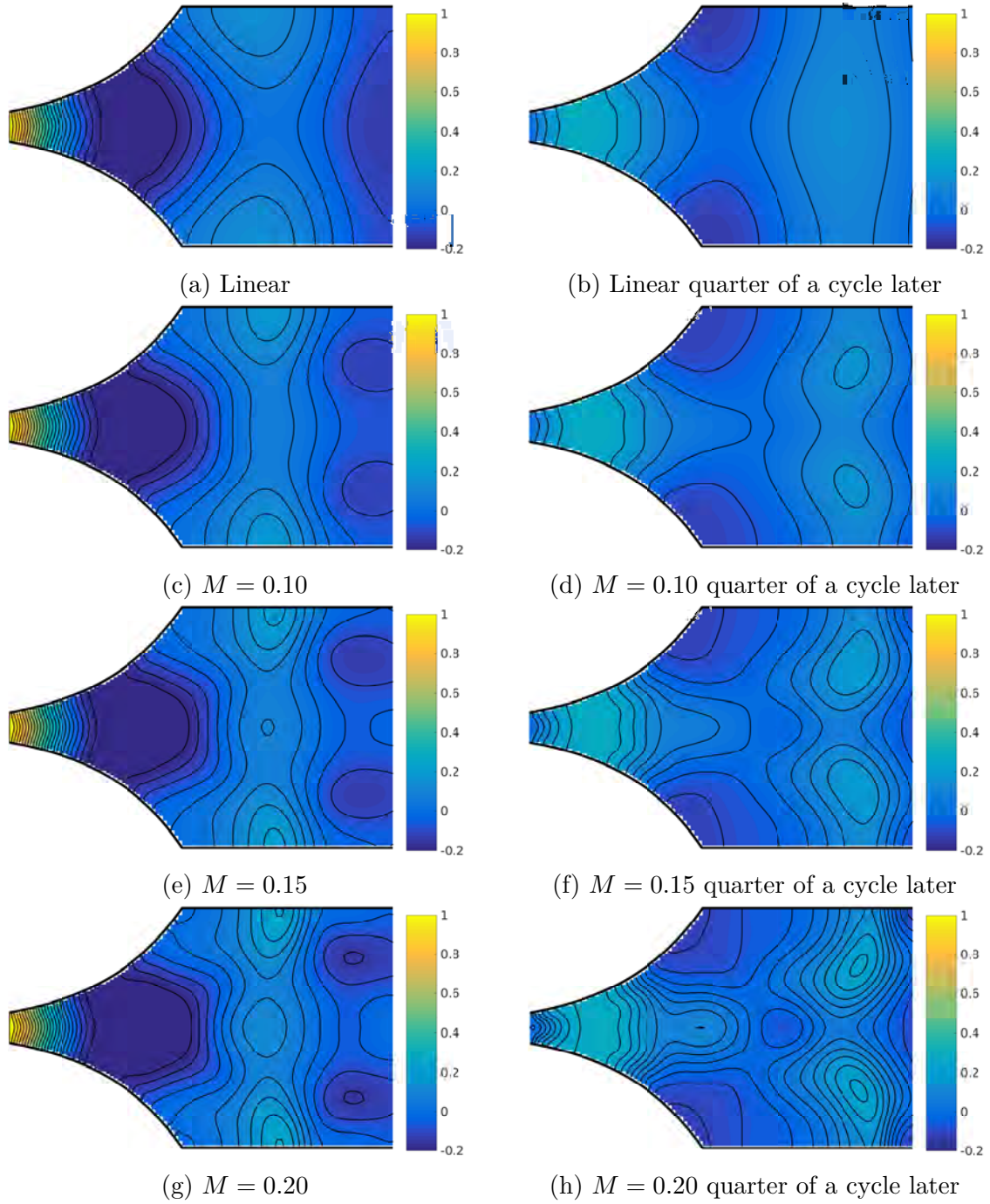


Fig. 3.10 Plots of the pressure cross section through the 3D exponential horn at various Mach numbers. Plots normalized to Mach number.

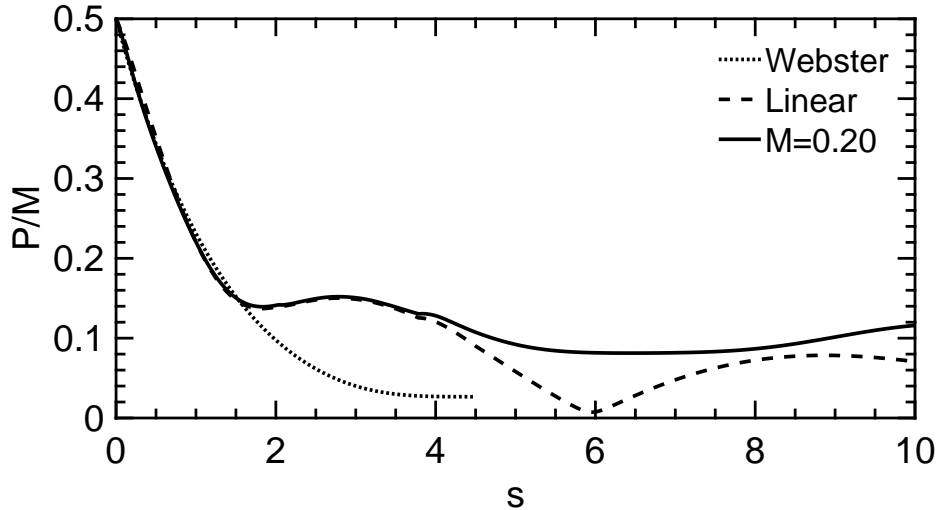


Fig. 3.11 Plots of normalized RMS along the horn centreline. Duct exit is at $s = 4.5$

up to an arc length of three times the wavelength. A radial cross section is also plotted at three times the wavelength for figures (a) (c) and (e). We examine three different torsions: $\tau h = 0.14$ —approximately the lowest torsion that can be taken without the duct self intersecting, $\tau h = 0.20$ —a slightly larger torsion and the maximum torsion for which the code is stable in the nonlinear regime (see the next section) and $\tau h = 1.00$ a significantly larger torsion, greater than the curvature.

For each of the ducts studied, there is not a great deal of difference on the pressure distributions within the duct as torsion is changed. As with a zero curvature duct without torsion, the regions of peak pressure lie on the outside of the bend with a “focussing” effect localising energy to a small region and producing greater maximal amplitude waves compared with the source amplitude. This effect is greater with the helical duct than a torsionless duct and increases as the torsion is increased (though this effect is slight and difficult to see in the plots). When we introduce nonlinearity in the next section, this will become more apparent.

3.5.4 Nonlinear Acoustics in Helical Ducts

We now turn our attention to the same ducts, now including nonlinear terms. Unfortunately, due to what appears to be numerical errors associated with finite truncation, inverting the eigenvector matrix of the linear operator \tilde{V} (c.f. equation (3.50) where the inverse is required) can prove inaccurate for higher frequencies, producing extremely large values which cause numerical instabilities. These errors arise suddenly as τ is increased—we observe growth in the maximal value of \tilde{V}^{-1} over several orders of

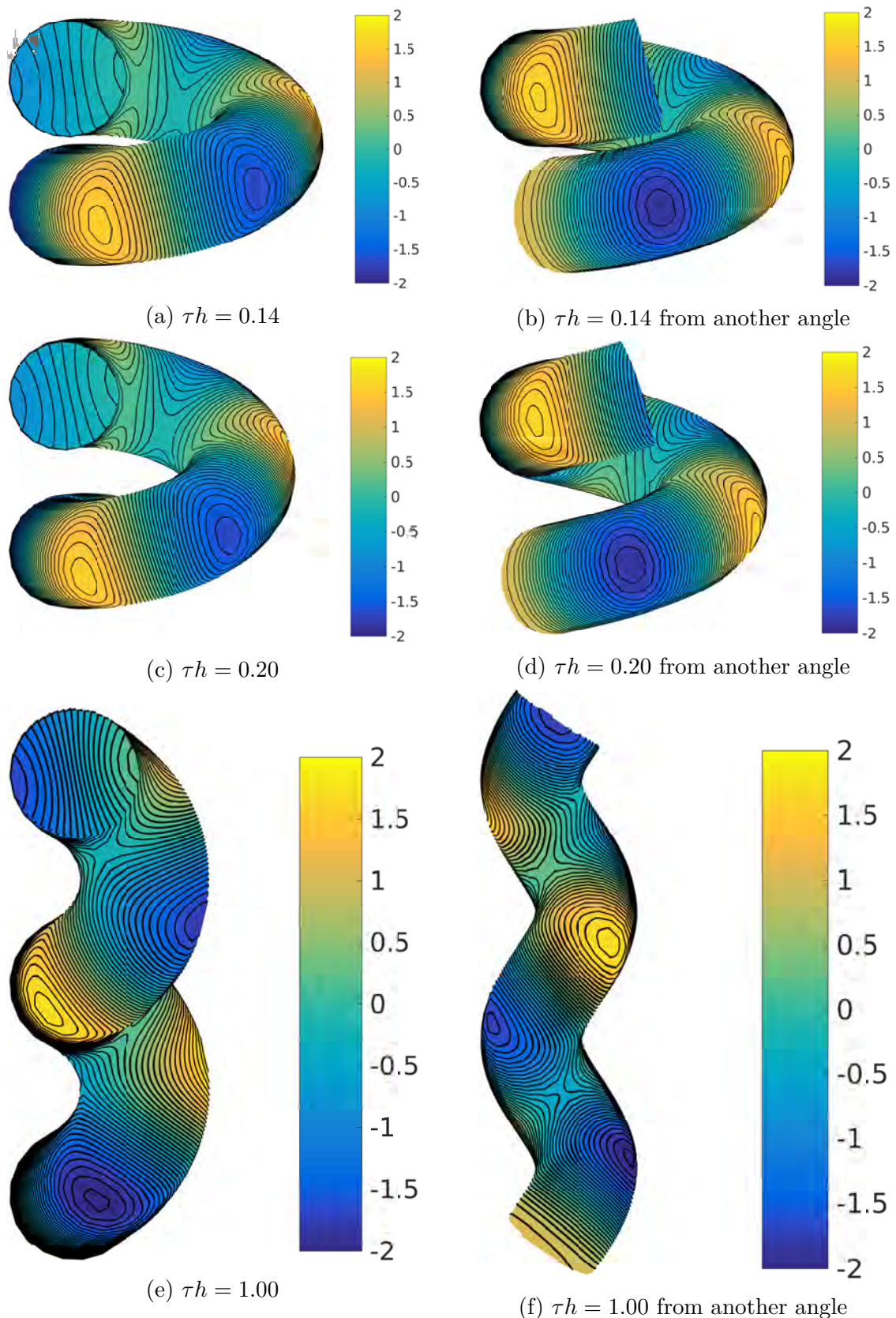


Fig. 3.12 Plots of the pressure distributions on the surface of the infinite helical duct. Linear acoustics. The source is at the bottom of the plots. Pressure normalized to source amplitude.

magnitude as τ is increased by a few percent. This first occurs when $\tau h > 0.2$ for the $a = 3$ harmonic when $\alpha_{\max} = 10$. As the values of τ at which this occurs is dependant on the number of modes taken, we conclude that this is a numerical artefact and not a bifurcation of the eigenvalues. In order to study nonlinearity in the high torsion duct, we must therefore approximate the infinite helical duct to a helical duct with an infinite torsionless duct of the same curvature. The plots are shown in figures 3.13 to 3.15.

We first note that, yet again, we have shock formation, with discontinuities in pressure occurring on the outside of the bend—even for high torsion ducts. We also observe that the focussing effect is far greater when nonlinear effects are taken into account—while the pressure reaches a peak of about 2 times the source pressure in the linear case for $\tau h = 0.14$, when we introduce nonlinearity this goes up to around 2.5 times. The region of high pressure can be seen to be not only more localized longitudinally, but also azimuthally. Though not plotted here, we would expect a radial cross section through the peak to show localization radially too (as with the torsionless curved duct of figure 3.9). As we increase the torsion this nonlinear focussing becomes more apparent. For $\tau h = 1.00$ the peak pressure was around 2 times the input pressure in the linear case (similar to the other ducts), but goes up to 4 times the pressure when nonlinearity is introduced, even for more modest Mach numbers when compared to the other ducts. While these high torsion (relative to curvature) ducts are uncommon in engineering applications (usually torsion will be minimised to save space), it is interesting to note that the torsion is another possible parameter which can be changed to alter acoustical properties of ducts.

3.6 Conclusion

In this chapter we have extended the method to solve for nonlinear acoustics in a general 3D duct with an infinite outlet. Aside from the rather lengthy derivation of the corresponding nonlinear tensors and matrices, much of the work has reduced to the same equations. As a result, with the correct choice of mode ordering, the 3D problem can be solved using all the machinery developed in the previous chapter.

In addition, we have developed a boundary condition for an infinite helical duct outlet revealing some interesting bifurcations of the eigenvalues of the linear operator as the torsion is varied, resulting in complex eigenvalues.

We have applied our method to curved ducts, showing not only localisation radially on the outside of the bend (as with 2D ducts), but also azimuthal localisation. The

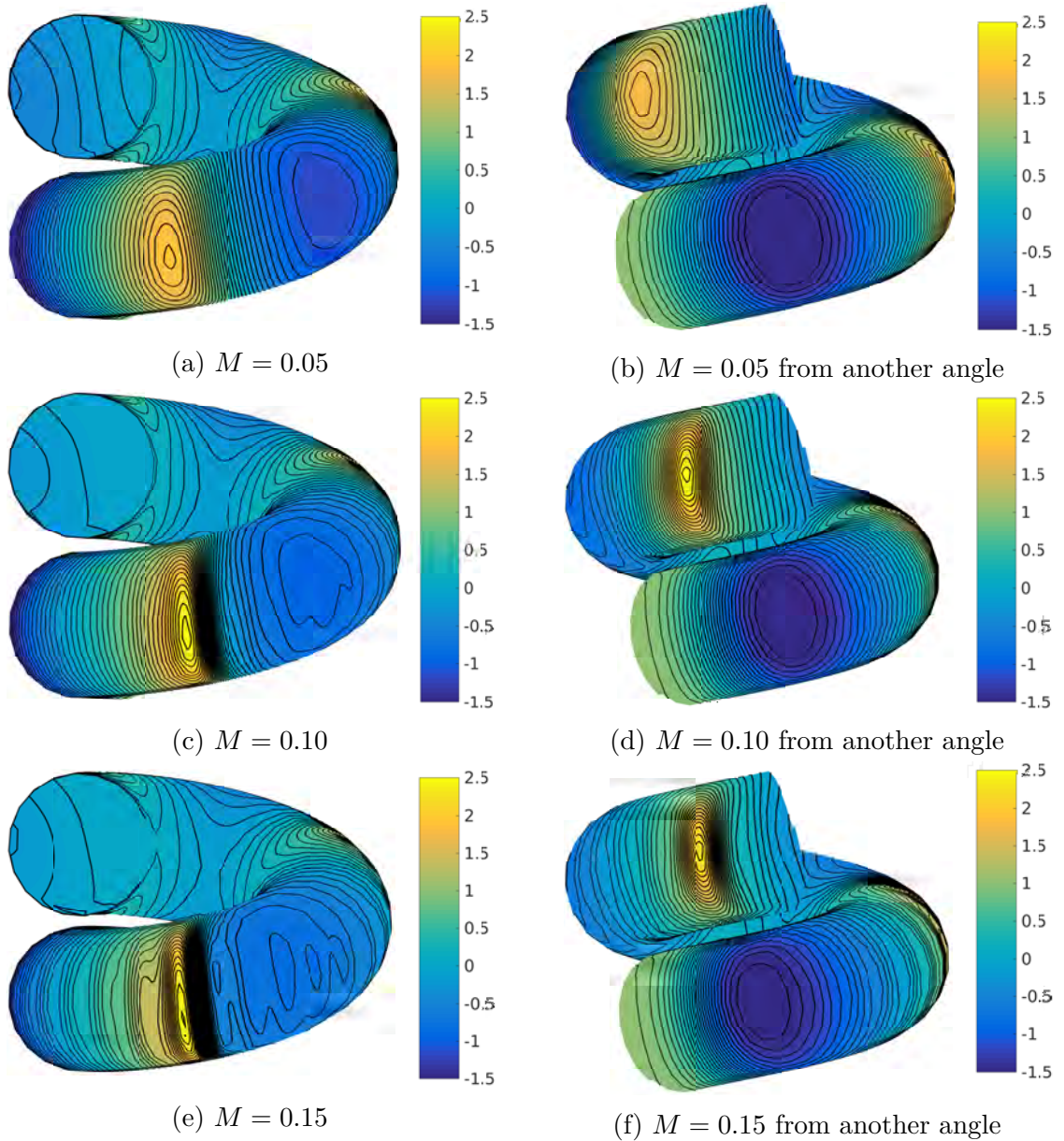


Fig. 3.13 $\tau h = 0.14$. Plots of the pressure distributions on the surface of a helical duct terminated by an infinite torsionless duct. The source is at the bottom of the plots. Pressure normalized to source Mach number.

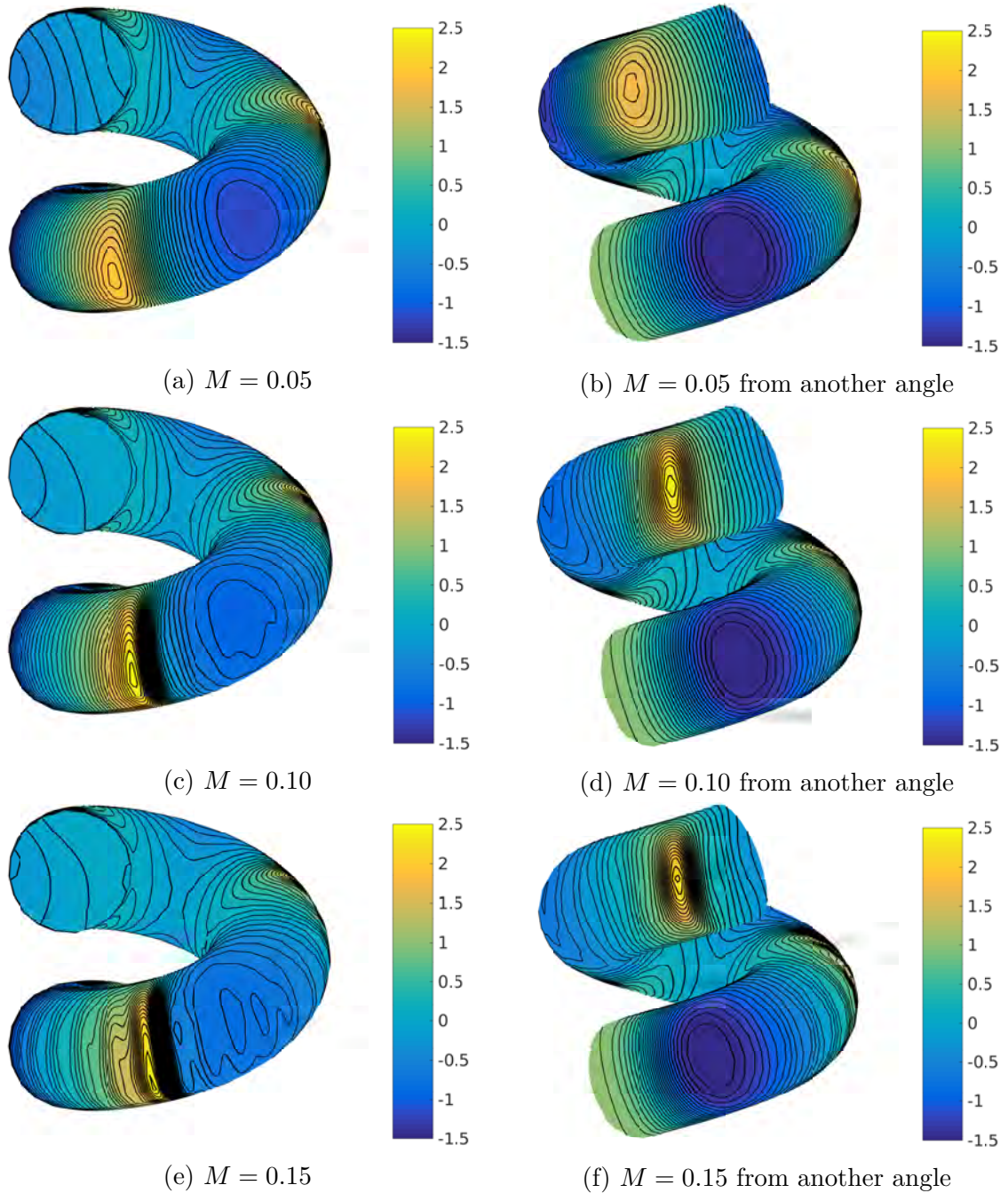


Fig. 3.14 $\tau h = 0.20$. Plots of the pressure distributions on the surface of a helical duct terminated by an infinite torsionless duct. The source is at the bottom of the plots. Pressure normalized to source Mach number.

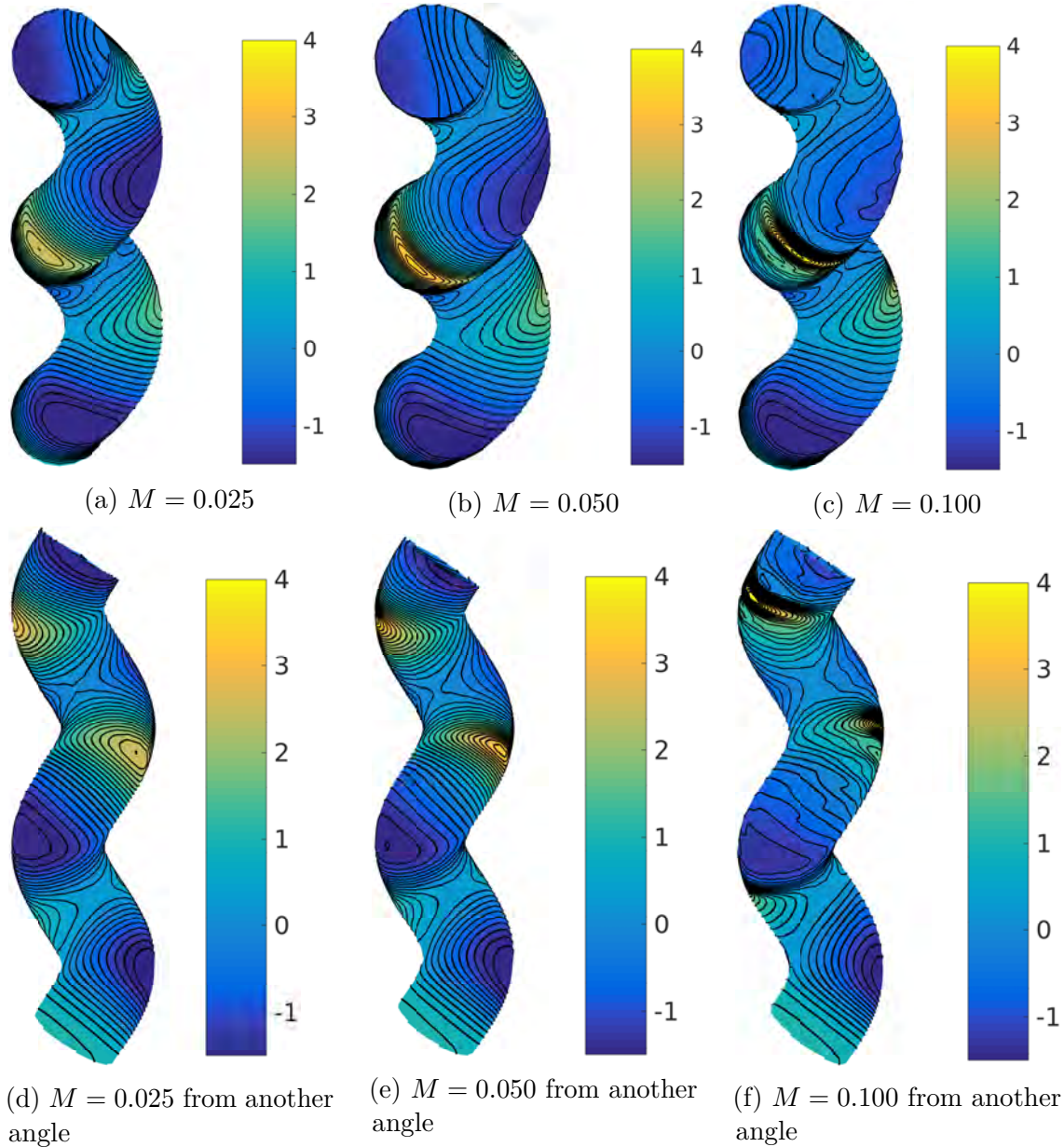


Fig. 3.15 $\tau h = 1.00$. Plots of the pressure distributions on the surface of a helical duct terminated by an infinite torsionless duct. The source is at the bottom of the plots. Pressure normalized to source Mach number.

method has also been applied to the exponential horn showing, as with the 2D duct, that as the Mach number is increased a greater amount of sound is radiated due to harmonic enrichment. Finally, we looked at the helical duct both in the linear and nonlinear regime, both showing stronger amounts of pressure localisation than the curved duct without torsion.

This concludes our study of ducts with an infinite outlet. In the next chapter we shall look at the more realistic scenario of a finite length duct radiating into free space.

Chapter 4

Open Ducts

4.1 Introduction

In this chapter we shall examine a more realistic boundary condition for the ducts—that of an open end termination, radiating into free space. For this chapter we shall be working in three dimensions, using the results of the previous chapter. The open duct boundary condition can be applied to 2D ducts, though this is not done here. In section 4.2, we work up to the open duct boundary condition result by first deriving the simpler and, at first, seemingly unrelated boundary conditions for a baffled duct and a dipole source. Using these two solutions, we produce a boundary condition for the linear and nonlinear admittance approximating radiation into free space. We also provide the method with which to calculate the pressure external to the duct. In section 4.3 we briefly discuss some of the numerical issues that arise with the method. Section 4.4 is a presentation of the analytic Wiener-Hopf solution and comparison with our numerical method, comparing both the resulting reflection coefficient, end correction and a resulting pressure profile. In section 4.5 we present results comparing various aspects of similar ducts with various geometrical properties changed. Cylindrical ducts of different aspect ratios, the effects of adding a bell, conical ducts, curved ducts and helical ducts are all considered, with resonances, radiation patterns and effects of nonlinearity all compared. This is all done from the perspective of musical acoustics where the ducts considered form idealizations of many common wind instruments. An understanding of some basic music theory is helpful but not necessary in this section. To conclude the chapter we look at a scaled model of a trombone in section 4.6.

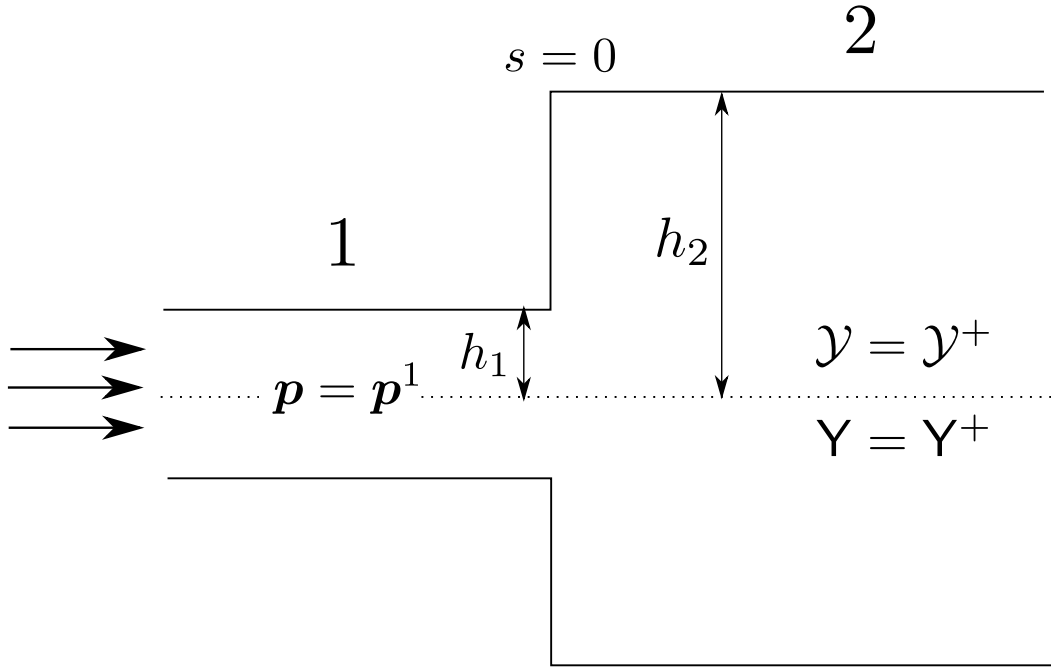


Fig. 4.1 Geometry of the baffled duct

4.2 Governing Equations

4.2.1 Baffled Ducts

We begin our analysis of open ducts with a simpler problem studied by Pagneux et al. (1996)—that of a discontinuity in the duct diameter, going from a smaller diameter h_1 to a larger diameter h_2 at $s = 0$. See figure 4.1. The problem is fully determined by an incoming pressure p^1 before the discontinuity in region 1, and a radiation condition after the discontinuity in region 2. To ensure we only have outgoing waves and decaying evanescent waves, we take $\mathbf{Y}^2 = \mathbf{Y}^+$ and $\mathcal{Y}^2 = \mathcal{Y}^+$ —that is the admittances to be the characteristic admittances in region 2. All of the other quantities are determined from these. We wish to find the admittances in region 1.

At $s = 0_+$ we have the hard walled boundary condition for $h_2 > r > h_1$ giving $u^2 = 0$ for $h_2 > r > h_1$. For $r < h_1$ we have continuity of pressure and normal velocity. That is $p^1 = p^2$ and $u^1 = u^2$ for $r < h_1$. Here, temporal Fourier series can be equated, yielding the same equation for each harmonic. Each harmonic can be expanded about the corresponding basis of straight duct modes for the relevant duct section

$$p^i = \sum_{\alpha=0}^{\infty} \psi_{\alpha}^i P_{\alpha}^i, \quad \text{for } i = 1, 2 \tag{4.1a}$$

$$u^i = \sum_{\alpha=0}^{\infty} \psi_{\alpha}^i U_{\alpha}^i, \quad \text{for } i = 1, 2 \quad (4.1b)$$

with the ψ given in the usual manner

$$\psi_{\alpha}^i = C_{\alpha}^i J_p \left(\frac{j_{pq} r}{h_i} \right) \cos \left(p\phi - \frac{\xi\pi}{2} \right) \quad \text{for } i = 1, 2 \quad (4.2)$$

normalized to the duct width

$$C_{\alpha}^i = \begin{cases} \frac{1}{\sqrt{\pi h_i^2 J_0^2(j_{0q})}} & p = 0 \\ \frac{1}{\sqrt{\frac{\pi h_i^2}{2} \left(1 - \frac{p^2}{j_{pq}^2} \right) J_p^2(j_{pq})}} & p > 0 \end{cases} \quad (4.3)$$

or the analogous 2D versions for a 2D problem.

Equating pressure across the surface $r < h_1$ we obtain

$$P_{\alpha}^1 = \int_{r < h_1} p^2 \psi_{\alpha}^1 dS = \int_{r < h_1} P_{\beta}^2 \psi_{\beta}^2 \psi_{\alpha}^1 dS = \int_{r < h_1} \psi_{\alpha}^1 \psi_{\beta}^2 dS P_{\beta}^2 = F_{\alpha\beta} P_{\beta}^2 \quad (4.4)$$

or, taking all of the harmonics into account and using our previous vector notation

$$\mathbf{p}^1 = \mathsf{F} \mathbf{p}_h^2 \quad (4.5)$$

where the subscript h denotes that this is the pressure in region 2 resulting from the hard walled baffled problem. The matrix F is given by

$$\mathsf{F}_{\alpha\beta}^a = \int_{r < h_1} \psi_{\alpha}^1 \psi_{\beta}^2 dS \quad \forall a \quad (4.6)$$

The integral is taken over the cross section and can be calculated analytically (see appendix B).

Similarly, we can equate the normal velocity across the surface for each of the harmonics, applying the no penetration condition for $h_2 > r > h_1$. At $s = 0$ we have

$$U_{\alpha}^2 = \int_{r < h_2} u^2 \psi_{\alpha}^2 dS = \int_{r < h_1} u^2 \psi_{\alpha}^2 dS = \int_{r < h_1} u^1 \psi_{\alpha}^2 dS = \int_{r < h_1} \psi_{\alpha}^2 \psi_{\beta}^1 dS U_{\beta}^1 = F_{\beta\alpha} U_{\beta}^1 \quad (4.7)$$

or

$$\mathbf{u}_h^2 = \mathsf{F}^T \mathbf{u}_h^1 \quad (4.8)$$

Together, equations (4.5) and (4.8) can be used to relate acoustical quantities from region 1 to region 2 and vice versa.

We now consider the impedance relations between the modes in regions 1 and 2

$$\mathbf{p}^1 = \mathbf{Z}_h^1 \mathbf{u}_h^1 + \mathcal{Z}_h^1[\mathbf{u}_h^1, \mathbf{u}_h^1] \quad (4.9a)$$

$$\mathbf{p}_h^2 = \mathbf{Z}^+ \mathbf{u}_h^2 + \mathcal{Z}^+[\mathbf{u}_h^2, \mathbf{u}_h^2] \quad (4.9b)$$

where $\mathbf{Z}^+ = (\mathbf{Y}^+)^{-1}$ is the characteristic linear impedance and $\mathcal{Z}^+ = -\mathbf{Z}^+ \mathcal{Y}^+[\mathbf{Y}^+, \mathbf{Y}^+]$ is the characteristic nonlinear impedance which comes from the general nonlinear tensor inversion rule

$$\mathcal{Y} = -\mathbf{Y} \mathcal{Z}[\mathbf{Y}, \mathbf{Y}] \Leftrightarrow \mathcal{Z} = -\mathbf{Z} \mathcal{Y}[\mathbf{Z}, \mathbf{Z}] \quad (4.10)$$

which can be derived as follows

$$\begin{aligned} \mathbf{p} &= \mathbf{Z} \mathbf{u} + \mathcal{Z}[\mathbf{u}, \mathbf{u}] \\ &= \mathbf{Z} \mathbf{Y} \mathbf{p} + \mathbf{Z} \mathcal{Y}[\mathbf{p}, \mathbf{p}] + \mathcal{Z}[\mathbf{Y} \mathbf{p}, \mathbf{Y} \mathbf{p}] \end{aligned} \quad (4.11)$$

where, upon equating orders of magnitude and cancelling the pressure modes, the result is obtained. From (4.9a) and (4.9b), using (4.5) and (4.8) we can eliminate \mathbf{u}_h^1 , \mathbf{p}_h^2 and \mathbf{u}_h^2

$$\begin{aligned} \mathbf{p}^1 &= \mathbf{F} \mathbf{p}_h^2 \\ &= \mathbf{F} \mathbf{Z}^+ \mathbf{u}_h^2 + \mathbf{F} \mathcal{Z}^+[\mathbf{u}_h^2, \mathbf{u}_h^2] \\ &= \mathbf{F} \mathbf{Z}^+ \mathbf{F}^T \mathbf{u}_h^1 + \mathbf{F} \mathcal{Z}^+[\mathbf{F}^T \mathbf{u}_h^1, \mathbf{F}^T \mathbf{u}_h^1] \\ &= \mathbf{F} \mathbf{Z}^+ \mathbf{F}^T \mathbf{Y}_h^1 \mathbf{p}^1 + \mathbf{F} \mathbf{Z}^+ \mathbf{F}^T \mathcal{Y}_h^1[\mathbf{p}^1, \mathbf{p}^1] + \mathbf{F} \mathcal{Z}^+[\mathbf{F}^T \mathbf{Y}_h^1 \mathbf{p}^1, \mathbf{F}^T \mathbf{Y}_h^1 \mathbf{p}^1] \end{aligned} \quad (4.12)$$

from which we can take orders of magnitude and cancel off \mathbf{p}^1 . We can do so as \mathbf{p}^1 is a free vector, unlike any of the other acoustical quantities we have eliminated. We obtain

$$\mathbf{Y}_h^1 = (\mathbf{F} \mathbf{Z}^+ \mathbf{F}^T)^{-1} \quad (4.13a)$$

$$\mathcal{Y}_h^1 = -\mathbf{Y}_h^1 \mathbf{F} \mathcal{Z}^+[\mathbf{F}^T \mathbf{Y}_h^1, \mathbf{F}^T \mathbf{Y}_h^1] \quad (4.13b)$$

This gives the admittance in region 1 at the duct exit. We can use the admittance equations to solve back from $s = 0_-$, taking into account any variations in the shape of the duct, to the source to find the admittance through the entire system. The pressure can then be solved for. This is the generalisation of the work presented by

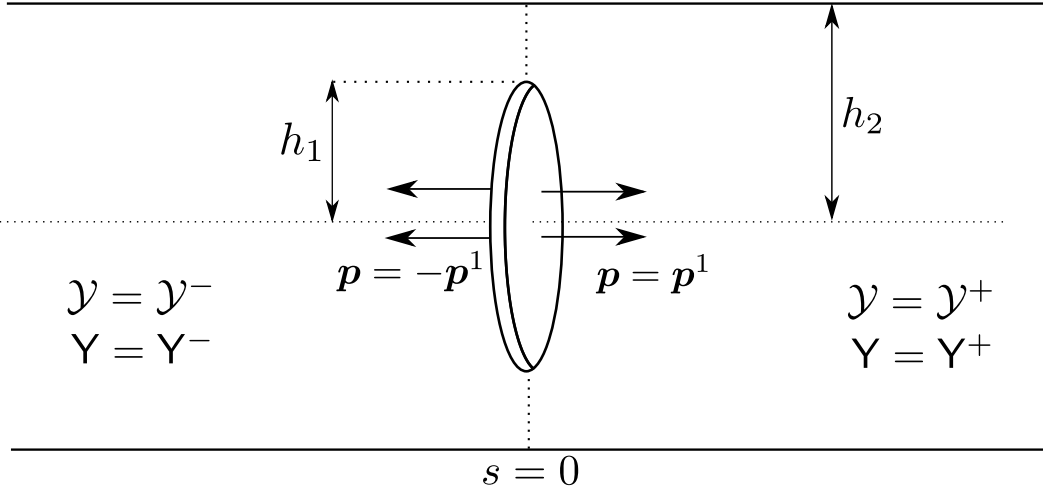


Fig. 4.2 Geometry of the dipole source

Pagneux et al. (1996) into the nonlinear regime for discontinuities in ducts. By taking a sufficiently large duct for $s > 0$ we approximate a duct exit with an infinite baffle.

4.2.2 Dipole Sources

We now address a different but related problem—a circular membrane of radius h_1 at $s = 0$ oscillating in a larger pipe of radius h_2 extending to infinity in both directions (see figure 4.2). The membrane acts as a dipole pressure source, with waves emanating in antiphase of each other either side of the dipole. We therefore have $p(s) = -p(-s)$ and the resulting Dirichlet boundary condition $p(s = 0) = 0$ for $h_2 > r > h_1$ due to the cancellation of the waves. We wish to prescribe a pressure p^1 on the membrane at $s = 0_+$ and, using the characteristic admittances of the outer duct $\mathbf{Y}^2 = \mathbf{Y}^+$ and $\mathbf{Y}^2 = \mathbf{Y}^-$ for $s > 0$, find the modal admittances on the membrane \mathbf{Y}^1 and \mathbf{Y}^1 at $s = 0$, $r < h_1$.

We can relate the modal pressure on the membrane to the modal pressure in the outer duct for $s > 0$ by applying continuity of pressure on the membrane $r < h_1$ and the zero pressure condition on $h_2 > r > h_1$. For each temporal harmonic we have

$$P_\alpha^2 = \int_{r < h_2} p^2 \psi_\alpha^2 dS = \int_{r < h_1} p^2 \psi_\alpha^2 dS = \int_{r < h_1} p^1 \psi_\alpha^2 dS = \int_{r < h_1} \psi_\beta^1 \psi_\alpha^2 dS P_\beta^1 = F_{\beta\alpha} P_\beta^1 \quad (4.14)$$

or

$$\mathbf{p}_d^2 = \mathbf{F}^T \mathbf{p}^1 \quad (4.15)$$

where the subscript d denotes that this is the resultant pressure from the dipole source. Similarly we can use continuity of normal velocity to relate velocity modes

$$U_\alpha^1 = \int_{r < h_1} u^2 \psi_\alpha^1 dS = \int_{r < h_1} \psi_\alpha^1 \psi_\beta^2 dS U_\beta^2 = F_{\alpha\beta} U_\beta^2 \quad (4.16)$$

or

$$\mathbf{u}_d^1 = \mathbf{F} \mathbf{u}_d^2 \quad (4.17)$$

As with the baffled duct, we can consider the admittance relations between the modes

$$\mathbf{u}_d^1 = \mathbf{Y}_d^1 \mathbf{p}^1 + \mathcal{Y}_d^1 [\mathbf{p}^1, \mathbf{p}^1] \quad (4.18a)$$

$$\mathbf{u}_d^2 = \mathbf{Y}^+ \mathbf{p}_d^2 + \mathcal{Y}^+ [\mathbf{p}_d^2, \mathbf{p}_d^2] \quad (4.18b)$$

and use (4.15) and (4.17) to find \mathbf{Y}^1 and \mathcal{Y}^1

$$\begin{aligned} \mathbf{u}_d^1 &= \mathbf{Y}_d^1 \mathbf{p}^1 + \mathcal{Y}_d^1 [\mathbf{p}^1, \mathbf{p}^1] \\ &= \mathbf{F} \mathbf{u}_d^2 \\ &= \mathbf{F} \mathbf{Y}^+ \mathbf{p}_d^2 + \mathbf{F} \mathcal{Y}^+ [\mathbf{p}_d^2, \mathbf{p}_d^2] \\ &= \mathbf{F} \mathbf{Y}^+ \mathbf{F}^T \mathbf{p}^1 + \mathbf{F} \mathcal{Y}^+ [\mathbf{F}^T \mathbf{p}^1, \mathbf{F}^T \mathbf{p}^1] \end{aligned} \quad (4.19)$$

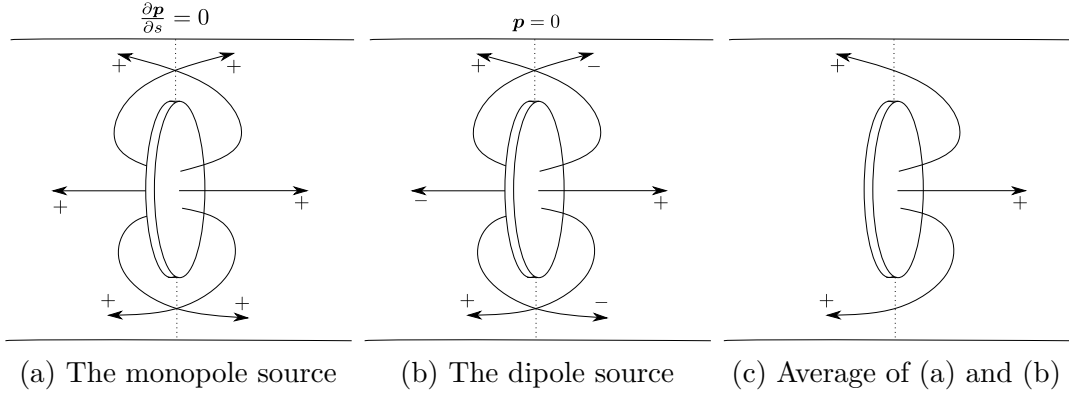
Equating the top and bottom lines, taking orders of magnitude and cancelling \mathbf{p}^1 (again, we can do so as it is a free vector) we obtain

$$\mathbf{Y}_d^1 = \mathbf{F} \mathbf{Y}^+ \mathbf{F}^T \quad (4.20a)$$

$$\mathcal{Y}_d^1 = \mathbf{F} \mathcal{Y}^+ [\mathbf{F}^T, \mathbf{F}^T] \quad (4.20b)$$

4.2.3 Unbaffled Ducts

We can now use the above solutions for the baffled duct and the circular dipole source to approximate radiation from an unbaffled duct into a larger duct. The baffled duct can be thought of—using the method of images—as a circular monopole source of radius $r = h_1$ at $s = 0$ inside a larger infinite duct of radius h_2 , with pressure waves radiating in the same phase for $s > 0$ and $s < 0$ (see figure 4.3a). At $s = 0$ we have the Neumann boundary condition $\frac{\partial p^2}{\partial s} = 0$ for $h_2 > r > h_1$. We can see by examining (3.6b) that this is indeed equivalent to the Dirichlet boundary condition $u^2 = 0$ for the velocity (correct up to $\mathcal{O}(M^2)$).



By taking the average of the solutions produced by this monopole source and the solutions produced by the dipole source, we produce a one sided radiator solution without baffles—the phases of the waves cancel appropriately (see figure 4.3c). This idea was first suggested by Jean Kergomard and used by Kemp et al. (2017), where they compared the solution to empirical measurements with good success. Here, we have extended this idea into the nonlinear regime.

We shall now think of our problem in three distinct regions (see figure 4.4). Region 1—the region of the inner duct $r < h_1$, extending for $s < 0$. Here, we specify the pressure \mathbf{p}^1 at $s = 0$. Regions 2/3—the outer region $r < h_2$, extending $-\infty < s < \infty$. Here, we ignore the inner duct (we are only considering the one sided radiation from the exit) and specify the boundary condition $\mathbf{Y} = \mathbf{Y}^\pm$ and $\mathcal{Y} = \mathcal{Y}^\pm$ for $s \gtrless 0$. In doing so we are ignoring scattering of the sound off of the exterior of the inner duct. From these boundary conditions (and making the approximation of no external scattering) we shall derive the admittances in the inner duct—the admittances for and unbaffled duct radiating into a larger duct \mathbf{Y}^1 and \mathcal{Y}^1 .

We begin by defining \mathbf{p}^2 as the average of the pressure contributions from the baffled and dipole solutions

$$\mathbf{p}^2 = \frac{1}{2} (\mathbf{p}_h^2 + \mathbf{p}_d^2) \quad (4.21)$$

This is related to the velocity in region 2 using the characteristic admittances boundary condition

$$\mathbf{u}^2 = \mathbf{Y}^+ \mathbf{p}^2 + \mathcal{Y}^+ [\mathbf{p}^2, \mathbf{p}^2] \quad (4.22)$$

The velocity modes in region 2 can be matched to region 1 by continuity of normal velocity

$$\mathbf{u}^1 = \mathsf{F} \mathbf{u}^2 \quad (4.23)$$

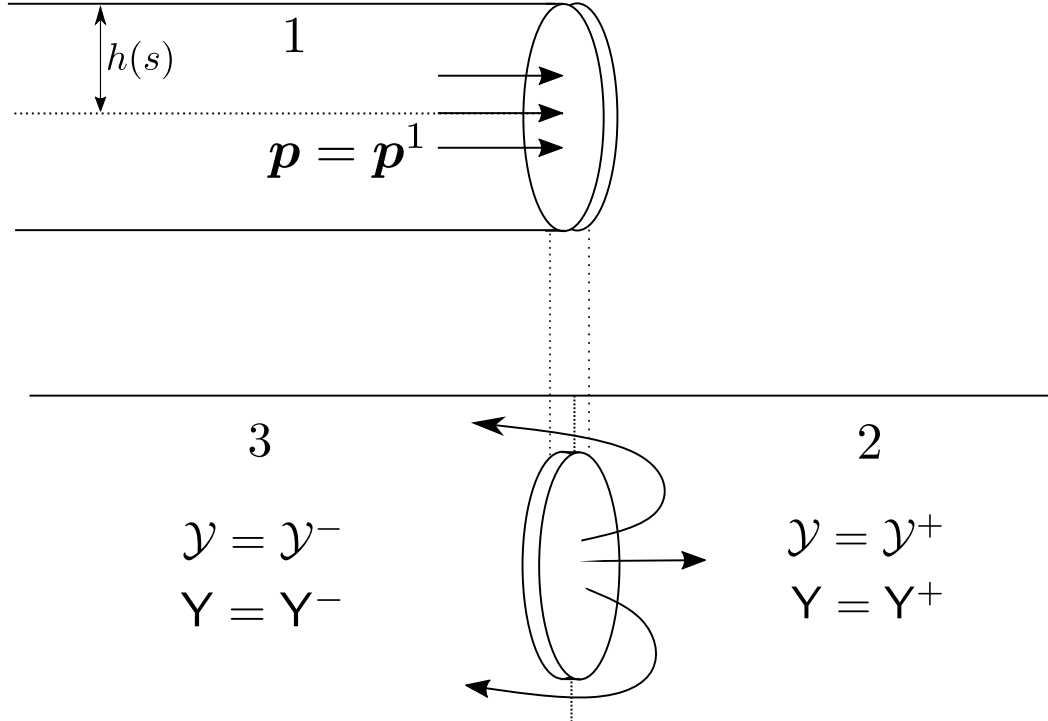


Fig. 4.4 Geometry of the open duct

This is related to our (free) pressure vector in region 1 by the (as yet unknown) impedances of region 1

$$\begin{aligned}
\mathbf{p}^1 &= Z^1 \mathbf{u}^1 + \mathcal{Z}^1[\mathbf{u}^1, \mathbf{u}^1] \\
&= Z^1 F \mathbf{u}^2 + \mathcal{Z}^1[F \mathbf{u}^2, F \mathbf{u}^2] \\
&= Z^1 F (Y^+ \mathbf{p}^2 + \mathcal{Y}^+[\mathbf{p}^2, \mathbf{p}^2]) + \mathcal{Z}^1[F Y^+ \mathbf{p}^2, F Y^+ \mathbf{p}^2] \\
&= Z^1 F \left(\frac{1}{2} Y^+ (\mathbf{p}_h^2 + \mathbf{p}_d^2) + \mathcal{Y}^+ \left[\frac{1}{2} (\mathbf{p}_h^2 + \mathbf{p}_d^2), \frac{1}{2} (\mathbf{p}_h^2 + \mathbf{p}_d^2) \right] \right) \\
&\quad + \mathcal{Z}^1 \left[\frac{1}{2} F Y^+ (\mathbf{p}_h^2 + \mathbf{p}_d^2), \frac{1}{2} F Y^+ (\mathbf{p}_h^2 + \mathbf{p}_d^2) \right]
\end{aligned} \tag{4.24}$$

We now express \$\mathbf{p}_h^2\$ and \$\mathbf{p}_d^2\$ in terms of \$\mathbf{p}^1\$. For the dipole solution this is given by (4.15). For the hard walled solution, we express \$\mathbf{p}_h^2\$ in terms of \$\mathbf{u}_h^2\$, use (4.8) to express \$\mathbf{u}_h^2\$ in terms of \$\mathbf{u}_h^1\$ and finally use the hard walled admittance relationship in region 1 to express \$\mathbf{u}_h^1\$ in terms of \$\mathbf{p}^1\$

$$\begin{aligned}
\mathbf{p}_h^2 &= Z^+ \mathbf{u}_h^2 + \mathcal{Z}^+[\mathbf{u}_h^2, \mathbf{u}_h^2] \\
&= Z^+ F^T \mathbf{u}_h^1 + \mathcal{Z}^+ [F^T \mathbf{u}_h^1, F^T \mathbf{u}_h^1] \\
&= Z^+ F^T (Y_h^1 \mathbf{p}^1 + \mathcal{Y}_h^1[\mathbf{p}^1, \mathbf{p}^1]) + \mathcal{Z}^+ [F^T Y_h^1 \mathbf{p}^1, F^T Y_h^1 \mathbf{p}^1]
\end{aligned} \tag{4.25}$$

Substituting these in we obtain

$$\begin{aligned} \mathbf{p}^1 = & \frac{1}{2} Z^1 F Y^+ \left(Z^+ F^T \left(Y_h^1 \mathbf{p}^1 + \mathcal{Y}_h^1[\mathbf{p}^1, \mathbf{p}^1] \right) + \mathcal{Z}^+ [F^T Y_h^1 \mathbf{p}^1, F^T Y_h^1 \mathbf{p}^1] + F^T \mathbf{p}^1 \right) \\ & + Z^1 F \mathcal{Y}^+ \left[\frac{1}{2} \left(Z^+ F^T Y_h^1 \mathbf{p}^1 + F^T \mathbf{p}^1 \right), \frac{1}{2} \left(Z^+ F^T Y_h^1 \mathbf{p}^1 + F^T \mathbf{p}^1 \right) \right] \\ & + \mathcal{Z}^1 \left[\frac{1}{2} F Y^+ \left(Z^+ F^T Y_h^1 \mathbf{p}^1 + F^T \mathbf{p}^1 \right), \frac{1}{2} F Y^+ \left(Z^+ F^T Y_h^1 \mathbf{p}^1 + F^T \mathbf{p}^1 \right) \right] \end{aligned} \quad (4.26)$$

We can, as usual, take orders of magnitude and cancel off \mathbf{p}^1 to obtain

$$\begin{aligned} I = & \frac{1}{2} Z^1 F Y^+ \left(Z^+ F^T Y_h^1 + F^T \right) \\ \Rightarrow Y^1 = & \frac{1}{2} \left(F F^T Y_h^1 + Y_d^1 \right) \end{aligned} \quad (4.27)$$

The matrix product $F F^T = I$ (see appendix C), and so the resulting linear impedance is the average of the hard walled and dipole impedances

$$Y^1 = \frac{1}{2} \left(Y_h^1 + Y_d^1 \right) \quad (4.28)$$

and for the nonlinear impedance

$$\begin{aligned} 0 = & \frac{1}{2} Z^1 F Y^+ \left(Z^+ F^T \mathcal{Y}_h^1 + \mathcal{Z}^+ [F^T Y_h^1, F^T Y_h^1] \right) \\ & + Z^1 F \mathcal{Y}^+ \left[\frac{1}{2} \left(Z^+ F^T Y_h^1 + F^T \right), \frac{1}{2} \left(Z^+ F^T Y_h^1 + F^T \right) \right] \\ & + \mathcal{Z}^1 \left[\frac{1}{2} F Y^+ \left(Z^+ F^T Y_h^1 + F^T \right), \frac{1}{2} F Y^+ \left(Z^+ F^T Y_h^1 + F^T \right) \right] \end{aligned} \quad (4.29)$$

The last term above can be expressed as

$$\mathcal{Z}^1 \left[\frac{1}{2} F Y^+ \left(Z^+ F^T Y_h^1 + F^T \right), \frac{1}{2} F Y^+ \left(Z^+ F^T Y_h^1 + F^T \right) \right] = \mathcal{Z}^1 [Y^1, Y^1] = -Z^1 \mathcal{Y}^1 \quad (4.30)$$

using (4.28) and the tensor inversion rule (4.10). We are therefore left with

$$\begin{aligned} Y^1 = & \frac{1}{2} \left(F F^T \mathcal{Y}_h^1 + F Y^+ \mathcal{Z}^+ [F^T Y_h^1, F^T Y_h^1] \right) \\ & + F \mathcal{Y}^+ \left[\frac{1}{2} \left(Z^+ F^T Y_h^1 + F^T \right), \frac{1}{2} \left(Z^+ F^T Y_h^1 + F^T \right) \right] \end{aligned} \quad (4.31)$$

for the nonlinear impedance. This can further be simplified using $\mathbf{F}\mathbf{F}^T = \mathbf{I}$ and by expressing \mathcal{Z}^+ in terms of \mathcal{Y}^+ using the tensor inversion rule

$$\mathcal{Y}^1 = \frac{1}{2} (\mathcal{Y}_h^1 - \mathbf{F}\mathcal{Y}^+[\mathbf{Z}^+\mathbf{F}^T\mathbf{Y}_h^1, \mathbf{Z}^+\mathbf{F}^T\mathbf{Y}_h^1]) \quad (4.32)$$

$$+ \mathbf{F}\mathcal{Y}^+ \left[\frac{1}{2} (\mathbf{Z}^+\mathbf{F}^T\mathbf{Y}_h^1 + \mathbf{F}^T), \frac{1}{2} (\mathbf{Z}^+\mathbf{F}^T\mathbf{Y}_h^1 + \mathbf{F}^T) \right] \quad (4.33)$$

By using these admittances, we can solve our admittance equations through the inner duct to our pressure source as before to find the admittance everywhere in the duct. Once these are found, we can solve for the pressure up to the duct opening. To find the pressure outside the duct in “free space” we first calculate \mathbf{u}_h^1 using

$$\mathbf{u}_h^1 = \mathbf{Y}_h^1 \mathbf{p}^1 + \mathcal{Y}_h^1 [\mathbf{p}^1, \mathbf{p}^1] \quad (4.34)$$

Next, we calculate $\mathbf{u}_h^2 = \mathbf{F}^T \mathbf{u}_h^1$ and use \mathbf{u}_h^2 to find \mathbf{p}_h^2 by equation (4.9b). We can find \mathbf{p}_d^2 by using $\mathbf{p}_d^2 = \mathbf{F}^T \mathbf{p}^1$. To get \mathbf{p}^2 we take the average of the baffled and dipole contributions

$$\mathbf{p}^2 = \frac{1}{2} (\mathbf{p}_h^2 + \mathbf{p}_d^2) \quad (4.35)$$

This can then be propagated along for $s > 0$ by solving the pressure equation with $\mathbf{Y} = \mathbf{Y}^+$ and $\mathcal{Y} = \mathcal{Y}^+$. For $s < 0$, we have $\mathbf{p}_h^3 = \mathbf{p}_h^2$ and $\mathbf{p}_d^3 = -\mathbf{p}_d^2$. We therefore have

$$\mathbf{p}^3 = \frac{1}{2} (\mathbf{p}_h^2 - \mathbf{p}_d^2) \quad (4.36)$$

This can be propagated in the negative s direction using the pressure equation with $\mathbf{Y} = \mathbf{Y}^-$ and $\mathcal{Y} = \mathcal{Y}^-$. As we have $p_h^2 = p_d^2 = p^1$ for $r < h_1$ at $s = 0_+$, we get $p^3 = 0$ for $r < h_1$ at $s = 0_-$ —i.e. the shadow of the duct opening. For $h_2 > r > h_1$, $p_d^2 = 0$ and so $p^3 = p^2 = p_h^2$ at $s = 0$ —i.e. continuity of pressure. We can use the calculated pressure in region 3 everywhere for $s < 0$, $r > h_1(s)$. Although this ignores the scattering from the external ducts wall the approximation is a good one.

4.3 Numerical Method

As with the previous chapter, the basic numerical machinery remains the same and shall not be discussed again. New numerical issues can now arise however, in particular relating to the \mathbf{F} matrix.

One finds that, in general, \mathbf{F} is not a numerically invertible matrix—for any finite truncation of \mathbf{F} , calculating the matrix \mathbf{F}^{-1} results in unwieldy numbers that do not

approximate the truncation of the inverse. This poses problems for calculating the impedances, for example \mathbf{Y}_h^1 . To overcome this issue, we take a larger number of modes outside the duct to inside. This is equivalent to taking \mathbf{F} to be a rectangular matrix of size $\alpha_{\max} \times \beta_{\max}$ with $\beta_{\max} > \alpha_{\max}$. We truncate external operators to maximum index β_{\max} and internal ones to α_{\max} . In doing so matrix products such as

$$\mathbf{Z}_h^1 = \mathbf{F}\mathbf{Z}^+\mathbf{F}^T \quad (4.37)$$

result in terms which are better converged to their true value. With an accurately calculated \mathbf{Z}_h^1 , we can invert to find the hard walled admittance. Without taking different numbers of modes inside and out, the matrix product for \mathbf{Z}_h^1 results in erroneous entries (particularly towards the bottom right corner of the matrix) that do not correctly represent the truncation of the matrix. Then, when inverted, the result is a matrix with large entries which does not even approximate the correct admittance.

The question naturally arises of how many modes one should to take. A good rule of thumb—based off our previous work with ducts of varying width—appears to be taking the modal ratio to be roughly the ratio of the duct widths (as a minimum at least). This means to well approximate radiation into free space, one must take a large ratio of inner to outer duct widths and consequently a large ratio of inner to outer duct modes. To produce good calculations in the inner duct, we must already take a reasonable number of modes—this implies we must take a very large number of modes in the outer duct in order to achieve a good inner to outer ratio of widths in order to approximate a free space. This can prove computationally taxing. If one only wishes to solve inside the duct (and not for the radiation from it) then this is less problematic—one can have a large duct ratio and large numbers of modes outside without much cost (the extra modes are only needed to calculate the admittances). In section 4.5 we generally take around 800 modes in the outer duct and 5 in the inner with a duct ratio of 80 for problems involving calculation of the resonances¹. If one wishes to find the radiation pattern from a duct, one may wish to use fewer modes externally to reduce the computational cost in finding the external pressure. In doing so we must limit the ratio of internal to external duct widths. The problem with this is that the “modal” behaviour becomes more apparent—one can observe the individual

¹Such few modes are taken with the inner duct for two reasons. The first, as previously noted, is that problems involving calculation of physical quantities such as the reflectance can be achieved to good accuracy with only a few modes—our tests with higher numbers have yielded very little difference. The second reason is that calculation of the resonances involves solving the admittance equations for each frequency (often up to 400 times). In the nonlinear regime this can take over a week on a single machine for only a few modes.

modal peaks rather than a smooth waveform. Parts of a solution can also decay if the modes are cut-off. In practice the duct width is usually the limiting factor in whether external modes are cut-on/off, so taking extra external modes will not improve the solution unless the external width is also increased². Higher frequency radiation patterns are easier to produce as higher frequencies have more cut-on modes for the same external width. In section 4.5, we generally take 5-20 inner modes (depending on the geometry) and 200 outer modes with a width ratio of 10. Such a width ratio is generally sufficient to produce smooth radiation patterns for the frequencies we are concerned with.

4.4 Comparison with the Wiener-Hopf Solution

Levine and Schwinger (1948) were able to use the Wiener-Hopf technique to find the exact analytical solution to radiation from an unflanged circular pipe in the linear regime. In this section we shall give a brief overview of their technique and compare results to our method. Our presentation follows that of Noble (1958).

We define a semi-infinite duct cylindrical duct for $-\infty < s < 0$, $r < h$. We wish to solve for the total velocity potential ϕ_t satisfying the linear wave equation

$$\frac{1}{r} \frac{\partial}{\partial r} \left(r \frac{\partial \phi_t}{\partial r} \right) + \frac{\partial^2 \phi_t}{\partial s^2} + k^2 \phi_t = 0 \quad (4.38)$$

By separating variables and applying the no penetration condition $\frac{\partial \phi_t}{\partial r} = 0$ on $r = h$, together with the regularity condition $\phi_t < \infty$ at $r = 0$ we obtain the solution

$$\phi_t = e^{iks} + R e^{-iks} + \sum_{q=1}^{\infty} b_q J_0 \left(\frac{r j_{0q}}{h} \right) \exp \left((j_{0q}^2 - k^2 h^2)^{1/2} (z/h) \right) \quad (4.39)$$

for an incident wave e^{iks} in the duct. Here, we are assuming that $k < j_{01} = 3.832\dots$ so that only the planar reflected mode can propagate. We separate the incident wave from the scattered $\phi_t = \phi + \phi_i$ for $r < h$ and Fourier transform the wave equation (4.38) w.r.t. s to obtain

$$\frac{1}{r} \frac{d}{dr} \left(r \frac{d\Phi_t}{dr} \right) - \gamma^2 \Phi_t = 0 \quad \text{for } r \geq h \quad (4.40a)$$

²Note that one cannot simply take only the cut-on external modes. The calculations involving F do not produce correct solutions due to lack of convergence. One must have a sufficient number of evanescent external modes

$$\frac{1}{r} \frac{d}{dr} \left(r \frac{d\Phi}{dr} \right) - \gamma^2 \Phi = 0 \quad \text{for } 0 \leq r \leq h \quad (4.40b)$$

where $\gamma = (\alpha^2 - k^2)^{1/2}$, with the transform variable $\alpha = \sigma + i\tau$. We take $k = k_1 + ik_2$ to have a small imaginary part, and define the branch of γ such that $\gamma \rightarrow \sigma$ for $\alpha = \sigma \rightarrow +\infty$, $\gamma = -ik$ for $\alpha = 0$ and $\gamma \rightarrow |\sigma|$ for $\alpha = \sigma \rightarrow -\infty$, with branch cuts shown in figure 4.5. The solutions to these equations are

$$\Phi_t = A(\alpha)K_0(\gamma r) \quad \text{for } r \geq h \quad (4.41a)$$

$$\Phi = B(\alpha)I_0(\gamma r) \quad \text{for } 0 \leq r \leq h \quad (4.41b)$$

where K_0 and I_0 are the modified Bessel functions. The solutions are such that we have a regular solution as $r \rightarrow 0$ and $\Phi_t \rightarrow 0$ as $r \rightarrow \infty$. We may decompose as follows

$$\Phi_{t+}(h) + \Phi_{t-}(h) = A(\alpha)K_0(\gamma h) \quad (4.42a)$$

$$\Phi_+(h) + \Phi_-(h) = B(\alpha)I_0(\gamma h) \quad (4.42b)$$

$$\Phi'_+(h) + \Phi'_-(h) = \gamma A(\alpha)K'_0(\gamma h) = \gamma B(\alpha)I'_0(\gamma h) \quad (4.42c)$$

where the Φ_+ and Φ_- are half range Fourier transforms analytic in $\text{Im } \alpha > k_2$ and $\text{Im } \alpha < k_2$ respectively

$$\Phi_+(\alpha, r) = \frac{1}{(2\pi)^{1/2}} \int_0^\infty \phi(s, r) e^{i\alpha s} ds \quad (4.43a)$$

$$\Phi_-(\alpha, r) = \frac{1}{(2\pi)^{1/2}} \int_{-\infty}^0 \phi(s, r) e^{i\alpha s} ds \quad (4.43b)$$

Equation (4.42c) comes from $\frac{\partial \phi_t}{\partial r} = \frac{\partial \phi}{\partial r}$ at $r = h$ for $-\infty < s < \infty$. We can eliminate A and B

$$\Phi_{t+}(h) + \Phi_{t-}(h) = K_0(\gamma h) \gamma^{-1} (K'_0(\gamma h))^{-1} (\Phi'_+(h) + \Phi'_-(h)) \quad (4.44a)$$

$$\Phi_+(h) + \Phi_-(h) = I_0(\gamma h) \gamma^{-1} (I'_0(\gamma h))^{-1} (\Phi'_+(h) + \Phi'_-(h)) \quad (4.44b)$$

We subtract these equations, noting that $\Phi'_-(h) = 0$ and

$$\Phi_{t+}(h) - \Phi_+(h) = \frac{1}{(2\pi)^{1/2}} \int_0^\infty e^{i(\alpha+k)s} ds = \frac{1}{(2\pi)^{1/2}} \frac{i}{\alpha + k} \quad (4.45)$$

Letting $F_- = \Phi_{t-}(h) - \Phi_-(h)$ we obtain

$$\frac{1}{(2\pi)^{1/2}} \frac{i}{\alpha + k} + F_- = \left(\gamma^2 h K'_0(\gamma h) I'_0(\gamma h) \right)^{-1} \Phi'_+(h) \quad (4.46)$$

Setting

$$K(\alpha) = -2K'_0(\gamma h) I'_0(\gamma h) = 2K_1(\gamma h) I_1(\gamma h) \quad (4.47)$$

we can decompose $K(\alpha)$ into a product $K(\alpha) = K_+(\alpha)K_-(\alpha)$ where K_+ and K_- are analytic in $\text{Im } \alpha > k_2$ and $\text{Im } \alpha < k_2$ respectively. We have

$$\log K_+(\alpha) = \frac{1}{2\pi i} \int_{-\infty+ic}^{\infty+ic} \frac{\log(2K_1(\gamma h) I_1(\gamma h))}{\zeta - \alpha} d\zeta, \quad \text{Im } \alpha > c \quad (4.48a)$$

$$\log K_-(\alpha) = -\frac{1}{2\pi i} \int_{-\infty+ic}^{\infty+ic} \frac{\log(2K_1(\gamma h) I_1(\gamma h))}{\zeta - \alpha} d\zeta, \quad \text{Im } \alpha < c \quad (4.48b)$$

with $-k_2 < c < k_2$. Using this, we can rearrange (4.46) to have positive functions on one side and negative on the other

$$\begin{aligned} (2\pi)^{-1/2} i(\alpha + k)^{-1} ((\alpha - k)K_-(\alpha) + 2kK_-(-k)) + (\alpha - k)K_-(\alpha)F_- \\ = -\frac{2}{(\alpha + k)hK_+(\alpha)} \Phi'_+(h) + \frac{i}{(2\pi)^{1/2}} \frac{2kK_-(-k)}{(\alpha + k)} \end{aligned} \quad (4.49)$$

Taking $\alpha \rightarrow \infty$, we see $|K_\pm| \sim |\alpha|^{-1/2}$ in the corresponding half planes, $F_- \sim |\alpha|^{-1}$ and $|\Phi'_+| \sim |\alpha|^{-1/2}$. By Liouville's theorem we see that the LHS=RHS=const=0. We are therefore left with

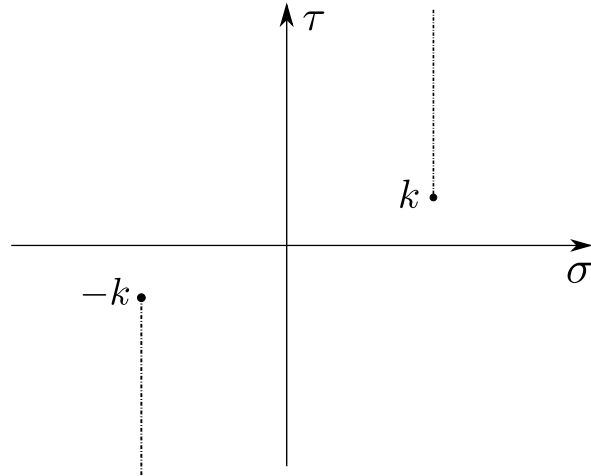
$$\Phi'_+(\alpha) = ikh(2\pi)^{-1/2} K_+(\alpha) K_-(-k) \quad (4.50)$$

Using this, together with (4.42c) we are able to find A and B , giving Φ_t and Φ . Inverting these transforms, we obtain the velocity potential in integral form

$$\phi_t = -\frac{ikh}{2\pi} K_-(-k) \int_{-\infty+ic}^{\infty+ic} K_+(\alpha) \frac{K_0(\gamma r)}{\gamma K_1(\gamma h)} e^{-i\alpha s} d\alpha \quad \text{for } r \geq h \quad (4.51a)$$

$$\phi = \frac{ikh}{2\pi} K_-(-k) \int_{-\infty+ic}^{\infty+ic} K_+(\alpha) \frac{I_0(\gamma r)}{\gamma I_1(\gamma h)} e^{-i\alpha s} d\alpha \quad \text{for } 0 \leq r \leq h \quad (4.51b)$$

with $-k_2 < c < k_2$. These can be used to plot the resulting field.

Fig. 4.5 Branch cuts of γ

We can also calculate the reflection coefficient R . By closing (4.51b) in the upper half plane we get a contribution from the pole at $\alpha = k$

$$-K_-(-k)K_+(k)e^{-iks} = -(K_+(k))^2e^{-iks} = Re^{-iks} \quad (4.52)$$

After some manipulations of integral 4.48a, one finds

$$R = \exp\left(-\frac{2kh}{\pi} \int_0^{kh} \frac{\arctan(-J_1(z)/Y_1(z))}{z(k^2h^2 - z^2)^{1/2}} dz\right) \quad (4.53)$$

where the branch of arctan is taken to be $[0, 2\pi]$.

We can also define the end correction. This is the theoretical point, outside the end of the duct from which the wave appears to reflect from. It is dependant on the width of the duct. For finite length ducts, this end correction relates to the resonances and so it is an important quantity to study. It is defined by the distance l outside the duct, at which point the reflected wave is in antiphase with the incident wave

$$Re^{-ikl} = -|R|e^{ikl} \quad (4.54)$$

For the cylindrical duct of our current problem it is given by

$$\frac{l}{h} = \frac{1}{\pi} \int_0^\infty \frac{\log(1/2K_1(z)I_1(z))}{z(k^2h^2 + z^2)^{1/2}} dz + \frac{1}{\pi} \int_0^{kh} \frac{\log(\pi J_1(z)(J_1^2(z) + Y_1^2(z))^{1/2})}{z(k^2h^2 - z^2)^{1/2}} dz \quad (4.55)$$

In the long wavelength limit $kh \ll 1$ this reduces to

$$\frac{l}{h} = \frac{1}{\pi} \int_0^\infty \frac{1}{z^2} \log \left(\frac{1}{2I_1(z)K_1 z} \right) dz = 0.6133\dots \quad (4.56)$$

the value found experimentally by Rayleigh (1878) amongst others.

Figures 4.6, 4.7 and 4.8 compare the reflection coefficient, the end correction and the pressure field produced by our method against the solution described above. As the pressure satisfies the same equation with identical boundary conditions, we can use the Levine and Schwinger solution to describe the pressure.

To compare the reflection coefficient, we first find the admittance as given by (4.28). Next, we calculate the reflectance matrix \mathbf{R} given by (2.114). From this we can calculate \mathbf{p}^- from an incident $\mathbf{p}^+ = (1, 0, 0, \dots)$. The modulus of the first element of \mathbf{p}^- gives the reflection coefficient. We calculate this taking 800 modes in the outer duct and 10 in the inner. For the ratio of outer to inner ducts, we compare both $h_2 = 80h$ and $h_2 = 200h$. While this second ratio exceeds our rule for matching the ratios of modes and ratios of duct diameters this does not cause errors in the planar modes we are interested in. We can see that in both cases, the numerical method provides a very good approximation to the analytic reflection coefficient. We observe that there are some artefacts—likely a result of resonances arising from having a finite width outer duct (and corresponding modes becoming cut-off/on outside), however these can be reduced in magnitude by taking a larger outer duct.

To calculate the end correction we follow the same procedure as above, but instead calculate the complex argument of the reflected wave, taking $l = -\arg(P_0^-)/(2k)$. The end correction is less well approximated by the numerical method—tending to over estimate, particularly for higher frequencies. That being said, the results are still fairly close and for sufficiently large outer duct we obtain the correct limiting value as $kh \rightarrow 0$ of 0.6133.

To compare the pressure we must modify the problem slightly. As we cannot solve backwards from the duct opening (the solution is numerically unstable due to the evanescent modes), we set our incident wave \mathbf{p}^+ to be the planar mode e^{iks} a wavelength from the duct opening. We solve our admittance from the duct opening to this point and using the admittance found there, calculate the reflectance matrix. Using this we can find \mathbf{p}^- and hence the total pressure $\mathbf{p} = \mathbf{p}^+ + \mathbf{p}^-$. This can be solved to the duct exit in the usual manner, and from there into the “free space” by the method described in the beginning of this chapter. Figure 4.8 shows the results for $k = 0.95k_c$ with $k_c = j_{01} = 3.832\dots$ the radial cutoff for the duct. We take 200

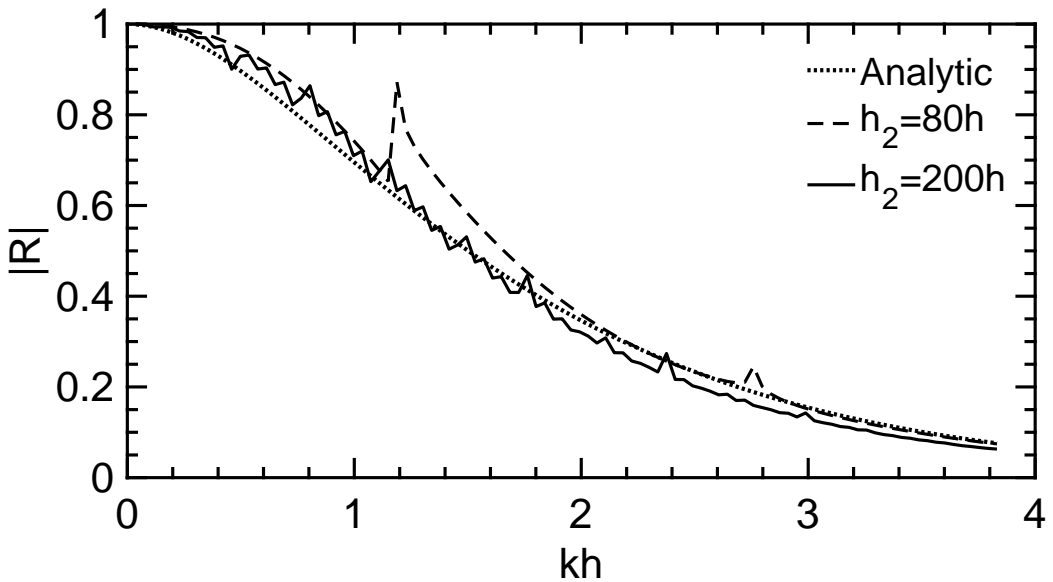


Fig. 4.6 Comparison of the reflection coefficient produced by our numerical method to the analytic solution of Levine and Schwinger (1948)

outer modes and 20 inner with a duct ratio of $h_2 = 10h$. The agreement between the solutions is very good—both inside the duct and the outside “free space”. We observe they both feature the highly nonplanar wave propagation inside the duct, and the localised radiated sound emanating from the front, featuring the characteristic curved wave fronts. We also note that the method does a good job of describing the circular wavefronts behind the opening, including in the proximity of the external duct wall. This suggests the approximation of ignoring the external scattering is a very good one, and the main issue of this method is simply taking a large enough outer duct to well approximate free space.

4.5 Results

We now turn our attention to ducts of finite length (as opposed to the semi-infinite duct of Levine and Schwinger) to analyse the effect of the duct geometry on both the resulting resonances and radiation patterns, with particular interest in musical acoustics. We also examine what effect nonlinearity has on these results. We shall begin with an introduction to resonances in a finite length duct and methods of calculating them.

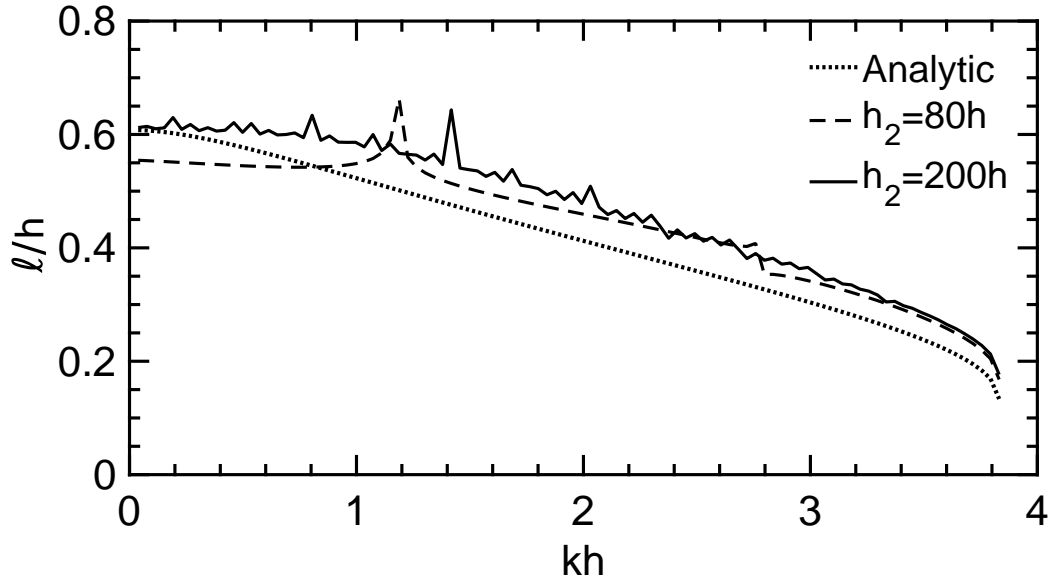


Fig. 4.7 Comparison of the end reflection produced by our numerical method to the analytic solution of Levine and Schwinger (1948)

4.5.1 Resonances in finite length duct

Finding the resonant frequencies of a duct is an eigenvalue problem depending on the boundary conditions both at the inlet and outlet of the duct. There are many possible methods to determine what constitutes a “resonance” in the duct—we shall consider several and justify our particular choice.

Amir et al. (1997), in their use of the multimodal method to find resonances in finite length ducts, examined the corner value of the impedance matrix Z_{00} . The justification in doing so is that the other elements—those representing the “self” impedances on the diagonal, and those representing “cross” impedances off the diagonal—have a very small value in comparison to Z_{00} and are very smooth as k is varied, yielding little information with regards to the resonances. This method works well in their paper, but has some drawbacks with regards to our needs—the obvious problem is that this cannot take into account any nonlinear effects. Another issue is that their paper only dealt with k below cutoff. For k greater than this, one would expect other elements—particularly on the diagonal—to yield the peaks and troughs characteristic of resonance. As we are dealing with harmonically rich sound, we would certainly have modes above the cutoff frequency.

A second approach that may come to one’s mind is to consider the nonlinear power reflectance used in section 2.8. While this can take into account higher modes and generalises to nonlinear systems, it turns out that the reflectance is not a particularly

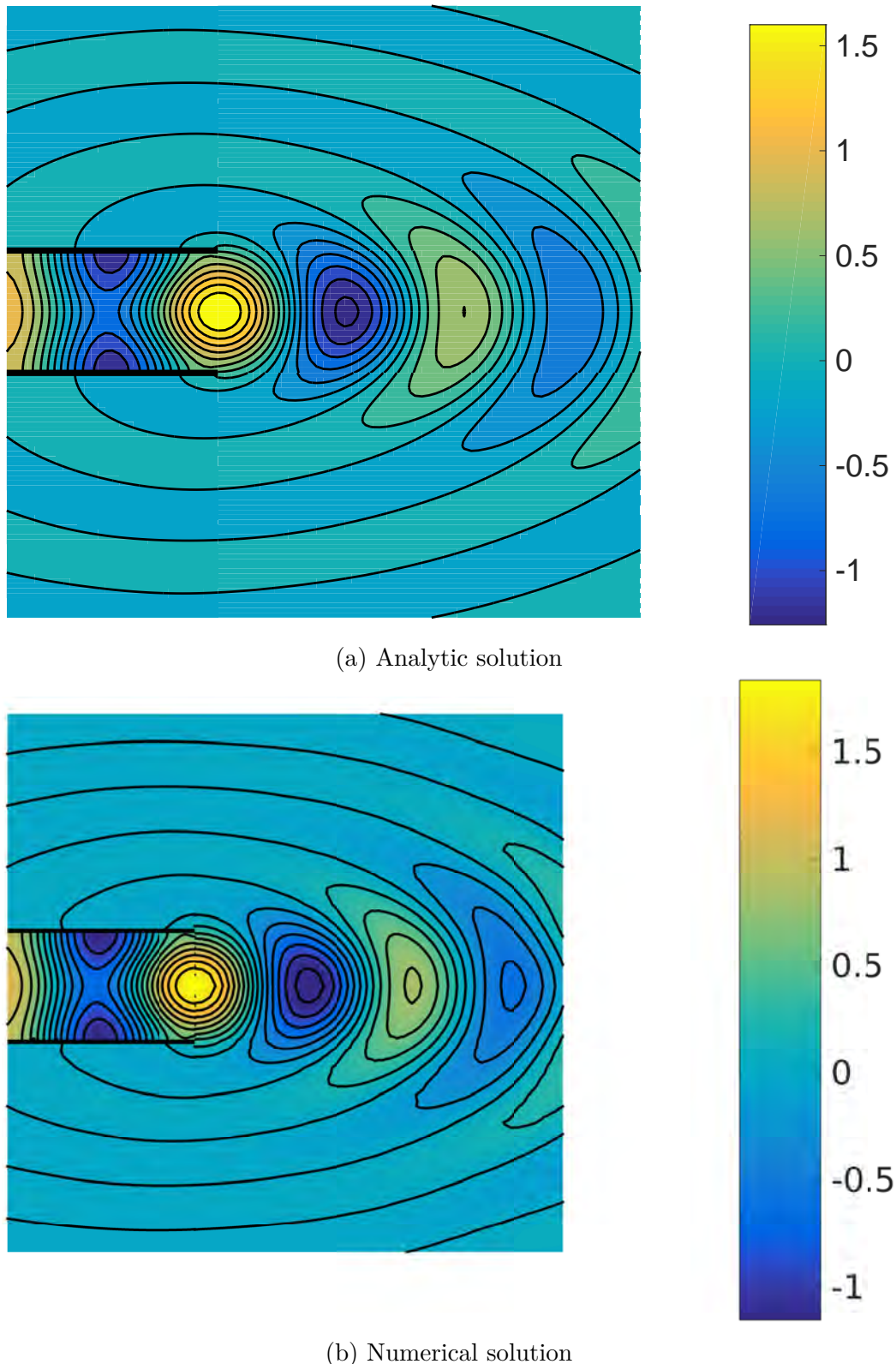


Fig. 4.8 Comparison of the pressure distributions by our numerical method to the analytic solution of Levine and Schwinger (1948)

useful measure to calculate the resonance—particularly from a numerical point of view. If we, as Levine and Schwinger, consider an incident plane wave $p^+ = e^{iks}$ and reflected wave $p^- = Re^{-iks}$ in a linear system, the corresponding velocities are $u^+ = e^{iks}$ and $u^- = -Re^{iks}$. The incident power is therefore $W^+ = 1$ and the total power is

$$W = 1 - |R|^2 + 2 \operatorname{Im}(Re^{-2iks}) \quad (4.57)$$

For resonance we must either have p^- either in phase with or out of phase with p^+ for $s = -L$ the length of the duct upstream. This corresponds to $\operatorname{Im}(Re^{2ikL}) = 0$. We can therefore see that W does indeed reveal aspects of resonance, however as R is itself a function k (with associated numerical errors), the plot of W does not clearly illustrate points of resonance. As higher cut-on modes are added (each with their own reflection infinitude), together with nonlinearities, W reveals little useful information as k is varied.

Instead, the approach we shall take is that used commonly by experimentalists in musical acoustics and consider the total impedance magnitude. Roughly speaking, wind instruments can be separated into two distinct categories—open and closed duct, referring to the boundary condition at the inlet. Open duct instruments—notably flutes of various kinds—are essentially open at both ends and as such, we would expect a similar admittance to that calculated at the beginning of the chapter at each end. This is a difficult eigenvalue problem to solve. A simpler approximation is to assume that the pressure in the inlet open end is approximately atmospheric, and as such we have a pressure node there. We would therefore expect resonances of such ducts to occur when the impedance is minimal at the inlet. For closed ducts—such as the clarinet, oboe, saxophone and the brass instrument family—the duct is essentially closed off by the reed or the player's lips. We would therefore expect a velocity node at resonance corresponding to a maximum of the impedance.

To define our impedance, we consider an incident plane wave \mathbf{p}^+ of amplitude M , the Mach number and wavenumber k . For most playing ranges in musical instruments, k is sufficiently below the first cut-off that the plane wave is a reasonable approximation. We then find the total pressure using the nonlinear reflectance

$$\mathbf{p} = \mathbf{p}^+ + \mathbf{p}^- = \mathbf{p}^+ + \mathsf{R}\mathbf{p}^+ + \mathcal{R}[\mathbf{p}^+, \mathbf{p}^+] \quad (4.58)$$

This total pressure takes into account any potential constructive/destructive interference which may occur as the phase of the reflective wave is altered by change to the incident Mach number, and so illustrates how resonances might change with *input* pressure

rather than total pressure at the inlet. The velocity \mathbf{u} can be found in the usual manner with the admittances. We can then find the total impedance magnitude as the ratio of RMS pressure over velocity

$$|Z| = \sqrt{\frac{|\mathbf{p}|^2}{|\mathbf{u}|^2}} = \sqrt{\frac{\sum_{a=1}^{\infty} \sum_{\alpha=0}^{\infty} 2|P_{\alpha}^a|^2}{\sum_{a=1}^{\infty} \sum_{\alpha=0}^{\infty} 2|U_{\alpha}^a|^2}} \quad (4.59)$$

In doing so we can observe when we are close to pressure or velocity nodes at the inlet, corresponding to resonances in open and closed ducts respectively, including when the signal is harmonically rich and nonplanar in form.

While these boundary conditions (pressure or velocity nodes at the inlet) are just approximations, they give good illustrations to the acoustic properties of the ducts we are about to study. In reality, with training, a skilled player can alter the boundary condition at the inlet of a duct—“lipping” up or down in the case of a flute, or altering the lip or reed tension in brass and other woodwind instruments respectively—to change the resonant properties of the instrument, ultimately affecting both pitch and timbre. We shall begin our study with the simplest case—a cylindrical tube.

4.5.2 Cylindrical Ducts

Figure 4.9 plots the inlet impedance as the wavenumber k is varied in the linear regime. We study two different duct aspect ratios: duct length $L = 8h$ and $L = 16h$ with h the radius. While the former may be considered a rather short tube compared to its diameter, particularly with regards to musical instruments (which often have very large aspect ratios), we shall use this to compare with other geometries—the exaggerated large diameter serving to more clearly illustrate the geometrical effects. For the $L = 8h$ duct the first cutoff occurs at $kL = 30.65\dots$

The figure clearly illustrates the resonance peaks. The higher aspect ratio duct has comparable resonances for the lower frequencies, but at higher frequencies the peaks are larger (corresponding to stronger resonances) and occur at higher frequencies. These results are not surprising—examining figure 4.6 we see that for a fixed k , $|R|$ increases as h decreases. Physically, a smaller opening does a better job of reflecting energy causing a stronger resonance. Also, from figure 4.7, a smaller duct opening produces a smaller end correction, effectively resulting in a shorter tube and a higher resonant frequency. For longer wavelengths, the proportion of this increase in effective duct length is smaller compared to the wavelength, so the effect of duct diameter is smaller at lower frequencies.

Table 4.1 collates the resonant frequencies of an open cylindrical duct (troughs in the impedance), their ratio to the fundamental resonant frequencies and the resulting musical interval to the fundamental. For the musically inclined reader these intervals are displayed in figure 4.10 taking the fundamental resonant frequency to be C. These pitches are notated using the closest equivalent in 24 tone equal temperament (24-TET) using quarter tone accidentals: ♭ (3/4 tone flat), ♯ (1/4 tone flat), ♮ (1/4 tone sharp) and ♯ (3/4 tone sharp). 24-TET divides the octave (a ratio of 1:2) into 24 equally spaced intervals (quarter tones) in contrast to the usual 12 intervals (semitones) used by traditional western music. We can also divide the octave into smaller intervals: *cents*. There are 100 cents in a semitone. Thus for two frequencies a and b , there are

$$\text{cents} = 1200 \log_2 \frac{b}{a} \quad (4.60)$$

cents between them.

Physically, this cylindrical open duct represents the acoustics in a flute type instrument. We see that the resonant frequencies—playable as harmonics by “overblowing”—all lie very close to musically important relationships (the octave, the fifth, the major third). Indeed, the reader may recognise these intervals approximate the harmonic series—integer multiples of the base frequency. Table 4.2 and figure 4.11 show the resulting pitches produced by the harmonic series. As notes on the harmonic series are integer multiples of the base frequency, the resulting harmonies produced by a combination of these tones typically sounds harmonious³. Instruments with many resonant frequencies which lie on the harmonic series also typically produce a richer timbre (or colour of the sound). One may note that the harmonic series itself does not perfectly match up with the notes of the western 12-TET (a fact well known to brass players as the 7th harmonic is noticeably out of tune). This is a consequence of splitting the octave logarithmically (producing irrational ratios) rather than using simple fractions (known as just intonation). This allows one to play in a variety of keys, all with the same tuning. Flute players will also be familiar with the harmonic series, typically utilising the first four harmonics, together with covering holes along the length of the instrument to effectively change the length of the duct, to achieve pitches over several octaves.

³Also, many of the resulting overtones produced by real instruments will coincide when two notes with a simple integer ratio are played together. If the ratios are more complex, many of the overtones can differ slightly causing a “beat” and perceived dissonance.

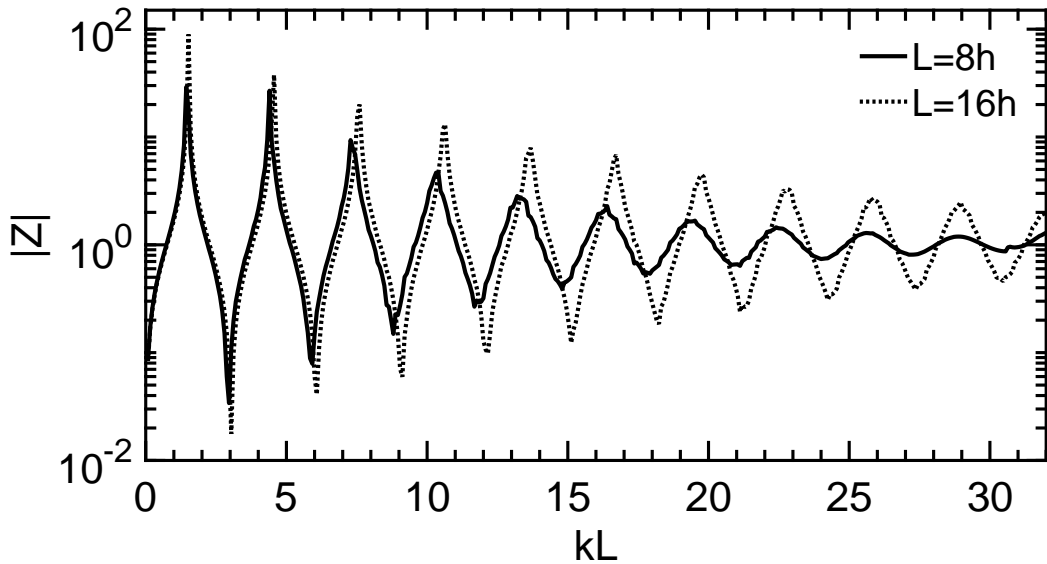


Fig. 4.9 Impedance plots for a cylindrical duct at different aspect ratios

We can also examine the pressure distribution inside such ducts. Figure 4.12 shows the results for an assortment of resonant frequencies. All plots are normalised to the input amplitude (as are all similar subsequent plots). We can see that there is destructive interference at the source on the left—the total pressure amplitude there is smaller than the input amplitude as a result of cancellation with the reflected waves from the opening. This is no surprise as these resonances correspond to troughs in the impedance (i.e. small pressure, large velocity). As the frequency is increased, it can be seen that the destructive interference is less, resulting in larger pressure amplitudes inside the duct (notably at the source). This is a result of the higher frequencies being reflected less strongly by the opening on the right. Instead, the energy is radiated out of the duct, as can be seen by the higher pressure amplitudes (as fraction of the input) outside of the duct for the higher frequencies. For the first few harmonics, the sound radiated out of the end of the duct is only a small fraction of the input. This corresponds to the usual playing frequencies of the flute. One can observe this in reality—typically little sound is radiated from the end of a flute, with the majority coming instead from the source at the mouthpiece. We also note that the 10th harmonic here corresponds to a frequency above the first cut-off, and subsequently we obtain reflected radially varying modes to a significant degree. This would be outside the range of a normal flute, but is included for interest.

We now turn our attention to closed cylindrical ducts. Physically these correspond most closely to a clarinet or a crude brass instrument such as the didgeridoo. The reed

Resonance	kL	Ratio to fundamental	Interval
1	2.96	1	Unison
2	5.92	2.00	Octave
3	8.80	2.97	Octave + Perfect Fifth (-14 cents)
4	11.68	3.95	2 Octaves (-24 cents)
5	14.80	5.00	2 Octaves + Major Third (-14 cents)
6	17.92	6.05	2 Octaves + Perfect Fifth (+17 cents)
7	21.12	7.14	2 Octaves + Minor Seventh (+2 cents)
8	24.00	8.11	3 Octaves (+23 cents)
9	27.10	9.16	3 Octaves + Major Second (+34 cents)
10	30.56	10.32	3 Octaves + Major Third (+42 cents)

Table 4.1 Resonant frequencies of a cylindrical open duct $L = 8h$ and the corresponding musical intervals

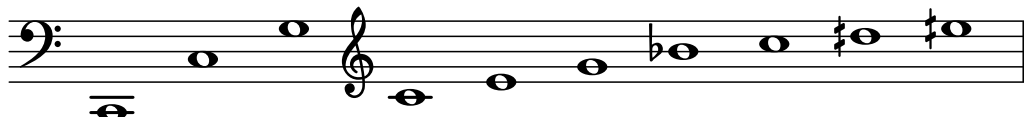


Fig. 4.10 Pitches produced by an open duct $L = 8h$

Resonance	Ratio to fundamental	Interval
1	1	Unison
2	2	Octave
3	3	Octave + Perfect Fifth (+2 cents)
4	4	2 Octaves
5	5	2 Octaves + Major Third (-14 cents)
6	6	2 Octaves + Perfect Fifth (+2 cents)
7	7	2 Octaves + Minor Seventh (-31 cents)
8	8	3 Octaves
9	9	3 Octaves + Major Second (+4 cents)
10	10	3 Octaves + Major Third (-14 cents)

Table 4.2 The harmonic series and the corresponding musical intervals

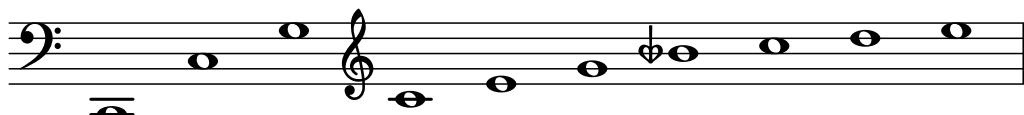


Fig. 4.11 The harmonic series

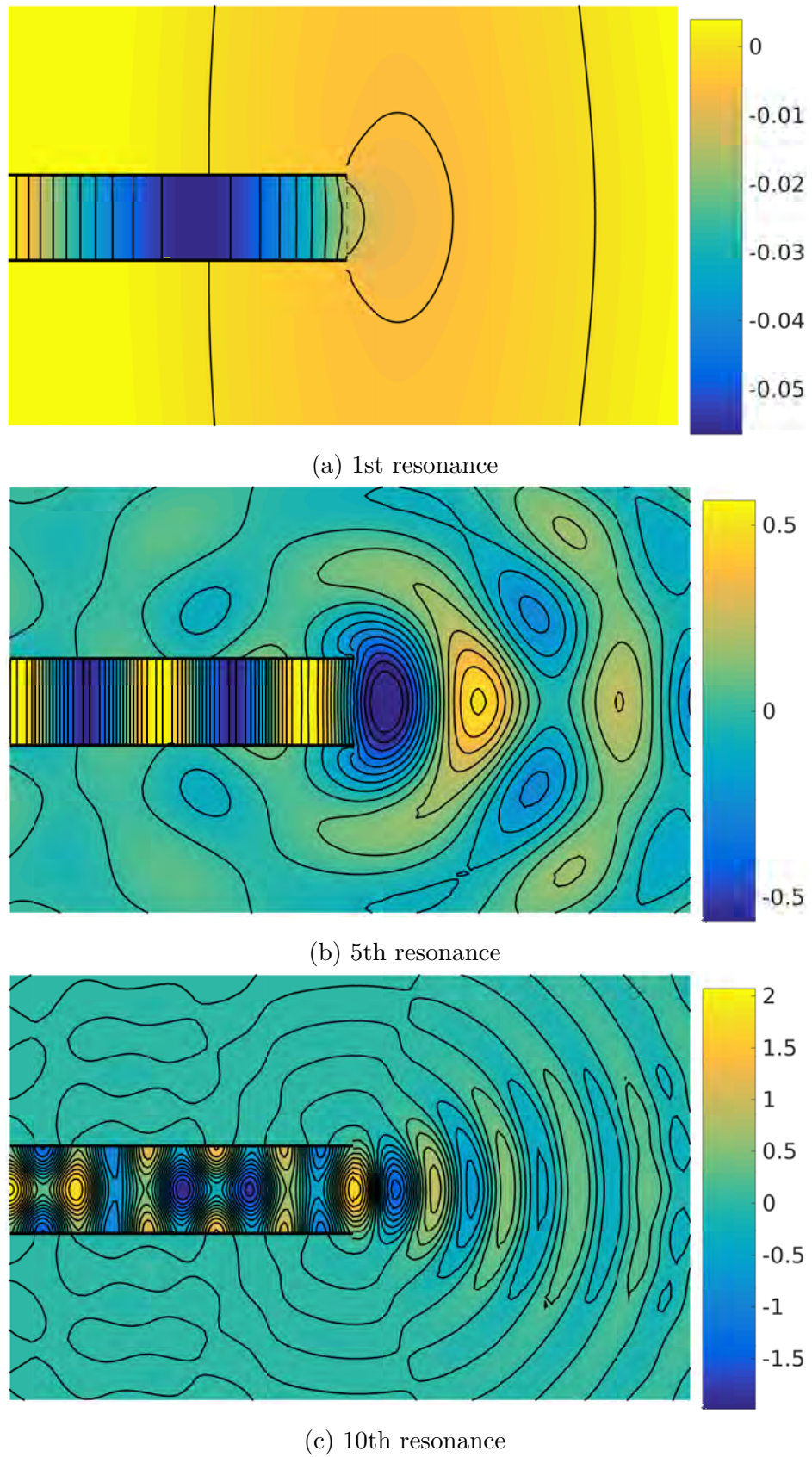


Fig. 4.12 Pressure profiles of the open duct $L = 8h$ at various resonant frequencies.

or the players lips allow very little air to flow and consequently we obtain peaks in the impedance at points of resonance. Table 4.3 shows the resonances produced and figure 4.13 shows the corresponding pitches (again, taking C to be the fundamental). The first thing to observe is that the pitches produced by the resonant frequencies have a much larger gap, lying close to the odd members of the harmonic series. Indeed, this is what is observed in the clarinet—overblowing the clarinet produces pitches a 12th above the fundamental (1 octave + a perfect fifth, or, equivalently 3:1). Also, as the instruments mainly resonates at the odd harmonics, it gives rise to the characteristic timbre of the instrument—a very “square” sound (as the square wave is comprised of only odd harmonics). Another related point to note is that the resonant frequency is much lower than the open duct, with the resonant wavelengths approximately $4L$, $4/3L$, $4/5L$ To contrast the resonant frequencies of the open duct are approximately $2L$, L , $2/3L$... (because of the radiation of energy out of the duct and the end correction, the actual wavelengths differ from these “ideal” values). As a result the clarinet, which is of similar size to the flute or oboe (which shall be addressed in section 4.5.4), can reach much lower notes than either of these two instruments. Also, as the spacing between its harmonics is much larger it has a correspondingly larger overall range.

Such a design is, however, not practicable for regular brass instruments which rely on altering the length of tubing to achieve chromaticism (all of the notes in the 12-TET scale). Such large gaps in pitch between the harmonics would require a significant amount of extra tubing as well as many complex valve mechanisms to achieve all the notes between adjacent harmonics. Instead, makers use the bell effect addressed in the next section.

Figure 4.14 displays some of the associated pressure plots with the closed duct. In contrast to the open duct, we have constructive interference at the source, producing a higher total peak amplitude compared to the input. As with the open duct, this effect diminishes as the frequency is increased—higher frequencies are reflected less strongly by the opening on the right, and more energy is radiated. We also note that the often cited condition of having a pressure node at the open end (giving rise to the ideal resonant wavelengths $4L$, $4/3L$, $4/5L$...) is very poor—the fifth resonance, for example, has a maximum at the opening. This is to be expected—having a pressure node would imply no radiated energy from the duct and hence no sound being radiated. While we have used this condition at the source end, the simplification is vastly easier to study than a full model of the player’s reed or lips and still provides useful information about the radiation from the other end.

Resonance	kL	Ratio to fundamental	Interval
1	1.44	1	Unison
2	4.40	3.06	Octave + Perfect Fifth (+34 cents)
3	7.28	5.06	2 Octaves + Major Third (+5 cents)
4	10.40	7.22	2 Octaves + Minor Seventh (+23 cents)
5	13.20	9.16	3 Octaves + Major Second (+36 cents)
6	16.40	11.38	3 Octaves + Tritone (+11 cents)
7	19.52	13.56	3 Octaves + Major Sixth (+13 cents)
8	22.40	15.56	4 Octaves (-49 cents)
9	25.60	17.78	4 Octaves + Major Second (-18 cents)
10	28.88	20.06	4 Octaves + Major Third (-9 cents)

Table 4.3 Resonant frequencies of a cylindrical closed duct $L = 8h$ and the corresponding musical intervals

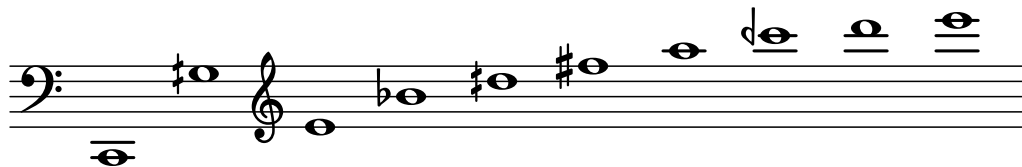


Fig. 4.13 Pitches produced by a closed duct $L = 8h$

We now look at how the aspect ratio of the cylindrical duct affects the properties of the sounds produced. We have already hinted at this effect previously, noting that higher frequency waves are radiated more strongly. By increasing the aspect ratio of the duct, we are effectively reducing the value of kh for each resonant frequency, meaning waves are reflected to a greater extent. Tables 4.4 and 4.5 show the resonant frequencies produced by an open and closed duct respectively with $L = 16h$. We also include the pitches produced by the closed duct (4.5)—the open duct produces approximately the same pitches in 24-TET. It can be seen that for these longer aspect ratio ducts, the resonant frequencies produced align much more closely with the harmonic series in the case of the open duct, and the odd harmonics in the closed duct case. The wavelengths themselves also align to the idealized wavelengths ($2L, L, 2/3L \dots$) and ($4L, 4/3L, 4/5L \dots$) of the open and closed duct respectively.

Plots 4.16 and 4.17 illustrate the pressure patterns produced. We see a significantly smaller peak pressure inside the open duct due to a greater fraction of energy being reflected in antiphase to the incident wave. The emitted radiation also has a smaller amplitude for the same reason—more is being reflected internally. For the fundamental mode, the cancellation at the source is so extreme that numerical instabilities arise in this case—the total pressure at the source is so small that the code becomes unstable

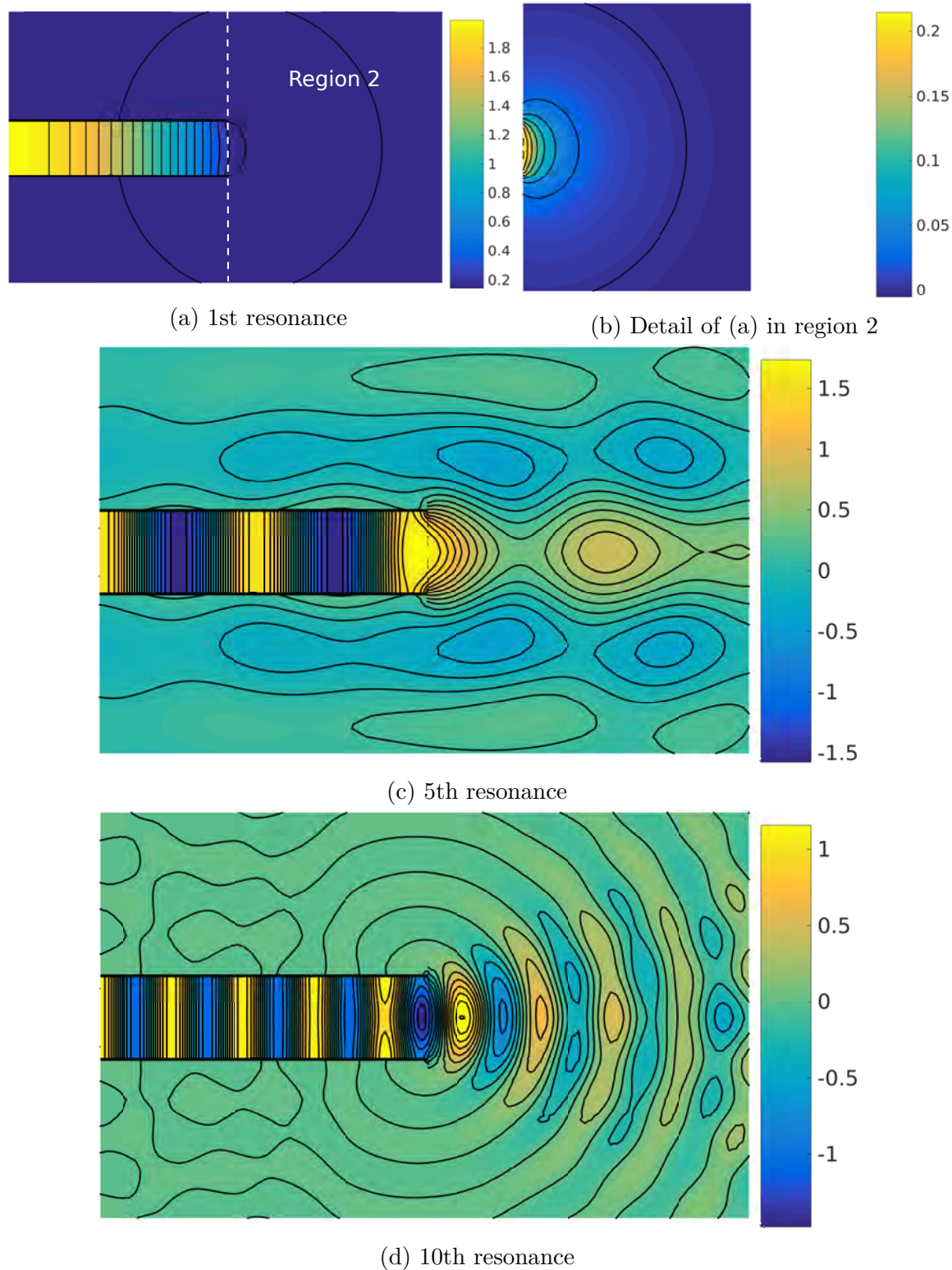


Fig. 4.14 Pressure profiles of the closed duct $L = 8h$ at various resonant frequencies.

Resonance	kL	Ratio to fundamental	Interval
1	3.04	1	Unison
2	6.08	2.00	Octave
3	9.12	3.00	Octave + Perfect Fifth (+2 cents)
4	12.16	4.00	2 Octaves
5	15.12	4.97	2 Octaves + Major Third (-23 cents)
6	18.24	6.00	2 Octaves + Perfect Fifth (+2 cents)
7	21.12	6.94	2 Octaves + Minor Seventh (-44 cents)
8	24.24	7.97	3 Octaves (-6 cents)
9	27.36	9.00	3 Octaves + Major Second (+4 cents)
10	30.48	10.03	3 Octaves + Major Third (-9 cents)

Table 4.4 Resonant frequencies of a cylindrical open duct $L = 16h$ and the corresponding musical intervals

Resonance	kL	Ratio to fundamental	Interval
1	1.52	1	Unison
2	4.56	3.00	Octave + Perfect Fifth (+2 cents)
3	7.60	5.00	2 Octaves + Major Third (-14 cents)
4	10.64	7.00	2 Octaves + Minor Seventh (-31 cents)
5	13.68	9.00	3 Octaves + Major Second (+4 cents)
6	16.72	11.00	3 Octaves + Tritone (-49 cents)
7	19.76	13.00	3 Octaves + Minor Sixth (+41 cents)
8	22.80	15.00	3 Octaves + Major Seventh (-12 cents)
9	25.76	16.95	4 Octaves + Minor Second
10	28.96	19.05	4 Octaves + Minor Third (+2 cents)

Table 4.5 Resonant frequencies of a cylindrical closed duct $L = 16h$ and the corresponding musical intervals

solving towards the exit as the pressure grows. To overcome this we apply a small detuning. In the closed duct the peak pressure internally is much larger than the $L = 8h$ duct, again as the waves are better reflected—this time in phase with the incident wave. The radiated sound is, as with the open duct, much smaller. We therefore see that, while the longer aspect ratio provides a better intonation (closer to pitches on the harmonic series) and also stronger resonances (note the larger impedance peaks in figure 4.9), increasing the response and ease of playing of the instrument, we sacrifice the volume of the instrument by reducing the amount of energy being radiated. This can be overcome somewhat by the addition of a bell, again, addressed in the next section.

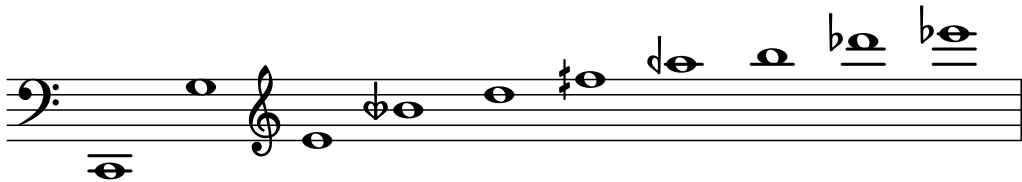


Fig. 4.15 Pitches produced by a closed duct $L = 16h$

Finally, for the cylindrical duct, we shall look at the effect nonlinearity has. The previous results were all produced in the linear regime. We now consider the addition of the nonlinear terms in the governing equations and the allowing of harmonic enrichment. Figure 4.18 compares the impedances of the linear and nonlinear regimes, with Mach number $M = 0.20$, for the $L = 8h$ duct. In this case the effect is rather minimal—little effect can be observed for smaller Mach numbers (hence the rather large value shown). At this value however, we can observe some features. First, the impedance peaks and troughs are of smaller size. This is not surprising based on our previous results—as the wave propagates from the source to the exit, nonlinearity transfers energy into the higher Fourier harmonics. We have already shown that the higher the value of kh , the more the sound is radiated rather than reflected internally. As such, the nonlinearity transfers the energy into higher frequency harmonics that are more easily radiated, reducing the total energy being reflected and reducing the corresponding strength of the resonance.

The next observation is a small shift in the frequency the resonance peaks occur at. As different frequencies have a slightly different effective length of duct due to the end correction effect, when the sound propagates in the nonlinear regime, the individual components of the spectrally enriched wave each reflect from different points. So, instead of a wave propagating and being reflected back from a single fixed point (and if the frequency is chosen correctly, the reflected wave will be in phase or anti-phase with the incident wave at resonance), we now have a wave propagating, transferring energy to higher frequency harmonics, each of which reflect from a different point (as well as getting radiated to a greater degree) causing the variety of harmonics to all be reflected back in different phases. At modest Mach numbers, the result is a flattening and a slight shifting of the resonance peak. At more extreme Mach numbers, we observe an “inversion” of the peak, producing two (or sometimes more) peaks in its place (see the 4th peak in 4.18). This is caused by a combination of both the reduction in the amplitude of the reflected fundamental (causing the primary resonance) together with the increase in amplitude of higher harmonics with slightly altered resonant frequencies adjacent to the resonant frequency of the fundamental.

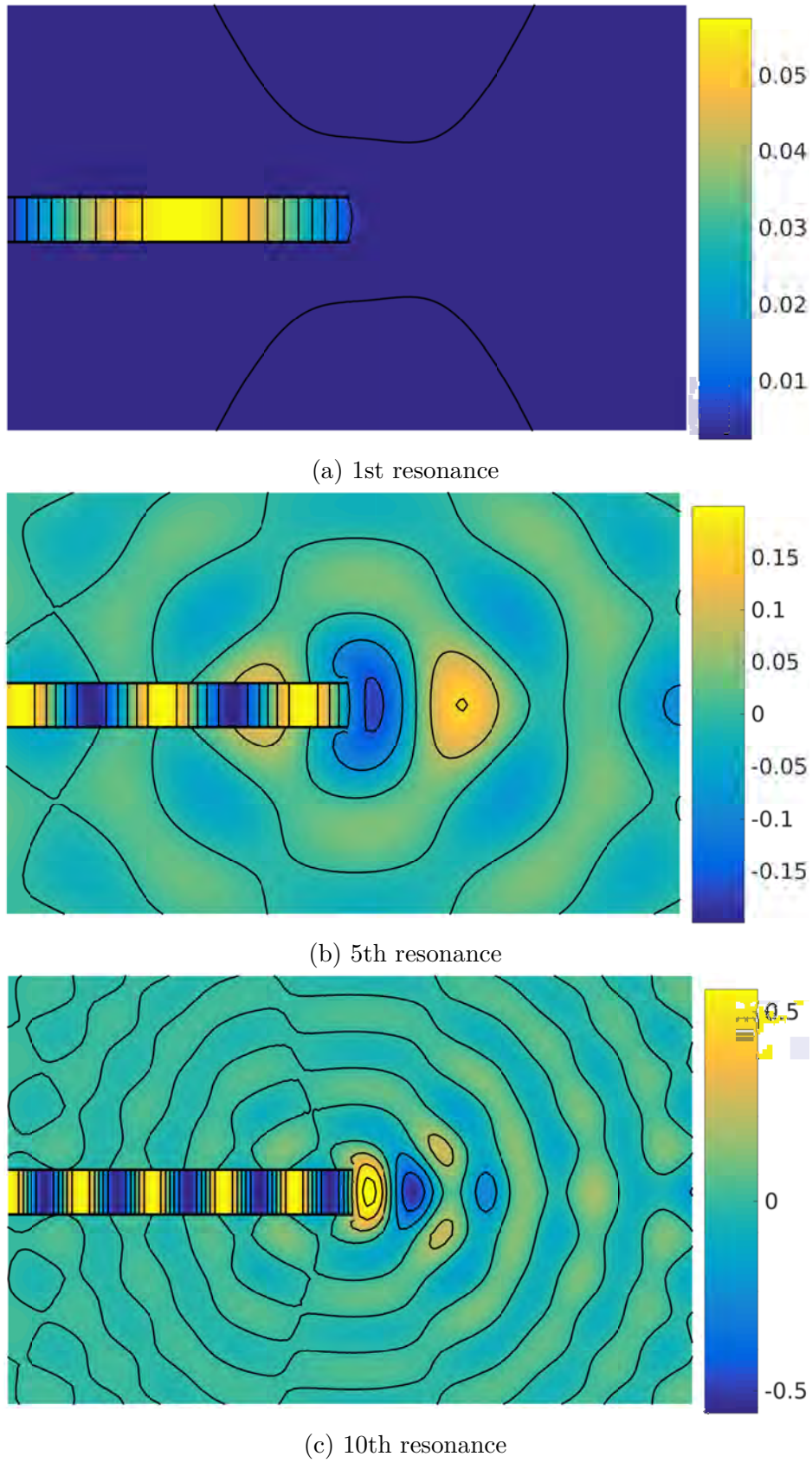


Fig. 4.16 Pressure profiles of the open duct $L = 16h$ at various resonant frequencies.

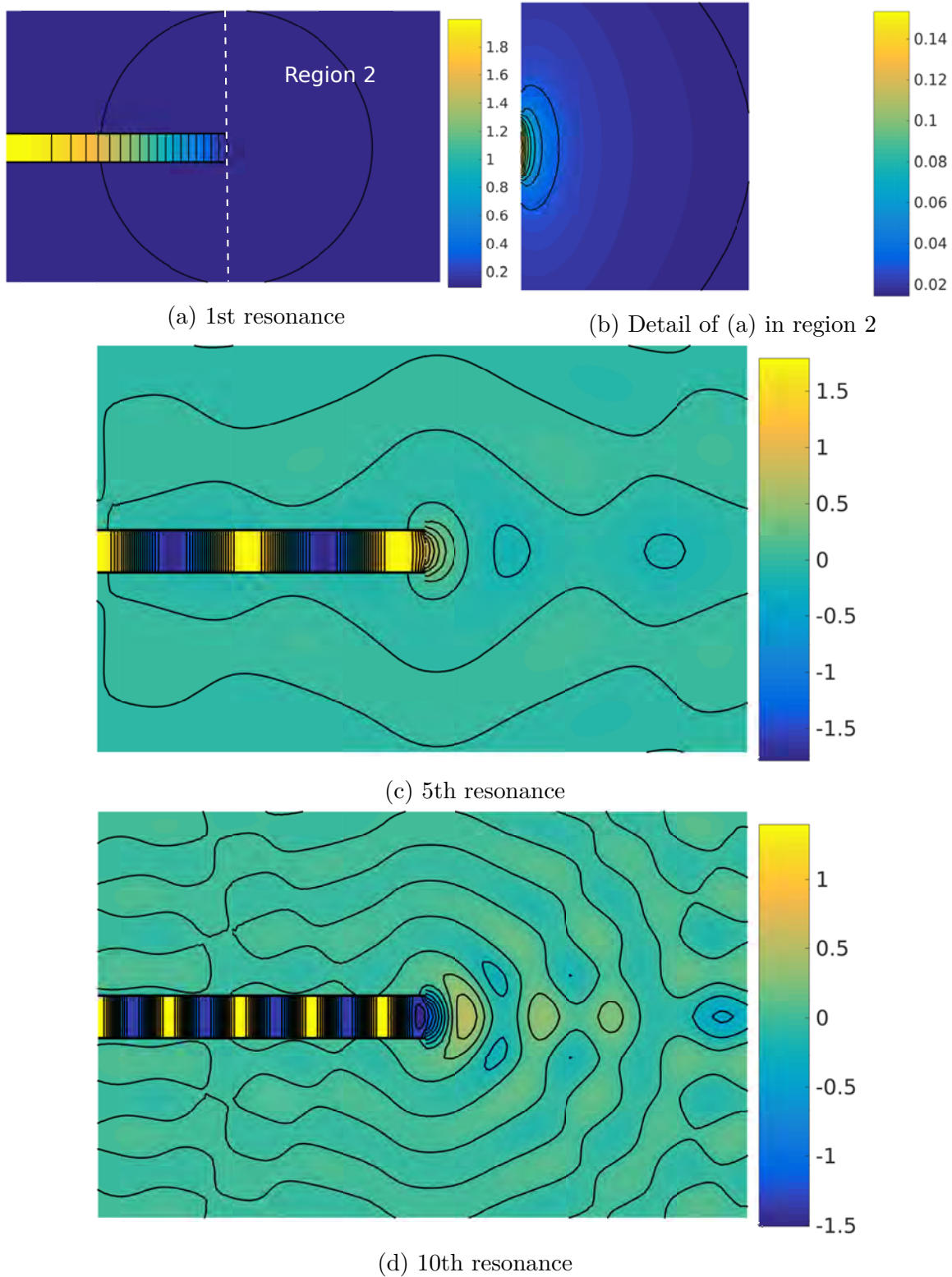


Fig. 4.17 Pressure profiles of the closed duct $L = 16h$ at various resonant frequencies.

For example, in table 4.3 (resonances of the closed duct $L = 8h$) the 4th resonance occurs at $kL = 10.40$. The closest frequencies the second Fourier harmonic could resonate at would be at either $kL = 19.52$ (the 7th resonance) or $kL = 22.40$ (the 8th resonance). These would correspond to a fundamental of either $kL = 9.76$ or $kL = 11.20$. If most of the energy is transferred to the second Fourier harmonic by nonlinear spectral enrichment, we would expect the resonance to shift to either of these two values. We also see that there is an open duct resonance at $kL = 21.12$ corresponding to reflection in anti-phase. If this were the second Fourier harmonic containing most of the energy, the fundamental would occur at 10.56 and we would expect an impedance trough there. Whether these “split” resonances actually occur physically is an open question though we suspect that this effect may be important in the overblowing of instruments—when they are played at sufficiently strongly to jump to new resonances.

Table 4.7 and 4.6 shows the new resonant frequencies and shift in resonant pitch (compared to the linear regime) for the open and closed $L = 8h$ cylindrical ducts at $M = 0.20$. When the resonance is split, the larger peak is chosen. It can be seen that, in this case, the nonlinearity generally causes a slight increase in pitch for most of the resonant frequencies by approximately a similar amount (aside from the lowest resonances). While this amount is small, for most of the resonances it is close to a quarter tone and would be clearly perceptible to even an untrained listener, especially if played against the linear frequency. Unfortunately, these pitch shifts do not appear to match very well what one would observe with the flute and clarinet (see Allen, 2003)—the flute tends to increase in pitch with amplitude (whereas we observed a drop in the fundamental and 2nd harmonic—the two most important for the flute) while the clarinet tends to drop in pitch with amplitude (observed for the fundamental, but not above). The reason is not entirely clear. One possible reason could be that we would need to use a more realistic aspect ratio duct with better aligned resonances. Another is the boundary condition at the inlet—we have not imposed the shape of the waveform at the exit. In reality, a reed could not deform into the higher modal shapes to any great extent. A third possibility is that the observed changes in pitch of the instruments do not result from nonlinear effects in the bore of the instruments, but rather in the source—either the sharp edge of the flute or the reed of the clarinet⁴.

⁴In fact, it is unlikely that the nonlinear effects in the bore would have a significant effect—at typical playing amplitudes the shock formation distance for most woodwind instruments is sufficiently large in relation to the length of the instruments that one would not expect much nonlinear behaviour in the bore.

We examine the modal amplitudes in more detail in figures 4.19 and 4.20. The plots illustrate the harmonic amplitudes through the centreline of the duct $-L \leq s \leq 0$ and the same distance into free space $0 \leq s \leq L$ for various Mach numbers at fixed frequency (so we are not accounting for the change in resonant frequency with amplitude). The plots show the characteristic oscillation in amplitude of standing waves inside the duct—not only for the fundamental, but also the higher harmonics. This confirms we are not only enriching the incident wave, but there is also backwards propagating harmonically rich sound causing various interactions in all the harmonics. As one would expect, the greater the Mach number the more enrichment there is (with a corresponding drop in the strength of the fundamental). This continues outside of the duct, where we see a decrease in fundamental and an increase in the other harmonic amplitudes with Mach number. This corresponds to shift in the spectral centroid—essentially the spectrum’s “centre of mass” and used as a measure of the “brassiness” or “brightness” of the sound (see Gilbert et al., 2008). As the spectral centroid is increased by the increased Mach number, the sound will qualitatively appear brassier.

Finally, we examine plots of the pressure distributions in the nonlinear regime. Figures 4.21 and 4.22 show the resulting pressure distributions produced by an sinusoidal planar incident wave of $M = 0.1$ in both the open and closed cases. Unfortunately, the numerical method is unstable when solving for the pressure at the fundamental when any significant numbers of spatial modes are taken. This is likely due to large numbers of reflected evanescent waves being produced that decay as $s \rightarrow -\infty$. Solving the equations forward leads to instability. Ignoring these, the solution remains stable, though as the shock formation distance is very large no appreciable change in the plot occurs and they are therefore not shown. For the remaining frequencies, we can clearly see shock formation inside the ducts. Such physical behaviour is confirmed in experiments by Hirschberg et al. (1996) for the trombone. We see that in all cases, the pressure distribution is highly non-planar—many of the excited higher frequencies from the harmonic enrichment are above the cut-off frequencies and allow the propagation of non-planar modes. We also observe clear nonlinear behaviour outside the duct. In figure 4.21a one can clearly observe a curved shock front emanating from the opening—as observed by Pandya et al. (2003) and reprinted in figure 1.2. For the 10th resonances, a series of shocks radiating from the opening can be seen—though as the frequency is higher, they are narrower and more difficult to see.

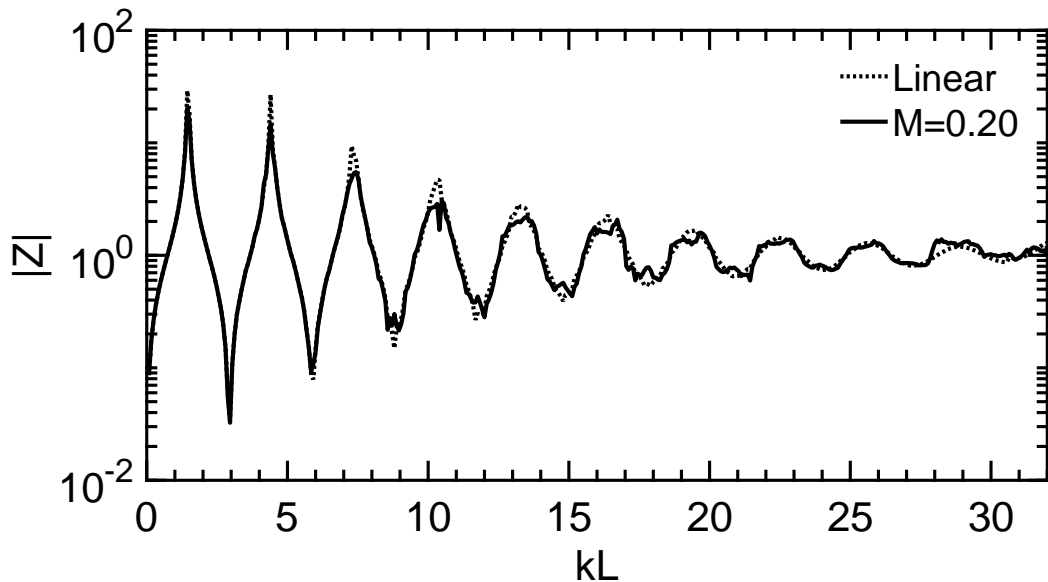


Fig. 4.18 Comparing impedance in the linear and nonlinear regime for a cylindrical duct with $L = 8h$

Resonance	kL	Change in pitch due to nonlinearity
1	2.94	-14 cents
2	5.84	-24 cents
3	8.96	+31 cents
4	12.00	+47 cents
5	15.12	+37 cents
6	18.24	+31 cents
7	21.44	+26 cents
8	24.32	+23 cents
9	27.44	+22 cents
10	30.88	+18 cents

Table 4.6 Resonant frequencies of the open cylindrical duct $L = 8h$ when $M = 0.20$ and the corresponding change in pitch compared with the linear regime

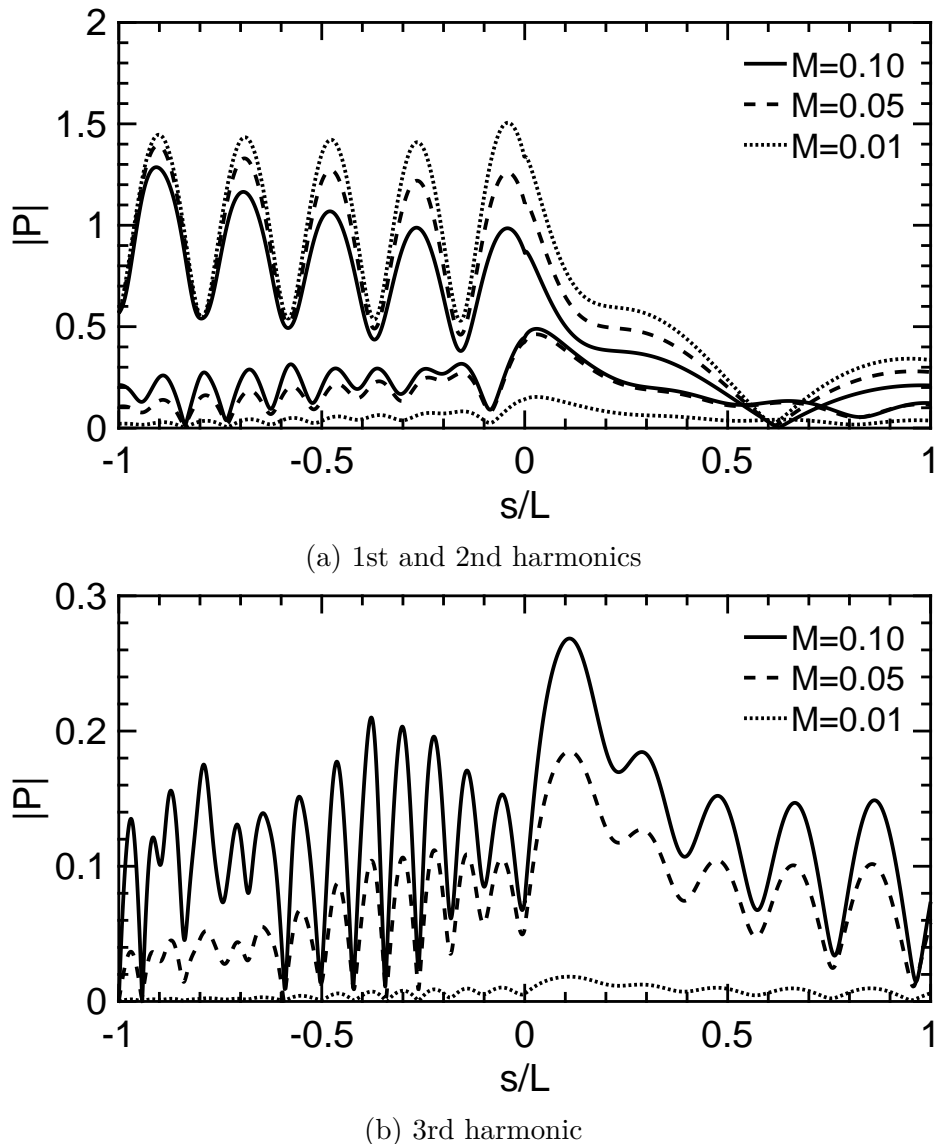


Fig. 4.19 Normalized harmonic amplitudes through the duct along the centreline at the 5th resonance for the open duct

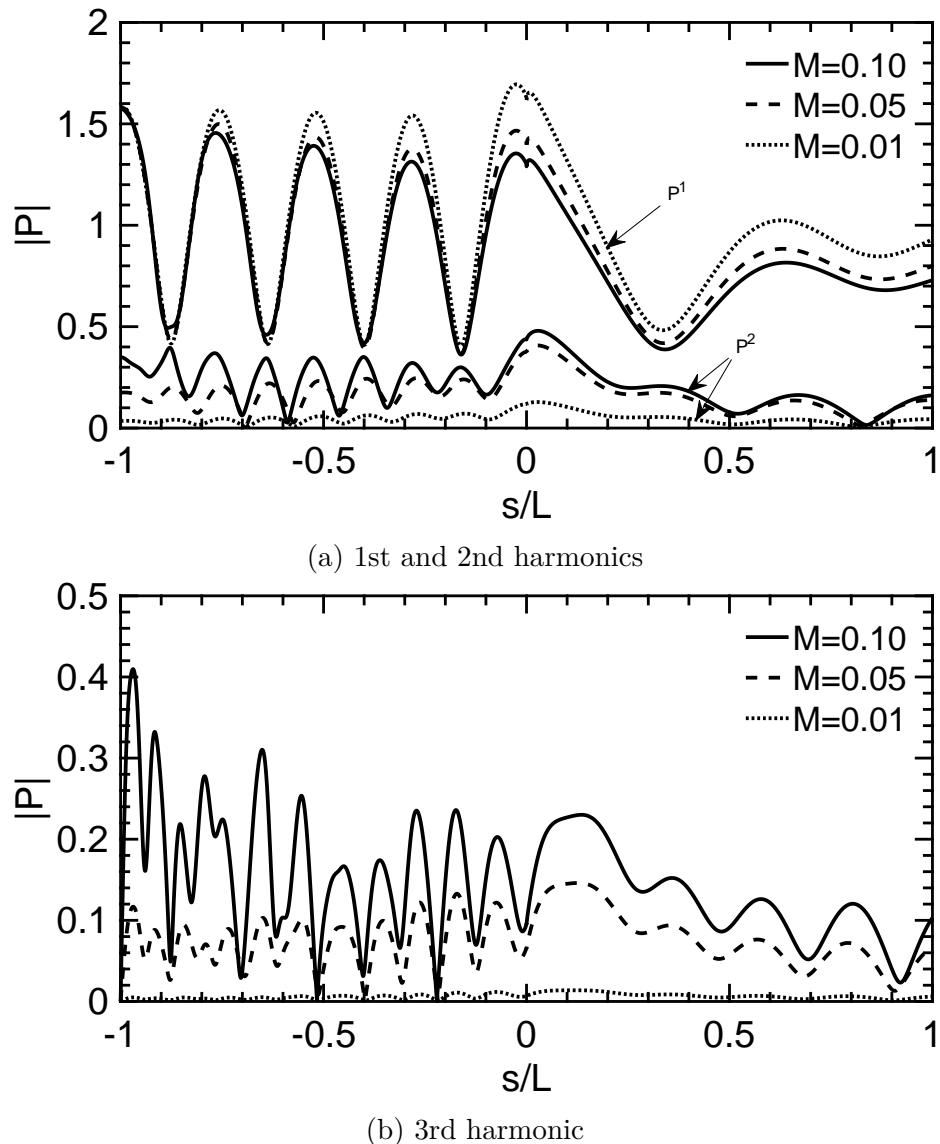
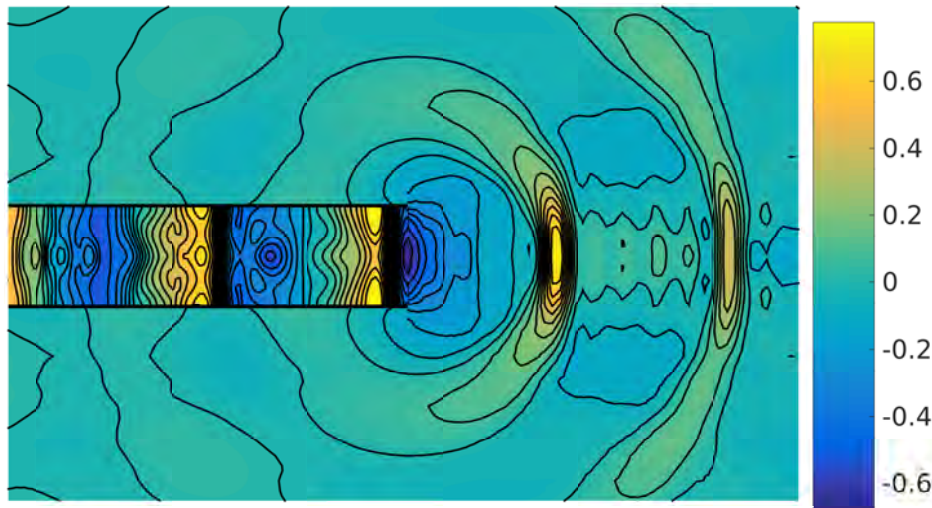
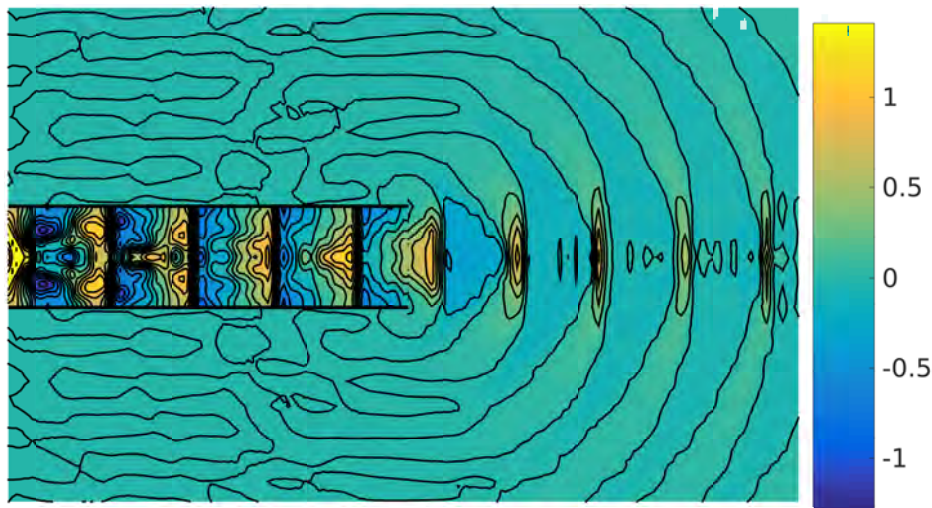


Fig. 4.20 Normalized harmonic amplitudes through the duct along the centreline at the 5th resonance for the closed duct



(a) 5th resonance



(b) 10th resonance

Fig. 4.21 Pressure profiles of the open duct $L = 8h$ at various resonant frequencies in the nonlinear regime $M = 0.1$.

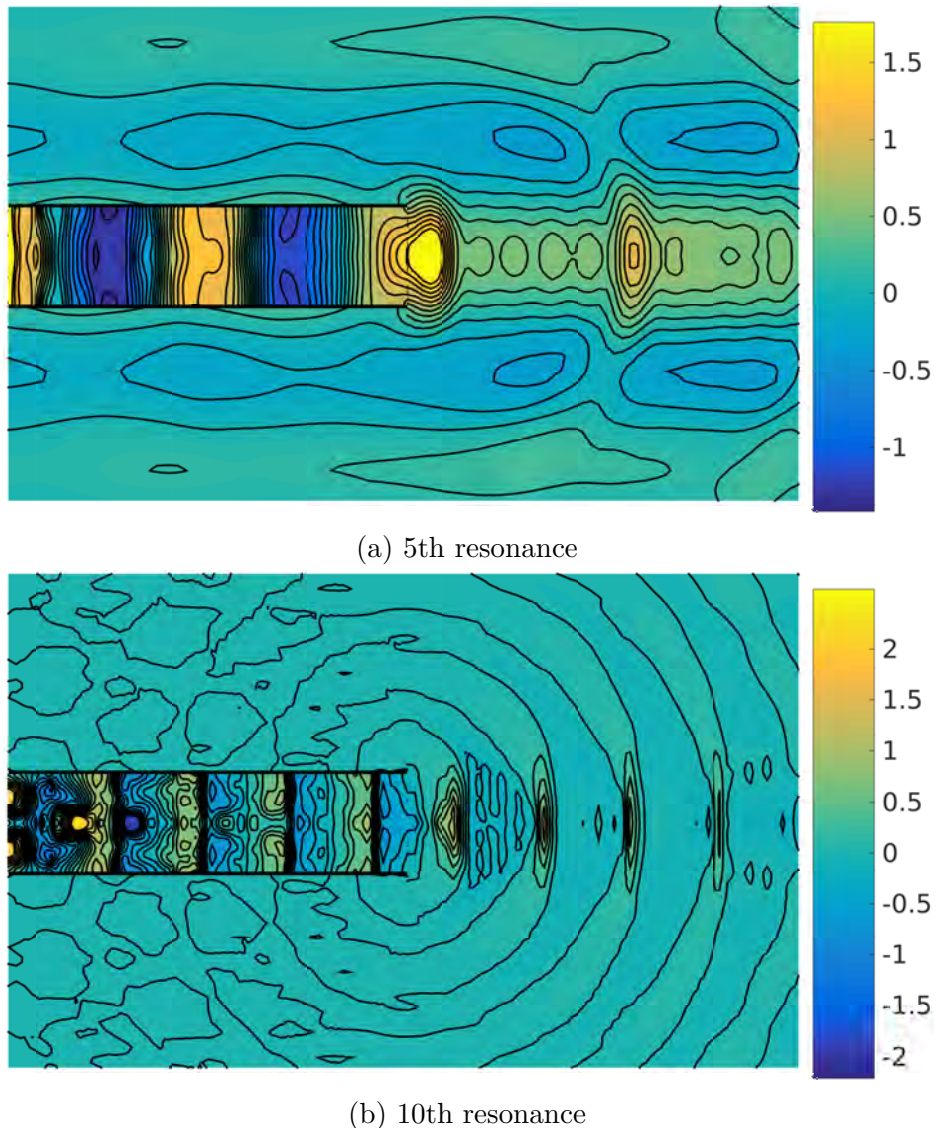


Fig. 4.22 Pressure profiles of the closed duct $L = 8h$ at various resonant frequencies in the nonlinear regime $M = 0.1$.

Resonance	kL	Change in pitch due to nonlinearity
1	1.46	-19 cents [†]
2	4.42	+10 cents
3	7.44	+38 cents
4	10.48	+13 cents
5	13.52	+41 cents
6	16.72	+33 cents
7	19.68	+14 cents
8	22.88	+36 cents
9	25.84	+16 cents
10	28.24	-39 cents

[†] While the nonlinear pitch appears higher compared with table 4.3, using a finer resolution shows the linear peak lies slightly ahead of the nonlinear one

Table 4.7 Resonant frequencies of the closed cylindrical duct $L = 8h$ when $M = 0.20$ and the corresponding change in pitch compared with the linear regime

4.5.3 The Effect of the Bell

We have seen in the previous section how a uniform cylindrical duct provides a good model of both the flute and the clarinet, giving rise to many of their observed characteristics (resonances close to the harmonic series for flutes and odd harmonics for the clarinet). Brass instruments—those whose mechanism of sound generation is the vibration of the players lips—can be thought of as a closed duct at one end (as with the clarinet) and hence can be modelled in the same manner. We have already suggested why the cylindrical duct would, however, make a poor resonator for a brass instrument—the gaps between the resonant frequencies are too large to make it musically useful on its own, and to achieve chromaticism one would need a large amount of extra tubing and complex valve work to attain all of the pitches in between the resonant frequencies. This is in contrast to woodwind instruments like the clarinet, which use finger holes to alter the effective length of the duct to achieve different notes⁵. To overcome these difficulties manufacturers introduce a bell at the end of the instrument—a large flaring of the duct diameter towards the duct exit. We shall examine the effect of doing so in this section.

⁵The medieval cornett—not to be confused with the modern cornet—is however an example of a brass instrument whose pitch is modified by finger holes, though it is a conical duct—dealt with in the next section—and regarded by modern standards as a very difficult instrument to play.

The duct we shall study is the so called Bessel horn, whose radius is given by

$$h(s) = \frac{m}{(-s)^\epsilon}, \quad \text{for } s < 0 \quad (4.61)$$

for parameter m and ϵ . The solution to Webster's horn equation

$$\frac{1}{\pi h^2} (\pi h^2 p')' + k^2 p = 0 \quad (4.62)$$

is

$$p(s) = As^{\epsilon+1/2} J_{\epsilon+1/2}(ks) + Bs^{\epsilon+1/2} Y_{\epsilon+1/2}(ks) \quad (4.63)$$

We therefore do not see the abrupt cut-off for low frequencies of the exponential horn (at least in the plane wave approximation of the Webster's horn equation). The parameter ϵ governs the flare of the bell and the corresponding attenuation of the sound. These ducts are studied particularly for their elegant analytic solution above, as well as their good approximation to the bells of real musical instruments. The specific horn we shall look at is

$$h(s) = \frac{0.25h_0^2}{0.25h_0 - s}, \quad \text{for } -8h_0 < s < 0 \quad (4.64)$$

for duct exit radius h_0 . This duct has the same length to exit radius ratio $L = 8h_0$ as the previous cylindrical duct studied. We can therefore compare the change in resonances caused exclusively by the shape of the duct without the worry of the change in radiation condition at the duct exit.

Figure 4.23 compares the impedance curves produced by this horn and the previous cylindrical duct. It can immediately be seen that the horn shape dramatically raises the pitches of the lowest resonances. Table 4.8 collates the resonances produced by a the horn closed at the throat end and their pitches are illustrated in figure 4.24. These frequencies can now be seen to lie much closer together—almost lying on the harmonic series. Such a brass instrument would now be musically useful—the harmonic series itself contains many of the most important pitches in a given key. Indeed, much of the early classical repertoire for the trumpet relies solely on pitches in the harmonic series (historically played by the natural trumpet without any valve work). Simple tunes may also be played, for example the ‘Last Post’ played by the British military relies solely on pitches from the harmonic series. A much smaller amount of additional tubing would be reacquired to achieve full chromaticism—ignoring the fundamental (for reasons that shall be covered in section 4.6), approximately 41% extra tubing (enough to lower the pitch by 6 semitones) is required to achieve all of the pitches as opposed to 59% (enough for 8 semitones) required for the cylindrical duct. As such,

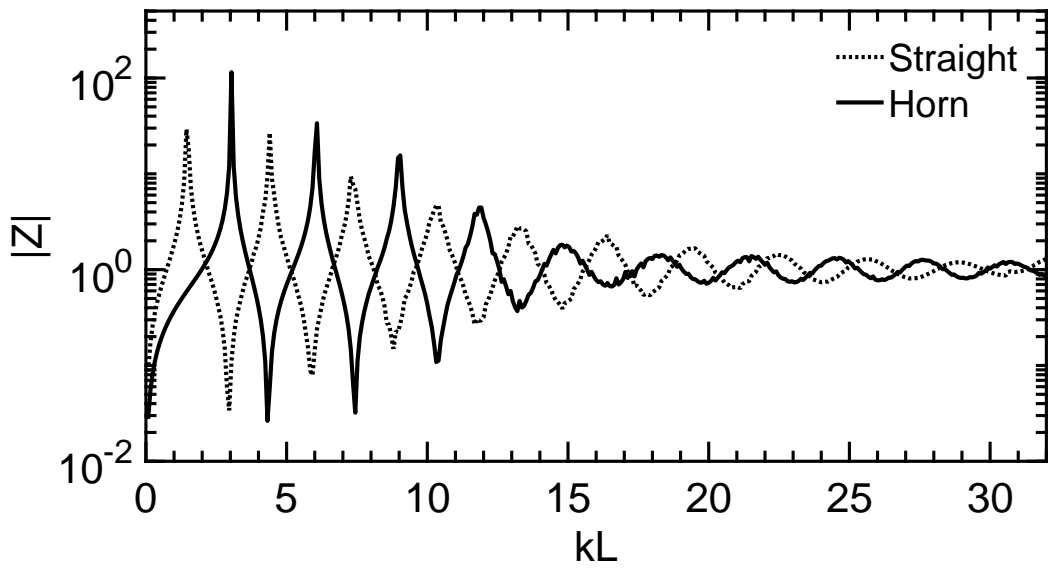


Fig. 4.23 Impedance plots for the horn compared to the equivalent length straight walled duct

this highlights the primary (though less well known) function of the bell—to tune the instrument.

The effect itself is caused by the varying reflectance throughout the duct. We have already demonstrated that as kh decreases, the amount of energy reflected is increased. Therefore at a fixed h in the duct, lower frequencies are more strongly reflected than the high ones. This effectively shortens the length of tubing for longer wavelengths causing the low resonant pitches to raise. For high frequencies the reflectance is much less, so the effective length of the duct is as it would be without any flare. The net effect is to raise the lower resonances, leaving the upper resonances (relatively) unchanged, resulting in a closer spacing of the available harmonics playable by the instrument. We note that as the ratio of length to opening is the same for the cylinder and horn, the strength of the resonances (shown by the size of peaks in impedance) is mostly unchanged—at the termination of both ducts, the reflectivity is the same.

Out of completeness, we can also examine the possible resonances for a horn open at both ends. This would correspond to a flute type instrument with a bell attached. Table 4.9 shows the resonances and figure 4.25 shows the resulting pitches. The pitches produced are both musically unrelated in any meaningful way (at least in a traditional western sense) and too close to provide any significant range. This explains why such instruments do not exist.

Figure 4.26 displays the pressure profiles produced by the duct as well as the details of the radiation pattern produced in region 2 in figure 4.27. We observe similar

Resonance	kL	Ratio to fundamental	Interval
1	3.04	1	Unison
2	6.08	2.00	Octave
3	9.04	2.97	Octave + Perfect Fifth (-13 cents)
4	11.92	3.92	2 Octaves (-35 cents)
5	14.80	4.86	2 Octaves + Minor Third (+40 cents)
6	18.32	6.02	2 Octaves + Perfect Fifth (+10 cents)
7	21.52	7.08	2 Octaves + Minor Seventh (-12 cents)
8	24.64	8.11	3 Octaves (+23 cents)
9	27.60	9.08	3 Octaves + Major Second (+22 Cents)
10	30.72	10.11	3 Octaves + Major Third (+4 cents)

Table 4.8 Resonant frequencies of the horn closed at one end

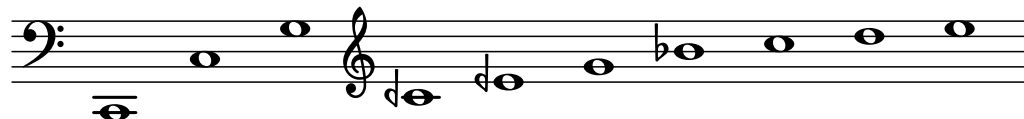


Fig. 4.24 Pitches produced by the horn closed at one end

Resonance	kL	Ratio to fundamental	Interval
1	4.32	1	Unison
2	7.44	1.72	Major Sixth (+41 Cents)
3	10.32	2.39	Octave + Minor Third (+8 cents)
4	13.20	3.06	Octave + Perfect Fifth (+33 cents)
5	16.56	3.83	Octave + Major Seventh (+26 cents)
6	19.92	4.61	2 Octaves + Major Second (+46 cents)
7	23.04	5.33	2 Octaves + Perfect Fourth (-2 cents)
8	26.00	6.01	2 Octaves + Perfect Fifth (+7 cents)
9	29.12	6.74	2 Octaves + Major Sixth (+4 Cents)

Table 4.9 Resonant frequencies of the horn open at both ends

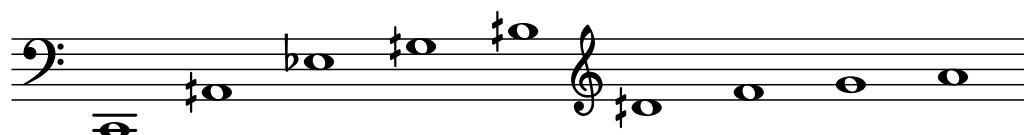


Fig. 4.25 Pitches produced by the horn open at both ends

phenomena to the cylindrical duct—constructive interference between the incident and reflected waves, the effect of which decreases as the pitch is increased, together with an increased amount of radiation with the pitch. As noted in previous chapters, the plane wave approximation is poor in the region of high flare towards the exit, where the wave profile takes on a more spherical shape. Compared to the cylindrical duct, this horn does not radiate as much sound. This is not surprising as the horn has a smaller input, so less energy is being put into the system. In reality, one would instead have a bell of larger radius than a comparable cylindrical duct. We shall analyse this towards the end of this section.

We now examine the effect nonlinearity has on the resonances of the horn. Figure 4.28 compares the linear and nonlinear regimes for different Mach numbers with 4.10 collating the resonant frequencies. It can be seen that nonlinearity has a much more drastic effect on the horn than the cylindrical duct—even for low Mach numbers. We see large amounts of the resonance splitting caused by the nonlinear harmonic enrichment and a strong reduction in the strength of the resonances. This reduction in the strength of the resonance is again caused by transference of energy in higher Fourier modes which are radiated more easily. In addition (when compared with the cylindrical duct), those that are reflected are done so from very different points in the duct—while there is a slight shift in the effective length of the duct for a cylindrical pipe, in the horn this is far more extreme, with the sound effectively being reflected from points all along the duct. As a result there is little coherence. We see that as the Mach number is increased, the peaks and troughs are increasingly governed by the resonances of the second Fourier harmonics of the signal, causing the splitting of the resonances. As the peaks lie close to the harmonic series (particularly for the first few modes) we see that peaks of the second harmonics still remain close to the fundamental. We hypothesise that this nonlinear behaviour is, in part, what results in the “overblowing” characteristic observed in brass instruments—that is when the player increases their playing amplitude sufficiently the instrument jumps to a new resonance. What we are observing here is the shift in the dominant form of reflected energy changing from the fundamental to the second harmonic—it is likely this would cause the player’s lips to resonate at this new frequency an octave up. This effect is particularly strong at the lowest resonances, when those resonances an octave up are also strong and energy is sufficiently reflected. For the higher pitches, the resonances of the second harmonic are weak enough to make this jump harder and the instrument itself behaves more like a loudspeaker. There are, of course, other factors at play such as the tension in the players lips being used to shift to different resonances (particularly the higher ones),

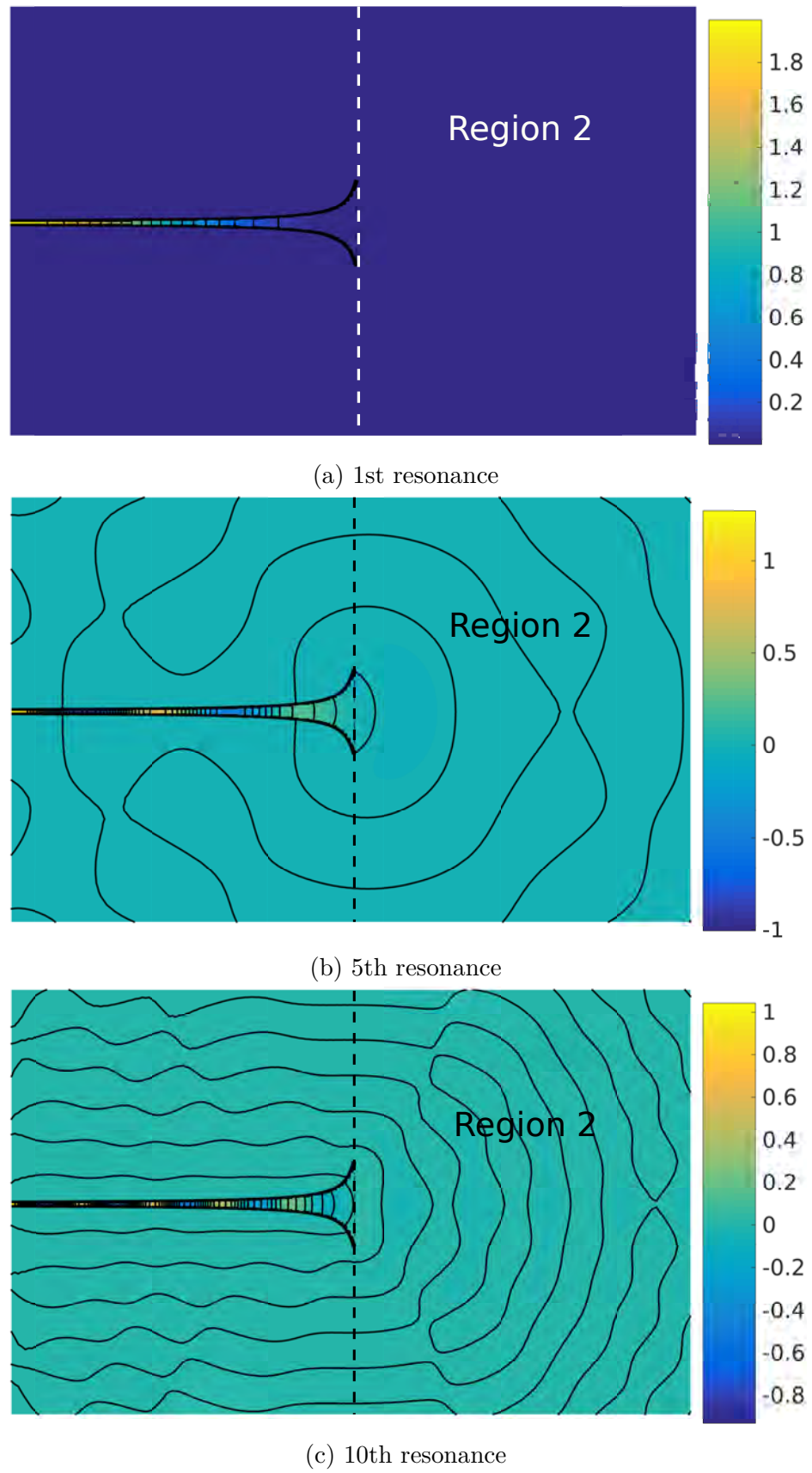


Fig. 4.26 Pressure profiles of the closed horn at various resonant frequencies.

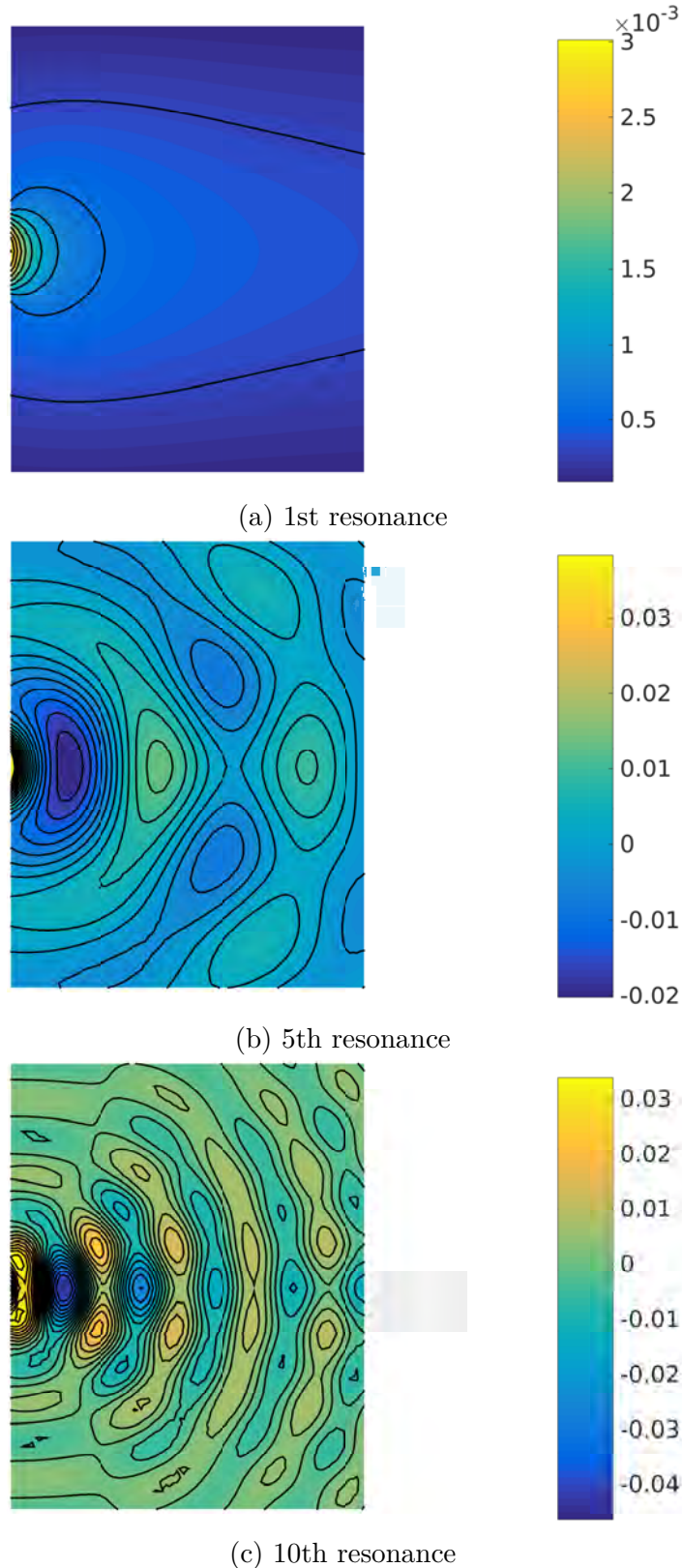


Fig. 4.27 Detail of radiation in region 2 from figure 4.26.

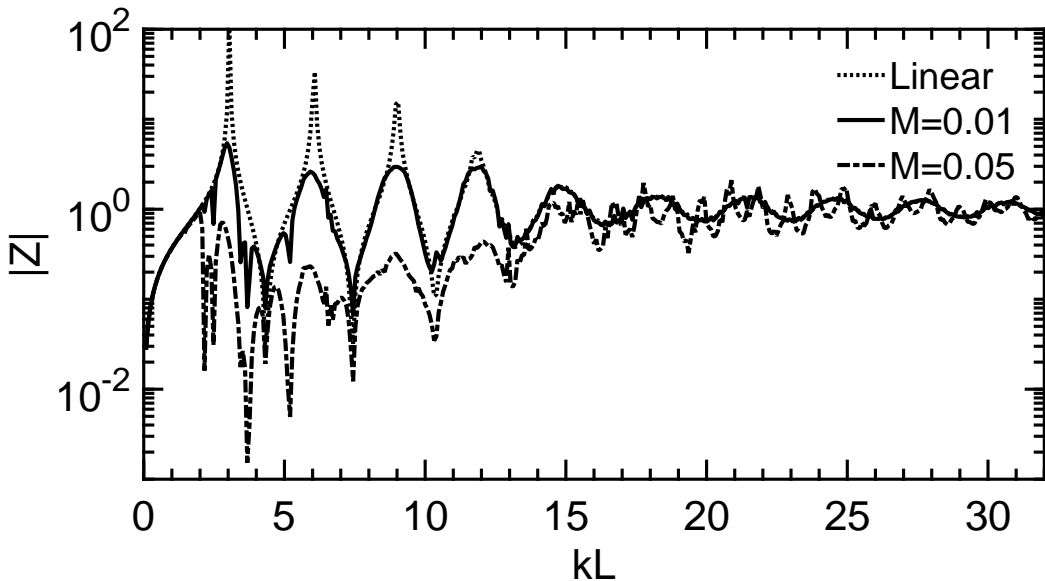


Fig. 4.28 Comparing impedance in the linear and nonlinear regime for the horn

but this may in part explain the effect. Further weight can be given to the argument if one returns to the cylindrical duct—the 2nd harmonics of the signal have a much smaller effect (and also the instruments themselves tend to be shorter implying less nonlinear enrichment) and so we would expect these to be harder to overblow. This is indeed observed with many woodwind instruments such as the clarinet, oboe or saxophone—they have an octave (or register) key to facilitate the production of these higher resonances.

Figures 4.29 and 4.30 show the pressure distributions in the nonlinear regime. Although difficult to see, there is wave steepening and, in the case of the 10th resonance, shock formation inside the duct. The exit distributions show more clearly some of the nonlinear effects: the 5th resonance has a larger amplitude pressure signal being radiated (the higher frequencies are reflected less) and a shock can clearly be seen radiated in the plot of the 10th resonance.

To conclude this section on the effect of the bell, we shall look at a horn with a larger exit radius in relation to the length of the duct. The duct we shall look at is given by radius

$$h(s) = \frac{3L^2/16}{(L/2) - s}, \quad \text{for } -L < s < 0 \quad (4.65)$$

This therefore has $L = 8h_{\text{input}}$ (as with the cylindrical duct) and $3L = 8h_{\text{exit}}$ (an exit three times the radius in comparison to the equivalent cylindrical duct studied). Figure 4.31 shows the resulting impedance plot. Compared to both the cylindrical duct and

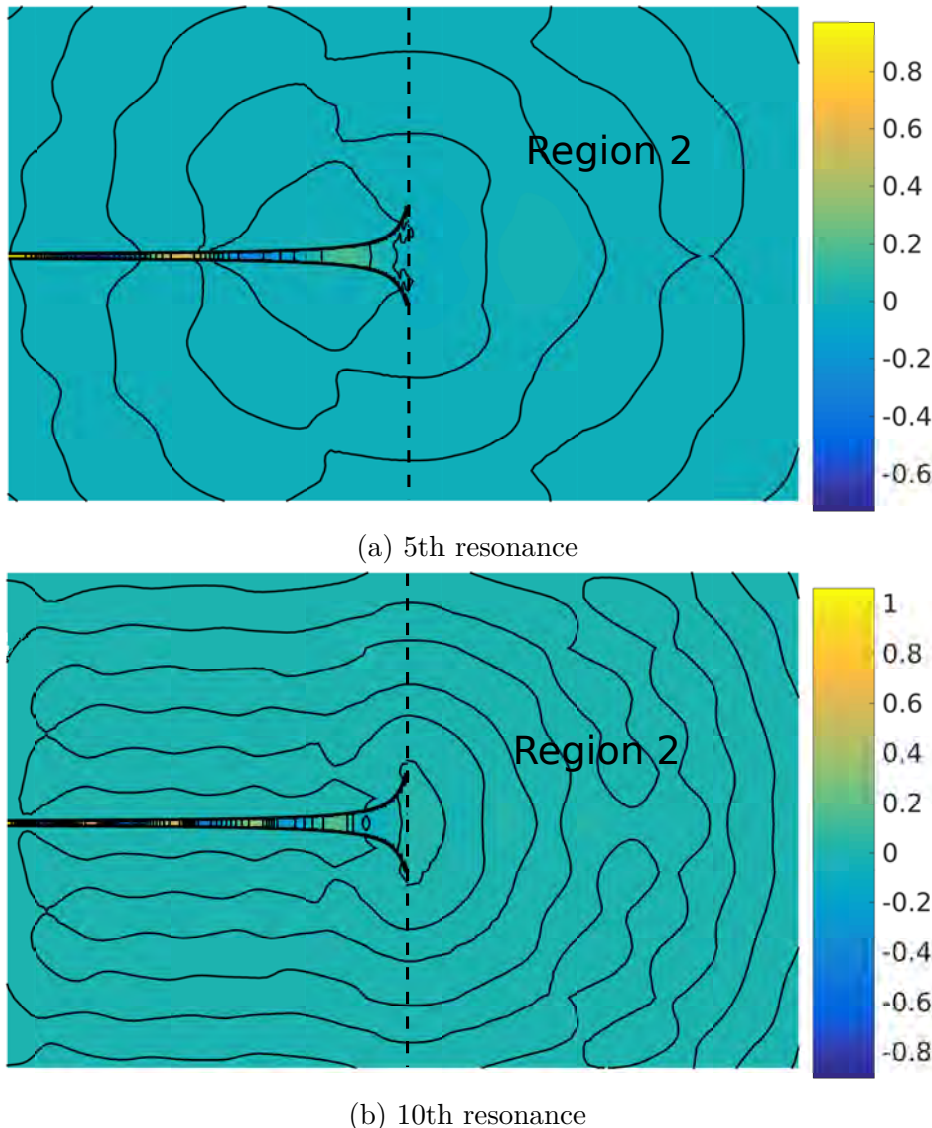


Fig. 4.29 Pressure profiles of the horn at various resonant frequencies in the nonlinear regime $M = 0.05$.

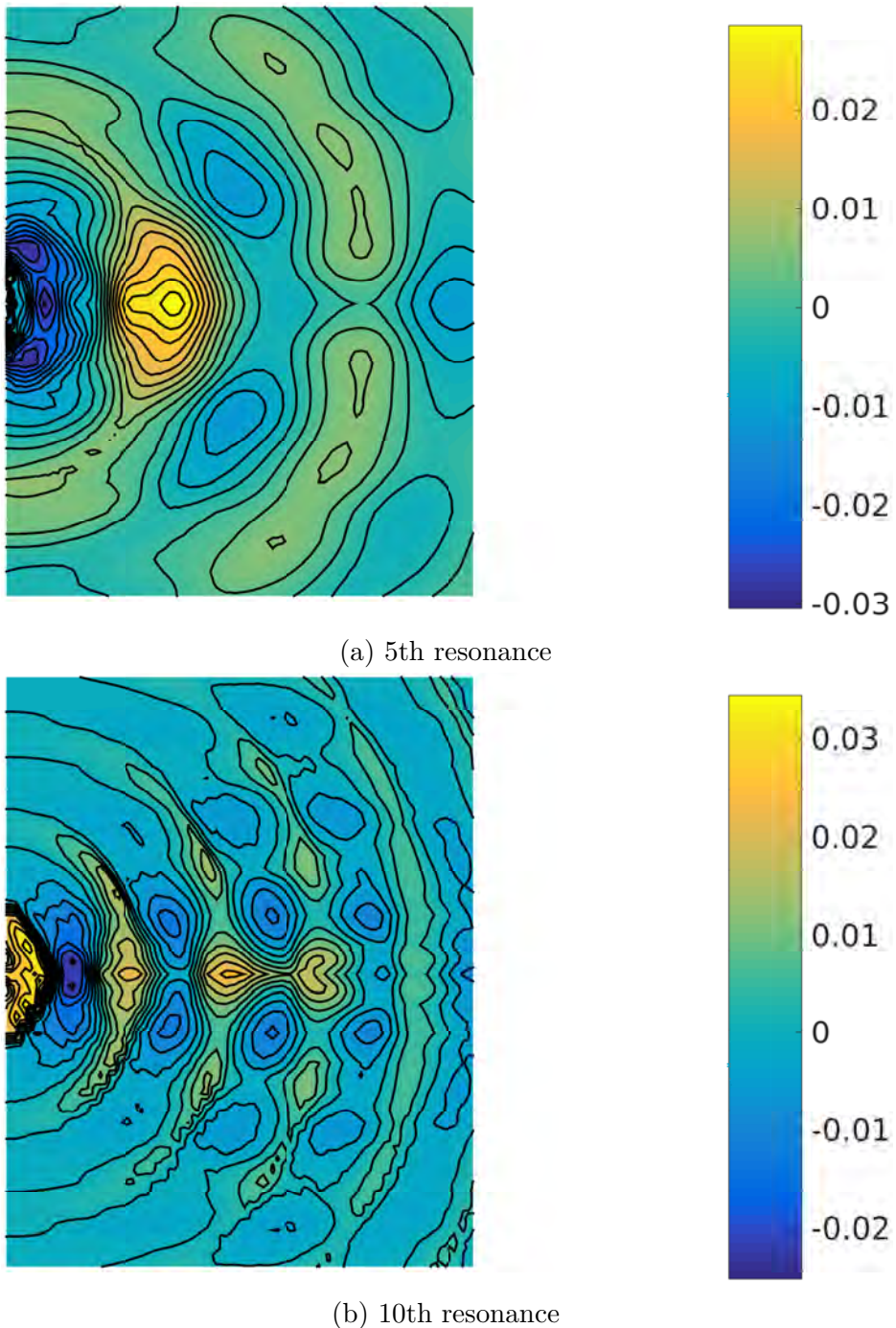


Fig. 4.30 Detail of the exit pressure in region 2 for the horn in the nonlinear regime $M = 0.05$.

Resonance	kL	Change in pitch due to nonlinearity
1	2.00 or 2.80	-725 cents or -68.40 cents
2	5.92	-46 cents
3	8.96	-15 cents
4	12.08	+11 cents
5	15.44	+73 cents
6	17.76	-53 cents
7	20.88	-52 cents
8	24.96	+22 cents
9	27.92	+20 cents
10	30.96	+13 cents

Table 4.10 Resonant frequencies of the horn when $M = 0.05$ and the corresponding change in pitch compared with the linear regime

the previous horn studied, we can see a marked decrease in the size of the peaks as the frequency is increased—the duct itself does not resonate particularly strongly, but rather radiates most of the energy. Indeed, after the first few peaks there is no real resonance observed and the instrument acts more like a loudspeaker. This is sometimes referred to as the cut-off frequency for an instrument (not to be confused with the modal cut-off frequency usually discussed in this thesis). This increased radiation can be seen in figure 4.32—much larger amplitudes propagate outside of the duct in comparison to the cylindrical duct. This therefore illustrates the second and more well known function of the horn—to make the instrument louder by increasing the amount of energy being radiated from a given size duct. The consequence of this however, as we have seen in the impedance plot, is that the strength of the resonances is also reduced making the instrument harder to play. A balance must therefore be struck by instrument manufacturers between these two aspects. Typically strong reflection of the first few resonances is good for ease of playing, while strong radiation of the higher harmonics is good for volume and brightness of sound.

4.5.4 Conical Ducts

The next duct we shall look at is, in fact, a special case of the Bessel horn with $\epsilon = -1$ —the conical duct. Well known conical ducts closed at the playing end are the oboe and saxaphone (the soprano saxaphone is essentially a conical version of the clarinet). From the Bessel horn solution to Webster's horn equation (4.63) with

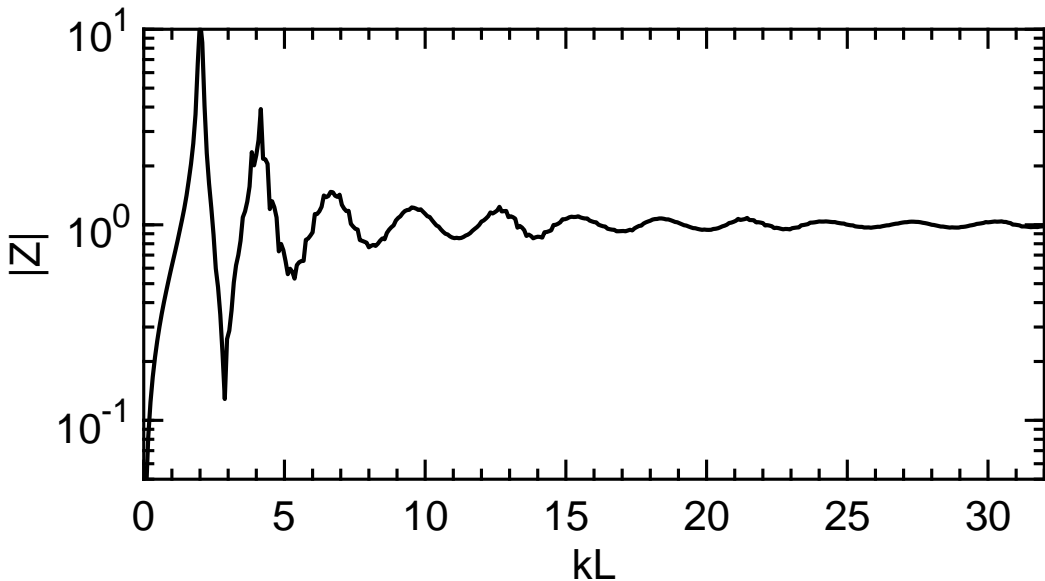


Fig. 4.31 Impedance of the horn given by (4.65)

$\epsilon = -1$, we obtain the solution

$$p(s) = A \frac{\cos ks}{s} + B \frac{\sin ks}{s} \quad (4.66)$$

for a horn extending from $0 < s < \infty$. We therefore expect in an idealised duct of length L , for the resonances to occur at the solutions of $\sin(kL) = 0$. That is $k = \pi/L, 2\pi/L, 3\pi/L, \dots$. This is in contrast to the idealized cylindrical duct closed at one end, whose resonances occur as solutions of $\cos(kL) = 0$. That is $k = \pi/(2L), 3\pi/(2L), 5\pi/(2L), \dots$. We would therefore expect the harmonics of the closed conical duct to lie on the harmonic series, but such an instrument to have a smaller range than the comparable cylindrical duct. Figure 4.33 shows the results for a conical duct

$$h(s) = (9L/8 + s)/9, \quad \text{for } -L < s < 0 \quad (4.67)$$

Again, this duct has the same exit ratio to length $L = 8h_{\text{exit}}$ as the cylindrical duct studied previously, so the reflection at the open end is comparable. Indeed, we see that the lower resonances of the cone, closed at the playing end, are shifted up. Table 4.11 displays the resonances and figure 4.34 shows the resulting pitches. We see that the resonant frequencies are closely aligned to the harmonic series—what is observed by both the oboe and saxophone. In contrast to the clarinet, which is of comparable length to the two aforementioned instruments, as the resonances are shifted up in the conical duct, the lowest playing notes are much higher. Also, as the spacing is much smaller,

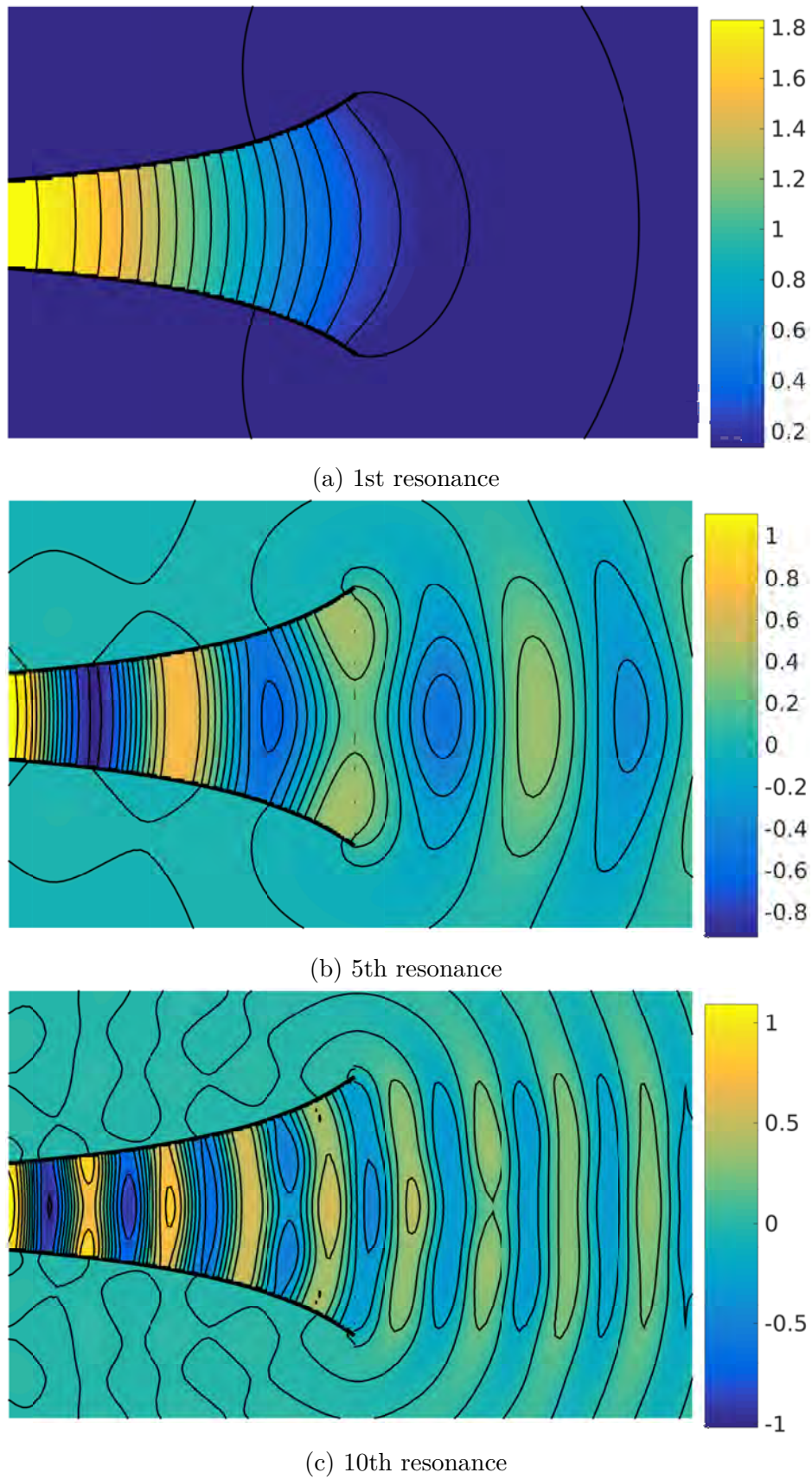


Fig. 4.32 Pressure profiles of the horn given by (4.65).

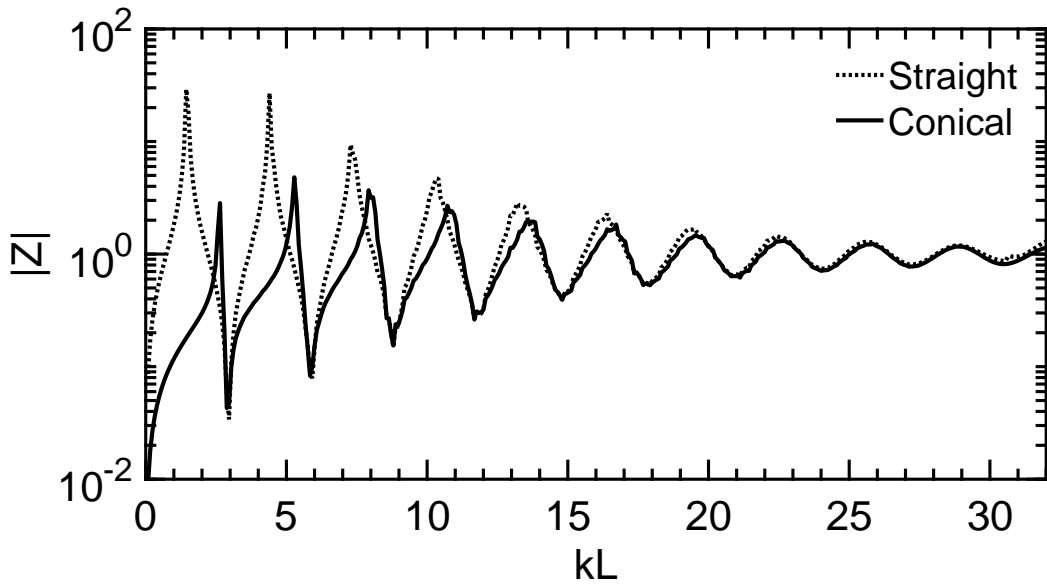


Fig. 4.33 Impedance plots for the conical duct compared to the equivalent length straight walled duct



Fig. 4.34 Pitches produced by the conical duct closed at one end

the oboe and soprano saxophone have a much smaller range. We previously noted that as the cylindrical duct only resonates at the odd harmonics, it is responsible for the square profile of the clarinet waveform and sound. The conical duct, on the other hand, has the full spectrum of harmonics and hence a correspondingly different timbre, richer in high harmonics. The difference in timbre between the soprano saxophone and the oboe is largely accounted for by the sound production means—a single reed for the former and double reed for the latter—though often, due to their similarity in tone, they can be substituted for each other in performance.

As an aside, one may have noticed the lack of shift in the resonant frequencies of the conical duct open at both ends (the impedance troughs). This would correspond to a conical flute. The resonant frequencies are displayed in table 4.12 and the corresponding pitches in figure 4.35. We see, that the resonances produced remain very close to the harmonic series. In fact, prior to the development of the Boehm flute, most flutes did have a conical shape (traditional flutes such as the tin whistle or recorder do indeed have a conical bore—though the duct decreases in width from the input). Such a

Resonance	kL	Ratio to fundamental	Interval
1	2.64	1	Unison
2	5.28	2.00	Octave
3	7.92	3.00	Octave + Perfect Fifth (+2 cents)
4	10.72	4.06	2 Octaves (+26 cents)
5	13.76	5.21	2 Octaves + Perfect Fourth (-42 cents)
6	16.72	6.33	2 Octaves + Minor Sixth (-4 cents)
7	19.52	7.39	2 Octaves + Major Seventh (-36 cents)
8	22.72	8.61	3 Octaves + Minor Second (+26 cents)
9	25.84	9.79	3 Octaves + Minor Third (+49 Cents)
10	28.88	10.94	3 Octaves + Perfect Fourth (+41 Cents)

Table 4.11 Resonant frequencies of the conical duct closed at one end

Resonance	kL	Ratio to fundamental	Interval
1	2.88	1	Unison
2	5.84	2.03	Octave (+23 cents)
3	8.80	2.97	Octave + Perfect Fifth (+34 cents)
4	11.68	4.06	2 Octaves (+23 cents)
5	14.80	5.14	2 Octaves + Major Third (+34 cents)
6	17.92	6.13	2 Octaves + Minor Sixth (-35 cents)
7	21.12	7.33	2 Octaves + Minor Seventh (-49 cents)
8	24.00	8.33	3 Octaves + Minor Second (-30 cents)
9	27.12	9.42	3 Octaves + Minor Third (-18 Cents)
10	30.48	10.58	3 Octaves + Perfect Fourth (-16 Cents)

Table 4.12 Resonant frequencies of the conical duct open at both ends

change has an effect on both the construction and slight variation in timbre, with, as we have shown here, little change in the resonant pitches produced.

Looking at the pressure profiles (figures 4.36 and 4.38 for the closed and open duct respectively, together with the exit details 4.37 and 4.39), there is little to be said that has not been previously mentioned. For the open conical duct, at the higher resonances the pressure at the input (on the left) is the largest throughout the duct, despite there being destructive interference from the reflected waves. This is because the wave amplitude decays sufficiently quickly that the “maximum” of the standing wave is in fact lower in amplitude than the (almost) node at the source (compare with the 1st resonance in which this is not the case). The radiation is less in amplitude than the equivalent cylindrical duct—again, as with the horn studied, this is because

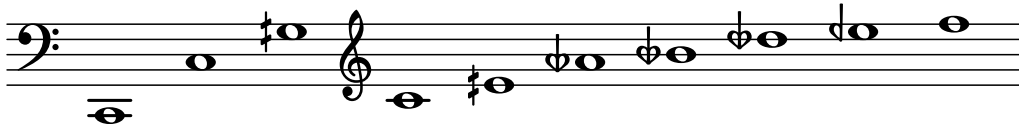


Fig. 4.35 Pitches produced by the conical duct open at both ends

Resonance	kL	Change in pitch due to nonlinearity
1	2.48	-108 cents
2	5.20	-26 cents
3	8.00	+17 cents
4	10.88	+26 cents
5	13.84	+10 cents
6	16.80	+8 cents
7	19.76	+21 cents
8	22.88	+12 cents
9	25.84	0
10	29.12	+14 cents

Table 4.13 Resonant frequencies of the closed conical duct when $M = 0.10$ and the corresponding change in pitch compared with the linear regime

we have a smaller input, so less energy going into the system. For a comparable source radius, we would expect the cone to be a superior radiator.

Again, as with the previous ducts, we shall look at the effect of nonlinearity. Figure 4.40 shows the results. Similarly to the cylindrical duct, we see a slight pitch shift—the first two resonances are lowered in pitch (the fundamental by a significant amount) and the remaining are raised slightly by a small but noticeable amount. The flattening of pitch with increased playing volume in the first two registers of the saxophone and oboe is indeed observed in practice (Allen, 2003). We do not see a significant amount of the splitting of the resonances, suggesting a weaker effect on the total resonance from the higher Fourier harmonics when compared to the horn. This gives further credence to the suggestion that this effect is responsible for the overblowing of wind instruments—both the saxophone and oboe are difficult to overblow without the aid of the octave key.

Figures 4.41 and 4.42 show the change in pressure distribution as nonlinearity is added. The uniform increase in duct width is sufficiently large to prevent the formation of shock waves—the energy is spread out too quickly. This is in contrast to the horn we studied which, although having rapid flare towards the exit, had a long enough section of relatively mild duct width change to facilitate shock formation. This can be

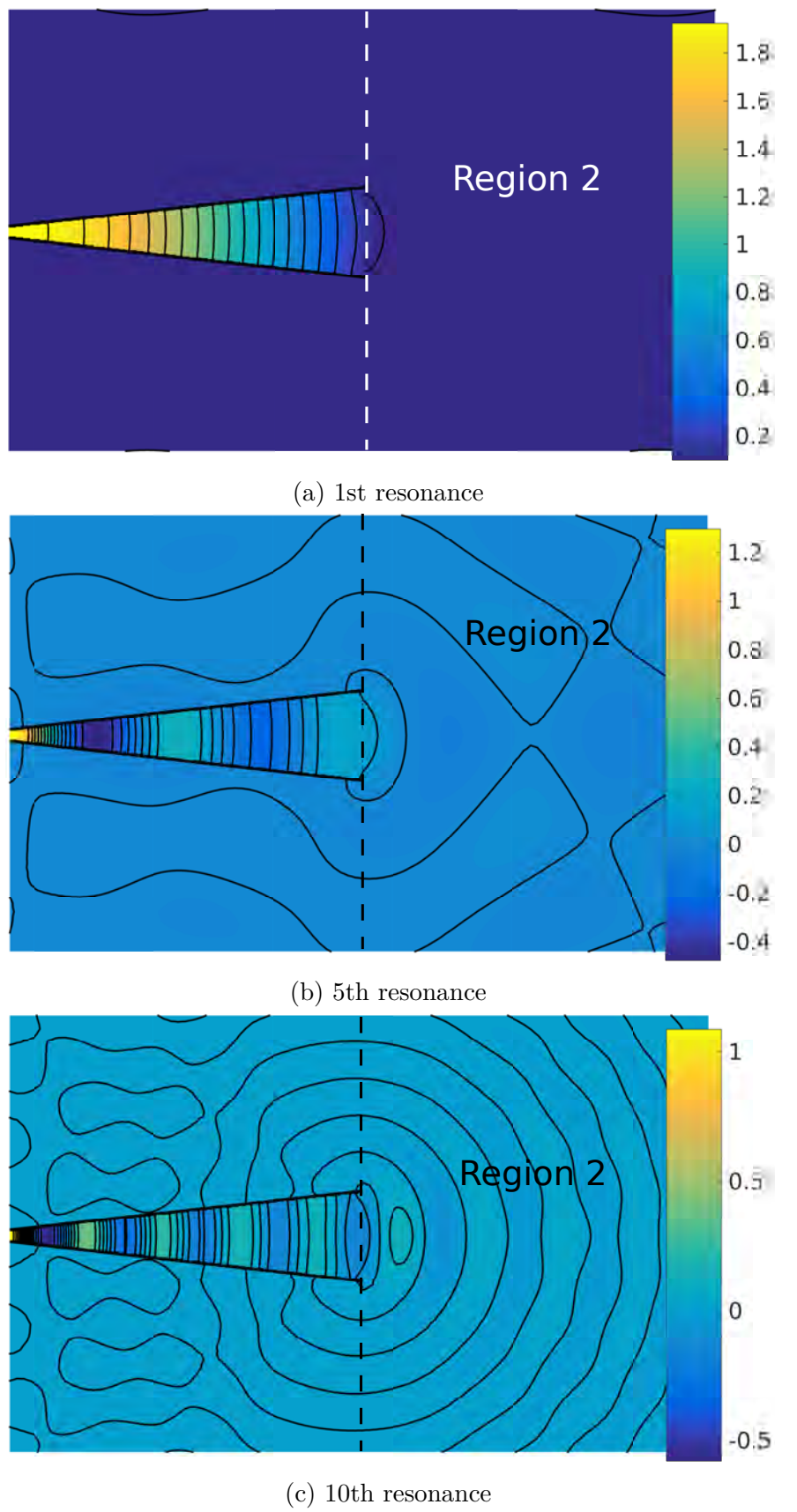


Fig. 4.36 Pressure profiles of the closed conical duct at various resonant frequencies.

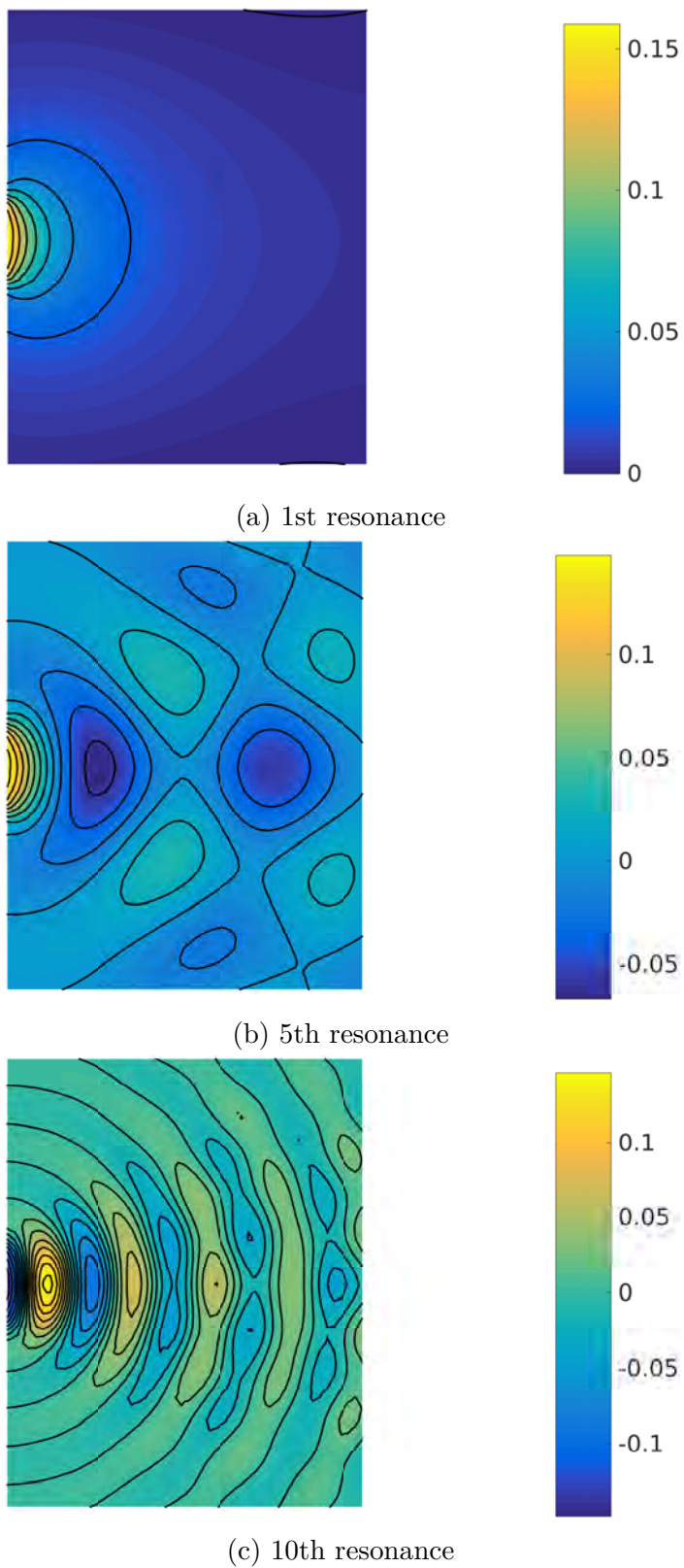


Fig. 4.37 Detail of radiation in region 2 from figure 4.36.

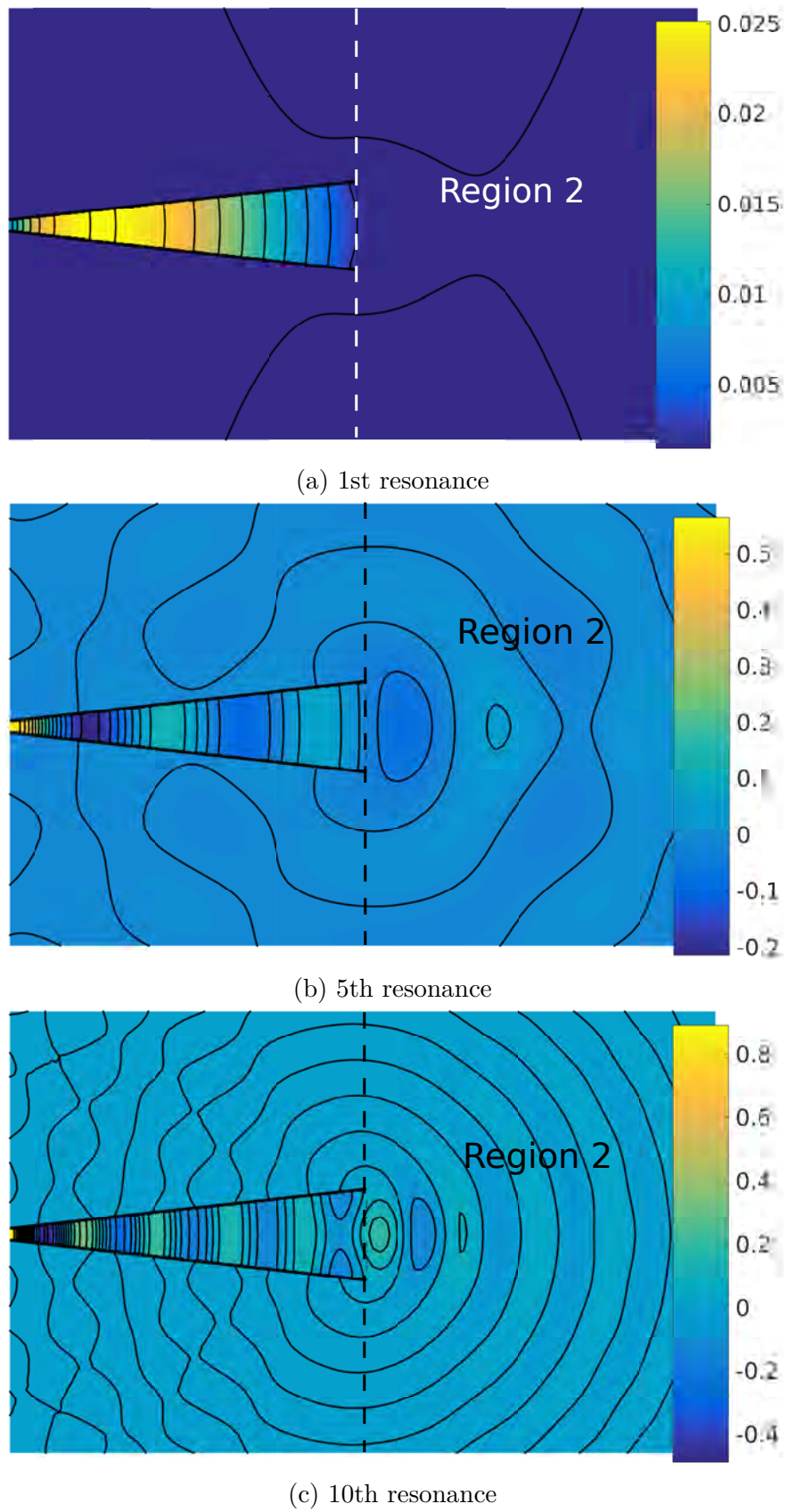


Fig. 4.38 Pressure profiles of the open conical duct at various resonant frequencies.

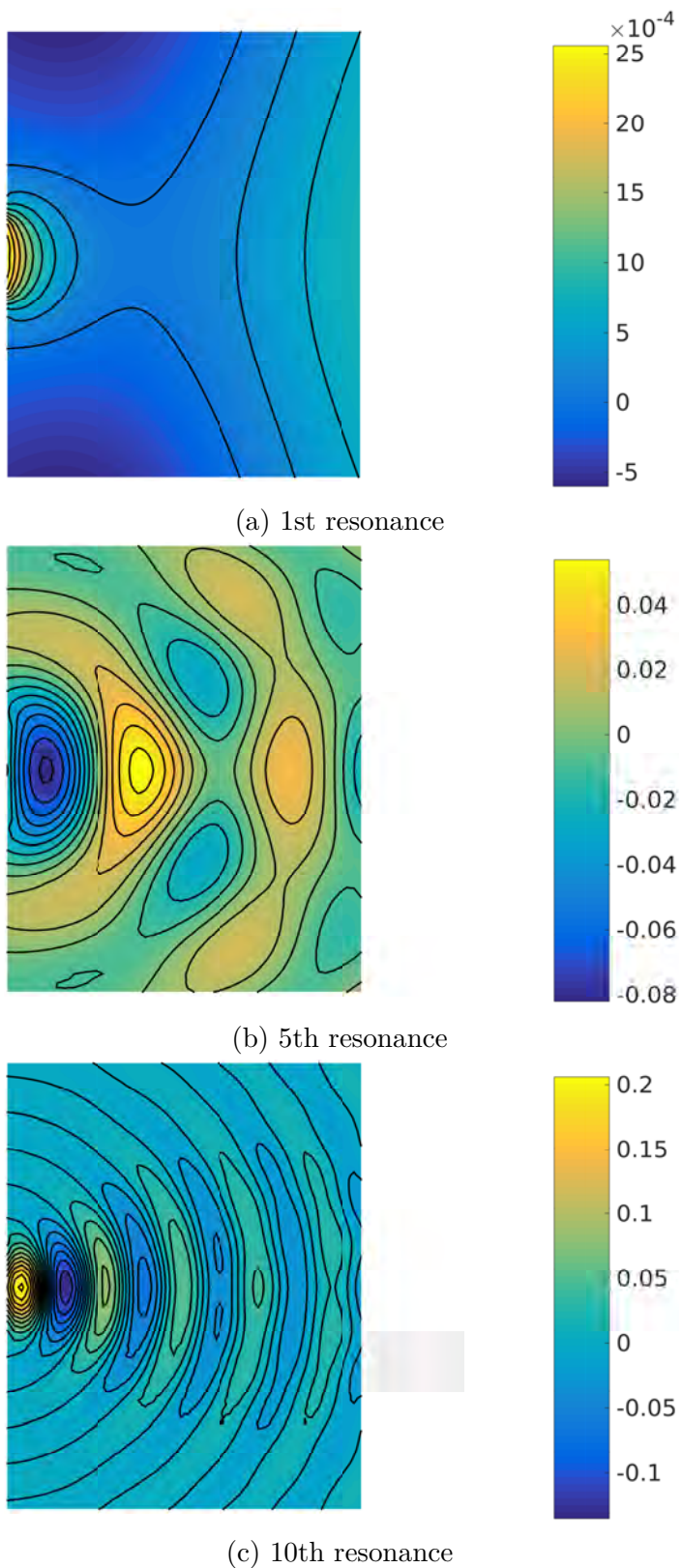


Fig. 4.39 Detail of radiation in region 2 from figure 4.38.

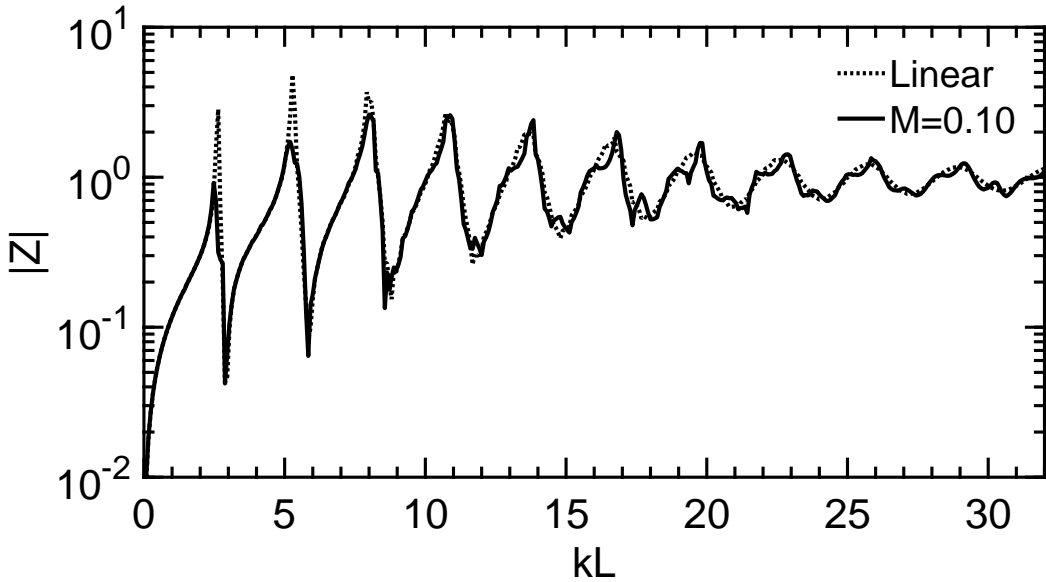


Fig. 4.40 Comparing impedance in the linear and nonlinear regime for the conical duct

quantified using the brassiness parameter Br defined by Myers et al. (2007) as

$$\text{Br} = z(0)/L_{\text{ecl}} \quad (4.68)$$

where $z(s)$ is a coordinate stretching function given by

$$z(s) = \int_{-L}^s \frac{h_{\text{input}}}{h(x)} dx \quad (4.69)$$

and we take L_{ecl} to be the equivalent cylindrical duct length $L_{\text{ecl}} = \pi/(2k)$ —that is the length of cylindrical duct required to produce the same fundamental frequency⁶. The coordinate stretching function z defines an equivalent length of cylindrical tubing required to produce the same degree of nonlinear spectral enrichment. This is normalised by the length of cylindrical tubing required to produce the same pitch resulting in a dimensionless parameter Br . This parameter characterises the spectral enrichment of a duct based on purely geometrical aspects irrespective of the overall pitch produced.

⁶This differs from Myers et al. (2007) who used the effective cone length. The reason for their choice of cone length would appear to be that the typical choice of reference frequency (the lowest playable note) for real brass instruments is *not* actually the fundamental, but rather the second harmonic (the fundamental not lying on the harmonic series of the instrument or typically playable—a topic discussed in more detail in section 4.6). This brings the reference frequency closer to that of the fundamental of a cone—double that of the cylinder. By choosing to normalise to a cone, most typical brassiness parameters for real brass instruments lie between 0 and 1. As we are studying many different duct types (not only those of brass instruments) and in a position to compare fundamentals, it is more sensible to normalise to a cylindrical duct.

For $\text{Br} < 1$ (corresponding to ducts with overall flare) we have less than an equivalent cylindrical duct, and for $\text{Br} > 1$ (corresponding to ducts with overall taper) we have more. For the ducts previously studied we have: $\text{Br} = 0.92$ for the cylindrical duct $L = 8h$ (note the difference to an ideal cylindrical pipe with $\text{Br} = 1$), $\text{Br} = 0.88$ for the horn and $\text{Br} = 0.46$ for the conical duct. Good agreement can therefore be seen between the brassiness parameter and the degree of shock formation in our model. Despite the small brassiness parameter and the lack of shock formation in the conical duct it is still sufficient, as shown before, to change the resonant frequencies.

4.5.5 Curved Ducts

We now look at curved ducts. Curved ducts appear in many wind instruments—any that require sufficiently long tubing that having a straight duct would prove unwieldy. This includes the lower pitched members of most instrument families discussed above—the bass flute (and sometimes the alto flute), the alto clarinet, most common brass instruments, the alto saxophone and the cor anglais (a lower member of the oboe family which features a curved inlet tube into the main bore of the instrument). We therefore wish to investigate what effect such curvature has on the resonant frequencies of such instruments.

To compare, we shall choose the cylindrical duct $L = 8h$ previously studied, bent into a U-bend. As previously mentioned, such a duct is very wide, but should serve to illustrate the effects of the curvature more clearly. With radial symmetry now broken in the duct, the smallest cut-off frequency is now $kh = j_{10} = 1.84\dots$ corresponding to $kL = 14.72\dots$ with our duct. This is well within the range of frequencies we have hitherto been looking at.

Figure 4.43 shows the resonance plot, comparing with the straight duct. The curvature, while making little difference at low frequencies, begins to strongly lower the pitch of the resonant frequencies. The strength of these resonances is also increased. This is consistent with what we have already discussed with regards to curved ducts in previous chapters—curvature increases the energy being reflected by the duct in comparison to a straight duct. Also, we noted that the pressure gets localised and travels around the outside of the bend. In doing so, the wave has a longer path to travel in comparison to an analogous straight duct. This effectively makes the duct longer and reduces the resonant frequency. This effect is only apparent close to, or above the first cut-off frequency. As shown by Rayleigh, sufficiently long wavelength waves do not perceive curvature. For a typical trombone with duct diameter $h \approx 13.5\text{mm}$ and speed of sound $c_0 = 340\text{m s}^{-1}$ we obtain a cut-off of 14.8kHz —well beyond the playing

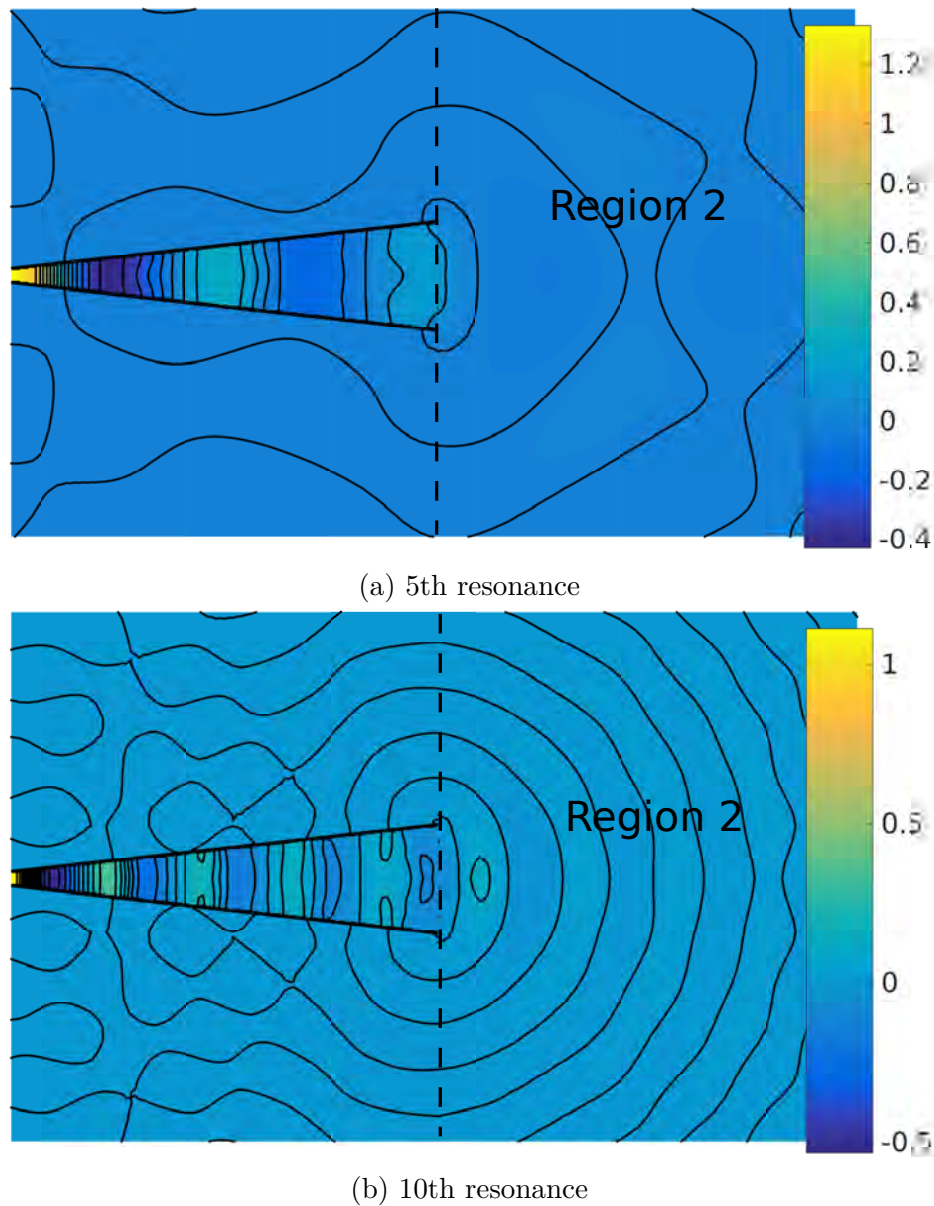


Fig. 4.41 Pressure profiles of the closed conical duct at various resonant frequencies in the nonlinear regime $M = 0.10$.

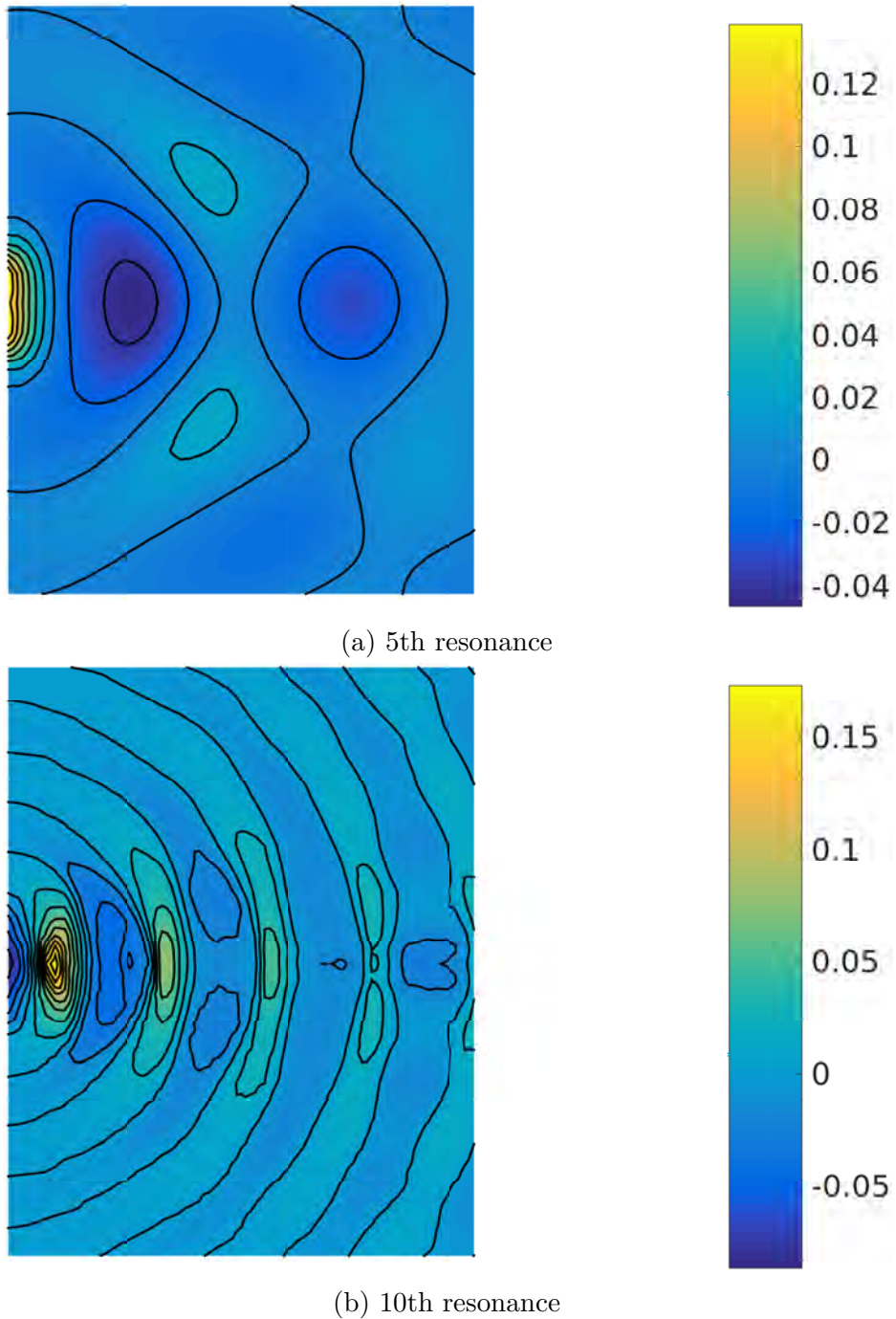


Fig. 4.42 Detail of the exit pressure in region 2 for the closed conical duct in the nonlinear regime $M = 0.10$.

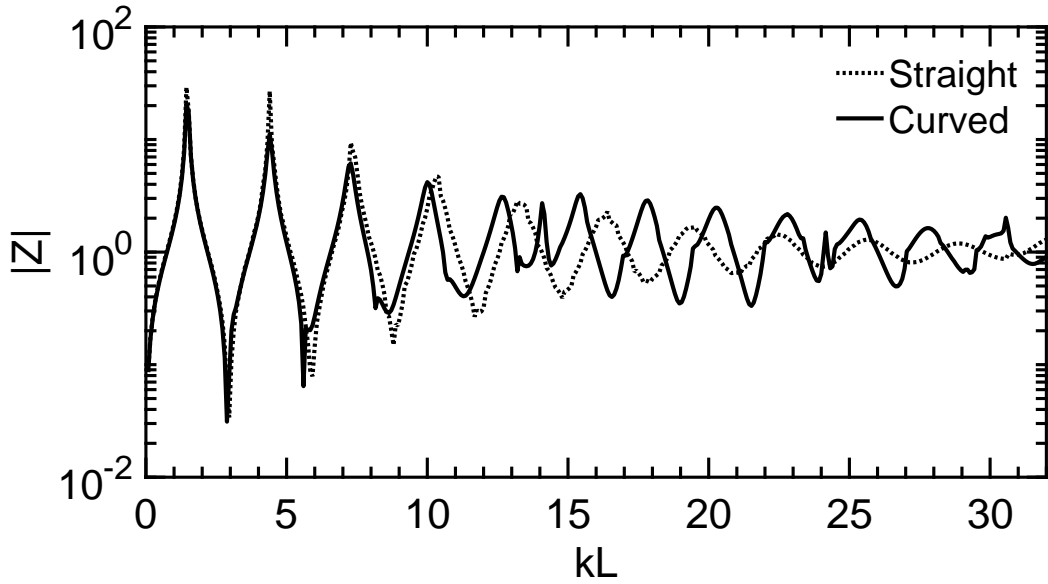


Fig. 4.43 Impedance plots for the curved duct compared to the equivalent length straight duct

range by an order of magnitude. As such, we would not expect the bends to have any significant effect on the pitch.

We also see a new type of resonance splitting—just below the first cut-off we see a new resonance spike. Instead of being caused by nonlinearities, this new spike is created by the curvature exciting and reflecting back higher spatial modes—the first azimuthal mode to be precise. While this would not be observed if the duct was driven by a rigid source (such as a loudspeaker), a flexible membrane would be forced to oscillate with amplitude proportional to $\cos(\theta)$ (with θ the angle measured from the plane of symmetry of the duct), even though the input wave is planar.

The pressure plots (figure 4.44) feature many of the characteristics noted in the previous two chapters—the excitement of non-planar modes (even below cut-off) and the strong localisation of the pressure around the outside of the bend. This is further exacerbated by the reflections from the duct exit. Whereas with the straight duct, peak pressure was only approximately $2\times$ the input at the source when the frequency was low—dropping off to a similar magnitude to the input as the frequency was increased—with the curved duct, peak pressure remains approximately $2\times$ the input across a wide range of frequencies, localised to the outer duct. In the previous chapters, we raised the question of whether this localisation of pressure has an effect on the sound radiated from the duct. For an infinite straight duct outlet, whether these high amplitude spatially localised waves could propagate was determined by the width of

Resonance	kL	Ratio to fundamental	Interval	Difference to Straight Duct
1	1.44	1	Unison	0
2	4.40	3.06	Oct. + Perfect Fifth (+34 cents)	0
3	7.28	5.06	2 Oct. + Major Third (+5 cents)	0
4	10.00	6.94	2 Oct. + Minor Seventh (-45 cents)	-68 cents
5	12.64	8.78	3 Oct. + Major Second (-39 cents)	-75 cents
5'	14.08	9.78	3 Oct. + Major Third (-13 cents)	N/A
6	15.44	10.72	3 Oct. + Perfect Fourth (+7 cents)	-104 cents
7	17.84	12.39	3 Oct. + Minor Sixth (-43 cents)	-156 cents
8	20.24	14.06	3 Oct. + Minor Seventh (-24 cents)	-175 cents
9	22.80	15.83	4 Oct. (-18 Cents)	-200 cents
10	25.36	17.61	4 Oct. + Major Second (-34 cents)	-225 cents
11	27.76	19.28	4 Oct. + Minor Third (+23 Cents)	-
12	30.56	21.22	4 Oct. + Perfect Fourth (-11 Cents)	-

Table 4.14 Resonant frequencies of the curved duct closed at one end and the comparison to the equivalent length straight duct

Resonance	kL	Ratio to fundamental	Interval	Difference to Straight Duct
1	2.88	1	Unison	-47 cents
2	5.60	1.94	Oct. (-49 cents)	-96 cents
3	8.64	3.0	Oct. + Perfect Fifth (+2 cents)	-31 cents
4	11.28	3.92	2 Oct. (-36 cents)	-60 cents
5	13.20	4.58	2 Oct. + Major Second (+36 cents)	-198 cents
5'	14.40	5.00	2 Oct. + Major Third (-14 cents)	N/A
6	16.56	5.75	2 Oct. + Tritone (+28 cents)	-137 cents
7	18.96	6.58	2 Oct. + Major Sixth (-33 cents)	-187 cents
8	21.52	7.47	2 Oct. + Major Seventh (-18 cents)	-189 cents
9	23.92	8.31	3 Oct. + Minor Second (-35 Cents)	-216 cents
10	26.64	9.25	3 Oct. + Minor Third (-49 cents)	-238 cents
11	29.28	10.17	3 Oct. + Major Third (+15 Cents)	-
12	31.52	10.94	3 Oct. + Perfect Fourth (+43 Cents)	-

Table 4.15 Resonant frequencies of the curved duct open at both ends and the comparison to the equivalent length straight duct

the outlet—if below the cut-off the radiation was planar, if above these higher modes could propagate. We can now address the more relevant question of the propagation into free space. We see that for low frequencies, radiation is largely similar and looks as if it were coming from a straight duct. For higher frequencies though, we observe an interesting phenomenon—in the 10th resonance plot we see two distinct beams of radiation emanating from the duct. One of these points down from the opening in the direction of the centre of curvature, the other approximately orthogonal to this, showing that the curvature affects the direction of sound radiation from a duct. We can show this in a more extreme manner by looking at the 12th resonance (figure 4.45). At this higher frequency, we can clearly see the sound beam angled downwards in the direction of the centre of curvature, suggesting that the second beam observed at the 10th resonance is caused by diffraction off the edge of the duct due to the larger wavelength. We therefore see that these higher duct modes do have an effect radiating into free space—they change the angle of the beam of sound radiated. Such an effect should, theoretically, be possible to observe. For a 1m long piece of tubing, the corresponding 12th resonance would be at 1654Hz—high pitched, but certainly audible and well within the range of even ordinary music (corresponding roughly to G_6^{\sharp}). The listener should perceive the sound to be louder slightly closer to the centre of the bend compared to standing directly in line with the duct exit. Whether this effect occurs in practice is an open question—other effects not included in our model, such as viscosity or wall losses, may reduce or eliminate this effect.

Figure 4.46 shows the nonplanar resonance 5' previously discussed. The second mode can clearly be seen to dominate the resonance in the duct, producing enormous peak amplitudes when compared with the planar resonances previously shown.

Examining the effect of nonlinearity (4.47), we see a modest effect, consistent with that previously observed. Aside from the first resonance, we see only small changes in pitch (see table 4.16). It is likely that as energy is now being distributed to different spatial modes, there is a weaker transference of energy into the higher temporal modes. As such, the manner in which the sound is reflected back into the duct is altered less than the analogous straight duct and, correspondingly, the change of pitch is smaller.

Finally, the plots for the nonlinear propagation in the curved ducts (figure 4.48) show the shock formation on the outer edge of the bend, as we have observed previously. Due to the very large amplitudes (and corresponding Mach numbers) created by the localisation at the edges, the shock dissipates energy rather quickly at the 10th resonance, so less energy is radiated.

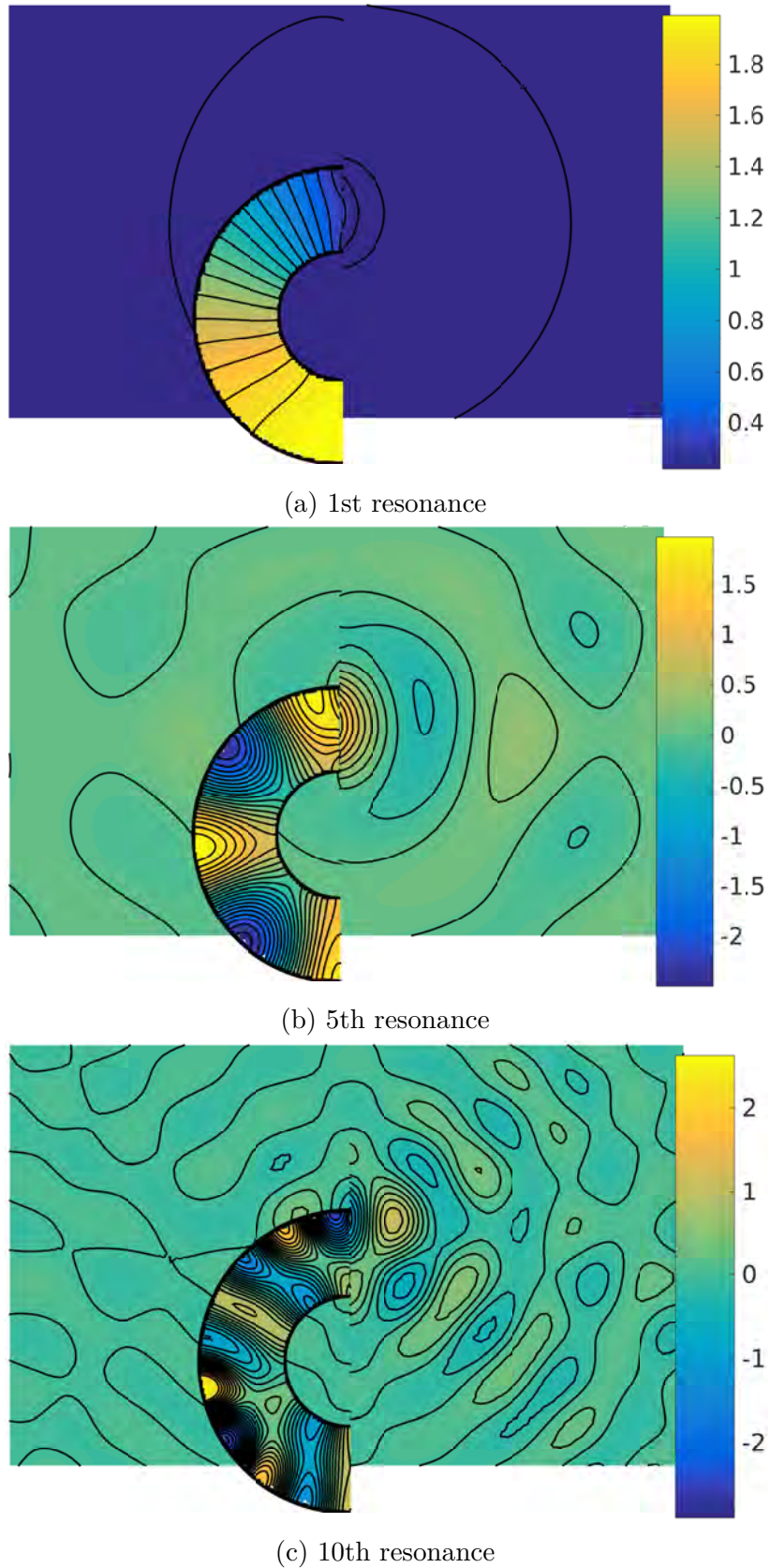


Fig. 4.44 Pressure profiles of the closed curved duct at various resonant frequencies.
Source at bottom.

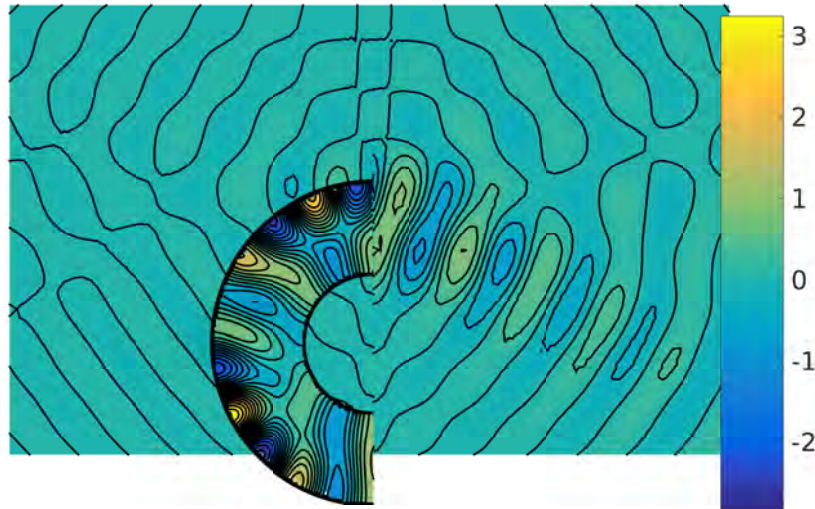


Fig. 4.45 12th resonance of the closed curved duct, illustrating the change in direction of radiation caused by curvature in the duct

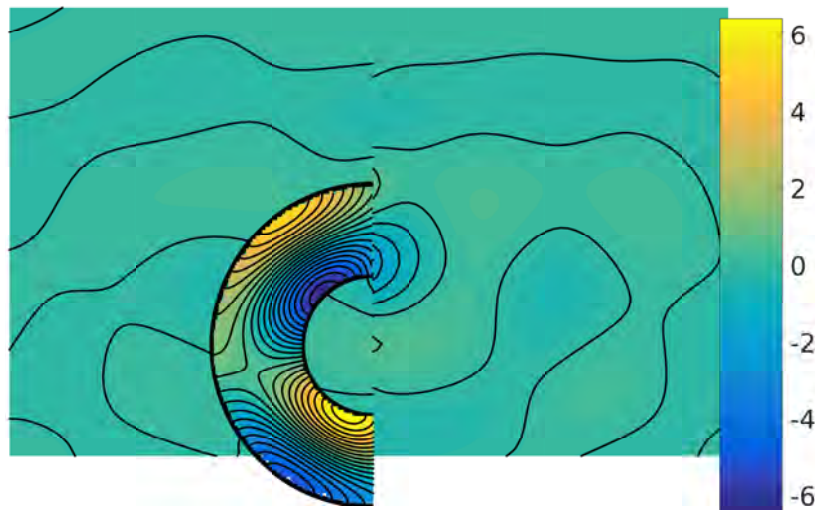


Fig. 4.46 The resonance 5' of the closed curved duct, illustrating higher modal resonances induced

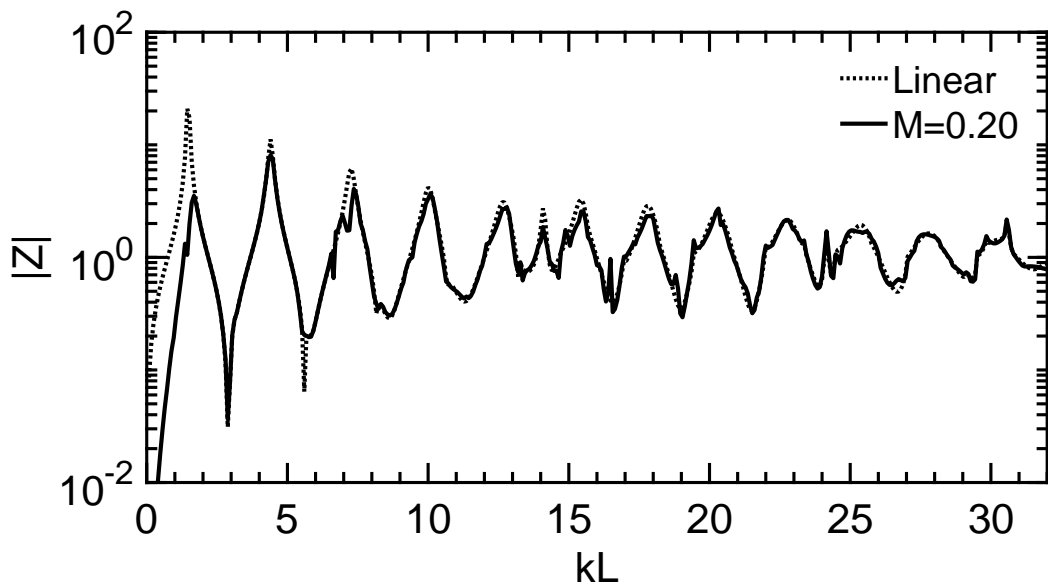


Fig. 4.47 Comparing impedance in the linear and nonlinear regime for the curved duct

Resonance	kL	Change in pitch due to nonlinearity
1	1.68	+267 cents
2	4.40	0
3	7.36	+19 cents
4	10.08	+14 cents
5	12.80	+21 cents
5'	14.08	0 cents
6	15.52	+9 cents
7	17.92	+8 cents
8	20.32	+7 cents
9	22.72	-6 cents
10	25.05	-21 cents
11	27.68	-5 cents
12	30.56	0

Table 4.16 Resonant frequencies of the closed curved duct when $M = 0.20$ and the corresponding change in pitch compared with the linear regime

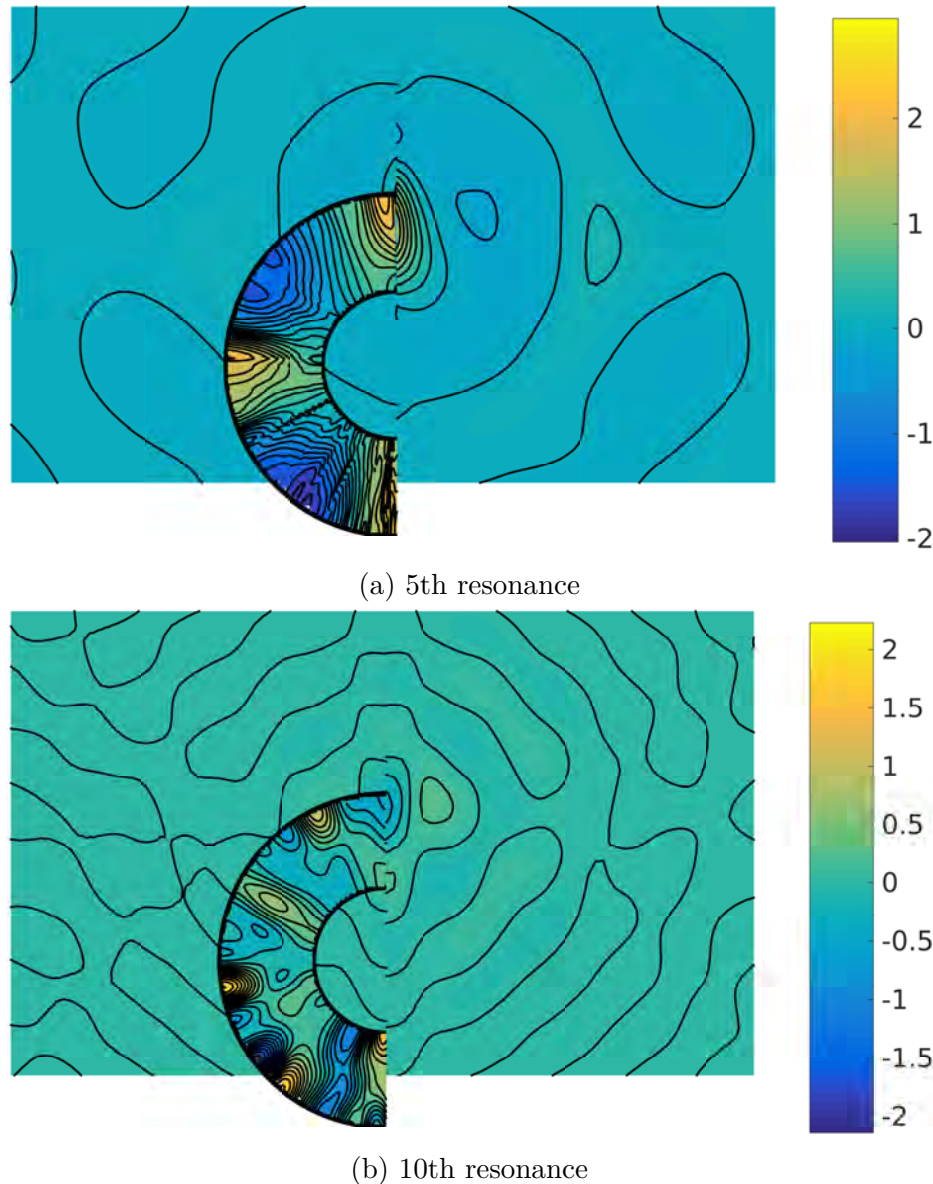


Fig. 4.48 Pressure profiles of the closed curved duct at various resonant frequencies in the nonlinear regime $M = 0.10$.

4.5.6 Helical Ducts

The final class of ducts we shall consider in this section is the helical duct, to examine the effect of torsion. Along with curvature, torsion also arises in most musical instruments with large ducts—it is advantageous to have the instruments curve in multiple planes to make them easier to hold. In a lot of cases, the torsion can be thought of as being a delta function—torsion without curvature does not affect the geometry of the duct itself, but rather the coordinate system we use to describe it. For instruments such as the trombone, the individual bends themselves lie in a plane (hence no torsion), but the successive bends do lie in different planes. As such, torsion must be included to describe the change in plane in which the curvature lies. There are, of course, instruments that include both torsion and curvature together, producing helical like structures. A notable example is the French horn.

The duct we shall study is a right handed helix, $L = 8h$, with curvature $\kappa = \pi/L$ (the same as the previous U-bend) and torsion $\tau = \sqrt{3}\pi/L$. We therefore have $\sqrt{\kappa^2 + \tau^2} = 2\pi/L$, so the helix goes through a full circular rotation (c.f. equation 3.58). Figure 4.49 shows the impedance comparison with the U-bend from the previous section. As both ducts have the same curvature, any difference is the result of torsion. It can be seen that, as with the comparison of the straight and curved duct, there is little difference below the first cut-off frequency $kL = 14.72\dots$. As we approach this frequency, and above, it can be seen that the addition of torsion to the duct further reduces the pitch of the resonant frequencies (see tables 4.17 and 4.18 for comparison). We do see that the strength of the resonances is also reduced (recall adding curvature increased the strength). This further decrease in pitch is a result in the increase in the length of path the pressure wave takes—the pressure is concentrated approximately along the edge of the duct in the direction opposite to the duct normal (see figure 4.50). This path has length (a and b are defined by equation 3.58)

$$\text{length of helical path} = 2\pi\sqrt{(a+h)^2 + b^2} = L\sqrt{1 + \frac{\pi}{4} + \left(\frac{\pi}{4}\right)^2} \approx 1.5499L \quad (4.70)$$

compared with the cylindrical U-bend studied previously

$$\text{length of circular path} = \pi(a+h) = (1 + \frac{\pi}{8})L \approx 1.3927L \quad (4.71)$$

If we calculate the theoretical drop in pitch from such an extension in length we obtain a -573 cents change going from the straight to the U-bend, and -185 cents going from the U-bend to the helical duct. These values are larger in magnitude than observed,

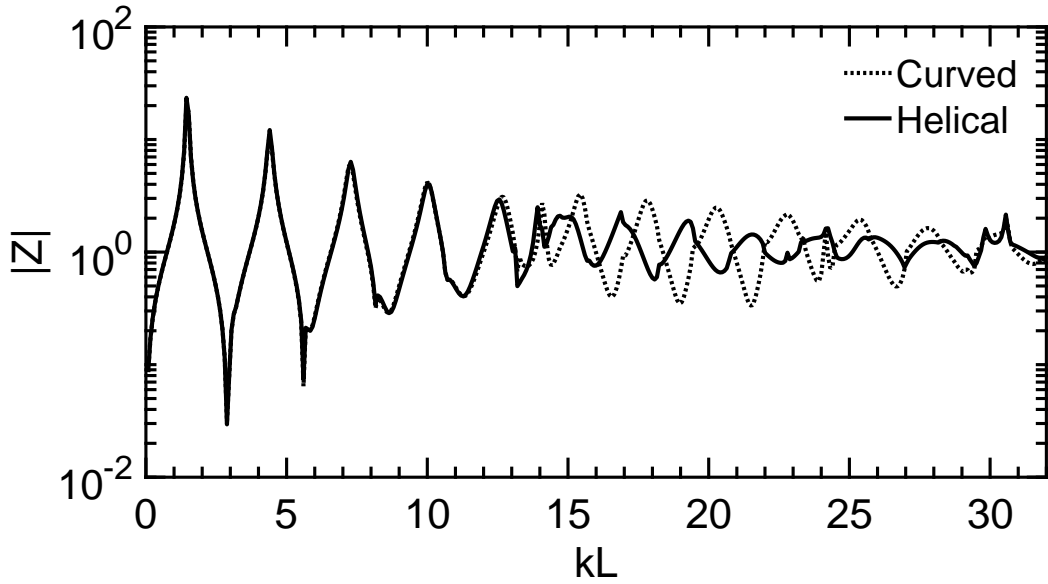


Fig. 4.49 Impedance plots for the helical duct compared to the equivalent length, equivalent curvature torsion free curved duct

but in the limit as $kL \rightarrow \infty$ we would expect the change in pitch to approach these values.

Figure 4.51 shows some of the resonant frequency pressure plots. The 3D plot of the pressure around the duct wall of the helix is superimposed onto the plot of the radiation in the plane containing \hat{t} and \hat{n} at the duct exit, going through the centreline (as such, the contours will not be continuous from the duct to the radiation). At the 10th resonance, we begin to see another angled radiation pattern, as with the U-bend. Figure 4.52 plots the 13th resonance. As with the U-bend, we see the sound beam being angled towards the centre of curvature (in the direction the normal points at the duct exit). From the different perspective, we also see the sound being deflected in the direction the binormal points at the duct exit. Therefore, both curvature and torsion can deflect the angle of radiation from an open duct in a three dimensional manner.

The effect of nonlinearity on the helical duct is very similar to that of the curved U-bend (see figure 4.53 and table 4.19). There is a raising of the fundamental and only modest changes in both directions beyond that. There is a degree of increased resonance splitting compared to the U-bend, suggesting that the helical duct may be easier to overblow.

To conclude this section, we present a plot of the nonlinear pressure distribution in figure 4.54, showing a degree of localisation.

Resonance	kL	Ratio to fundamental	Interval	Difference to torsion free duct
1	1.44	1	Unison	0
2	4.40	3.06	Oct. + Perfect Fifth (+34 cents)	0
3	7.28	5.06	2 Oct. + Major Third (+5 cents)	0
4	10.00	6.94	2 Oct. + Minor Seventh (-45 cents)	0
5	12.56	8.72	3 Oct. + Major Second (-50 cents)	-11 cents
5'	13.92	9.67	3 Oct. + Minor Third (+28 cents)	-20 cents
6	14.72	10.22	3 Oct. + Major Third (+24 cents)	-83 cents
7	16.88	11.72	3 Oct. + Perfect Fifth (-39 cents)	-96 cents
8	19.28	13.39	3 Oct. + Major Sixth (-8 cents)	-84 cents
9	21.52	14.94	3 Oct. + Major Seventh (-18 Cents)	-100 cents
10	24.24	16.83	4 Oct. + Minor Second (-12 cents)	-78 cents
11	25.92	18.00	4 Oct. + Major Second (+4 Cents)	-119 cents
12	28.32	19.67	4 Oct. + Major Third (-43 Cents)	-132 cents
13	30.56	21.22	4 Oct. + Perfect Fourth (-11 Cents)	-

Table 4.17 Resonant frequencies of the helical duct closed at one end and the comparison to the equivalent length, equivalent curvature torsion free duct

Resonance	kL	Ratio to fundamental	Interval	Difference to torsion free duct
1	2.88	1	Unison	0
2	5.60	1.94	Oct. (-49 cents)	0
3	8.64	3.0	Oct. + Perfect Fifth (+2 cents)	0
4	11.28	3.92	2 Oct. (-36 cents)	0
5	13.20	4.58	2 Oct. + Major Second (+36 cents)	0
6	15.92	5.53	2 Oct. + Tritone (-40 cents)	-68 cents
7	18.08	6.28	2 Oct. + Minor Sixth (-20 cents)	-82 cents
8	20.40	7.08	2 Oct. + Minor Seventh (-11 cents)	-93 cents
9	22.56	7.83	3 Oct. (-36 Cents)	-101 cents
10	24.72	8.58	3 Oct. + Minor Second (+22 cents)	-129 cents
11	26.96	9.36	3 Oct. + Minor Third (-28 Cents)	-143 cents
12	29.44	10.22	3 Oct. + Major Third (+24 Cents)	- 118 cents

Table 4.18 Resonant frequencies of the helical duct open at both ends and the comparison to the equivalent length, equivalent curvature torsion free duct

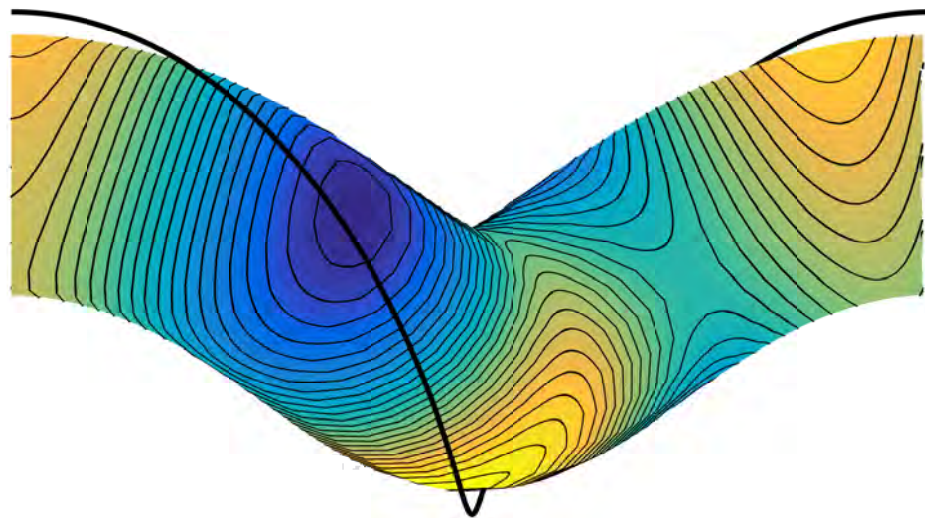


Fig. 4.50 Plot of the duct at resonance with the path $\mathbf{x}(s) = \mathbf{q}(s) - h\hat{\mathbf{n}}(s)$ highlighted

Resonance	kL	Change in pitch due to nonlinearity
1	1.60	+182 cents
2	4.48	+31 cents
3	7.44	+38 cents
4	9.92	-13 cents
5	12.56	0
5'	13.84	-10 cents
6	14.88	+19 cents
7	16.88	0 cents
8	19.04	-22 cents
9	21.60	+6 cents
10	24.16	-6 cents
11	25.52	-27 cents
12	28.32	0
13	30.56	0

Table 4.19 Resonant frequencies of the closed helical duct when $M = 0.20$ and the corresponding change in pitch compared with the linear regime

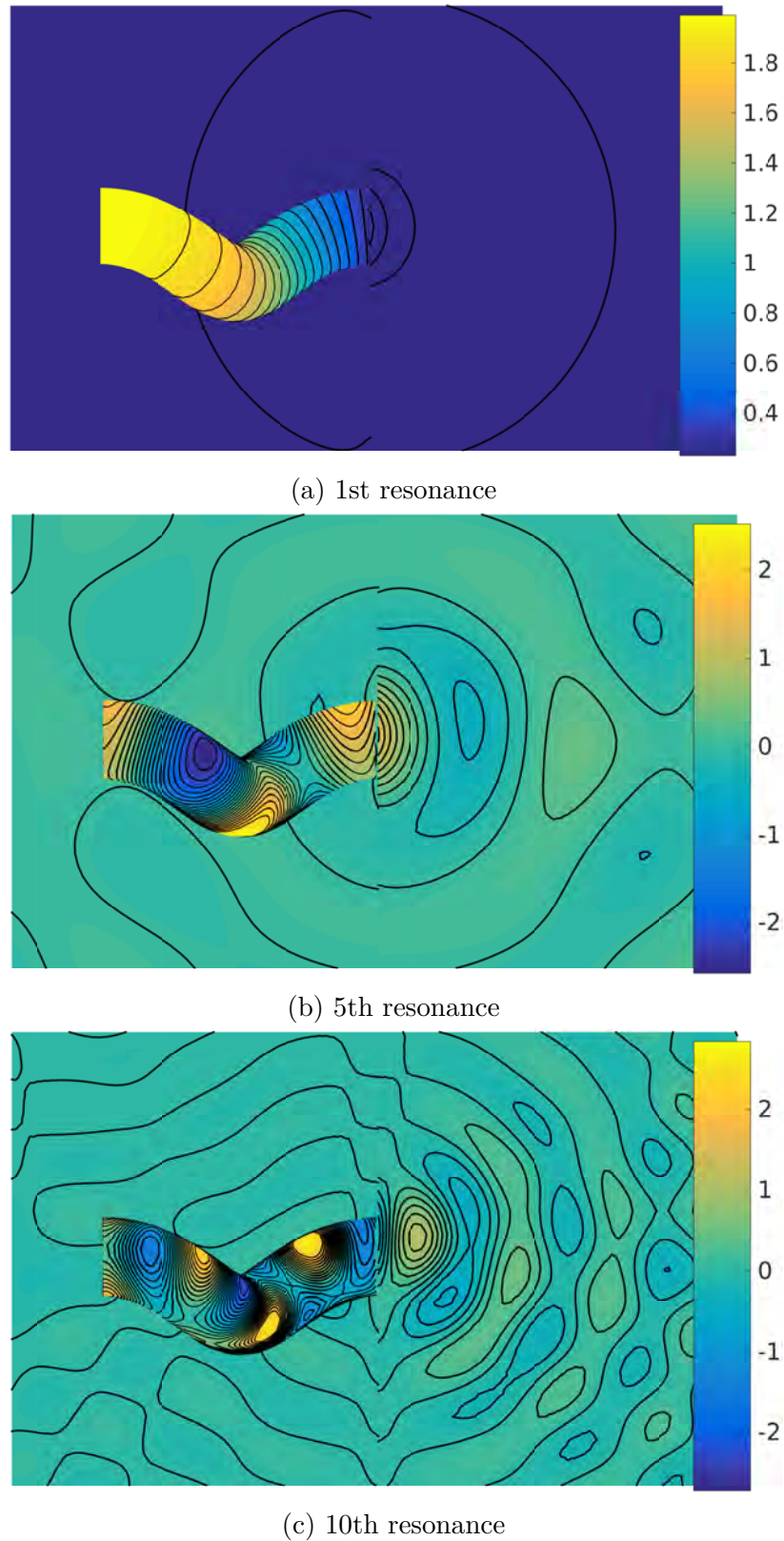
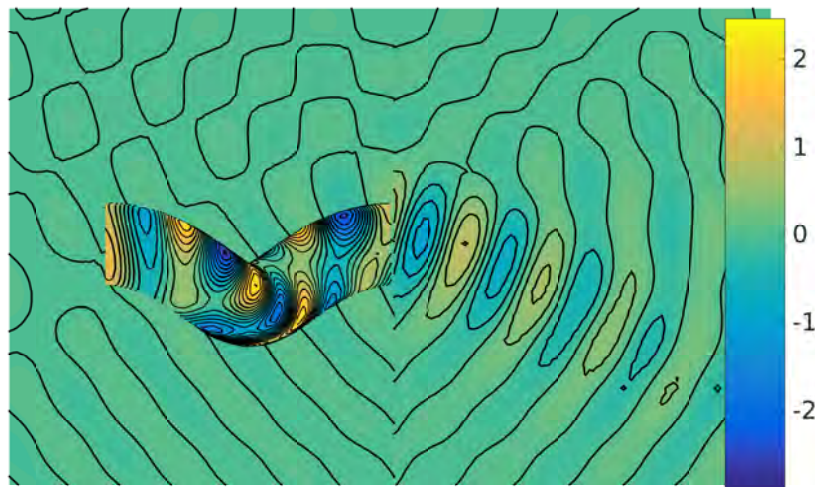
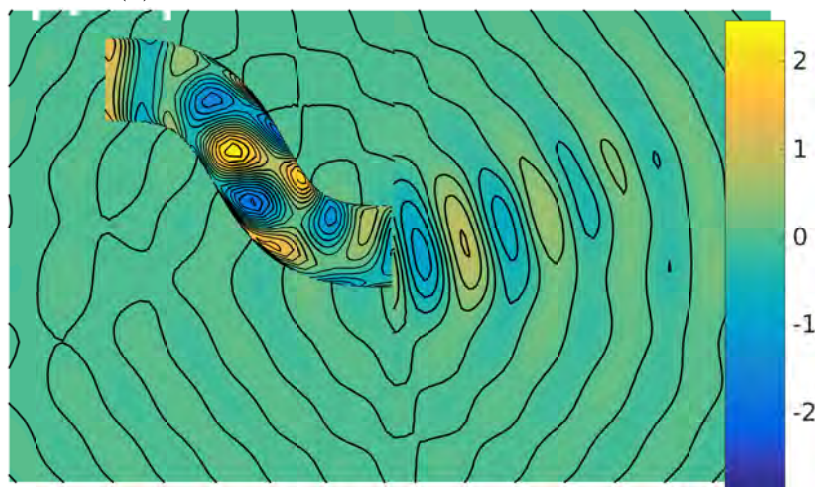


Fig. 4.51 Pressure profiles of the closed helical duct at various resonant frequencies. Source to the left.



(a) Duct binormal at exit going into the page.



(b) Duct normal at exit coming out of the page.

Fig. 4.52 13th resonance from different perspectives showing angled radiation

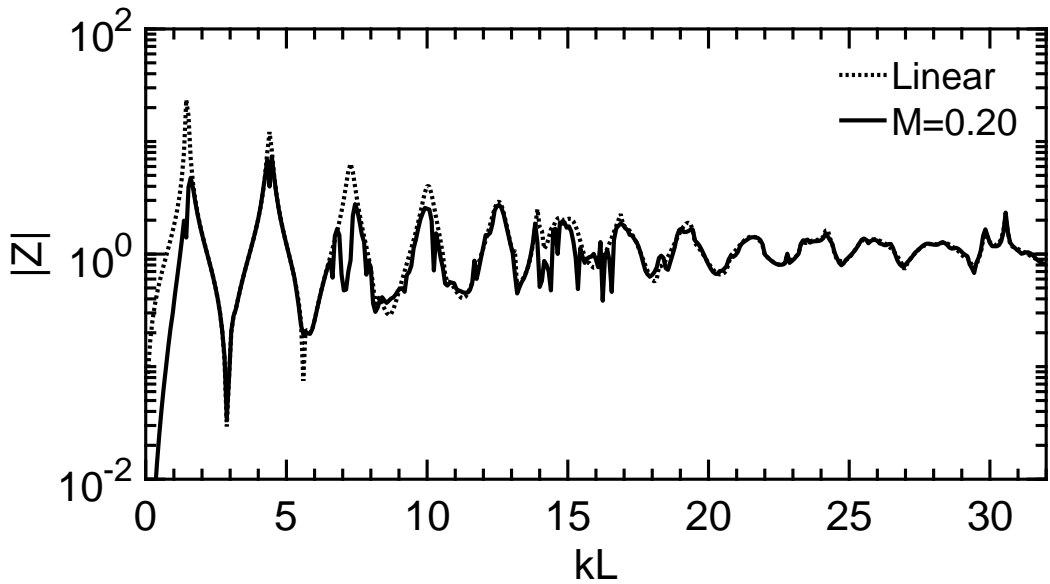
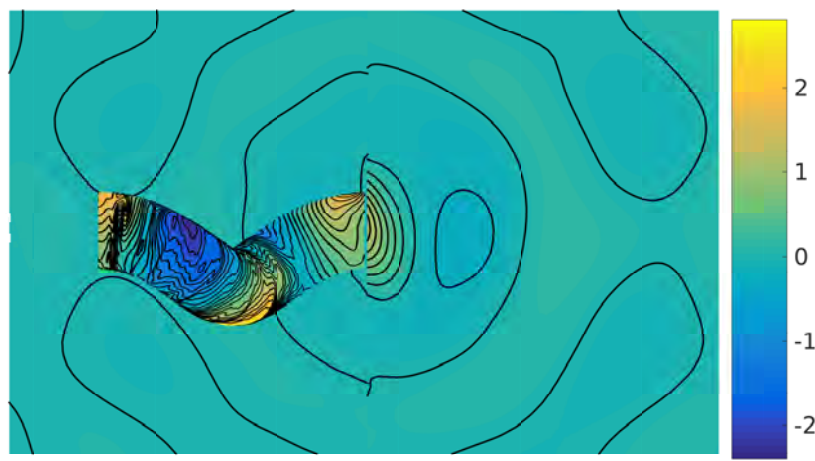


Fig. 4.53 Comparing impedance in the linear and nonlinear regime for the helical duct

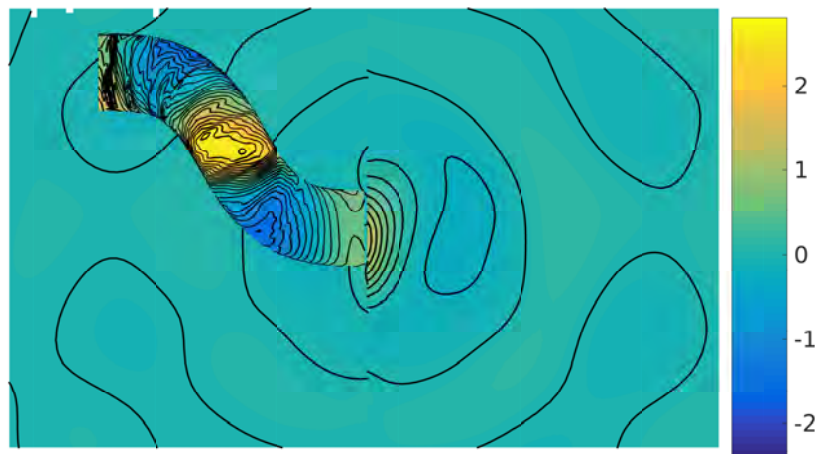
4.6 Acoustics in a Trombone

In the final section of this chapter we shall combine many of the previously studied duct sections into a model of a realistic instrument—the trombone. While the description of the duct we shall give is just an approximation to an actual trombone (and hence have rather poor intonation), it shall serve to demonstrate what aspects such as curvature and nonlinearity have of the effect of the resonant frequencies.

The duct we shall study is described in table 4.20. Figure 4.55 displays the impedance plot for the trombone model with table 4.21 collating the resonant frequencies. Here, we have taken the speed of sound $c_0 = 340\text{ms}^{-1}$ and density of air $\rho_0 = 1.2\text{kg m}^{-3}$. This has many characteristics of an actual impedance curve for a trombone and some differences. The pitches produced by the resonant frequencies are in roughly the correct area, although the intonation of such an instrument would be very poor—the modes 2, 3 and 4 approximately follow the harmonic series of A (i.e. a semitone flat from the actual B♭ of the tenor trombone), modes 5-8 approximate the harmonic series of B♭ (so approximately correct) and modes 10-15 approximate the harmonic series of C (a tone sharp). As such, the instrument has interval spacing too wide. Adjusting the parameters of this model produces rather significant changes to the resonant frequencies in ways which are not easily predictable—changes by several mm in the duct bore can shift frequencies by a few Hz, which for the lower frequencies corresponds to changes in pitch of the order of semitones. As a result, we see that



(a) Duct binormal at exit going into the page.



(b) Duct normal at exit coming out of the page.

Fig. 4.54 5th resonance at $M = 0.1$

Part	Description	Radius (mm)	Arclength (mm)
Mouthpiece	Straight section	$20 - 13.25s/25$	$0 \leq s \leq 25$
Inlet to first bend	Straight section	6.75	$25 \leq s \leq 735$
Slide bend	Circular bend, $\kappa = 1/48\text{mm}^{-1}$	6.75	$735 \leq s \leq 886$
First bend to tuning slide	Straight section, $\tau = \pi/(2 \times 950)$	6.75	$886 \leq s \leq 1863$
Tuning slide	Circular bend, $\kappa = 1/79\text{mm}^{-1}$	$6.75 + \frac{3.18(s-1836)}{248}$	$1863 \leq s \leq 2084$
Pre-bell	Straight section	9.93	$2084 \leq s \leq 2134$
Bell	Straight section	$1777/(2368 - s)^{5/6}$	$2134 \leq s \leq 2612$

Table 4.20 Description of the trombone model

the parameters of such an instrument—such as the bore diameter, bell profile and mouthpiece shape—must all be carefully chosen to insure the correct tuning.

Despite the intonation problems of the model chosen, we can observe some important features—notably that the first resonant frequency does not lie on the harmonic series of the subsequent pitches, instead being slightly flat. This is indeed what is observed by brass instrument players—the lowest notes commonly played on a brass instrument is not the fundamental but instead the second member of the harmonic series an octave up. The fundamental can be played by skilled players as a “pedal note” using higher resonances to achieve the pitch. We also observe the decaying of the resonances around 1000Hz as with experimental observations.

We can also examine another property of the instrument not previously mentioned—the effect of the mouthpiece. Here, we have made the simple approximation of the mouthpiece to a cone. We can compare this to a trombone of the same length without this mouthpiece added. Figure 4.56 displays the results. Whereas the effect of the bell was to raise the pitch of the lower resonances by effectively shortening the instrument for them, the mouthpiece can be seen to lower the pitches of the resonances—particularly the higher ones. It also raises the impedance resulting in stronger resonances. The mouthpiece is therefore not simply a piece of equipment to make playing the instrument easier, but also serves to tune the instrument—the balance between the raising of the low pitches via the bell and lowering of higher pitches by the mouthpiece shifting the resonances onto the harmonic series.

We can also compare the above instruments to an identical one without curvature. Doing so produces an impedance plot that is essentially identical. This is consistent with what we have seen previously with the U-bend duct studied—the bend makes

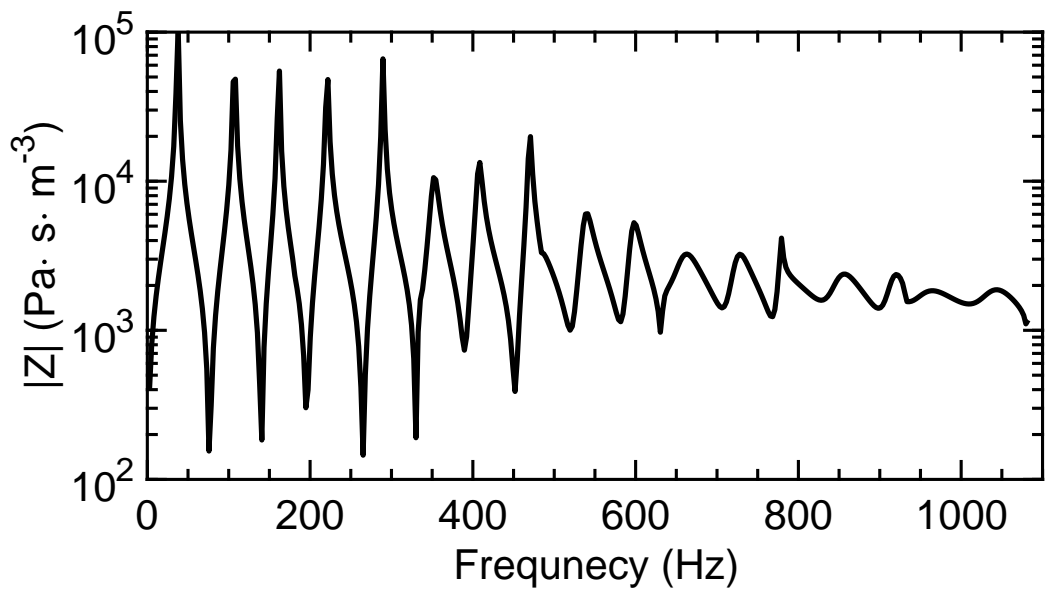


Fig. 4.55 Impedance plots for the trombone

Resonance	Frequency (Hz)	Pitch
1	38	E_1^b
2	108	A_2 (-32 cents)
3	162	E_3 (- 30 cents)
4	222	A_3 (+16 cents)
5	290	D_4 (-22 cents)
6	352	F_4 (+15 cents)
7	409	A_4^b (-25 cents)
8	471	B_4^b (+18 cents)
9	541	D_5^b (-41 cents)
10	598	D_5 (+32 cents)
11	663	E (+10 cents)
12	728	F_5^b (-25 cents)
13	779	G_5 (-11 cents)
14	858	A_5 (-44 cents)
15	920	B_6^b (-22 cents)

Table 4.21 Resonant frequencies of the trombone model, taking $A_4 = 440\text{Hz}$

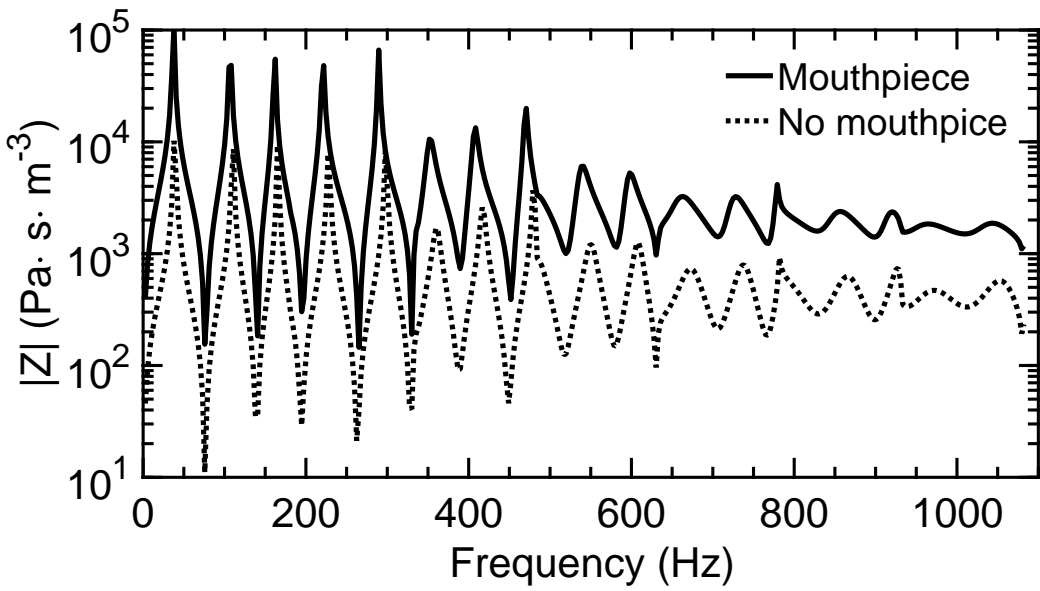


Fig. 4.56 Comparing the impedance for two identical length trombones—with and without a mouthpiece

little difference below the first cut-off frequency, which in this example is 14.8kHz—an order of magnitude above the playing range.

Figures 4.57 and 4.58 show the pressure profiles at some of the resonant frequencies. As before, there is stronger radiation from the instrument at higher frequencies.

To conclude, we shall now look at nonlinearity in this trombone model. Figure 4.59 shows the results. While at first the effect looks rather extreme for even small Mach numbers (do note however, that this is *input* Mach number and not total—the total is approximately double due to the addition of the reflected wave, so $M = 0.05$ corresponds to an SPL of approximately 174dB—a rather large playing amplitude) it can be seen on closer inspection that the nonlinearity primarily decreases the strength of the resonances—as we have observed before for the horn. The transference of energy into the higher Fourier harmonics results in a greater radiation of energy from the duct. A large amount of resonance splitting can be observed at the lower duct modes corresponding to higher harmonics dominating the resonance—likely resulting in the instrument overblowing at the octave. This effect is less at the higher resonances—radiation is sufficiently strong that the higher Fourier modes do not dominate the resonance. There is also a change in frequency of the resonant pitches. As these are dependant on the relationship between the various resonant frequencies—which for this instrument model are a rather poor (there is a very weak alignment with the harmonic series)—we cannot conclude with any certainty the effect of nonlinearity on the pitch

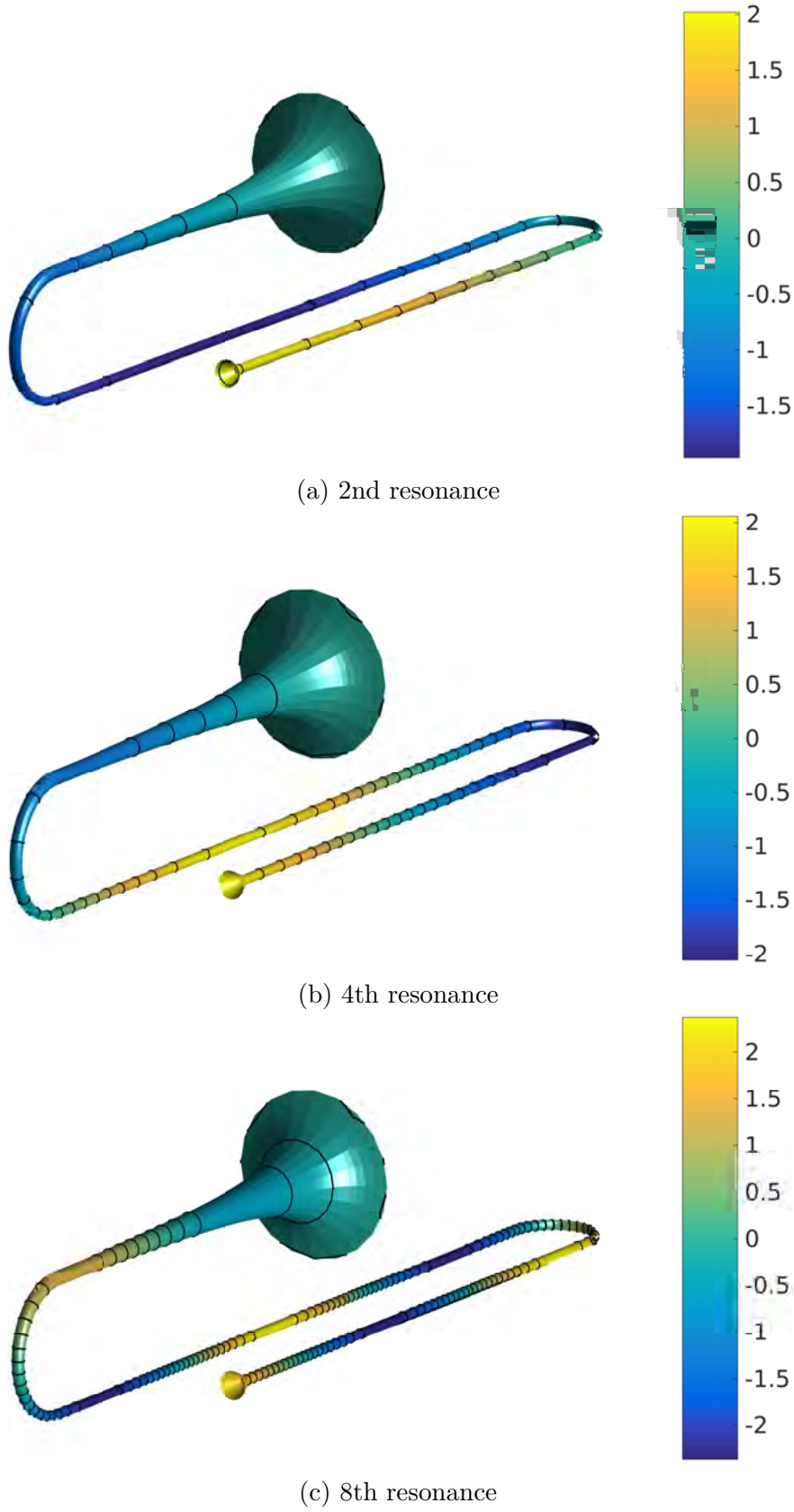


Fig. 4.57 Pressure profiles of the trombone.

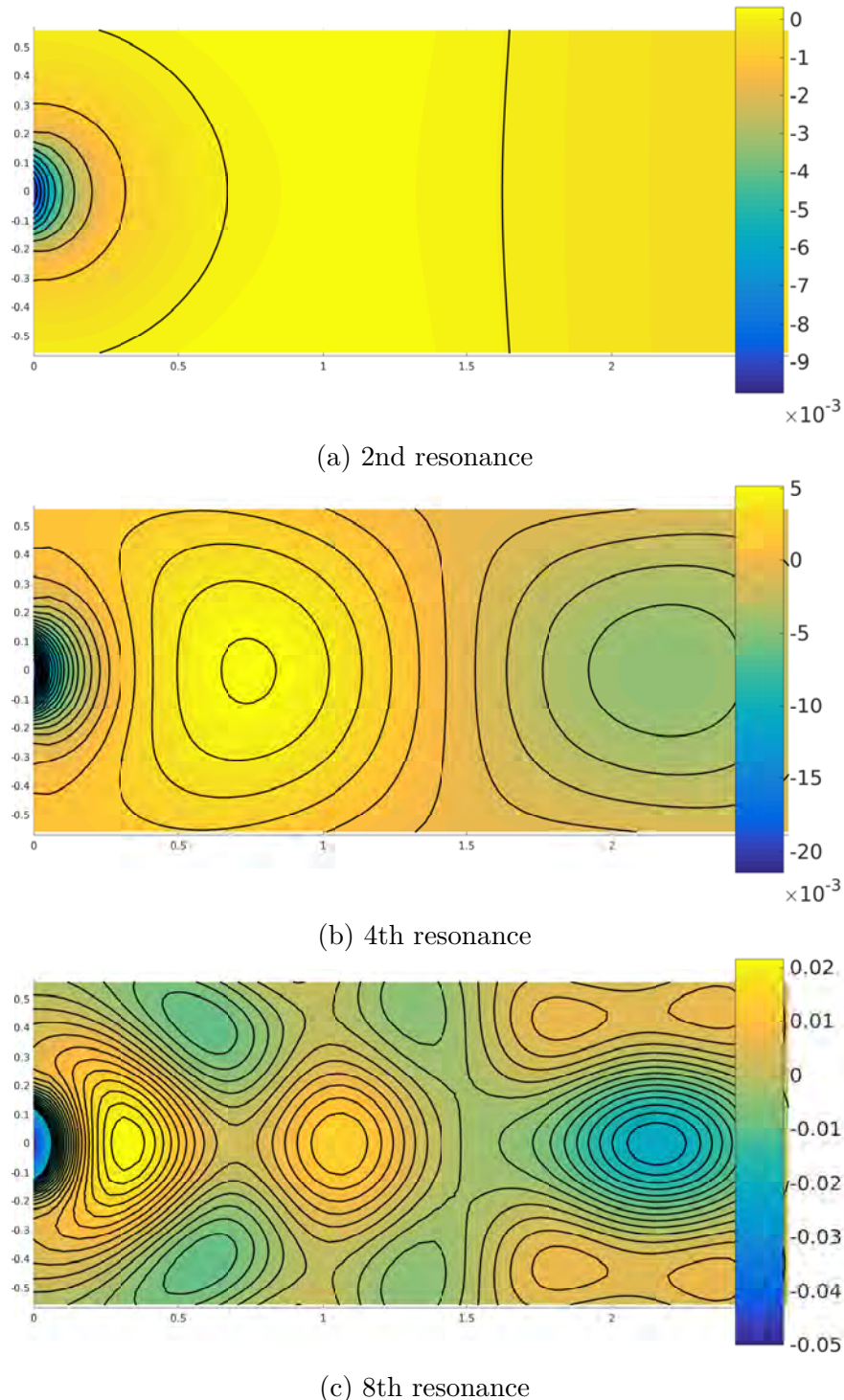


Fig. 4.58 Detail of exit pressure from the trombone. Distance in metres. Bell radius $\approx 0.11\text{m}$. Radiation from the left.

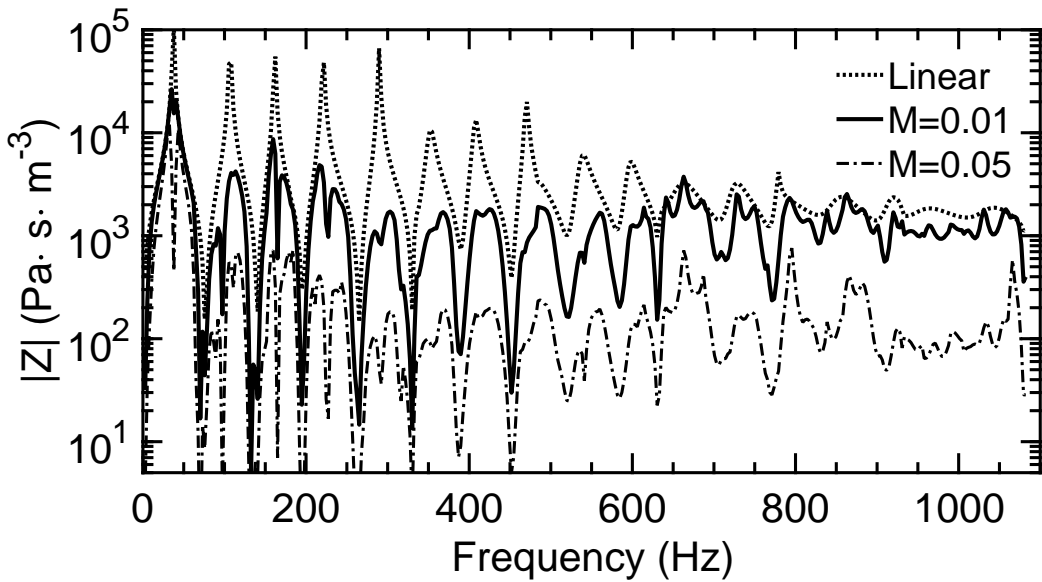


Fig. 4.59 Comparing the impedance for the trombone model at various Mach numbers

of the trombone. From our model, we observe both shifts up and down, with most being shifted up—see table 4.22 (where the resonant frequency is strongly forked, we have noted both pitches). With a more accurate model of a trombone, using actual measurements with more detail we would be able to determine how the pitch is affected with playing amplitude for each of the resonant frequencies. As we have already noted, the pitch of the resonant frequencies is very sensitive to changes in parameters of the instrument—different models of instruments themselves have different intonations (though to a much smaller extent than ours). As such, it may be possible that different instrument models may behave differently when played at louder volumes, with some increasing in pitch (on certain notes) while others decrease—all depending on the slight deviation each resonant frequency has from the harmonic series.

To finish this chapter, we examine the pressure profiles through the duct in the nonlinear regime. These are shown in detail in figure 4.60. These are analogous plots to those produced by Hirschberg et al. (1996) in their celebrated paper (frequency is roughly that of their figure 3). At a Mach number of 0.1 the peak pressure amplitude we obtain in the mouthpiece is approximately 20kPa—this is comparable to that of Hirschberg et al.. However, due to the driving of the lips their pressure source is highly non-sinusoidal. This is an important factor not taken into account in our work—as the input pressure signal from the player’s lips is highly nonlinear—involving sharp spikes in pressure—the shock formation distance is greatly reduced for a similar amplitude input (remember that shock formation distance is inversely proportional to the pressure

Resonance	Frequency (Hz)	Change in pitch due to nonlinearity
1	33 or 43	-244 cents or +214 cents
2	116	+124 cents
3	160 or 184	-21 cents or +220 cents
4	216 or 244	-47 cents or +163 cents
5	303	+75 cents
6	368	+77 cents
7	428	+79 cents
8	487	+58 cents
9	560	+60 cents
10	614	+45 cents
11	663	0 cents
12	747	+45 cents
13	795	+152 cents
14	866	+16 cents
15	925	+9 cents

Table 4.22 Resonant frequencies of the trombone model at $M = 0.05$ and the corresponding change in pitch compared with the linear regime

gradient at the source) when compared with a sinusoidal input. As such, we do not observe a great deal of shock formation until the Mach number is very large. We could use an input matching experimentally observed waveforms, but as these vary greatly depending on frequency and amplitude these would not generalize to other situations and, hence, is not done here. Despite our (almost) sinusoidal input (it does in fact have a degree of harmonic enrichment from reflected waves), we observe shock formation—prominent in the pipe and being radiated from the bell. One thing to note when comparing with experiment is that our pressure waveform has little decay when compared with our source pressure. This is to be expected as we are solving the inviscid equations with no loss mechanisms (aside from reflected waves going out of the input and radiation going out of the bell). The results of Hirchberg et. al. show a marked decrease in pipe pressure compared to mouthpiece—likely a result of viscosity. This suggests an important factor missing from our model is viscosity. Despite this, the exit pressure is comparable with peaks of just over 1kPa and troughs of much small amplitude. Finally, figure 4.61 displays the pressure profile through the whole instrument and the subsequent radiation pattern. Although difficult to make out, there is noticeable bunching up of the contour lines in front of regions of high pressure (after the first bend and just before the second) corresponding to shock formation within the instrument. The radiation pattern on the other hand clearly shows a series of shock

waves radiating from the bell of the instrument. These shock waves have a distinctive curved profile and show a strong resemblance to the Schlieren image produced by Pandya et al. (2003) reprinted here at the very beginning of this thesis in figure 1.2.

This concludes our study of the trombone and of nonlinear acoustics in open ducts.

4.7 Conclusion

In this chapter we have extended the work of the previous two chapters to account for finite length ducts with an opening into free space. This boundary condition found by approximating free space with a much larger external cylinder, using the average of the monopole and dipole sources in the external duct and ignoring the external surface of the inside duct, has been shown to be a very good one in comparison with the exact Wiener-Hopf solution. Indeed, this method of solution—aside from the obvious ease with which it can be applied to our modal method and subsequently be used to extend the problem to a nonlinear regime—is, in some respects, superior to the Wiener-Hopf solution. By solving in a modal manner, we are able to find the entire pressure field at each s by integrating the required ODE step by step. In contrast, to find the pressure field using the Wiener-Hopf method, one must evaluate complex contour integrals at each s , r and θ . In practice this takes much longer.

In the results, we have been able to replicate much of the acoustic properties of flutes, clarinets, oboes, saxophones and brass instruments using simple duct models. Many classic results are produced by our method, such as the tuning and radiation effects of the instrument’s bell. Curvature was shown to reduce the pitch of the resonant frequencies of the duct by increasing the length of path the pressure wave travels. This effect was further increased by torsion. This effect was only significant near and above the first cut off frequency of the duct. At high frequencies a change in the radiation angle was also noted for curved and helical ducts. Nonlinearity was shown to change the resonant frequencies of the ducts with shifts both up and down depending on the geometry. For horns (and other ducts to a lesser extent), we observed a splitting of the resonance peaks whereby the single peak of the linear regime is split into two or more smaller peaks. We suggested this effect was caused by higher harmonics dominating the resonance and may be responsible for overblowing in brass instruments. To conclude the chapter, we looked at a full trombone model. Despite issues with the sensitivity of the model to the instrument parameters, we were able to demonstrate the effect of a simple conical mouthpiece in lowering the resonances, the lack of effect the bends have on the resonances (as predicted in the previous work) and the formation of shock waves

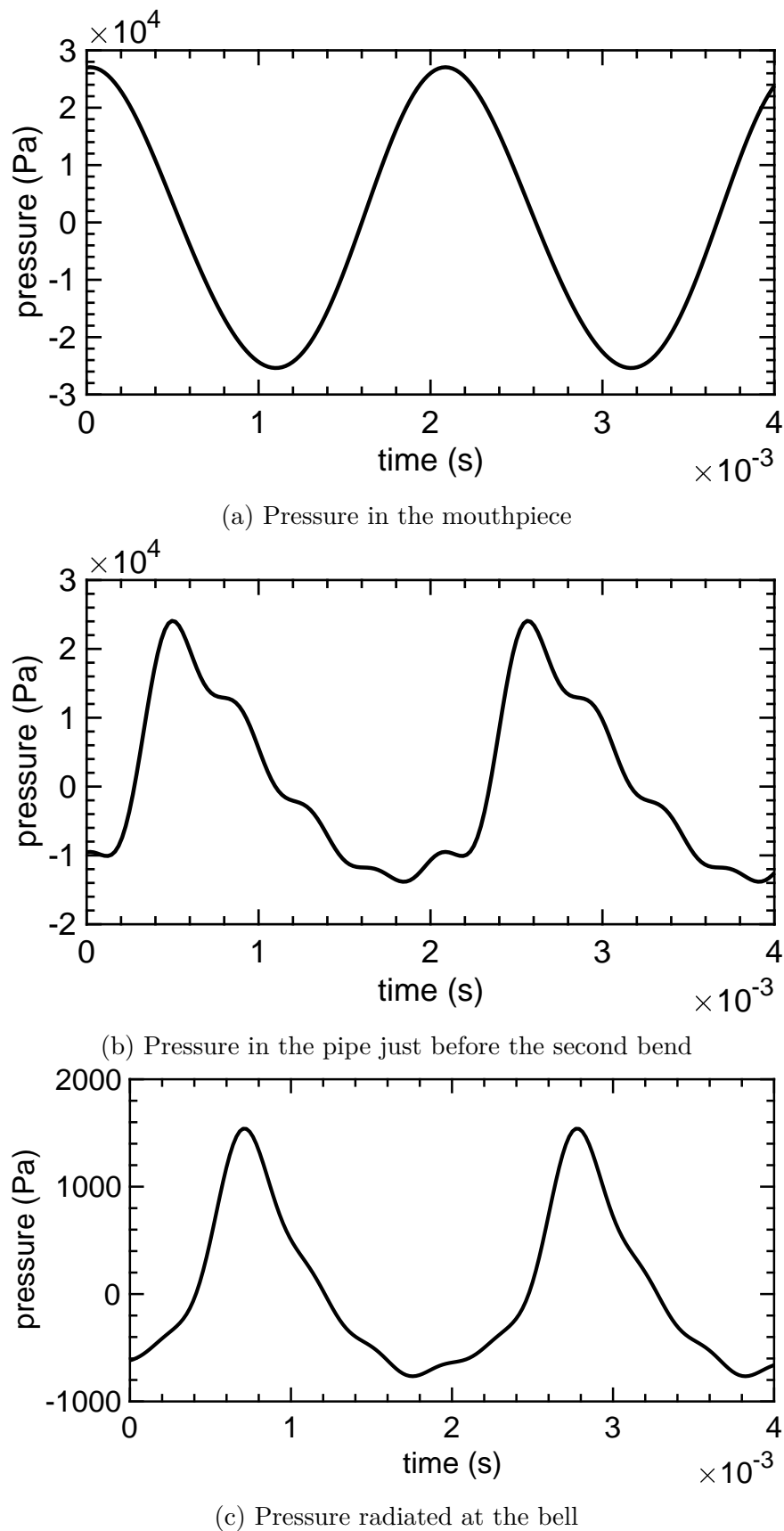


Fig. 4.60 Pressure at different locations through the instrument



(a) Pressure in the trombone

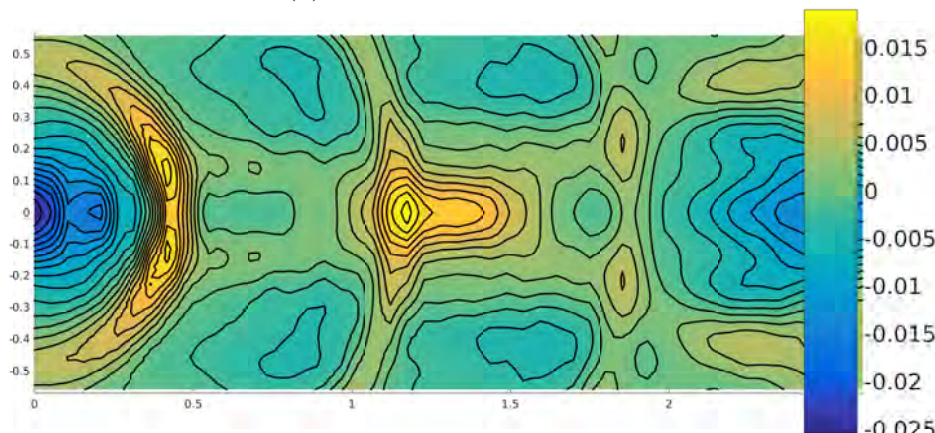
(b) Pressure radiated. Bell radius $\approx 0.11\text{m}$. Radiation from the left.

Fig. 4.61 Pressure distributions for the trombone model in the nonlinear regime $M = 0.1$ at the 8th resonance. Normalized to Mach number.

in the bore at expected amplitudes. Comparing with the work of Hirschberg et al. (1996) we noted that viscosity may play an important role and should be included in future work. The method did however produce the expected curved shock fronts observed by Pandya et al. (2003) radiated from the bell of the instrument.

This concludes our study of open ducts and presentation of the method in general.

Chapter 5

Conclusion

This thesis has established a method to solve for weakly nonlinear acoustics in a general shaped duct in both 2 and 3 dimensions for both infinite ducts and those of finite length. Alongside this method a notation has been developed that greatly simplifies the resulting algebra associated with such problems. Using this method results were produced highlighting the importance of both geometry and nonlinearity, as well as their interplay, in the acoustics of various ducts. Applications for such a method and the results it produces are wide ranging: from musical acoustics (the focus of this thesis) to the aeroacoustics of jet engines—any duct for which the finite amplitude of the sound wave is important is amenable to solution under this method.

In chapter 2 the 2D derivation of the method was presented. Using a coordinate system based on the centreline of the duct together with the normal distance to the centreline a set of equations was derived for the temporal Fourier modes of the acoustic quantities. By expressing these as an infinite sum of straight duct spatial modes and subsequently eliminating the transverse velocity, an equation for the pressure and longitudinal velocity components was derived. Elimination of the transverse velocity components after decomposing in the modal basis was found to be algebraically simpler (and required in the nonlinear case) when compared with the elimination prior used by Félix and Pagneux (2001). Subsequent work showed the two methods resulted in the same final equations. To solve the resulting equations, a coupling between the pressure and velocity modes was established introducing the new nonlinear admittance term central to this thesis. The resulting equations for both the linear and the nonlinear admittance were derived—both numerically stable (and hence showing the admittance is a more natural parameter to work with compared with Félix and Pagneux’s use of the impedance). Finally the resulting pressure equation was derived. This equation is numerically stable (for the most part) and allows for the solving of both forward and

backwards propagating waves together with the nonlinear interaction between the two—this is especially noteworthy given that the equation is a first order ODE to be solved in one direction only. Boundary conditions were derived for an infinite duct outlet, both for the linear admittance (generalising previous work to infinite curved outlets) and the new nonlinear admittance. The stability of these solutions was checked and seen to be stable. Special cases were considered showing the method permits the Fubini (1935) and Sawtooth solutions in 1D, is equivalent to the 2D straight duct method of Fernando et al. (2011) (under certain circumstances), reduces to Webster’s horn equation (Webster, 1919) for variable width ducts and reduces to the method of Félix and Pagneux (2001) in the linear limit. Numerical issues were discussed—particularly the size of the nonlinear admittance term. The first order exponential integrator method was presented as a solution to this problem—requiring fewer evaluations, but still providing a good deal of accuracy. The exact numerical viscosity required for a sawtooth wave after finite truncation was also derived. After some manipulation this was shown to reduce (under certain simplifications) to the “mode number squared” rule heuristically derived by other authors. Results were presented showing almost perfect agreement with the analytic Blackstock (1966) solution and the results of Fernando et al. (2011) and the work of Félix and Pagneux (2001) (in the linear limit). New results showed shocks forming on the outside of bends (to a much larger amplitude than the equivalent straight duct) and increased radiation from exponential horns. Modes which transmit no power in the linear regime were also found to do so in the nonlinear regime—despite being cut-off. Finally, the second chapter introduced the new nonlinear reflectance parameter. In a similar vein to the nonlinear admittance this allowed for the study of the strength of reflectance not only as a function of frequency, but also the amplitude of a signal. In doing so, possible improvements to the agreement with experimental work of Cabelli (1980) were shown. The nonlinear reflectance could also be used to separate the nonlinear superposition of forward and backwards components into its constituent parts.

Chapter 3 extended the work of chapter 2 into 3 dimensions. Using the orthogonal coordinate system of Germano (1982) and again expanding about the basis of straight duct modes, equations for the modal amplitudes in a 3D duct were derived—allowing for both curvature and torsion in the duct. From these, the transverse and azimuthal velocities were eliminated—in contrast to Félix and Pagneux (2002) who eliminated before modal decomposition. Again, these different methods produced the same results numerically, though unlike the 2D cases this was not proved analytically. From the equations for velocity and pressure modes the 3D equations for the linear admittance,

nonlinear admittance and the pressure modes was derived in the same algebraic form as the 2D duct, meaning the same computational machinery and many of the analytic results derived for the 2D duct remain the same in 3D. Boundary conditions were again discussed—being identical in form to the 2D duct for torsion free ducts. The boundary conditions for an infinite helical duct were also presented and discussed—the addition of torsion causing interesting bifurcations in the wavenumber eigenvalues resulting in complex values. These imply the existence of modes which decay as they propagate. Changes in eigenvalues with curvature was also mentioned, showing expected splitting of eigenvalues with symmetry breaking. Results were shown for a curved duct, the exponential horn and helical ducts. Curved ducts, as with 2D, showed shock formation on the outer edge of the bend with increases in localisation both radially and azimuthally as Mach number is increased. The horn showed a greater transmission of energy with the Mach number. Helical ducts showed a greater focussing effect than the torsion free ducts—higher pressure regions on the outside of the bend. This effect was much more apparent when nonlinearity was added with higher torsion resulting in much higher peak pressure amplitudes.

Chapter 4 extended the work of the previous two chapters to finite length ducts. The primary focus was on 3D ducts, though the method is amenable to 2D as well. Simpler duct openings were first considered—the baffled duct and the radiation from a dipole source. Using these two solutions, following the work of Kemp et al. (2017), an approximation to the radiation from an open ended duct into a larger duct was made—extending the previous work into the nonlinear regime and providing a more rigorous derivation. This approximation ignores the scattering off of the external boundary of the duct. This provides the open ended boundary condition for the linear and nonlinear admittance. The exact analytical solution of Levine and Schwinger (1948) for the radiation from a cylindrical duct was presented. Comparison with the modal solution derived showed very good agreement. The concept of resonances in such ducts was discussed and a definition was presented utilising the RMS impedance. Using this definition we examined the resonances of several archetypal ducts: the cylindrical, the Bessel horn, the conical, a curved U-bend and a helical ducts. Such investigations were sufficient to describe a large portion of the acoustical properties of most common wind instruments including flutes, clarinets, oboes, saxophones and the brass family. Nonlinearity was also introduced in such ducts, typically giving rise to small but noticeable shifts in pitches the instruments resonate at, together with a reduction in strength of resonance and a greater amount of sound being radiated. An interesting effect was observed in the case of the horn, whereby the resonance

was dominated by the higher temporal modes causing the resonance peaks to split into two (or sometimes more) peaks. It was suggested that such an effect may be in part responsible for the shift in octaves as an instrument is played at loud volumes. Curved ducts were found to reduce the pitch of the resonant frequencies and increase the strength of the resonance at sufficiently high frequencies for the wavefront to be non-planar—a result of the pressure being localised around the outer side of the duct having to travel a greater distance. At very high frequencies a change in the angle of the beam of radiation was observed from the curved duct—pointing in the direction of the centre of curvature. Similar effects were observed with the helical duct—a further decrease in the pitch of the resonances with the pressure being localised to the wall opposite to the direction of the duct normal at each point—creating a longer path than the torsion free duct. The radiation beam at high frequencies was also directed both in the direction of the centre of curvature of the duct and in the direction of the duct binormal at the duct's exit for high frequencies. Finally, an approximate model of the trombone was considered. Sensitivity in the duct parameters was observed producing differences in the tuning of the instrument. Comparison with and without a simple conical mouthpiece showed a mouthpiece reduces the resonant frequency of the higher duct modes helping with the tuning of the instrument. Curvature showed no difference in the resonant pitches—the instrument bore was too narrow. Nonlinearity was also introduced and consequently shock formation was observed in the instrument at realistic pressure amplitudes. Pitch shifts were also observed, but it was noted that a more realistic instrument model with correct intonation would be required to conclude the resultant pitch shifts with nonlinearity. A large amount of resonance splitting was also observed. It was also noted that decay observed in the pipe was much less than that experimentally observed suggesting the need for the incorporation of a viscosity model into the equations. Curved shock fronts radiating from the bell, as shown experimentally by Pandya et al. (2003), were also observed.

Not dealt with in detail in the body of the text are two additional lines of inquiry covered in the appendices D and E. The first is a substitution, greatly simplifying the governing equations and potentially reducing computational complexity of the method. The second is a small change to the admittance boundary conditions employed, allowing one to solve inverse problems—under certain conditions and certain approximations—in a numerically stable manner. Due to time limitations, neither of these avenues have been pursued to any significant degree, but are included to illustrate additional possible avenues of research.

5.1 Further Work

Aside from the two appendices just mentioned in the previous section, there are many other possible avenues to pursue with this method. We shall note some of them here.

- *Viscosity.* As previously noted, an important aspect missing from the method is the incorporation of viscosity. The method, as presented, gives a fairly complete description of *inviscid* duct acoustics, where the only loss mechanisms are radiation and dissipation at the shock. A complete model for duct acoustics should also include viscosity. How viscosity could be incorporated into the model is likely a very tricky problem. Authors typically work with the viscous Burger's equation when dealing with viscous nonlinear acoustics. This is a popular equation as it can be transformed into the linear diffusion equation by the Cole-Hopf transformation (see Hamilton and Blackstock, 1998, chapter 4). Using this solution, one can obtain the Keck-Beyer solution Keck and Beyer (1960) for weak waves (when the shock formation distance is larger than the absorption length associated with thermoviscous losses)—the limit of which is the Fubini (1935) solution previously encountered in chapter 2. For strong waves one obtains the Fay (1931) solution which, in the limit as the ratio of absorption length to shock formation distance tends to infinity, tends to the sawtooth solution also previously encountered. These two solutions are, however, only relevant for planar waves. As we have seen—particularly with strongly curved ducts—the pressure can become highly nonplanar and localised to the edge of the duct walls. In such a situation it is likely that viscous boundary layers become important. One common approach to account for boundary losses is to add an attenuation operator $L(u)$ to the Burger's equation involving a fractional derivative (Blackstock, 1985)

$$L(u) = B\sqrt{2} \frac{\partial^{1/2}}{\partial t^{1/2}} u. \quad (5.1)$$

The addition of such a parameter typically causes rounding of the positive parts of the waveform and cusping of the negative parts. Again, this only takes into account planar wave propagation, but motivates how one may address the problem. One may be able to expand the pressure and velocity about a basis of duct modes satisfying some boundary condition arising from the boundary layer problem and have a related attenuation term in the governing equations. No attempt at this has been made for the present work and is purely speculative.

- *Finite relaxation.* In a similar vein, one could also address attenuation as a result of a finite relaxation time. For such a fluid, the sound speed increases monotonically from c_0 (the equilibrium sound speed) to c_∞ (the frozen sound speed) as the frequency of the signal is increased. Example plots in Hamilton and Blackstock (1998, chapter 5) for a sinusoidal source propagating in a monorelaxing thermoviscous fluid are highly reminiscent of the wave profile in the pipe of Hirschberg et. al. (figure 3 in Hirschberg et al. at fortissimo and figure 3 in Hamilton and Blackstock chapter 5 p.157) —both showing a shock preceded by a rounded asymmetric wave profile, suggesting this could be the dominant form of attenuation.
- *Mean flow.* In appendix A we justify the ignoring of modes of zero frequency—the zero velocity mode equation is decoupled from the acoustical quantities and is hence not induced by them, while a zero pressure mode is induced but is an order of magnitude smaller than we are interested in locally (and so is ignored). This however, says nothing about a mean flow induced externally. Such a situation would better model acoustics in the exhaust of a jet aircraft (or a more light-hearted example—a novice brass player who has yet to control airflow properly) where the acoustics are advected through the duct.

These form the largest unexplored avenues relating to this research. There are also smaller loose ends which could also be explored

- *Equivalence to Fernando et al. (2011)* In section 2.4.2 we gave a partial proof of the equivalence between this method and that of Fernando et. al., where the form of the pressure was assumed from the velocity potential. If this could be derived from the nonlinear admittance this would complete the proof. Progress may be possible using the simplification of appendix D.
- *3D equivalence results.* In chapter 3 we did not show analytically that the method reduces to that of Félix and Pagneux (2002) (unlike with the 2D). To do so one would need to evaluate the infinite matrix products given in the definition of \mathbf{M} and show they converge to the solution presented by Félix and Pagneux (who derived their formula by eliminating the transverse and azimuthal velocity components before expanding about a basis of duct modes). To do so is more difficult as the Ψ matrices themselves do not have nice forms (by virtue of being integrals over Bessel functions of different orders and their derivatives, as opposed to regular trigonometric functions in 2D).

- *Eigenvalues of the helical duct.* While we have observed bifurcations in the eigenvalues of the linear operator relating to an infinite helical duct, we have made no attempt to determine how and why such bifurcations occur, and at what values of torsion and curvature they happen.
- *Resonance splitting.* We have observed the phenomenon in our results of the resonance peaks becoming split into two or more smaller peaks as nonlinearity is introduced and Mach number is increased (particularly for horns). We have suggested this is due to the change in dominance in the resonance from the fundamental to the second Fourier harmonic with the possibility of this being in part responsible for the overblowing effect in brass instruments. More work—both numerical with this method, and experimental—is needed to explore this claim and the nature of this effect in general.
- *A more realistic trombone model.* As mentioned in the section, an accurate model of a real trombone would provide better theoretical results as to the effects of nonlinearity in the instrument. From this it would also be possible to ascertain what attenuation effects of those mentioned above are important.

Finally, more results should be produced using this method. The focus of this thesis has been an exposition of this method and derivation of the required boundary conditions to run it. The results shown here are mainly to demonstrate the capabilities of such a method, with the particular example of musical acoustics used to illustrate this. This is barely scratching the surface of the possible uses, with others including aeroacoustics (jet aircraft air intakes and exhausts), archeoacoustics (reconstructing the sounds of ancient instruments), bioacoustics (studying the sounds produced by now extinct creatures such as the woolly mammoth) amongst many more. This method could also be used to help investigate in greater detail the theoretical aspects of sound propagation in curved and flared ducts. We have illustrated some qualitative effects such as the localisation of pressure in a bend and the increased radiation from horns and given explanations from a modal perspective. Different perspectives could also be used to further explain these effects such as ray tracing. Such a method may, however, find its biggest usage amongst engineers, where it provides a fast, stable and computationally cheap solution to problems that may have otherwise been tackled by large scale finite element approaches consuming large amounts of computational resources. The ability to produce a solution to a nonlinear acoustics problem in complex geometry (even if rough) in less than ten minutes on a basic desktop computer should be of interest to many in the field.

References

- Airy, G. B. (1849). On a difficulty in the problem of sound. *Phil. Mag., Ser*, 3(1849):34.
- Allen, F. J. (2003). Intonation tendencies of wind instruments. *Texas Bandmasters Association Journal*, 4(4).
- Amir, N., Pagneux, V., and Kergomard, J. (1997). A study of wave propagation in varying cross-section waveguides by modal decomposition. part ii. results. *The Journal of the Acoustical Society of America*, 101(5):2504–2517.
- Anderson, E., Bai, Z., Bischof, C., Blackford, L. S., Demmel, J., Dongarra, J., Du Croz, J., Greenbaum, A., Hammarling, S., McKenney, A., et al. (1999). *LAPACK Users' guide*. SIAM.
- Bi, W., Pagneux, V., Lafarge, D., and Aurégan, Y. (2006). Modelling of sound propagation in a non-uniform lined duct using a multi-modal propagation method. *Journal of Sound and Vibration*, 289(4-5):1091–1111.
- Blackstock, D. T. (1966). Connection between the fay and fubini solutions for plane sound waves of finite amplitude. *The journal of the Acoustical Society of America*, 39(6):1019–1026.
- Blackstock, D. T. (1985). Generalized burgers equation for plane waves. *The Journal of the Acoustical Society of America*, 77(6):2050–2053.
- Blake, E. W. (1848). A determination of the general law according to which pulses differing in intensity are propagated in elastic media, with remarks on the received theory of the velocity of sound. *American Journal of Science and Arts (1820-1879)*, 5(15):372.
- Brambley, E. and Peake, N. (2008). Sound transmission in strongly curved slowly varying cylindrical ducts with flow. *Journal of Fluid Mechanics*, 596:387–412.
- Burgers, J. (1948). A mathematical model illustrating the theory of turbulence. volume 1 of *Advances in Applied Mechanics*, pages 171 – 199. Elsevier.
- Cabelli, A. (1980). The acoustic characteristics of duct bends. *Journal of sound and vibration*, 68(3):369–388.
- Campos, L. (1984). Some general properties of the exact acoustic fields in horns and baffles. *Journal of Sound and Vibration*, 95(2):177–201.

- Challis, J. (1848). On the velocity of sound, in reply to the remarks of the astronomer royal. *The London, Edinburgh, and Dublin Philosophical Magazine and Journal of Science*, 32(218):494–499.
- Earnshaw, S. (1860). On the mathematical theory of sound. *Philosophical Transactions of the Royal Society of London*, 150:133–148.
- Eisner, E. (1967). Complete solutions of the “Webster” horn equation. *The Journal of the Acoustical Society of America*, 41(4B):1126–1146.
- Euler, L. (1759). De la propagation du son. *Mémoires de l’Académie des Sciences de Berlin*, pages 428–507.
- Fay, R. D. (1931). Plane sound waves of finite amplitude. *The Journal of the Acoustical Society of America*, 3(2A):222–241.
- Félix, S. and Pagneux, V. (2001). Sound propagation in rigid bends: A multimodal approach. *The Journal of the Acoustical Society of America*, 110(3):1329–1337.
- Félix, S. and Pagneux, V. (2002). Multimodal analysis of acoustic propagation in three-dimensional bends. *Wave Motion*, 36(2):157–168.
- Fernando, R., Druon, Y., Coulouvrat, F., and Marchiano, R. (2011). Nonlinear waves and shocks in a rigid acoustical guide. *The Journal of the Acoustical Society of America*, 129(2):604–615.
- Fubini, E. (1935). Anomalie nella propagazione di onde acustiche di grande ampiezza. *Alta Frequenza*, 4:530–581.
- Germano, M. (1982). On the effect of torsion on a helical pipe flow. *Journal of Fluid Mechanics*, 125:1–8.
- Gilbert, J., Dalmont, J.-P., Potier, R., and Reby, D. (2014). Is nonlinear propagation responsible for the brassiness of elephant trumpet calls? *Acta Acustica united with Acustica*, 100(4):734–738.
- Gilbert, J., Menguy, L., and Campbell, M. (2008). A simulation tool for brassiness studies. *The Journal of the Acoustical Society of America*, 123(4):1854–1857.
- Hamilton, M. F. and Blackstock, D. T. (1990). On the linearity of the momentum equation for progressive plane waves of finite amplitude. *The Journal of the Acoustical Society of America*, 88(4):2025–2026.
- Hamilton, M. F. and Blackstock, D. T. (1998). *Nonlinear acoustics*, volume 1. Academic press San Diego.
- Hirschberg, A., Gilbert, J., Msallam, R., and Wijnands, A. (1996). Shock waves in trombones. *The Journal of the Acoustical Society of America*, 99(3):1754–1758.
- Hugoniot, P. H. (1887). Sur la propagation du mouvement dans les corps et spécialement dans les gaz parfaits. *Journal de l’École Polytechnique. Paris*, 57:3–97.

- Keck, W. and Beyer, R. T. (1960). Frequency spectrum of finite amplitude ultrasonic waves in liquids. *The Physics of Fluids*, 3(3):346–352.
- Kemp, J. A., Lopez-Carromero, A., and Campbell, M. (2017). Pressure fields in the vicinity of brass musical instrument bells measured using a two dimensional grid array and comparison with multimodal models. *Proceedings of the 24th International Congress on Sound and Vibration*.
- Ko, S.-H. (1979). Three-dimensional acoustic waves propagating in acoustically lined cylindrically curved ducts without fluid flow. *Journal of Sound and Vibration*, 66(2):165 – 179.
- Krasnushkin, P. E. (1945). The waves in curved tubes. *Uchenyye Zapiski MGU (Scientific Reports of Moscow State University)*, 75(2):9 – 27.
- Kuznetsov, V. (1971). Equation of nonlinear acoustics. *Sov. Phys. Acoust.*, 16(4):467–470.
- Lagrange, J. L. (1760). Nouvelles recherches sur la nature et la propagation du son. *Miscellanea Taurinensis*, 2:11–172.
- Levine, H. and Schwinger, J. (1948). On the radiation of sound from an unflanged circular pipe. *Phys. Rev.*, 73:383–406.
- McTavish, J. P. and Brambley, E. J. (2018). Nonlinear sound propagation in 2D curved ducts: A multimodal approach. Submitted to Journal of Fluid Mechanics.
- Moler, C. and Van Loan, C. (2003). Nineteen dubious ways to compute the exponential of a matrix, twenty-five years later. *SIAM review*, 45(1):3–49.
- Myers, A., Gilbert, J., Pyle, B., and Campbell, M. (2007). Non-linear propagation characteristics in the evolution of brass musical instruments design. In *International Congress on Acoustics (19th ICA)*.
- Newton, I. (1687). Of motion propagated through fluids. In *Philosophiae naturalis principia mathematica*, chapter 8. J. Societatis Regiae ac Typis J. Streater.
- Noble, B. (1958). *Methods Based on the Wiener-Hopf Technique for the Solution of Partial Differential Equations*. AMS Chelsea Publishing Series. Chelsea Publishing Company.
- Pagneux, V., Amir, N., and Kergomard, J. (1996). A study of wave propagation in varying cross-section waveguides by modal decomposition. part i. theory and validation. *The Journal of the Acoustical Society of America*, 100(4):2034–2048.
- Pandya, B. H., Settles, G. S., and Miller, J. D. (2003). Schlieren imaging of shock waves from a trumpet. *The Journal of the Acoustical Society of America*, 114(6):3363–3367.
- Poisson, S. D. (1808). Mémoire sur la théorie du son. *Journal de l’École polytechnique*, 7:365–370.

- Rankine, W. J. M. (1870). On the thermodynamic theory of waves of finite longitudinal disturbance. *Philosophical Transactions of the Royal Society of London*, 160:277–288.
- Rayleigh, J. W. S. (1878). *The Theory of Sound*, volume 2. Macmillan.
- Rayleigh, J. W. S. (1910). Aerial plane waves of finite amplitude. *Proceedings of the Royal Society of London Series A*, 84:247–284.
- Rendón, P. L., Orduña-Bustamante, F., Narezo, D., Pérez-López, A., and Sorrentini, J. (2010). Nonlinear progressive waves in a slide trombone resonator. *The Journal of the Acoustical Society of America*, 127(2):1096–1103.
- Riemann, B. (1860). Über die fortpflanzung ebener luftwellen von endlicher schwingungsweite. *Abhandlungen der Gesellschaft der Wissenschaften zu Göttingen*, 8:43–65.
- Rienstra, S. (1984). Acoustic radiation from a semi-infinite annular duct in a uniform subsonic mean flow. *Journal of Sound and Vibration*, 94(2):267 – 288.
- Rostafinski, W. (1972). On propagation of long waves in curved ducts. *The Journal of the Acoustical Society of America*, 52(5B):1411–1420.
- Rostafiński, W. (1991). *Monograph on propagation of sound waves in curved ducts*. National Aeronautics and Space Administration.
- Stevenson, A. F. (1951). Exact and approximate equations for wave propagation in acoustic horns. *Journal of Applied Physics*, 22(12):1461–1463.
- Stokes, G. G. (1848). On a difficulty in the theory of sound. *The London, Edinburgh, and Dublin Philosophical Magazine and Journal of Science*, 33(223):349–356.
- Taylor, G. I. (1910). The conditions necessary for discontinuous motion in gases. *Proceedings of the Royal Society of London A*, 84(571):371–377.
- Thompson, M. W. and Strong, W. J. (2001). Inclusion of wave steepening in a frequency-domain model of trombone sound production. *The Journal of the Acoustical Society of America*, 110(1):556–562.
- Ting, L. and Miksis, M. J. (1983). Wave propagation through a slender curved tube. *The Journal of the Acoustical Society of America*, 74(2):631–639.
- Webster, A. G. (1919). Acoustical impedance and the theory of horns and of the phonograph. *Proceedings of the National Academy of Sciences*, 5(7):275–282.
- Weinstein, L. A. (1948). Rigorous solution of the problem of an open-ended parallel-plate waveguide. *Izvestija Akademija Nauk SSSR, Serija Fizicheskaja*, 12:144–165.

Appendix A

Modes of Zero Frequency

In this appendix we justify ignoring the modes of zero frequency. From (2.14a), setting $a = 0$ we obtain

$$\nabla \cdot \mathbf{U}^0 = \sum_{b=-\infty}^{\infty} (-ikP^{-b}P^b - ikU^{-b}U^b - ikV^{-b}V^b) \quad (\text{A.1})$$

where we have substituted for the differential terms on the RHS. It can clearly be seen that upon summation, the RHS vanishes and we are left with the classical incompressibility condition $\nabla \cdot \mathbf{U}^0 = 0$. As such, the modes U^0 are decoupled from the acoustic modes and we do not have acoustic streaming. As we are not imposing any mean flow in the duct and none is induced by the acoustic phenomena, we ignore the modes U^0 .

By taking (2.18b) and (2.18c), and the linear relationship between P^a and U^a given by (2.29), it can be seen that (2.14b) reduces to

$$\nabla P^0 = - \sum_{b=-\infty}^{\infty} \nabla \left(\frac{1}{2} U^{-b} U^b - \frac{1}{2} P^{-b} P^b \right) \quad (\text{A.2})$$

for $a = 0$. Therefore we have

$$P^0 = - \langle \mathcal{L} \rangle \quad (\text{A.3})$$

where $\mathcal{L} = \hat{\mathbf{u}}^2/2 - \hat{p}^2/2$ is the Lagrangian density of energy and $\langle \rangle$ denotes time average. As this is an order of magnitude smaller than the other pressure terms (noting that while we have retained terms of $\mathcal{O}(M^2)$ in our equations, their effect is cumulative whereas the local sound pressure we are interested in is $\mathcal{O}(M)$), it does not affect our governing equations. It can therefore be ignored in calculations and makes little difference to the final pressure profile.

Appendix B

Analytic Expressions for the Ψ Matrices

B.1 2D

$$\Psi_{pq} = \delta_{pq}, \quad (\text{B.1a})$$

$$\Psi_{[p]q} = \begin{cases} C_p C_q \frac{p^2((-1)^{p+q}-1)}{p^2-q^2} & p \neq q \\ 0 & p = q, \end{cases} \quad (\text{B.1b})$$

$$\Psi_{pq}[r] = \begin{cases} C_p C_q \frac{(p^2+q^2)(h_+-h_-)^2((-1)^{p+q}-1)}{\pi^2(p^2-q^2)^2} & p \neq q \\ (h_+ + h_-)/2 & p = q, \end{cases} \quad (\text{B.1c})$$

$$\Psi_{[p]q}[r] = \begin{cases} C_p C_q \frac{p^2(h_+(-1)^{p+q}-h_-)}{p^2-q^2} & p \neq q \\ 1/2 & p = q, \quad p \neq 0 \\ 0 & p = 0, \end{cases} \quad (\text{B.1d})$$

$$\Psi_{\{p\}q} = \begin{cases} -\left(\frac{h'_+ - h'_-}{h_+ - h_-}\right)(1 - \delta_{p0}/2) & p = q \\ -C_p C_q ((-1)^{p+q} h'_+ - h'_-) \frac{p^2}{p^2-q^2} & p \neq q, \end{cases} \quad (\text{B.1e})$$

$$\Psi_{pqr} = C_p C_q C_r \frac{(h_+ - h_-)}{4} \left(\delta_{p,q+r} + \delta_{p,|q-r|} + \delta_{p,0} \delta_{q,r} + \delta_{p,0} \delta_{q,0} \delta_{r,0} \right), \quad (\text{B.1f})$$

$$\Psi_{[p]qr} = \begin{cases} C_p C_q C_r \frac{p^2((-1)^{p+q+r}-1)(p^2-q^2-r^2)}{(p+q+r)(p+q-r)(p-q+r)(p-q-r)} & p \neq |q+r|, \quad p \neq |q-r| \\ 0 & \text{else,} \end{cases} \quad (\text{B.1g})$$

$$\Psi_{pqr}[r] = \begin{cases} C_p C_q C_r ((-1)^{p+q+r} - 1) \frac{(h_+ - h_-)^2}{4\pi^2} \left(\dots \right) & p \neq |q+r|, \quad p \neq |q-r| \\ \frac{1}{(p+q+r)^2} + \frac{1}{(p-q+r)^2} + \frac{1}{(p+q-r)^2} + \frac{1}{(p-q-r)^2} & \text{else} \\ 0 & \end{cases} \quad (\text{B.1h})$$

$$\Psi_{[p]qr}[r] = \begin{cases} C_p C_q C_r \frac{(h_+(-1)^{p+q+r}-h_-)p^2(p^2-q^2-r^2)}{(p+q+r)(p+q-r)(p-q+r)(p-q-r)} & p \notin \{|q+r|, |q-r|\}, \\ \frac{C_p C_q C_r}{8} (h_+ - h_-) p \left(\frac{1}{q+r} + \frac{1}{q} + \frac{1}{r} \right) & p = q+r, \\ \frac{C_p C_q C_r}{8} (h_+ - h_-) p \left(\frac{1}{q} - \frac{1}{r} + \frac{1}{q-r} \right) & p = q-r, \\ \frac{C_p C_q C_r}{8} (h_+ - h_-) p \left(\frac{1}{r} - \frac{1}{r} + \frac{1}{r-q} \right) & p = r-q, \\ \frac{C_p C_q C_r}{4} (h_+ - h_-) & p = q, r = 0 \\ \frac{C_p C_q C_r}{4} (h_+ - h_-) & p = r, q = 0 \\ 0 & \text{else} \end{cases} \quad (\text{B.1i})$$

$$\Psi_{\{p\}qr} = -\frac{(h'_+ - h'_-)}{2(h_+ - h_-)} \Psi_{pqr} + \frac{h_- h'_+ - h_+ h'_-}{h_+ - h_-} \Psi_{[p]qr} - \frac{h'_+ - h'_-}{h_+ - h_-} \Psi_{[p]qr}[r], \quad (\text{B.1j})$$

$$\frac{\partial}{\partial s}(\Psi_{pqr}) = -\frac{1}{2} \left(\frac{h'_+ - h'_-}{h_+ - h_-} \right) \Psi_{pqr}. \quad (\text{B.1k})$$

B.2 3D

Unlike with the 2D duct we cannot give analytical expressions for the Ψ matrices. We can however make progress in simplifying them. The integrals for which they represent can be split into their radial and angular parts. So for example (no summation)

$$\Psi_{[\alpha](\beta)\gamma}[r(1 - \kappa r \cos \phi)] = \chi_{[\alpha]\beta\gamma}[r] \Theta_{\alpha(\beta)\gamma} - \kappa \chi_{[\alpha]\beta\gamma}[r^2] \Theta_{\alpha(\beta)\gamma}[\cos \phi] \quad (\text{B.2})$$

with

$$\chi_{[\alpha]\beta\gamma} = \int_0^h \frac{d}{dr} \left(C_\alpha J_p \left(\frac{j_{pq}r}{h} \right) \right) C_\beta J_s \left(\frac{j_{st}r}{h} \right) C_\gamma J_u \left(\frac{j_{uv}r}{h} \right) dr \quad (\text{B.3a})$$

$$\Theta_{\alpha(\beta)\gamma} = \int_0^{2\pi} \cos(p\phi - \xi\pi/2) \frac{d}{d\theta} \left(\cos(s\phi - \eta\pi/2) \right) \cos(u\phi - \zeta\pi/2) d\theta \quad (\text{B.3b})$$

where $\alpha \mapsto (p, q, \xi)$, $\beta \mapsto (s, t, \eta)$ and $\gamma \mapsto (u, v, \zeta)$. The χ integrals involving derivatives can be simplified as follows

$$\chi_{[\alpha]\beta}[r] = C_\alpha C_\beta \int_0^h p J_p \left(\frac{j_{pq} r}{h} \right) J_s \left(\frac{j_{st} r}{h} \right) dr - C_\alpha C_\beta \int_0^h \frac{j_{pq} r}{h} J_{p+1} \left(\frac{j_{pq} r}{h} \right) J_s \left(\frac{j_{st} r}{h} \right) dr \quad (\text{B.4})$$

The Θ integrals can be calculated analytically

$$\Theta_{\alpha\beta} = \pi \delta_{ps} \delta_{\xi\eta} (1 + \delta_{p0} (-1)^\xi) \quad (\text{B.5a})$$

$$\Theta_{\alpha\beta} [\cos \phi] = \pi / 2 \delta_{\xi\eta} (\delta_{p+s,1} (-1)^\xi + \delta_{|p-s|,1}) \quad (\text{B.5b})$$

$$\Theta_{(\alpha)\beta} = p \pi \delta_{ps} (\delta_{\xi 1} \delta_{\eta 0} - \delta_{\xi 0} \delta_{\eta 1}) \quad (\text{B.5c})$$

$$\Theta_{(\alpha)\beta} [\cos \phi] = p \pi / 2 (\delta_{p+s,1} + \delta_{|p-s|,1}) (\delta_{\xi 1} \delta_{\eta 0} - \delta_{\xi 0} \delta_{\eta 1}) \quad (\text{B.5d})$$

$$\begin{aligned} \Theta_{\alpha\beta\gamma} = & \pi / 2 \left(\delta_{p+s,u} (\delta_{\xi+\eta,\zeta} - \delta_{\xi 1} \delta_{\eta 1} \delta_{\zeta 0}) + \delta_{p+u,s} (\delta_{\xi+\zeta,\eta} - \delta_{\xi 1} \delta_{\eta 0} \delta_{\zeta 1}) \right. \\ & \left. + \delta_{s+u,p} (\delta_{\eta+\zeta,\xi} - \delta_{\xi 0} \delta_{\eta 1} \delta_{\zeta 0}) + \delta_{p0} \delta_{s0} \delta_{u0} (\delta_{\xi 0} \delta_{\eta 0} \delta_{\zeta 0} - \delta_{\xi+\eta+\zeta,2}) \right) \end{aligned} \quad (\text{B.5e})$$

$$\begin{aligned} \Theta_{\alpha\beta\gamma} [\cos \phi] = & \pi / 4 \left(\delta_{|p+s+u|,1} (\delta_{\xi 0} \delta_{\eta 0} \delta_{\zeta 0} - \delta_{\xi+\eta+\zeta,2}) + \delta_{|p+s-u|,1} (\delta_{\xi+\eta,\zeta} - \delta_{\xi 1} \delta_{\eta 1} \delta_{\zeta 0}) \right. \\ & \left. + \delta_{|p-s-u|,1} (\delta_{\eta+\zeta,\xi} - \delta_{\xi 0} \delta_{\eta 1} \delta_{\zeta 1}) + \delta_{|p-s+u|,1} (\delta_{\xi+\zeta,\eta} - \delta_{\xi 1} \delta_{\eta 0} \delta_{\zeta 1}) \right) \end{aligned} \quad (\text{B.5f})$$

$$\begin{aligned} \Theta_{\alpha\beta\gamma} [\sin \phi] = & \pi / 4 \left((\delta_{p+s+u,-1} - \delta_{p+s+u,1}) (\delta_{\xi 1} \delta_{\eta 1} \delta_{\zeta 1} - \delta_{\xi+\eta+\zeta,1}) \right. \\ & + (\delta_{p-s-u,-1} - \delta_{p-s-u,1}) \delta_{|\xi-\eta-\zeta|,1} + (\delta_{p+s-u,-1} - \delta_{p+s-u,1}) \delta_{|\xi+\eta-\zeta|,1} \\ & \left. + (\delta_{p-s+u,-1} - \delta_{p-s+u,1}) \delta_{|\xi-\eta+\zeta|,1} \right) \end{aligned} \quad (\text{B.5g})$$

$$\begin{aligned} \Theta_{(\alpha)\beta\gamma} = & p \pi / 2 \left(\delta_{p0} \delta_{s0} \delta_{u0} (\delta_{\xi+\eta+\zeta,-} - \delta_{\xi 1} \delta_{\eta 1} \delta_{\zeta 1}) + \delta_{p,s+u} (\delta_{\xi-\eta-\zeta,1} - \delta_{\xi-\eta-\zeta,-1}) \right. \\ & \left. + \delta_{p+s,u} (\delta_{\xi+\eta-\zeta,1} - \delta_{\xi+\eta-\zeta,-1}) + \delta_{p+u,s} (\delta_{\xi-\eta+\zeta,1} - \delta_{\xi-\eta+\zeta,-1}) \right) \end{aligned} \quad (\text{B.5h})$$

$$\begin{aligned} \Theta_{(\alpha)\beta\gamma} [\cos \phi] = & p \pi / 4 \left(\delta_{p+s+u,1} (\delta_{\xi+\eta+\zeta,1} - \delta_{\xi 1} \delta_{\eta 1} \delta_{\zeta 1}) + \delta_{|p-s-u|,1} (\delta_{\xi-\eta-\zeta,1} - \delta_{\xi-\eta-\zeta,-1}) \right. \\ & \left. + \delta_{|p+s-u|,1} (\delta_{\xi+\eta-\zeta,1} - \delta_{\xi+\eta-\zeta,-1}) + \delta_{|p-s+u|,1} (\delta_{\xi-\eta+\zeta,1} - \delta_{\xi-\eta+\zeta,-1}) \right) \end{aligned} \quad (\text{B.5i})$$

We also have

$$\Psi_{\{\alpha\}\beta} = \chi_{\{\alpha\}\beta} \Theta_{\alpha\beta} + \chi_{\alpha\beta} \Theta_{\{\alpha\}\beta} \quad (\text{B.6})$$

with

$$\chi_{\{\alpha\}\beta} = - \frac{h'}{h} (\chi_{[\alpha]\beta}[r] + \chi_{\alpha\beta}) \quad (\text{B.7a})$$

$$\theta_{\{\alpha\}\beta} = -\tau \Theta_{(\alpha)\beta} \quad (\text{B.7b})$$

Similarly,

$$\frac{d}{ds} \left(\Psi_{\alpha\beta\gamma}[r] \right) = \frac{d}{ds} \left(\chi_{\alpha\beta\gamma}[r] \right) \Theta_{\alpha\beta\gamma} \quad (\text{B.8})$$

with

$$\frac{d}{ds} \left(\chi_{\alpha\beta\gamma}[r] \right) = -\frac{3h'}{h} \chi_{\alpha\beta\gamma}[r] + hh' C_\alpha C_\beta C_\gamma J_p(j_{pq}) J_s(j_{st}) J_u(j_{uv}) - \frac{h'}{h} \chi_{[\alpha]\beta\gamma} - \frac{h'}{h} \chi_{\alpha[\beta]\gamma} - \frac{h'}{h} \chi_{\alpha\beta[\gamma]} \quad (\text{B.9})$$

B.3 Open Ducts

For 3D ducts with $\alpha \mapsto (p, q, \xi)$ and $\beta \mapsto (s, t, \eta)$, F is given by

$$F_{\alpha\beta} = C_\alpha^1 C_\beta^2 \frac{j_{pq} J_{p-1}(j_{pq}) J_p \left(\frac{h_1}{h_2} j_{pt} \right) - \frac{h_1}{h_2} j_{pt} J_p(j_{pq}) J_{p-1} \left(\frac{h_1}{h_2} j_{pt} \right)}{\frac{j_{pt}^2}{h_2^2} - \frac{j_{pq}^2}{h_1^2}} \Theta_{\alpha\beta} \quad (\text{B.10})$$

for $p = s$ with any of p, q or $t \neq 0$

$$F_{\alpha\beta} = C_\alpha^1 C_\beta^2 \frac{h_1^2}{2} \Theta_{\alpha\beta} \quad (\text{B.11})$$

for $p = s = 0$ and $q = t = 0$ and

$$F_{\alpha\beta} = 0 \quad (\text{B.12})$$

otherwise.

Appendix C

Inverting \mathbf{F}

By equating normal velocities for the hard walled problem and applying the no penetration condition for $r > h_1$ we obtained (4.8):

$$\mathbf{u}_h^2 = \mathbf{F}^T \mathbf{u}_h^1 \quad (\text{C.1})$$

We may also match velocities from region 2 into region 1

$$U_\alpha^1 = \int_{r < h_1} u^2 \psi_\alpha^1 dS = \int_{r < h_1} \psi_\alpha^1 \psi_\beta^2 dS U_\beta^2 = F_{\alpha\beta} U_\alpha^2 \quad (\text{C.2})$$

or

$$\mathbf{u}_h^1 = \mathbf{F} \mathbf{u}_h^2 \quad (\text{C.3})$$

although this does not imply the boundary condition we required for the derivation of the impedance in region 1. We can combine these two relationships between region 1 and 2

$$\mathbf{u}_h^1 = \mathbf{F} \mathbf{F}^T \mathbf{u}_h^1 \quad (\text{C.4a})$$

$$\mathbf{u}_h^2 = \mathbf{F}^T \mathbf{F} \mathbf{u}_h^2 \quad (\text{C.4b})$$

From equation (C.4a) we can cancel off the \mathbf{u}_h^1 as they are free vectors (strictly speaking we take \mathbf{p}^1 to be our free vector, but as the relationship between \mathbf{p}^1 and \mathbf{u}^1 is invertible, \mathbf{u}_h^1 can be treated as free) to obtain

$$\mathbf{F} \mathbf{F}^T = \mathbf{I} \quad (\text{C.5})$$

We are unable to do the same for equation (C.4b) as \mathbf{u}_h^2 is *not* free (there is no invertible relationship between \mathbf{u}_h^2 and \mathbf{p}^1 as \mathbf{u}_h^2 is defined such that $u^2 = 0$ for $r > h_1$). We may only conclude that \mathbf{u}_h^2 is an eigenvalue of $\mathbf{F}^T \mathbf{F}$. See Pagneux et al. (1996).

A similar argument can be made with the dipole problem, exchanging \mathbf{p} 's for \mathbf{u} 's to obtain the same result.

Appendix D

A Simplifying Substitution

D.1 2D

A substitution can be made to greatly simplify the derivation of the governing equations. We start by rearranging equations (2.18a), (2.18b) and (2.18c) to obtain

$$\begin{aligned} & -\text{i}akP^a + \frac{1}{1-\kappa r} \frac{\partial U^a}{\partial s} + \frac{1}{1-\kappa r} \frac{\partial}{\partial r} ((1-\kappa r)V^a) \\ &= \sum_{b=-\infty}^{\infty} \frac{-\text{i}ak}{2} \left(\left(1 + \frac{B}{A}\right) P^{a-b} P^b + U^{a-b} U^b + V^{a-b} V^b \right), \end{aligned} \quad (\text{D.1a})$$

$$- \text{i}ak(1-\kappa r)U^a + \frac{\partial P^a}{\partial s} = \sum_{b=-\infty}^{\infty} \frac{1}{2} \frac{\partial}{\partial s} \left(P^{a-b} P^b - U^{a-b} U^b - V^{a-b} V^b \right), \quad (\text{D.1b})$$

$$- \text{i}akV^a + \frac{\partial P^a}{\partial r} = \sum_{b=-\infty}^{\infty} \frac{1}{2} \frac{\partial}{\partial r} \left(P^{a-b} P^b - U^{a-b} U^b - V^{a-b} V^b \right) \quad (\text{D.1c})$$

From these equations we can introduce a modified pressure

$$\hat{P}^a = P^a + \frac{1}{2} \sum_{b=-\infty}^{\infty} \left(U^{a-b} U^b + V^{a-b} V^b - P^{a-b} P^b \right) \quad (\text{D.2})$$

reducing the above equations, correct to second order, to

$$\begin{aligned} & -\text{i}ak\hat{P}^a + \frac{1}{1-\kappa r} \frac{\partial U^a}{\partial s} + \frac{1}{1-\kappa r} \frac{\partial}{\partial r} ((1-\kappa r)V^a) \\ &= \sum_{b=-\infty}^{\infty} -\text{i}ak \left(U^{a-b} U^b + V^{a-b} V^b + \frac{B}{2A} \hat{P}^{a-b} \hat{P}^b \right), \end{aligned} \quad (\text{D.3a})$$

$$- \text{i}ak(1-\kappa r)U^a + \frac{\partial \hat{P}^a}{\partial s} = 0 \quad (\text{D.3b})$$

$$-iakV^a + \frac{\partial \hat{P}^a}{\partial r} = 0 \quad (\text{D.3c})$$

We can then proceed as before using this new variable \hat{P} . As this substitution is identical at order M , we do not need to invert the transform. As with the modes of zero frequency (appendix A) we are only interested in the variables locally to order M (we retain $\mathcal{O}(M^2)$ terms in equations as the effect of nonlinear terms is cumulative over distance).

Using this substitution the modal equations reduce to

$$\mathbf{u}' + \mathsf{Mp} + \mathsf{Gu} = \mathcal{A}[\mathbf{u}, \mathbf{u}] + \mathcal{B}[\mathbf{p}, \mathbf{p}], \quad (\text{D.4a})$$

$$\mathbf{p}' - \mathsf{Nu} - \mathsf{H}\mathbf{p} = 0 \quad (\text{D.4b})$$

with identical linear matrices and new nonlinear tensors

$$\mathcal{A}_{pqr}^{ab} = -iak\Psi_{pqr}[1 - \kappa r] \quad (\text{D.5a})$$

$$\mathcal{B}_{pqr}^{ab} = \frac{ia}{(a-b)bk}\Psi_{pst}[1 - \kappa r]\Psi_{s[q]}\Psi_{t[r]} - iak\frac{B}{2A}\Psi_{pqr}[1 - \kappa r] \quad (\text{D.5b})$$

This is clearly a vast simplification removing many of the nonlinear tensors and simplifying the remaining ones. Aside from ease in derivation and the clear computational benefits, this substitution may also be more useful for theoretical work. It is hoped that this may lead to a complete proof of equivalence with the method of Fernando et al. (2011).

D.2 3D

As with the 2D ducts, the same substitution can be used in the 3D case. Beginning with (3.6a), (3.6b), (3.6c) and (3.6d)

$$\begin{aligned} & -iakP^a + \frac{1}{1 - \kappa \cos \phi} \frac{\partial U^a}{\partial s} + \frac{\partial V^a}{\partial r} + \frac{1}{r}V^a - \frac{\kappa \cos \phi}{1 - \kappa r \cos \phi}V^a + \frac{1}{r} \frac{\partial W^a}{\partial \theta} + \frac{\kappa \sin \phi}{1 - \kappa r \cos \phi}W^a \\ &= \sum_{b=-\infty}^{\infty} -\frac{iak}{2} \left(\left(1 + \frac{B}{A}\right) P^{a-b}P^b + U^{a-b}U^b + V^{a-b}V^b + W^{a-b}W^b \right), \end{aligned} \quad (\text{D.6a})$$

$$\begin{aligned} & -iak(1 - \kappa r \cos \phi)U^a + \frac{\partial P^a}{\partial s} \\ &= \sum_{b=-\infty}^{\infty} \frac{1}{2} \frac{\partial}{\partial s} \left(P^{a-b}P^b - U^{a-b}U^b - V^{a-b}V^b - W^{a-b}W^b \right), \end{aligned} \quad (\text{D.6b})$$

$$\begin{aligned} & -\text{i}akV^a + \frac{\partial P^a}{\partial r} \\ = & \sum_{b=-\infty}^{\infty} \frac{1}{2} \frac{\partial}{\partial r} (P^{a-b}P^b - U^{a-b}U^b - V^{a-b}V^b - W^{a-b}W^b), \end{aligned} \quad (\text{D.6c})$$

$$\begin{aligned} & -\text{i}akrW^a + \frac{\partial P^a}{\partial \theta} \\ = & \sum_{b=-\infty}^{\infty} \frac{1}{2} \frac{\partial}{\partial \theta} (P^{a-b}P^b - U^{a-b}U^b - V^{a-b}V^b - W^{a-b}W^b). \end{aligned} \quad (\text{D.6d})$$

Again, making the substitution for P

$$\hat{P}^a = P^a + \frac{1}{2} \sum_{b=-\infty}^{\infty} (U^{a-b}U^b + V^{a-b}V^b + W^{a-b}W^b - P^{a-b}P^b) \quad (\text{D.7})$$

the equations reduce to

$$\begin{aligned} & -\text{i}ak\hat{P}^a + \frac{1}{1-\kappa \cos \phi} \frac{\partial U^a}{\partial s} + \frac{\partial V^a}{\partial r} + \frac{1}{r} V^a - \frac{\kappa \cos \phi}{1-\kappa r \cos \phi} V^a + \frac{1}{r} \frac{\partial W^a}{\partial \theta} + \frac{\kappa \sin \phi}{1-\kappa r \cos \phi} W^a \\ = & \sum_{b=-\infty}^{\infty} -\text{i}ak (U^{a-b}U^b + V^{a-b}V^b + W^{a-b}W^b + \frac{B}{2A} \hat{P}^{a-b} \hat{P}^b), \end{aligned} \quad (\text{D.8a})$$

$$-\text{i}ak(1-\kappa r \cos \phi)U^a + \frac{\partial \hat{P}^a}{\partial s} = 0, \quad (\text{D.8b})$$

$$-\text{i}akV^a + \frac{\partial \hat{P}^a}{\partial r} = 0, \quad (\text{D.8c})$$

$$-\text{i}akrW^a + \frac{\partial \hat{P}^a}{\partial \theta} = 0. \quad (\text{D.8d})$$

from which the simplified governing equations can be derived

$$\mathbf{u}' + \mathbf{Mp} + \mathbf{Gu} = \mathcal{A}[\mathbf{u}, \mathbf{u}] + \mathcal{B}[\mathbf{p}, \mathbf{p}] \quad (\text{D.9a})$$

$$\mathbf{p}' - \mathbf{Nu} - \mathbf{H}\mathbf{p} = 0 \quad (\text{D.9b})$$

As with the 2D duct, the linear matrices are identical. The nonlinear tensors become

$$\mathcal{A}_{\alpha\beta\gamma}^{ab} = -\text{i}ak\Psi_{\alpha\beta\gamma}[1-\kappa r \cos \phi] \quad (\text{D.10a})$$

$$\begin{aligned} \mathcal{B}_{\alpha\beta\gamma}^{ab} = & -\text{i}ak \left(\Psi_{\alpha\mu\nu}[1-\kappa r \cos \phi] \mathbf{V}_{\mu\beta}^{a-b} \mathbf{V}_{\nu\gamma}^b + \Psi_{\alpha\mu\nu}[1-\kappa r \cos \phi] \mathbf{W}_{\mu\beta}^{a-b} \mathbf{W}_{\nu\gamma}^b \right. \\ & \left. + \frac{B}{2A} \Psi_{\alpha\beta\gamma}[1-\kappa r \cos \phi] \right) \end{aligned} \quad (\text{D.10b})$$

greatly simplifying the derivation and the resulting expressions for the 3D duct.

Appendix E

Nonlinear Inverse Method

By means of a simple trick, we can find the inverse to problems posed in this thesis at no additional computational cost. If, instead of taking Λ as defined in section 2.3, we take its complex conjugate then we swap the direction of propagation while retaining decaying evanescent modes (merely taking the negative of Λ would swap the direction of propagation *and* cause evanescent modes to be growing in the positive s direction). In doing so we, solve for *incoming* waves in a numerically stable manner—recall that provided we have decaying evanescent modes the boundary conditions for Υ and \mathcal{Y} are stable. Decaying evanescent modes also keep the pressure equation stable—having modes that grow cause the equation to be inherently unstable. Using this method we can take the duct exit as our new source, choose an exit condition we desire, solve to the inlet (using this change of impedance to keep the wave propagation from inlet to outlet) and hence find the requisite inlet condition to produce the desired outlet pressure.

Some solutions do not have an inverse, for example a “backwards sawtooth” waveform—a sawtooth pressure profile with $p(\bar{s}(t) - \delta s) < p(\bar{s}(t) + \delta s)$ with $\bar{s}(t)$ the position of the shock at time t . Any nonlinear propagation will smooth out the discontinuity. Other inverse problems have a non-unique solution. The “regular sawtooth” (achieved from, for example, a sinusoidal pressure source propagating in the nonlinear regime down a duct) does not have a unique inverse—indeed, any pressure source will eventually attain this shape after sufficient distance—once a shock has been formed, information is lost about the initial waveform. As such, we must confine the inverse method to be within shock formation distance. In doing so, we can drop the numerical viscosity from the simulation as this is only strictly necessary after shock formation (if we kept the ordinary viscosity propagating forward, we would have to add energy in the form of “anti viscosity” to the system in the inverse method, causing numerical

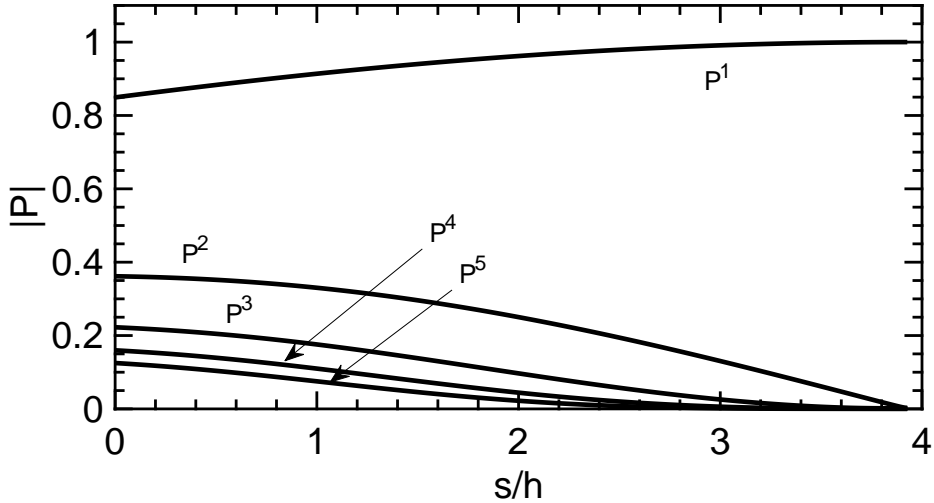


Fig. E.1 Modal amplitudes of nonlinear propagation down a 1D duct to achieve a sinusoidal wave

instabilities). A third category for which the the inverse method does not work is for wave profiles involving a large number of evanescent modes. To achieve such a wave profile, one would need to have an exponentially large initial solution. In practice, any evanescent modes will decay fast enough to be unnoticeable at any appreciable distance and so do not have an inverse in any meaningful sense.

In cases when an inverse does exist the method can produce good results. Figure E.1 shows propagation down a 1D duct from an initial condition produced by the inverse method—the goal solution is a sinusoidal waveform. The figure clearly shows the higher harmonics transferring their energy *to* the fundamental—something we have not encountered before in the thesis (and is not commonly mentioned in the literature, if at all). This is the result of having something akin to the “backwards sawtooth” mentioned before as an initial condition—the nonlinearity straightens out the waveform. An important point to note here is that that this is an effect of the phase of the initial harmonics. While phase is not usually an important feature in acoustics—humans cannot hear the difference between signals whose harmonics are in different phases—here, the initial phase differences (together with nonlinearity) cause the signal to reduce in harmonic complexity with distance—something which would be heard. If one were to listen to this, one would hear the sound getting *mellower* as the sound gets louder, up to a point (at which the sine wave begins to steepen again in the other direction, enriching the sound once more). To the author’s knowledge, no such effect has been tested for.

Another, more complicated example considered is the curved duct from chapter 3 (and also studied by Félix and Pagneux, 2002). Figure E.2 shows the modal amplitudes through the duct in both linear and nonlinear regimes (with normalized amplitudes). The desired waveform is a planar sinusoidal wave at the duct exit. In both cases, the exit solution achieved is very close to that desired, with higher modes and harmonics decaying in amplitude towards the exit leaving the remaining planar mode (despite many of these higher modes initially growing in the bend). Figure E.3 shows the resulting pressure distributions. Both clearly show an almost planar waveform at the duct exit (to the bottom) resulting from a nonplanar source (to the left). In the nonlinear case, we can see a shock. This is, in fact, a manufactured shock (not resulting from the nonlinearity)—looking closer one sees the high pressure ahead of the low. We are sending this “backwards shock” into the duct, and the nonlinearity and curvature are smoothing it out into a planar sinusoidal profile at the exit.

To what extent this method is useful—or indeed practicable—is not known, but it is included here out of interest.

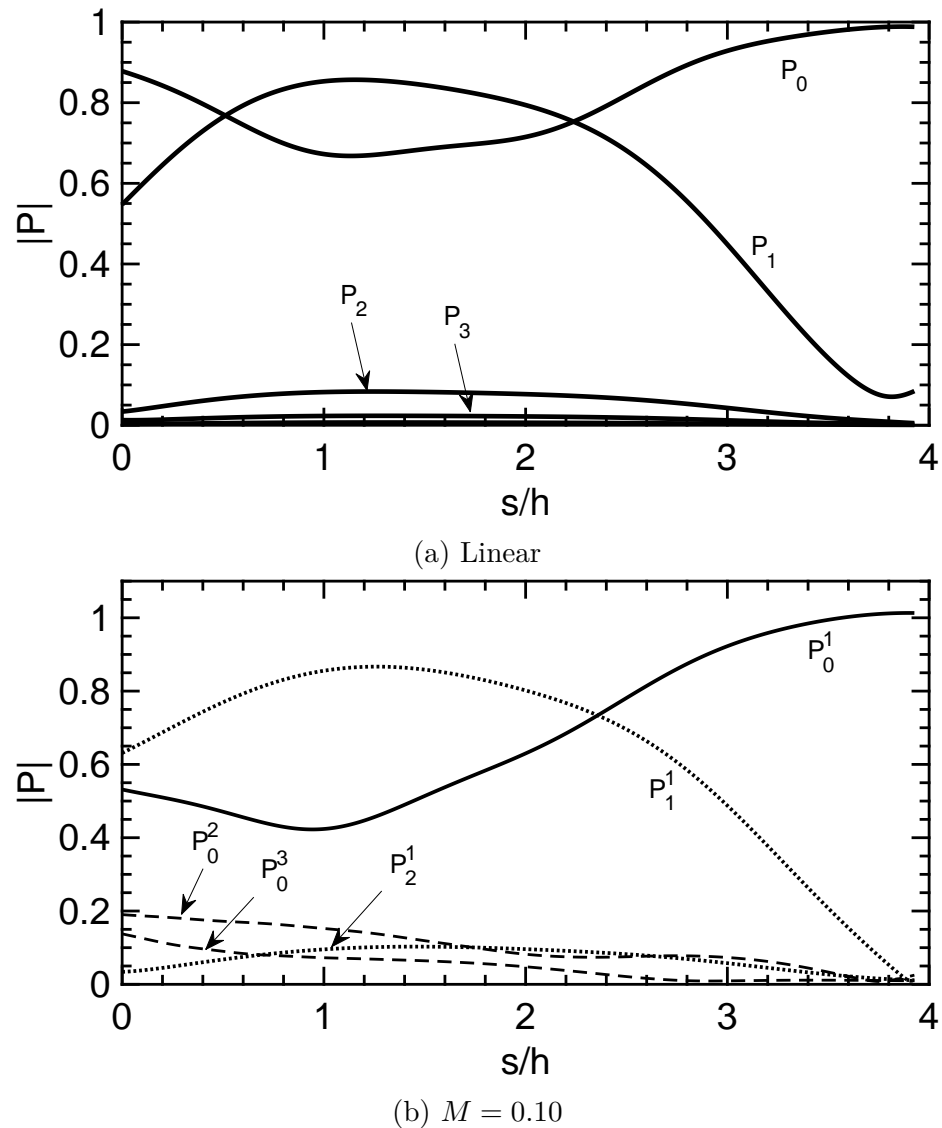


Fig. E.2 Modal amplitudes through the duct from an initial condition calculated by the inverse method

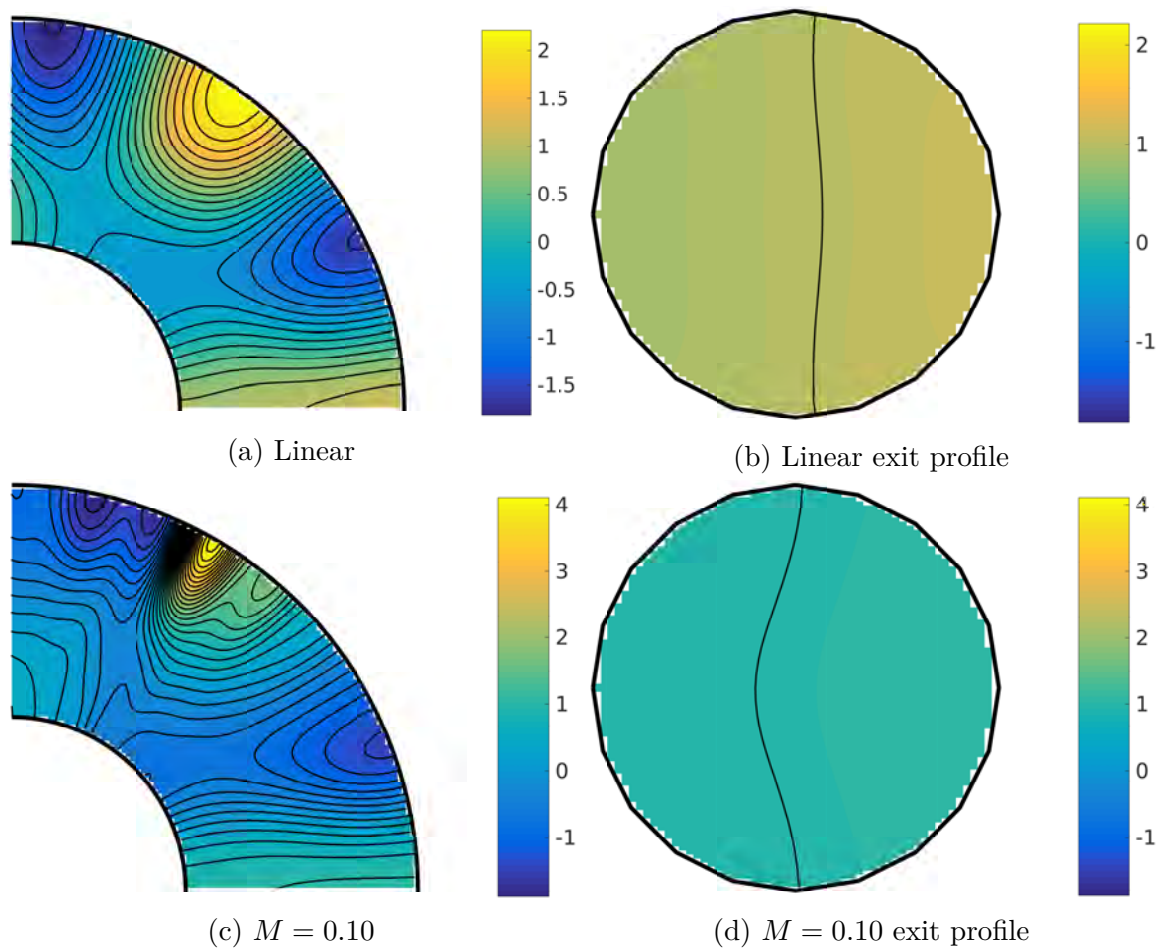


Fig. E.3 Pressure profile of the curved duct from chapter 3 with initial condition calculated by the inverse method